UNIVERSITY OF PERUGIA

UNIVERSITY OF COPENHAGEN
FACULTY OF SCIENCE

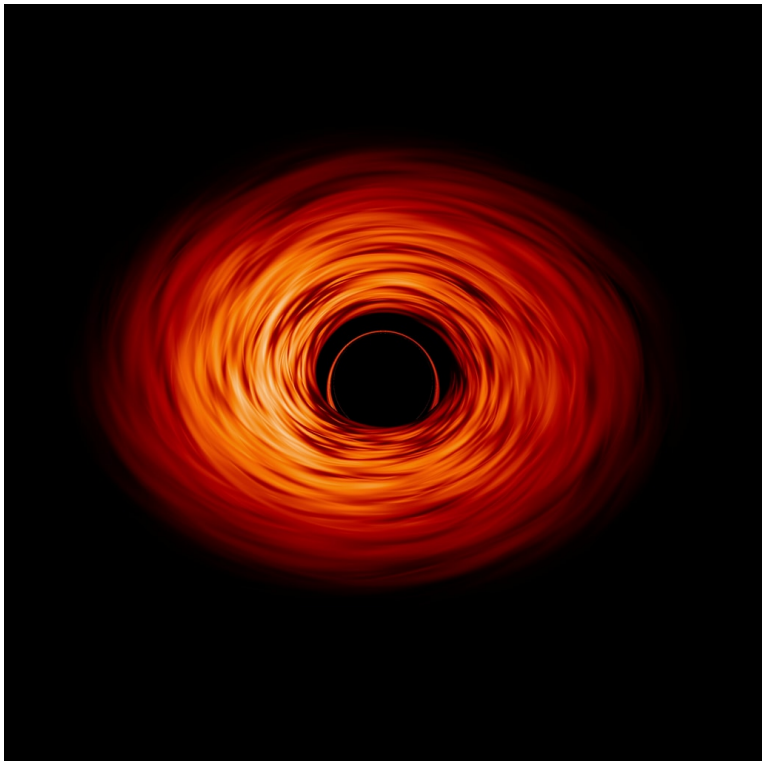

PhD thesis

Black hole dynamics in tidal environments

Daniele Pica

Advisors: Troels Harmark, Marta Orselli

Submitted: October 31, 2024

This thesis has been submitted to the PhD School of The Faculty of Science, University of Copenhagen and to the PhD school of the University of Perugia

Front Picture Credit: NASA's Goddard Space Flight Center/Jeremy Schnittman.

Declaration of Authorship

I, Daniele Pica, declare that this thesis titled "Black hole dynamics in tidal environments" is the outcome of my own work and of the scientific collaborations listed below, except where specific reference is made to the work of others. This Thesis is based on the following research papers published either in preprint servers and in peer-reviewed journals and listed in chronological order.

- *Event horizon of a charged black hole binary merger.*

  AUTHORS:
  D. Mar´in Pina, M. Orselli, D. Pica

  JOURNAL:
  Physical Review D, volume 106, article id. 084012 (2022).

  DOI: 10.1103/PhysRevD.106.084012

  URL: https://doi.org/10.1103/PhysRevD.106.084012

  PREPRINT: https://arxiv.org/abs/2204.08841

  COMMENTS:
  Part of the content of this paper has been adapted in Sec. 3.1 of this Thesis.

- *Tidal deformations of a binary system induced by an external Kerr black hole.*

  AUTHORS:
  F. Camilloni, G. Grignani, T. Harmark, R. Oliveri, M. Orselli, D. Pica

  JOURNAL:
  Physical Review D, volume 107, article id. 084011 (2023).

  DOI: 10.1103/PhysRevD.107.084011

  URL: https://doi.org/10.1103/PhysRevD.107.084011

  PREPRINT: https://arxiv.org/abs/2301.04879

  COMMENTS:
  Part of the content of this paper has been adapted in Sec. 2.1.

- *Binary mergers in strong gravity background of Kerr black hole.*

  AUTHORS:
  F. Camilloni, T. Harmark, G. Grignani, M. Orselli, D. Pica

  JOURNAL:
  Monthly Notices of the Royal Astronomical Society, volume 531, Issue 1, Pages 1884 - 1904 (2024).

DOI: 10.1093/mnras/stae1093

URL: https://doi.org/10.1093/mnras/stae1093

Preprint: https://arxiv.org/abs/2310.06894

Comments:

Part of the content of this paper has been adapted in Sec. 1.2.

The papers listed above are the outcome of my research activity, conducted at the University of Perugia and at the University of Copenhagen between November 2021 and November 2024.

Part of the Thesis has been available through arxiv.org with these references:

- 10.1103/PhysRevD.106.084012,
  PDF available at https://arxiv.org/abs/2204.08841.
- 10.1103/PhysRevD.107.084011,
  pdf available at https://arxiv.org/abs/2301.04879.
- 10.1093/mnras/stae1093.
  pdf available at https://arxiv.org/abs/2310.06894.

Contents

Introduction

Since their first detection back in 2015 [1], gravitational waves have provided us invaluable information about the Universe [2–7], especially when it comes to black holes and binary systems. In fact the first signal of gravitational waves not only represents the first direct proof of the existence of binary black hole (BBH) systems but also it gives us confirmation that black holes do merge out there in the Universe. Since then, we detected an increasing number of binary black hole mergers [8], motivating the scientific community to analyse in detail the dynamical evolution of BBH systems, with a particular attention on possible formation channels for black hole - black hole binaries [9–11] and moreover possible mechanisms that could lead to mergers happening on an a timescale shorter than the age of the Universe [12–14]. The latter problem arises from the fact that for a BBH system to merge by emission of gravitational waves on a reasonable timescale[1], it requires either the binary to have a large eccentricity (close to 1) or the two companions to be very close to each others. This can be seen by simply considering that the timescale needed for a BBH system to merge by emission of gravitational waves is proportional to a prefactor given by $\left(1-e^2\right)^{7/2}$ [15, 16], where e is the eccentricity of the binary system. It is clear that as the eccentricity approaches 1, the emission of gravitational waves becomes more efficient leading to a faster merger. On the other hand, if we assume that the BBH system is a circular one ($e = 0$), the merger time due to emission of gravitational waves can be written as [17]

$$\tau_{\rm GW} = \frac{5}{256}\frac{c^5}{G^3}\frac{a^4}{M^2\mu} = 10^{10}\,\text{years}\left(\frac{20M_\odot}{M}\right)^2\frac{5M_\odot}{\mu}\left(\frac{a}{0.0888\,\text{AU}}\right)^4, \qquad (1)$$

where a is the semi-major axis of the binary, M and μ are respectivey the total mass and the reduced mass of the system, namely $M = m_1 + m_2$ and $\mu = m_1 m_2/(m_1 + m_2)$, with $m_{1,2}$ the masses of the two black holes. For a BBH system similar to the one detected with the first gravitational wave signal GW150914 [1], i.e. $M = 65\,M_\odot$ and $\mu = 16\,M_\odot$, the merger time would be smaller than the age of the Universe if its semi-major axis is smaller than $a \leq 0.23\,\text{AU}$.

[1] Here with reasonable we mean a timescale shorter than the age of the Universe.

One possible merging channel that could speed up the merger of a BBH system consists in assuming that the binary system is not an isolated one but instead it is interacting with an external third object, forming a triple system [17–24]. The presence of a third body can lead to faster mergers, compared to the case of an isolated binary, mostly because of the so-called von Zeipel - Lidov - Kozai (ZLK) mechanism [25–29], i.e. a secular effect in triple systems that can trigger oscillations in both the eccentricity and inclination of the BBH system in a periodic fashion. During these oscillations the eccentricity of the BBH system can reach values close to 1, yielding to a more efficient emission of gravitational waves and thus to a faster merger [19, 20, 30].

This has motivated people in recent years to study black hole triple systems in different context: analysing possible formation channels [31–34], studying secular effects in triple systems [20, 35–40], including relativistic effects to the evolution of the BBH system [41–45] and investigating non-secular effects such as resonances [46–49]. In all these contexts triple systems have been studied assuming that the distance between the binary system and the tertiary was large enough to use Newtonian physics to describe the dynamical evolution of the triple system, using a Post Newtonian (PN) expansion to include relativistic effects. This approach works very well in astrophysical settings where the distances at play are large enough compared to the characteristic scales of the three objects in the triple system. However, motivated by the fact that the upcoming interferometers LISA [50] and the Einstein Telescope [51] will be able to detect gravitational waves emitted by binaries in triple systems evolving in a strong gravity regime, i.e. when the distances at play are of the same order of the characteristic scale of the tertiary object, people have started to focus their attention on possible mechanisms leading to the formation of BBH systems close to an external supermassive black hole. These mechanisms are usually referred to as *migration mechanisms* [52–57] and can efficiently lead to binaries merging in regions close to the center of galaxies where strong gravitational effects can significantly affect the evolution of the system. Moreover in this context, Extreme Mass Ratio Inspirals (EMRIs) play a key role in the future of gravitational waves and in analysing the strong gravity regime [58–63]. EMRIs are binary systems where the primary companion is much larger than the secondary one and, as a consequence of this huge difference in the masses, the latter is expected to undergo several orbital cycles in the near-horizon region of the former where its evolution is dominated by strong gravity effects [50, 64]. Recent works have shown how a fraction of EMRI systems are expected to be b-EMRIs, i.e. binary Extreme Mass Ratio Inspirals, where the lighter companion is not a single compact object but rather a binary system, making b-EMRIs actually hierarchical triple systems [65–68]. Again, the large difference in the masses between the binary system and the primary companion in the b-EMRI makes it so that the former will spend the last phase of its evolution in the strong gravity region around the latter, where it will emit gravitational waves detectable by the future interferometers.

In these scenarios, where the binary system is close to the tertiary object, the Newtonian approximation breaks down and we need to use General Relativity instead to describe properly the dynamics of the triple system. This motivates us to analyse, in this thesis, black hole triple systems in the context of a strong gravity regime, using General Relativity instead of Newtonian Physics to describe the evolution and the dynamics of a BBH system orbiting closely around a supermassive black hole. More in details, this thesis is structured as it follows:

- In Chapter 1 we analyse how the dynamics of a BBH system, with two black holes of comparable masses, is affected by the presence of an external supermassive Kerr black hole. We start by giving a brief overview about triple systems in the Universe, mentioning possible formation channels and introducing the stability condition needed for a triple system to evolve without being disrupted. Next we introduce the concept of *secular timescale* and we focus our attention on the ZLK mechanism, providing the key elements for understanding how it works and presenting a brief review on how it has been described previously in the literature. We then move to the original contribution in this research field, i.e. the analysis of the ZLK mechanism in the context of strong gravity regime. This is done by describing the BBH system using the point particle approximation, i.e. assuming that the distance between the two black holes is larger than their characteristic size, but the tidal interaction between the binary and the external body is treated in a full General Relativistic manner, describing the supermassive black hole through the Kerr metric. This approach allows us to introduce strong gravity effects, generated by the tertiary, in the dynamical evolution of the BBH system. Practically speaking this is done by introducing the multipole electric $\mathcal{E}_{a_1,a_2,\dots,a_j}$ and magnetic tidal moments $\mathcal{B}_{a_1,a_2,\dots,a_j}$, which encode all the information about the tidal interaction between the binary system and the supermassive Kerr black hole. We carry out the analysis in two different reference frames, a local-inertial one moving together with the BBH system and a non-inertial one associated with an asymptotic observer. We find that strong gravity effects can significantly enhance the ZLK mechanism, leading to a higher frequency for the eccentricity and inclination oscillations which results in a faster merger for the binary system compared to the one predicted by the Newtonian description of the triple system. Moreover with our approach we can provide a complete expression for the *gyroscope precession*, i.e. the precession of the angular momentum of the BBH system around the direction identified by the angular momentum of the external black hole, which expanded with a PN expansion gives back the results already known in the literature plus new higher order corrections. We also check that we included the effect of the spin of the supermassive

black hole consistently in the dynamics of the BBH system by using again a PN expansion and checking that the lower orders agree with the already known results in previous works. Finally we conclude our analysis by studying the peak frequency of the gravitational waves emitted by the binary system in the strong gravity regime, more precisely in the extreme case where the BBH system is orbiting along the Innermost Stable Circular Orbit (ISCO) of the supermassive Kerr black hole, including the effect of the gravitational redshift and connecting our results with the future space-based interferometers. We show how the Newtonian description cannot capture properly the dynamics of the BBH system in the strong gravity regime and, as consequence, how a General Relativistic description is needed to correctly understand the merger of a binary system in this extremely important scenario for the future of gravitational waves.

- In Chapter 2 we analyse the scenario of an EMRI system, where the two companions are a Schwarzschild black hole and a test particle, orbiting around a supermassive Kerr black hole. Firstly we give a brief overview on EMRIs, enlightening their properties, possible formation channels and their relevance for the future interferometers such as LISA. We then move to the original part of this Chapter, which consists in studying how a tidal environment, sourced by a supermassive Kerr black hole, deforms the orbits of the test particle around the Schwarzschild black hole in the EMRI system, focusing our attention on the ISCO and the light ring. To this end we start by constructing the electric and magnetic tidal moments, up to the first order in their multipole expansion, which encode all the information about the source of the tidal environment and which we use to describe the interaction between the external body and the EMRI. Note that the electric tidal moments were already known in the literature [69], while the magnetic ones have never been computed before in a generic scenario and thus they represent a novel result. Following Ref. [70], we use the electric and magnetic tidal moments to write the metric for a tidally deformed Schwarzschild black hole which we then use, together with the four-velocity of the test particle, to build the Hamiltonian describing the EMRI system in a tidal environment. Finally we apply this formalism to study how the ISCO and the light ring of the Schwarzschild black hole get deformed by the presence of an external tidal field. In particular we are interested in tidal effects that stick to the dynamics of the test particle for more than just one orbit around the primary companion, thus for this reason we eliminate the fast motion in the dynamics of the EMRI system by averaging over one orbital cycle of the test particle around the Schwarzschild black hole. This allows us to find the secular shifts induced by the external supermassive black hole on the parameters characterizing the ISCO and

the light ring of the EMRI. The tidal corrections are written in terms of an effective perturbative parameter, which contains all the information about the tidal environment and the orientation of EMRI system with respect to its orbit around the Kerr black hole. In our analysis we find that depending on the orientation, which is specified thanks to a set of Euler angles, the presence of a tidal field can either shrink or expand the radial position of both the ISCO and the light ring. Moreover there is a specific configuration for the binary for which the two orbits do not feel the presence of the external tidal field and thus they do not get deformed. Lastly we also show how in the case of strong gravity regime, i.e. when the EMRI system is orbiting closely to the supermassive black hole, the tidal deformations are stronger than the ones in the scenario where the binary is far away from the source of the tidal field. This last scenario has already been analysed, in less general settings, in Refs. [71, 72] and we recover their results by choosing a specific orientation for the binary system and by taking the limit $\hat{r} \to \infty$, where $\hat{r}$ represents the distance between the EMRI system and the source of the tidal environment.

- In Chapter 3 we focus our attention on charged black hole binaries. Given that it is widely believed that charged black holes do not exist in the Universe, we start this Chapter by presenting some motivations for which we should include the presence of charge in binary systems. Firstly we review some possible charging mechanisms that could potentially lead black holes to have a small amount of electric charge which might be preserved thanks to the presence of an electromagnetic field [73]. Secondly we include the possibility of having magnetically charged black holes, which are more stable than their electric counterparts [74] and have drawn a lot of attention in the scientific community in recent years [74–77]. Thirdly we argue that the inclusion of an extra parameter in the description of a BBH system allows us to study a more general scenario than the one depicted by only neutral black holes, since it can be used as a toy model to describe the more astrophysically relevant (but often computationally harder to analyse) case of spinning black holes. After giving some motivations for including the charge in BBH systems, we introduce the original part of this Chapter, which consists in analysing two different aspects of charged binaries.

  In the first one we study the evolution and the formation of the event horizon during the merger of an EMRI system, where the lighter companion is a charged black hole. Following Ref. [78], this can be done analytically by implementing the EMR limit, which consists in taking $m/M \to 0$, where m and M are the masses of respectively the secondary and the primary companions in the EMRI. To study the evolution of the event horizon of the charged black hole during the merger we need to be able to analyse its geometrical structure, thus the EMR limit must

be satisfied by keeping the size of the smaller object fixed while sending the size of the larger one to infinity, namely $M \to \infty$. Then, in this approximation, the procedure to extract the evolution of the event horizon during the merger proceeds as follows: we start by considering the configuration of the event horizon at future null infinity and we trace back in time the null geodesics generating the event horizon until they meet each others in a caustic point [78]. We compute different parameters characterizing the merger of the EMRI system, such as the pinch-on coordinate representing when the two black holes touch, the duration of the merger and the increase in the area of the event horizon of the charged black hole. What we find, comparing our results with the ones obtained in the case of a neutral EMRI [78], is that as the charge of the small black hole increases, the merger happens closer to its center and becomes quicker. Lastly we extend our analysis to the case of a charged BBH merger in higher dimensions than 4, where after extracting numerically the evolution of the event horizon during the merger we find that in $D > 4$ dimensions, as a consequence of the steeper r dependence in the metric describing the charged black hole [2], the merger happens faster and closer to the center of the small black hole in the EMRI system compared to the astrophysical scenario in 4 dimensions.

In the second part of Chapter 3 instead, we analyse the dynamics of an EMRI system moving in a tidal environment which we will keep completely general, without specifying its source. We will follow the same steps introduced in Chapter 2 for the case of a neutral EMRI, but this time the primary companion in the binary system will be a charged black hole described by the Reissner–Nordström (RN) metric and moreover we will consider the secondary companion to carry a small amount of charge. Our goal in this analysis is to first write down the metric of a tidally deformed RN black hole, which we do by following Ref. [77], and second to use this result to study how the dynamics of the test particle in the EMRI system is affected by the presence of an external tidal environment, in particular focusing our attention on the role of the charge of the primary companion in the tidal deformations induced on the dynamics of the binary system. As a practical application of our formalism we compute the tidal shifts induced on the parameters characterizing the ISCO and the light ring of the RN black hole, showing how they change as the charge increases until it reaches is maximum value at extremality. We find that as the charge increases, the tidal corrections become smaller approaching their minimum (but finite) value for an extremal black hole. This is a consequence of the fact that as the charge of the RN black hole reaches its maximum value, its throat elongates,

[2] Here the charged black hole will be described using the Reissner–Nordström metric and r represents the radial coordinate in the charged spacetime.

dragging both the ISCO and the light ring closer to its center, resulting in a suppression of the tidal effects. Moreover, since both the primary and the secondary companions in the EMRI system possess a charge, the tidal deformations will have both a gravitational and an electromagnetic contribution. In our analysis we will consider only gravitational static tides, thus the gravitational contribution in the tidal effects will be larger than its electromagnetic counterpart.

- In Chapter 4 we present our concluding remarks and possible future directions for the analysis presented in this thesis.

Chapter 1

Triple Systems and Secular Effects

It is widely known that almost every large galaxy has a supermassive black hole at its center [79, 80]. Thus for two compact objects forming a binary system in these environments it is very unlikely to evolve as an isolated binary since they will feel the presence of the supermassive black hole in their dynamical evolution. Moreover back in the late 1900s, it was already known that at least 35% of stars binaries had a third companion moving on a wider orbit [81] and today more analysis on triple stars systems have confirmed that they are quite common in the Universe [82–87]. A clear example of a triple system is the 4U 1820-30 low-mass X-ray binary whose short binary period has been explained by including the presence of a third companion [88, 89]. Triple systems are also very relevant in the formation and evolution of giant gas planets, especially if these objects form in stellar environments where they form a binary system star-Hot Jupiter. It has been shown how the presence of a third body orbiting these binaries can induce a migration mechanism that would help us understand how these systems form and evolve [90–94]. Even by looking at our surroundings we can find a lot of examples of triple systems: the most obvious one is the Sun-Earth-Moon system, which has been widely studied, but also smaller objects, such as asteroids, can form binary systems [95–98] and be affected by the presence of the Sun. Finally in recent years a lot of binary black hole systems have been detected with LIGO-Virgo-Kagra thanks to the emission of gravitational waves [99]. In this context the interaction of a binary black hole system with a third body, thus forming a triple system, can alter significantly the signature of the gravitational wave detected [100–105], giving us a better insight on what is really happening out there in the Universe. Moreover the presence of a third companion altering the evolution and merger of a binary black hole system is a very common scenario, especially if the binary is forming in dense stellar systems [106–110].

Even though there are different mechanisms that can lead to the formation

of stable triple systems, such as binary - binary encounters [31] or binary - single - single interactions [32], there are also a lot of scenarios where strong gravitational perturbations between the inner and outer orbit or mass loss from stellar wind can contribute to the ejection of one of the three bodies, leading to the disruption of the triple system [111, 112]. Thus to study the stability of triple systems and to understand in which astrophysical scenarios it is possible for them to evolve dynamically in a stable configuration for a long period of time is of paramount importance. On this context, in the literature have been proposed different stability criteria for triple systems that relate the parameters of the inner binary with the ones of the outer binary. One of the most used in astrophysical settings is the one proposed by Mardling and Aarseth in 2001 [113] which states:

$$a_{\rm out} > 2.8\, a_{\rm in} \left[(1+q_{\rm out}) \frac{1+e_{\rm out}}{(1-e_{\rm out})^{1/2}} \right]^{2/5}, \tag{1.1}$$

where $a_{\rm out}(a_{\rm in})$ is the semi-major axis of the outer (inner) binary, $e_{\rm out}$ is the outer eccentricity and $q_{\rm out} = m_3/(m_1+m_2)$ with m_3 the mass of the tertiary while m_1 and m_2 are the masses of the two bodies in the inner binary. A simplified version of this stability criteria is the one presented in [35, 114], which relates the semi-major axes ($a_{\rm out}$, $a_{\rm in}$) and the masses (m_3, m_1, m_2) of the inner and outer binaries, namely

$$a_{\rm out} \geq r_{\rm tide} \approx a_{\rm in} \left(3 \frac{m_3}{m_1+m_2} \right)^{1/3}. \tag{1.2}$$

The two stability conditions defined in (1.1) and (1.2) imply that in order for a triple system to be stable a hierarchical configuration is required. This means that the outer orbit needs to be much larger than the inner one ($a_{\rm out} > a_{\rm in}$), in other words the third body has to be sufficiently far away from the inner binary in order to avoid tidal disruption phenomena. For the purpose of this thesis we will focus our attention only on stable triple systems. The hierarchical configuration required means that the dynamics of the system will take place on a timescale much longer than both the orbital period of the inner and outer binary [115], usually called *secular timescale*. Thus in order to study the evolution of the orbital parameters describing the two orbits, we need to apply the *secular approximation*, which consists in averaging out the fast timescales characterizing the triple system.

1.1 von Zeipel Lidov Kozai Mechanism

One of the most, if not the most, relevant secular effect is the von Zeipel - Lidov - Kozai (ZLK) mechanism, which in this subsection we quickly review, enlightening the most relevant results achieved in the literature in the past

years. This part of the thesis, namely the review of the ZLK mechanism, is heavily based on Ref. [20].

To find the first trace of the ZLK mechanism in literature we have to go way back to 1910, when the astronomer and mathematician Edvard Hugo von Zeipel published his paper on the periodic motion of comets [25], where he already introduced all the key elements describing the ZLK mechanism. Unfortunately his work on the subject went unnoticed until recent years and the credits for this mechanism have been usually given for a long time only to the Soviet scientist Michail L'vovich Lidov and the Japanese astronomer Yoshihide Kozai, who independently established in the 1960s the theoretical framework for this phenomenon. The former showed in his paper [26], focused on the motion of satellites, that it is possible for the argument of pericenter of a perturbed orbit to librate rather than circulate [116], while the latter reached the same conclusion on his paper [27] where he analysed how the secular motion of asteroids with a high inclination is affected by the presence of Jupiter.

Both Lidov and Kozai in their above mentioned works were interested in a hierarchical three body system, consisting in an *inner binary* formed by two objects with masses m_1 and m_2 and a third much more massive object m_3 orbiting around (m_1, m_2) on a much larger orbit than the inner one, which is usually referred to as the *outer orbit*, forming with the center of mass of the inner binary the so called *outer binary* as depicted in Fig. 1.1. In this setup it is possible to study the dynamics of the problem using the secular approximation where, on a timescale much longer than the period of both the inner and outer orbit, the interaction between the two makes them exchange angular momentum in such a way that their mutual inclination and both the eccentricities of the two orbits can oscillate in time, keeping fixed the semi-major axes of both the inner (a_1) and outer (a_2) orbit [117]. Moreover in the hierarchical approximation it is possible to treat the inner and outer orbit separately as two Keplerian orbits, using Newtonian physics to describe their motion. As a consequence the Hamiltonian of the triple system can be written as the sum of contributions describing the motion of the inner binary, i.e. the relative motion of the body with mass m_1 around the body with mass m_2, the dynamics of the outer binary, i.e. the one describing the motion of the third body with mass m_3 around the center of mass of the inner binary, plus a third term describing the gravitational interaction between the two orbits [118]. Given that both the semi-major axes of the inner and outer orbits remain constant during the secular evolution of the triple system, and given the hierarchical nature of the problem which ensures that $a_1 \ll a_2$, it is natural to use the ratio a_1/a_2 as a small perturbative parameter to expand the gravitational potential describing the interaction between the inner and outer binary [26,27]. Thus the Hamiltonian of a hierarchical triple system can

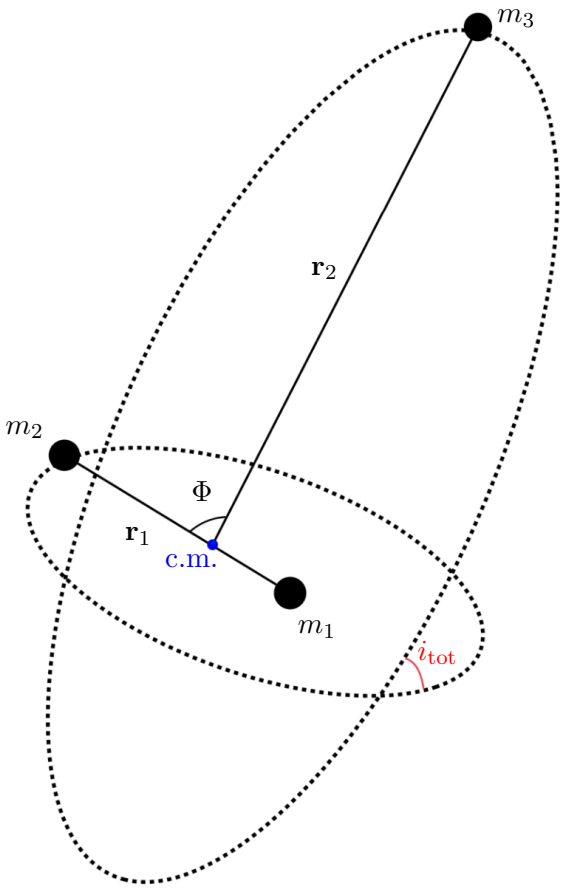

Figure 1.1: Schematic representation of a three body system (not in scale). The two bodies m_1 and m_2 form the inner binary, where $\mathbf{r}_1$ is the relative distance between them. C.m. represents the center of mass of the inner binary and together with the tertiary body m_3, placed at a distance $\mathbf{r}_2$ from the c.m., form the outer binary. Finally $i_{\rm tot}$ represents the total inclination between the inner orbit and the outer one, while Φ defines the angle between $\mathbf{r}_1$ and $\mathbf{r}_2$.

the be written as [20, 118]

$$\begin{aligned} H =& \frac{Gm_1m_2}{2a_1} + \frac{Gm_3(m_1+m_2)}{2a_2} \\ &+ \frac{G}{a_2}\sum_{n=2}^{\infty}\left(\frac{a_1}{a_2}\right)^n M_n \left(\frac{r_1}{a_1}\right)^n \left(\frac{a_2}{r_2}\right)^{n+1} P_n\left(\cos\Phi\right), \end{aligned} \tag{1.3}$$

where we introduced $\mathbf{r}_1$ and $\mathbf{r}_2$ as the vectors identifying respectively the relative position from m_1 to m_2 and from m_3 to the center of mass of the inner binary, as depicted in Fig. 1.1. Moreover G is the gravitational constant, P_n the Legendre polynomials, Φ the angle between $\mathbf{r}_1$ and $\mathbf{r}_2$ and finally M_n is defined as

$$M_n = m_1m_2m_3\frac{m_1^{n-1}-(-m_2)^{n-1}}{(m_1+m_2)^n}. \tag{1.4}$$

Given that both the inner and outer motions are periodic, as usually in celestial mechanics, it is convenient to analyse the problem using the action-angle formalism. After choosing the z axis along the direction of the total angular momentum, i.e. working in the *invariable plane* reference frame, we can use the Delaunay variables [119] to treat the dynamics of our hierarchical triple system. This set of variables consist in three angles and three conjugate momenta for both the inner and outer orbit. Firstly we introduce the angle variables, using the subscript 1 (2) for the inner (outer) elements:

- *mean anomalies*: they tell us where the objects are in their orbits and we denote them as l_1 and l_2;
- *arguments of periastron*: they define the position of the eccentricity vectors, we indicate them with g_1 and g_2;
- *longitudes of ascending nodes*: they represent the angle between the reference direction and the direction of the ascending node, where this last one is the point where the orbit crosses the plane of reference. We denote them with h_1 and h_2.

The conjugate momenta associated with these angle variables are respectively:

- the conjugate momenta to the mean anomalies, L_1 and L_2, which are defined as
$$L_1 = \mu_1\sqrt{Gma_1}, \quad L_2 = \mu_2\sqrt{GMa_2}; \tag{1.5}$$
- the conjugate momenta to the arguments of periastron, G_1 and G_2, which can be written as
$$J_1 = L_1\sqrt{1-e_1^2}, \quad J_2 = L_2\sqrt{1-e_2^2}; \tag{1.6}$$

- the conjugate momenta to the *longitudes of ascending nodes*, $J_{1,z}$ and $J_{2,z}$, which can be written as

$$J_{1,z} = J_1 \cos i_1, \quad J_{2,z} = J_2 \cos i_2; \tag{1.7}$$

where we introduced the eccentricity e_1 for the inner orbit and e_2 for the outer one, the reduced mass μ_1 (μ_2) and the total mass m (M) for the inner (outer) binary defined as

$$\begin{aligned} \mu_1 &= \frac{m_1 m_2}{m_1 + m_2}, \quad \mu_2 = \frac{m_3(m_1 + m_2)}{m_1 + m_2 + m_3}, \\ m &= m_1 + m_2, \quad M = m_1 + m_2 + m_3, \end{aligned} \tag{1.8}$$

and finally i_1 (i_2) which represents the inclination of the inner (outer) orbit with respect to the direction of the total angular momentum $\mathbf{J}_{\rm tot}$, as can be seen from Fig. 1.2. The conjugate momenta to the arguments of periastron, J_1 and J_2, can be interpreted as the absolute values for the angular momentum vectors ($\mathbf{J}_1$ and $\mathbf{J}_2$) respectively of the inner and outer orbit while the action variables associated to the longitudes of ascending nodes, $J_{1,z}$ and $J_{2,z}$, represent the z-component of $\mathbf{J}_1$ and $\mathbf{J}_2$. Given the choice we made for our reference system, i.e. the z axis aligned with the direction of the total angular momentum, it is straightforward to check that the magnitude of $\mathbf{J}_{\rm tot}$ is given by

$$J_{\rm tot} = J_{1,z} + J_{2,z}. \tag{1.9}$$

Moreover we can write some geometrical relations between the angular momenta of the system which will be useful later in this section, namely

$$\cos i_{\rm tot} = \frac{J_{\rm tot}^2 - J_1^2 - J_2^2}{2 J_1 J_2}, \tag{1.10}$$

$$J_{1,z} = \frac{J_{\rm tot}^2 + J_1^2 - J_2^2}{2 J_{\rm tot}}, \tag{1.11}$$

$$J_{2,z} = \frac{J_{\rm tot}^2 + J_2^2 - J_1^2}{2 J_{\rm tot}}, \tag{1.12}$$

where $\mathbf{J}_{\rm tot} = \mathbf{J}_1 + \mathbf{J}_2$ and we introduced the total inclination $i_{\rm tot} = i_1 + i_2$, see Fig. 1.2.

With the introduction of the mean anomalies l_1 and l_2 for both the inner and outer orbit it is immediate to isolate the short timescales in the Hamiltonian (1.3) that has to be averaged out in order to study the *secular dynamics* of the triple system and thus the ZLK mechanism. This can be done since, as we already mention above, the two orbits can be treated as Keplerian ones with conserved energies, and this allow us to use the secular approximation. There are different ways to get rid of the short timescales in the Hamiltonian, one of them is to average out the mean anomalies l_1 and l_2 by simply

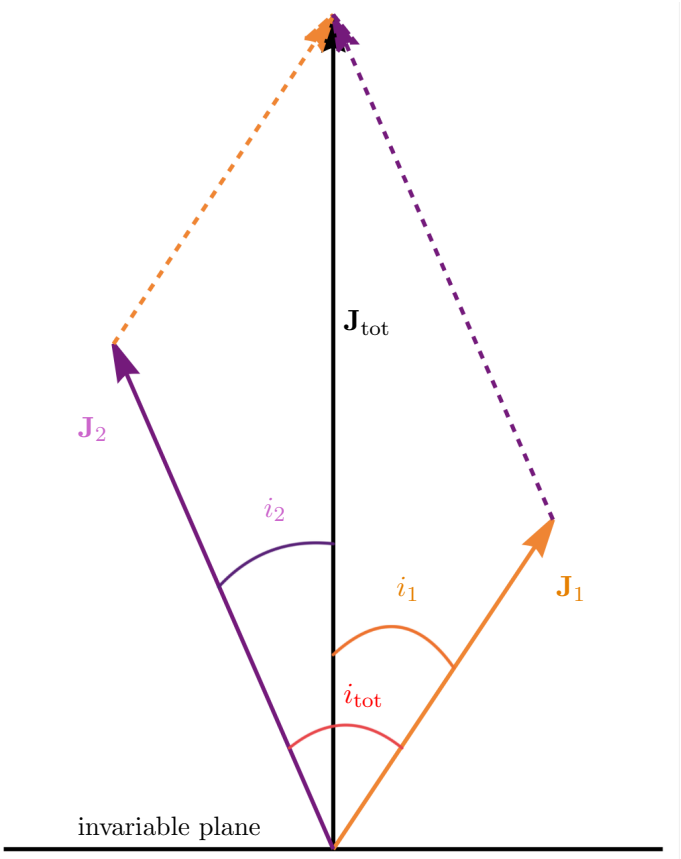

Figure 1.2: Schematic representation of the angular momentum vectors. $\mathbf{J}_1$ and $\mathbf{J}_2$ represent respectively the angular momentum of the inner and outer binary, while $\mathbf{J}_{\rm tot} = \mathbf{J}_1 + \mathbf{J}_2$ is the total angular momentum, aligned along the z-axis and perpendicular to the invariable plane. Meanwhile i_1 and i_2 depict the inclination of the inner and outer angular momenta with respect to $\mathbf{J}_{\rm tot}$. Finally $i_{\rm tot}$ denotes the total mutual inclination, i.e. $i_{\rm tot} = i_1 + i_2$.

integrating the Hamiltonian (1.3) as [120]

$$\langle H \rangle = \frac{1}{(2\pi)^2} \int_0^{2\pi} dl_1 \int_0^{2\pi} dl_2 \, H. \tag{1.13}$$

Another method to study the secular dynamics is to use a canonical transformation, usually called the von Zeipel transformation [121], where a time independent generating function periodic in l_1 and l_2 is introduced to get rid of the mean anomalies in the Hamiltonian [37].

As the analytical mechanics teaches us, every time the Hamiltonian does not depend on an angle variable, its conjugate momentum is conserved. In our case this means that after averaging out l_1 and l_2, the conjugate momenta L_1 and L_2 are conserved. This can be seen explicitly by writing down the

equations of motions [122]:

$$\begin{aligned} \frac{dL_k}{dt} &= \frac{\partial H}{\partial l_k}, \quad & \frac{dl_k}{dt} &= -\frac{\partial H}{\partial L_k}, \\ \frac{dJ_k}{dt} &= \frac{\partial H}{\partial g_k}, \quad & \frac{dg_k}{dt} &= -\frac{\partial H}{\partial J_k}, \\ \frac{dJ_{k,z}}{dt} &= \frac{\partial H}{\partial h_k}, \quad & \frac{dh_k}{dt} &= -\frac{\partial H}{\partial J_{k,z}}, \end{aligned} \tag{1.14}$$

where $k = 1, 2$. By using the explicit expressions (1.5), (1.6) and (1.7) for the conjugate momenta it is possible to use the equations of motion defined in (1.14) to study the evolution of the orbital parameters such as the eccentricity and the inclination angle between the inner and outer orbit, namely

$$\begin{aligned} \frac{de_k}{dt} &= \frac{\partial e_k}{\partial J_k}\frac{\partial H}{\partial g_k}, \\ \frac{d\cos i_k}{dt} &= \frac{\dot{J}_{k,z}}{J_k} - \frac{\dot{J}_k}{J_k}\cos i_k. \end{aligned} \tag{1.15}$$

The conservation of L_1 and L_2 yields to the fact that both the semi-major axes a_1 and a_2 of the inner and outer orbit remain constant during the evolution of the triple system. Thus, as already pointed out previously, the ratio a_1/a_2 is a good small perturbative parameter that we can use to expand the interaction part of the Hamiltonian (1.3).

1.1.1 Quadrupole Approximation

The expansion of the Hamiltonian (1.3) is a multipole expansion where the first order is called *quadrupole approximation* and it is proportional to $\left(a_1/a_2\right)^2$. This level of approximation was already reached by the pioneers von Zeipel, Kozai and Lidov in their works mentioned above and they found that not only the total angular momentum of the triple system $\mathbf{J}_{\rm tot}$ is conserved but also the angular momentum $\mathbf{J}_2$ of the outer orbit remains constant during the secular evolution [123]. This means that the quadrupole approximation can be used only to describe scenarios where the outer orbit is symmetric under rotation, i.e. when we have an outer axisymmetric potential.

For the scope of this thesis we will restrict ourselves to analyse the most simple case that satisfies the quadrupole approximation, i.e. the scenario where the outer orbit is circular. To study the evolution of the orbital parameters it is convenient to rewrite explicitly the Hamiltonian (1.3) in terms of the Delaunays variables we introduced above. Up to the quadrupole order

this yields to

$$H = \frac{Gm_1m_2}{2a_1} + \frac{Gm_3(m_1+m_2)}{2a_2} + 4\frac{G^2(m_1+m_2)^7m_3^7}{16(m_1m_2)^3(m_1+m_2+m_3)^3}\frac{L_1^4}{L_2^6}\left(\frac{r_1}{a_1}\right)^2\left(\frac{a_2}{r_2}\right)^3(3\cos 2\Phi+1) \tag{1.16}$$

The next step in studying the secular dynamics of the triple system is to eliminate the short timescales associated with the inner and outer orbits. This can be achieved by integrating out the mean anomalies l_1 and l_2 from the Hamiltonian (1.16), leading to the secular quadrupolar Hamiltonian [37]:

$$\begin{aligned} H_{\rm quad} = \frac{C_2}{8}\Big[&(1+3\cos(2i_2))\left((2+3e_1^2)(1+3\cos(2i_1))+30e_1^2\cos(2g_1)\sin^2 i_1\right)\\ &+3\cos(2\Delta h)\left(10e_1^2\cos(2g_1)(3+\cos(2i_1))+4(2+3e_1^2)\sin^2 i_1\right)\sin^2 i_2\\ &+12(2+3e_1^2-5e_1^2\cos(2g_1))\cos(\Delta h)\sin(2i_1)\sin(2i_2)\\ &+120e_1^2\sin(2g_1)\left(\sin i_1\sin(2i_2)\sin(\Delta h)-\cos i_1\sin^2 i_2\sin(2\Delta h)\right)\Big], \end{aligned} \tag{1.17}$$

where C_2 can be written as

$$C_2 = \frac{G^2}{16}\frac{\left[(m_1+m_2)m_3\right]^7}{\left[(m_1+m_2+m_3)m_1m_2\right]^3}\frac{L_1^4}{L_2^3J_2^3}, \tag{1.18}$$

and we defined $\Delta h = h_1 - h_2$. To further simplify the expression (1.17) we can use a well known procedure called *elimination of nodes* [27, 124], which consists in setting

$$h_1 - h_2 = \pi. \tag{1.19}$$

It is important to mention that this relation can only be used when the total angular momentum of the system is conserved, as it is in our case. A common mistake when applying the elimination of nodes is to naively conclude that, since the Hamiltonian no longer depends on the angles h_1 and h_2, the associated conjugate momenta $J_{1,z}$ and $J_{2,z}$ are conserved. As shown by previous works in the literature [37, 124] this is not always the case and can lead to significantly different equations of motion. To avoid this mistake one should apply the condition (1.19) only after deriving the equations of motion for the triple system, or alternately the elimination of nodes can be directly used on the Hamiltonian (1.17) as long as the evolution equations for the inclination i_1 and i_2 are derived from the conservation of the total angular momentum $J_{\rm tot}$ and not from the canonical relations defined in (1.14). For a more detailed analysis on the elimination see [37, 124]. Note that it is also possible to study the evolution of the triple system avoiding the elimination of nodes, see [125–128].

Since in our analysis the total angular momentum is conserved, we can safely apply the relation (1.19) to the quadrupolar Hamiltonian defined in (1.17), which simplifies to

$$H_{\rm quad} = C_2 \left[(2+3e_1^2)(3\cos^2 i_{\rm tot} - 1) + 15 e_1^2 \sin^2 i_{\rm tot} \cos(2g_1) \right], \tag{1.20}$$

where C_2 is defined in (1.18) and $i_{\rm tot} = i_1 + i_2$ is the total inclination, see Fig. 1.2.

With this Hamiltonian we can explicitly write the evolution equation for the eccentricity of the inner binary, from the first equation in (1.15) follows that

$$\frac{de_1}{dt} = C_2 \frac{1-e_1^2}{J_1} 30 e_1 \sin^2 i_{\rm tot} \sin(2g_1). \tag{1.21}$$

Note that from the definition itself of J_1 in (1.6), setting $\dot{e}_1 = 0$ also means $\dot{J}_1 = 0$ and, by looking at eq. (1.21), it is immediate to see that this condition is satisfied when $g_1 = n\pi/2$, with $n = 0, 1, 2, ...$, more specifically $n = 0$ corresponds to the minimum value for the eccentricity while $n = 1$ to the maximum one. Moreover from the definition of $J_{k,z}$ in (1.7) we also find that $\dot{J}_1 = 0$ implies $\dot{J}_{1,z} = 0$ which yields to $\dot{i}_1 = 0$. This tells us that to an extremum in the eccentricity corresponds an extremum for the inclination of the inner binary. We can use the conservation of the total angular momentum $\mathbf{J}_{\rm tot}$ to derive a relation between the eccentricity of the inner binary e_1 and the total inclination $i_{\rm tot}$. We start by writing the relation (1.10) in terms of the eccentricities e_1 and e_2 and the conjugate momenta L_1 and L_2

$$L_1^2(1-e_1^2) + 2L_1 L_2 \sqrt{(1-e_1^2)} \cos i_{\rm tot} = J_{\rm tot}^2 - J_2^2, \tag{1.22}$$

where we set $e_2 = 0$ since we are interested in an outer circular orbit. Note how the right-hand side is fixed by the initial condition since both the total angular momentum and the one of the outer orbit are constant at the quadrupole level of approximation[1]. To study how the eccentricity e_1 and the total inclination of the triple system evolve in time, the relation (1.22) must be supplemented with the two relations obtained by imposing the conservation of energy for both the minimum ($g_1 = 0$) and maximum ($g_1 = \pi/2$) eccentricity case in (1.20), which respectively yield to

$$\begin{aligned} \frac{H_{\rm quad}}{2C_2} &= 3\cos^2 i_{\rm tot}(1-e_1^2) - 1 + 6e_1^2, \\ \frac{H_{\rm quad}}{2C_2} &= 3\cos^2 i_{\rm tot}(1+4e_1^2) - 1 - 9e_1^2. \end{aligned} \tag{1.23}$$

[1] Note how the conservation of J_2 holds only up to the quadrupole approximation, and it is a consequence of the fact that the Hamiltonian (1.20) does not depend on g_2. The conservation of the angular momentum for the outer orbit at this level of approximation is usually known as "happy coincidence" [123].

After fixing the initial conditions for the eccentricity e_1 and the argument of periastron g_1 to zero for simplicity, we can re-write eq. (1.22) and eq. (1.23) respectively as:

$$\begin{aligned}\sqrt{1-e_1^2}\cos i_{\rm tot} &= \cos i_0 + \frac{L_1}{2L_2}e_1^2,\\ (1-e_1^2)\cos^2 i_{\rm tot} &= \cos^2 i_0 - 2e_1^2,\\ (1+4e_1^2)\cos^2 i_{\rm tot} &= \cos^2 i_0 + 3e_1^2,\end{aligned} \tag{1.24}$$

where i_0 is the initial value for the total inclination of the system. After combining these equations we end up with a relation that give us the maximum eccentricity that the inner binary can reach during its secular evolution as a function of the initial mutual inclination, namely

$$\left(\frac{L_1}{L_2}\right)^2 e_1^4 + \left(3 + 4\frac{L_1}{L_2}\cos i_0 + \left(\frac{L_1}{2L_2}\right)^2\right)e_1^2 + \frac{L_1}{L_2}\cos i_0 - 3 + 5\cos^2 i_0 = 0. \tag{1.25}$$

To get a better understanding of how the maximum eccentricity is related to the initial mutual inclination of the triple system, we can analyse eq. (1.25) in the test particle approximation (also known as the TPQ limit [30]), where we assume that $L_2 \gg L_1$. This condition holds in the scenario we are analysing since we assume a hierarchical configuration for the triple system, i.e. m_3 is much larger than both m_1 and m_2. In the TPQ limit eq. (1.25) takes a more simple expression, namely

$$e_1^2 = 1 - \frac{5}{3}\cos^2 i_0. \tag{1.26}$$

This equation can also be obtained by computing the Hamiltonian of the triple system directly in the TPQ approximation [129–131], where usually one of the two objects in the inner binary is assumed to be a test particle, i.e. $m_2 \to 0$ or equivalently $m_1 \to 0$. The main difference with the case where all three masses are non-negligible is that in the test particle approximation the Hamiltonian does not depend on the angle variable h_1, and can be written as[2] [30, 132]

$$H^{\rm TPQ}_{\rm quad} = \frac{3}{8}\frac{Gm_1m_3}{a_2}\left(\frac{a_1}{a_2}\right)^2\left[-\frac{e_1^2}{2} + \left(1+\frac{3}{2}e_1^2\right)\cos^2 i_{\rm tot} + \frac{5}{2}e_1^2\sin^2 i_{\rm tot}\cos(2g_1)\right], \tag{1.27}$$

where we already set $e_2 = 0$. Thus the conjugate momentum associated to h_1, i.e. the z component of the angular momentum of the inner binary $J_{1,z}$, is conserved

$$J_{1,z} = \sqrt{1-e_1^2}\cos i_{\rm tot} = \text{const}. \tag{1.28}$$

[2]Here we choose $m_2 \to 0$ but we could have choose also $m_1 \to 0$ without loss of generality.

From this relation follows that

$$J_{1,z} = \sqrt{1 - e_{1,\max}^2}\cos i_{\mathrm{tot,min}} = \sqrt{1 - e_{1,0}^2}\cos i_{\mathrm{tot},0}, \tag{1.29}$$

where the subscript 0 denotes the initial values. As we did before this equation must be supplemented with the conservation of energy for the minimum (maximum) eccentricity case, which is obtained by setting $g_1 = 0\,(g_1 = \pi/2)$ in (1.27), respectively yielding to

$$\begin{aligned} E_0\,(g_1 = 0) &= 2e_{1,\min}^2 + (1 - e_{1,\min}^2)\cos^2 i_{\mathrm{tot,max}}, \\ E_0\,(g_1 = \pi/2) &= -3e_{1,\max} + (1 + 4e_{1,\max}^2)\cos^2 i_{\mathrm{tot,min}}. \end{aligned} \tag{1.30}$$

Solving together eq. (1.29) and the second equation in (1.30) allow us to find the maximum value reachable by the eccentricity of the inner binary e_1 and the minimum value for the total mutual inclination i_{tot}. After fixing the initial conditions to $e_{1,0} = g_{1,0} = 0$ we find

$$\begin{aligned} e_{1,\max} &= \sqrt{1 - \frac{5}{3}\cos^2 i_{\mathrm{tot},0}}, \\ \cos i_{\mathrm{tot,min}} &= \pm\sqrt{\frac{3}{5}}. \end{aligned} \tag{1.31}$$

These angles are known as the *Kozai angles* and they represent the interval where the initial value for the mutual inclination should lie in order to trigger the exchange of angular momentum between the inner and outer orbit and thus to induce the ZLK mechanism. In formula

$$39.9^\circ < i_{\mathrm{tot},0} < 140.77^\circ. \tag{1.32}$$

To fully appreciate the oscillations induced on the eccentricity of the inner orbit and the mutual inclination of the triple system by the ZLK mechanism, it is useful to plot how e_1 and i_{tot} evolve as a function of time. To achieve this we first need to derive the full set of equations of motion for the orbital parameters of the triple system and then to integrate them. For the ease of notation we do this in Appendix A and we show the result in Fig. 1.3. [3]

One final remark on the TPQ approximation is that it is possible to define a new constant of motion [133]

$$\begin{aligned} C_{\mathrm{ZLK}} &= \frac{1}{2}\left[-\frac{e_1^2}{2} + \left(1 + \frac{3}{2}e_1^2\right)\cos^2 i_{\mathrm{tot}} + \frac{5}{2}e_1^2\sin^2 i_{\mathrm{tot}}\cos(2g_1)\right] - \frac{1}{2}J_{1,z}^2 \\ &= e_1^2\left(1 - \frac{5}{2}\sin^2 i_{\mathrm{tot}}\sin^2 g_1\right), \end{aligned} \tag{1.33}$$

[3] In Appendix A we write the equations of motion up to the octupole order in the expansion for the Hamiltonian (1.3). However to reproduce Fig. 1.3 we are only interested in the quadropole contributions to those equations, i.e. the terms proportional to C_2.

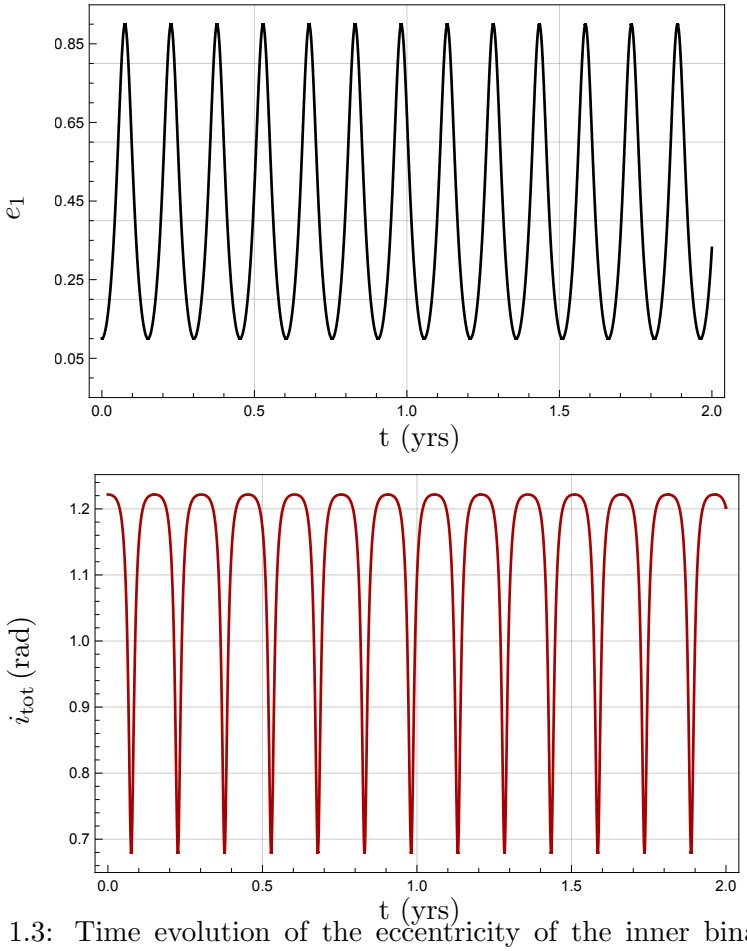

Figure 1.3: Time evolution of the eccentricity of the inner binary e_1 (top panel) and the total inclination of the triple system $i_{\rm tot}$ (bottom panel) as a function of time (years) in the quadrupole approximation. Here we choose the following parameters: $m_1 = m_2 = 10 M_\odot$, $m_3 = 2 \times 10^9 M_\odot$, $a_2 = 150\,\mathrm{AU}$, $a_1 = 0.1\,\mathrm{AU}$, $e_2 = 0$ and, as initial conditions we fixed $e_1^0 = 0.1$, $g_1^0 = 0^\circ$ and $i_{\rm tot}^0 = 70^\circ$. Notice how when the eccentricity reaches its maximum value, the total inclination reaches its minimum and vice versa.

which plays a relevant role in the test particle approximation when expanding the Hamiltonian (1.3) to higher orders than the quadrupole one, see [20, 128] for a more detailed analysis.

1.1.2 Octupole Approximation

The next order in the expansion of the Hamiltonian (1.3) beyond the quadrupole one is called *octupole approximation* and can introduce some significant differences in the dynamics of the triple system compared to the previous case we analysed. The tidal part of the Hamiltonian (1.3) (i.e. the third term in the expression for H) expanded up to the octupole order can be written as

$$H_{\rm tidal} = H_{\rm quad} + \epsilon\, H_{\rm oct}, \tag{1.34}$$

where $H_{\rm quad}$ is the quadrupole contribution to the Hamiltonian and it is the same ad the one defined in (1.20) while $H_{\rm oct}$ is the octupole contribution which can be written as

$$\begin{aligned} H_{\rm oct} = C_2 \left[(2+3e_1^2)(3\cos^2 i_{\rm tot} - 1) + 15 e_1^2 \sin^2 i_{\rm tot} \cos(2g_1)\right] \\ + C_3 e_1 e_2 \left[\theta + 10 \cos i_{\rm tot} \sin^2 i_{\rm tot} (1-e_1^2) \sin g_1 \sin g_2\right], \end{aligned} \tag{1.35}$$

where

$$C_3 = -\frac{15}{16}\frac{G^2}{4} \frac{\left[(m_1+m_2)m_3\right]^9}{\left[(m_1+m_2+m_3)m_1 m_2\right]^4} \frac{m_1-m_2}{m_1 m_2} \frac{L_1^6}{L_2^3 J_2^5}, \tag{1.36}$$

and

$$\epsilon = \frac{m_1-m_2}{m_1+m_2}\frac{a_1}{a_2}\frac{e_2}{1-e_2^2}, \tag{1.37}$$

and finally

$$\begin{aligned} \theta = -\left[4 + 3e_1^2 - \frac{5}{2}\left(1 + 5e_1^2 - 7e_1^2 \cos(2g_1)\right)\sin^2 i_{\rm tot}\right] \\ \times \left[\cos g_1 \cos g_2 + \cos i_{\rm tot} \sin g_1 \sin g_2\right]. \end{aligned} \tag{1.38}$$

Here we already applied to the Hamiltonian the elimination of nodes, i.e. $h_1 - h_2 = \pi$, to simplify the expression but this does not mean that the z components of the angular momenta for the inner and outer orbits are conserved. From the definition of ϵ in (1.37) we can see immediately that if the outer orbit is circular, i.e. $e_2 = 0$, then the octupole part of the Hamiltonian goes to zero and does not contribute to the dynamics of the triple system. This tells us also that the quadrupole approximation we studied above is more than enough to describe a triple system when the inner binary is moving along a circular outer orbit.

To further simplify the analysis of the octupole approximation we also take the test particle limit on the Hamiltonian (1.34), assuming that one of the two masses in the inner binary goes to zero. At the test particle octupole (TPO) level the Hamiltonian can be written as [20, 30]

$$H_{\rm tidal}^{\rm TPO} = \frac{3}{8}\frac{Gm_1m_3}{a_2(1-e_2^2)^{3/2}}\left(\frac{a_1}{a_2}\right)^2\left(F_{\rm quad}+\epsilon^{\rm TPO}\,F_{\rm oct}\right), \tag{1.39}$$

where

$$\epsilon^{\rm TPO} = \frac{a_1}{a_2}\frac{e_2}{1-e_2^2}, \tag{1.40}$$

moreover $F_{\rm quad}$ is the quadrupole contribution to the Hamiltonian which is defined between brackets in (1.20):

$$F_{\rm quad} = -\frac{e_1^2}{2}+\left(1+\frac{3}{2}e_1^2\right)\cos^2 i_{\rm tot}+\frac{5}{2}e_1^2\sin^2 i_{\rm tot}\cos(2g_1), \tag{1.41}$$

and finally $F_{\rm oct}$ represents the octupole contribution to the tidal part of the Hamiltonian, which can be written as

$$\begin{aligned} F_{\rm oct} =& \frac{5}{16}\left(e_1+\frac{3}{4}e_1^3\right)\Big[\left(1-11\cos i_{\rm tot}-5\cos^2 i_{\rm tot}+15\cos^3 i_{\rm tot}\right)\cos(g_1-h_1)\\ &+\left(1+11\cos i_{\rm tot}-5\cos^2 i_{\rm tot}-15\cos^3 i_{\rm tot}\right)\cos(g_1+h_1)\Big]\\ &-\frac{175}{64}e_1^3\Big[\left(1-\cos i_{\rm tot}-\cos^2 i_{\rm tot}+\cos^3 i_{\rm tot}\right)\cos(3g_1-h_1)\\ &+\left(1+\cos i_{\rm tot}-\cos^2 i_{\rm tot}-\cos^3 i_{\rm tot}\right)\cos(3g_1+h_1)\Big]. \end{aligned} \tag{1.42}$$

Compared to the quadrupole approximation, at the octupole level the dynamics of the triple system changes significantly. First of all, the z component of the outer angular momentum $\mathbf{J}_{2,z}$ is no longer conserved even in the test particle limit. Moreover the eccentricity of the inner binary e_1 can reach very high values that can lead to the *orbital flip* of the system, i.e. the total inclination $i_{\rm tot}$ can go from $i_{\rm tot} < 90^\circ$ to $i_{\rm tot} > 90^\circ$ [20, 30, 134, 135]. In Fig. 1.4 we show the time evolution for the eccentricity e_1, the inclination i_1 and the z component of the angular momentum of the inner binary up to the octupole level of approximation. From the inclination plot, i.e. the mid panel, we can see clearly how periodically the inclination of the inner binary goes from $i_1 > 90^\circ$ to $i_1 < 90^\circ$, thus describing the flip of the orbit. As already mention above the orbital flip is a new effect that does not occur at the quadrupole level of approximation. To make this even more clear in the bottom panel of Fig. 1.4 we plot the z component of the inner angular momentum $J_{1,z}$ (normalized to the total angular momentum) for both the octupole approximation (blue line) and the quadrupole one (cyan line). The quadrupole result describes an orbit

that remains always prograde during the secular evolution of the triple system while the octupole result represents an orbits that periodically oscilates from a prograde orbit to a retrograde one, as expected. It is also possible to find an analytical condition for the orbital flip in terms of the initial conditions for the triple system. This is done in [20, 128] where after averaging over a quadrupole cycle, they define a new constant of motion as

$$C = F(C_{\rm ZLK}) - \epsilon \cos\Omega, \tag{1.43}$$

where $C_{\rm ZLK}$ is defined in (1.33)[4], ϵ is the octupole pre-factor defined in (1.37), $\cos\Omega$ can be written as

$$\cos\Omega = \frac{\cos i_{\rm tot} \sin h_1 \sin g_1 - \cos g_1 \cos h_1}{\sqrt{1 - \sin^2 i_{\rm tot} \sin^2 g_1}}, \tag{1.44}$$

and lastly $F(C_{\rm ZLK})$ is defined as

$$F(C_{\rm ZLK}) = \frac{32\sqrt{3}}{\pi} \int_{\frac{3-3C_{\rm ZLK}}{3+2C_{\rm ZLK}}}^{1} \frac{K(x) - 2E(X)}{(41x-21)\sqrt{2x+3}} dx, \tag{1.45}$$

where $K(x)$ and $E(x)$ are the complete elliptic function of the first and second kind, defined as

$$\begin{aligned} K(m) &= \int_0^{\pi/2} \frac{1}{\sqrt{1 - m\sin^2\theta}} d\theta, \\ E(m) &= \int_0^{\pi/2} \sqrt{(1 - m\sin^2\theta)} d\theta. \end{aligned} \tag{1.46}$$

To find a criterion for the orbital flip, i.e. when $J_{\rm tot,z}$ changes sign, we recall that during a flip $J_{\rm tot,z} = 0$. We can use this together with the constants defined in (1.33) and (1.43) to write a required condition for the octupole pre-factor ϵ for the orbital flip to occur, namely

$$\epsilon > \epsilon_c, \tag{1.47}$$

where ϵ_c is defined as

$$\epsilon_c = \frac{1}{2} \max\left(|\Delta F(x)|\right), \tag{1.48}$$

with $\Delta F(x) = F(x) - F(C_{\rm ZLK,0})$ and $C_{\rm ZLK,0} < x < C_{\rm ZLK,0} + \frac{1}{2}(1-e_{1,0}^2)\cos i_{\rm tot,0}$, where the 0 subscript denotes the initial values for the parameters. The condition (1.47) takes a simple expression when $e_{1,0} \ll 1$, which implies $C_{\rm ZLK,0} \ll 1$, $J_{\rm tot,z} = \cos i_{\rm tot,0}$ and thus $i_{\rm tot,0} \geq 61.7°$:

$$\epsilon > \frac{1}{2} F\left(\frac{1}{2}\cos^2 i_{\rm tot,0}\right). \tag{1.49}$$

[4]Note that at the octupole level of approximation this is no longer a constant as it was in the quadrupole one.

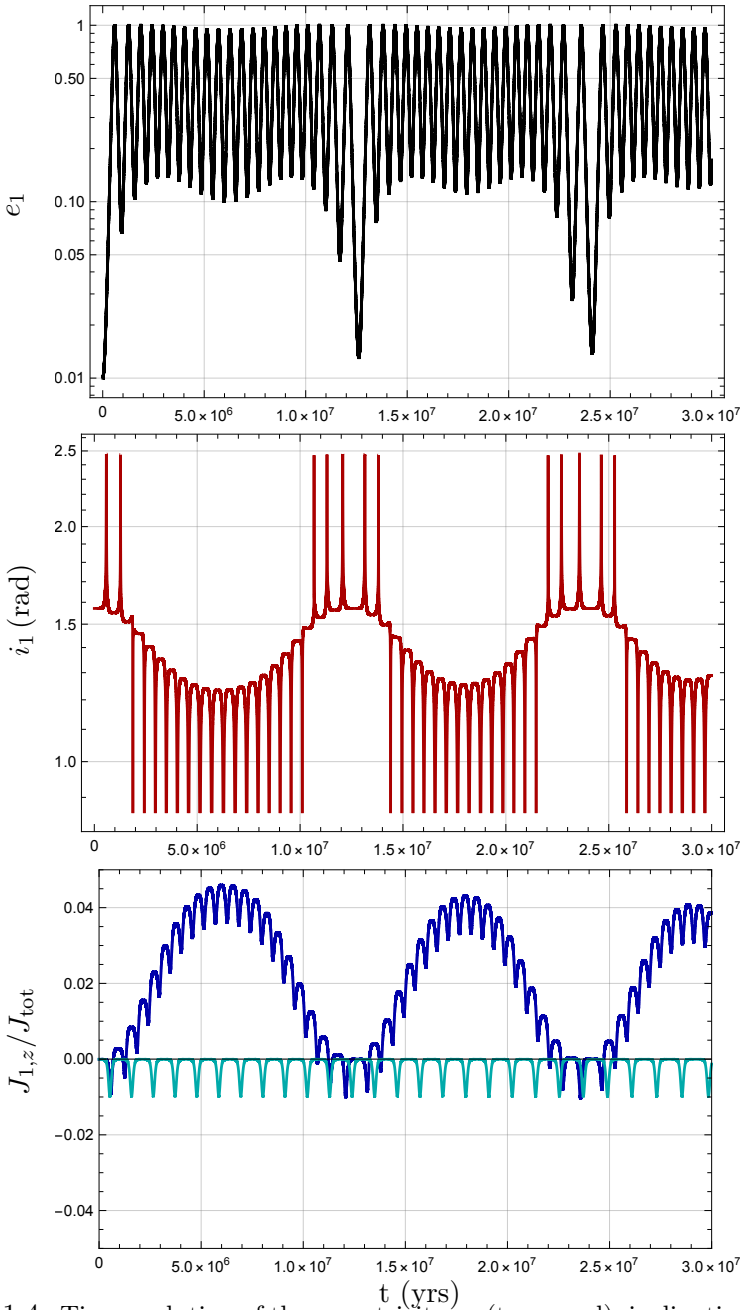

Figure 1.4: Time evolution of the eccentricity e_1 (top panel), inclination (mid panel) and z component of the angular momentum $J_{1,z}$ (bottom panel) of the inner binary system. Here we solve the evolution equations for the orbital parameters up to the octupole approximation. Following refs. [37,136], in this plot we choose the following parameters: $m_1 = 1M_\odot$, $m_2 = 0.65M_\odot$, $m_3 = 0.6M_\odot$, $a_1 = 60\,\text{AU}$ and $a_2 = 800\,\text{AU}$. As initial conditions instead we have $e_1^0 = 0.01$, $e_2^0 = 0.6$, $i_1^0 = 90.02°$, $i_2^0 = 7.98°$, $g_1^0 = g_2^0 = 0°$.By looking at the mid and bottom panels we can see how the inclination of the inner binary system goes from $i_1 > 90°$ to $i_1 < 90°$, i.e. at the octupole level of approximation the orbit of the inner binary oscillates periodically between a prograde orbit and a retrograde orbit (in relation with the total angular momentum). Note how the orbital flip is a completely new effect that is not present at the quadrupole level of approximation. This is clear by looking at the bottom panel where we plot the ratio between the z component of the angular momentum of the inner binary and the total angular momentum both in the octupole approximation (blue line) and in the quadrupole one (cyan line).

It is worth mentioning that to study the orbital flip here we restricted ourselves to an initial inclination which satisfies the condition (1.32). This is also known as the "high initial inclination regime" [20], where the orbital flip is usually accompanied by a chaotic behaviour for the triple system which is not present at the quadrupole level of approximation [20, 30, 134, 135]. It is also possible to see the orbital flip effect even when the condition (1.32) is not satisfied and the total inclination $i_{\rm tot}$ is well below the threshold, namely $i_{\rm tot} < 39.9°$. We usually refer to this scenario as "low initial inclination regime" [20] and in this context the orbital flip does not present a chaotic behaviour and it is well regular, happening on a timescale which is much shorter compared to the one of the high inclination flip. See ref. [20, 137] for a more detailed analysis.

1.1.3 General Relativity contribution

Even if the ZLK mechanism was already known in the early 1910s, it started to get a lot of attention in the scientific community only in recent times, probably after two important astrophysical achievements: the discover of the eccentric planet 6 Cyg B [138] and the hierarchical triple stellar system Algon [139]. In recent years people started to explore the ZLK mechanism more in detail, adding Post Newtonian corrections to the dynamics of the triple system [40,42] and including effects from general relativity [45,140,141] that can significantly affect the time evolution of the orbital parameters of the triple system. In this context one of the effects that we must take into account to get a more realistic picture for the evolution of a triple system is the precession of the periapsis, which can suppress significantly the oscillations on the eccentricity (and inclination) induced by the ZLK mechanism. The precession of the periapsis for the inner binary can be written as [142]

$$\left(\frac{dg_1}{dt}\right)_{\rm PN} = \frac{3(G(m_1+m_2))^{3/2}}{a_1^{5/2}c^2(1-e_1^2)}. \tag{1.50}$$

In principle we should also take into account the PN precession of the outer orbit but its contribution is not really relevant to the evolution of the triple system and thus in this analysis we neglect it. The timescale associated with the precession in (1.50) can be written as [20, 43]

$$T_{\rm PN}^{\rm inner} \sim 2\pi \frac{a_1^{5/2}c^2(1-e_1^2)}{3\left[G(m_1+m_2)\right]^{3/2}}. \tag{1.51}$$

To understand when the PN precession becomes relevant in the dynamics of the triple system, it is also useful to introduce the timescale associated with the ZLK oscillations at the quadrupole level of approximation, which can be written as [143]

$$T_{\rm quad} \sim \frac{16}{15}\frac{a_2^3(1-e_2^2)^{3/2}(m_1+m_2)^{1/2}}{a_1^{3/2}m_3G^{1/2}}. \tag{1.52}$$

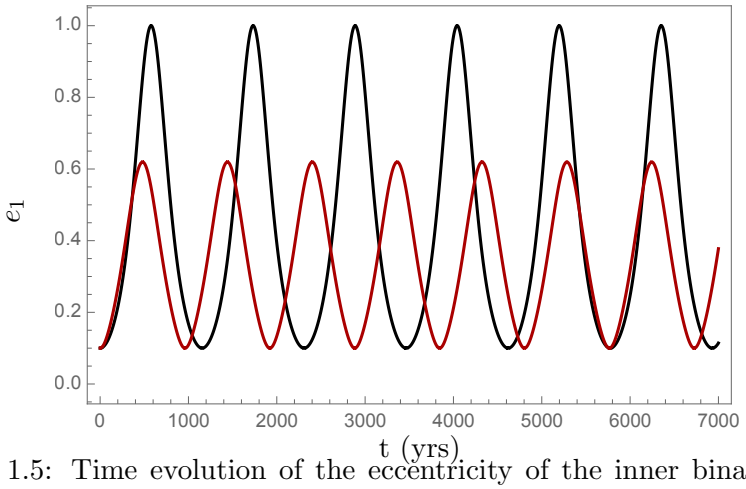

Figure 1.5: Time evolution of the eccentricity of the inner binary e_1. The black line represents the result obtained by solving the evolution equations including only the ZKL quadrupole contributions while for the red line we also included the PN precession contribution for the inner binary defined in (1.50). We used the same parameters in both case, i.e. $m_1 = m_2 = 10M_\odot$, $m_3 = 4 \times 10^6 M_\odot$, $a_1 = 0.1\,\mathrm{AU}$, $e_2 = 0$, $a_2 = 380\,\mathrm{AU}$, and the same initial conditions, namely $e_1^0 = 0.1$, $g_1^0 = g_2^0 = 0°$ and $i_{\rm tot}^0 = 89.4°$. We can see that with just the inclusion of the PN precession for the inner binary, the ZKL oscillations are suppressed and the maximum value that the eccentricity can reach during its time evolution is much smaller compared to one in the case where the precession is not included.

When the timescale in (1.51) of the PN precession shorter than the one in (1.52) of the ZLK mechanism then the oscillations of the inner orbit eccentricity e_1 induced by the exchange of the angular momentum between the inner and outer orbit are suppressed, see for example [141, 144] and Fig. 1.5. Interesting when the PN precession and the quadrupole ZKL timescales become comparable, i.e. $T_{\rm quad} \sim T_{\rm PN}^{\rm inner}$, the eccentricity of the inner binary can grow close to unity [20, 43, 141, 144]. The maximum value that e_1 can reach in this scenario is simply given by the following relation, as pointed out in Refs. [20, 141]

$$\epsilon_{\rm GR}\left(\frac{1}{j_{1,\rm min}}-1\right)=\frac{9}{8}\frac{e_{1,\rm max}^2}{j_{1,\rm min}^2}\left(j_{1,\rm min}^2-\frac{5}{3}\cos^2 i_{\rm tot,0}\right), \tag{1.53}$$

where $j_{1,\rm min}=\sqrt{1-e_{1,\rm max}^2}$ and $\epsilon_{\rm GR}$ is a dimensionless parameter defined as

$$\epsilon_{\rm GR}=\frac{3G(m_1+m_2)^2a_2^3(1-e_2)^{3/2}}{a_1^4c^2m_3}=\frac{T_{\rm quad}}{T_{\rm PN}^{\rm inner}}(1-e_1^2). \tag{1.54}$$

Note that in the absence of PN precession, i.e. $\epsilon_{\rm GR} = 0$, the relation (1.53) yields to the usual condition for the maximum eccentricity, i.e. the one pre-

sented in (1.31).

The inclusion of the PN precession becomes relevant to get a more accurate simulation for the merger of two compact objects in a binary perturbed by a third body since it can alter the dynamical evolution of the system, see for example Refs. [19, 145–149].

1.2 Binary mergers in strong gravity background of Kerr black hole

So far we provided a brief review on how the ZLK mechanism works and how it has been analysed in the literature in the past years. The stability conditions (1.2) and (1.1) require the triple system to be hierarchical, namely $a_2 \gg a_1$. This condition, together with fact that during the secular evolution of the triple systems the semi-major axes of both the inner and outer orbit remain constant, has led to a natural perturbative approach to study the dynamics of the system, expanding the Hamiltonian in terms of the small parameter a_1/a_2 as showed in (1.3). In this approximation the masses of the three bodies in the triple system are left unconstrained, meaning that the three objects can have comparable masses as long as the binary system is orbiting far away from the third companion with an orbital velocity $v \sim \sqrt{(m_1+m_2+m_3)/a_2} \ll 1$ [70]. This is usually referred as the *weak field approximation*, where the three objects in the triple system can be treated as point-particles and Newtonian physics can be used to efficiently describe the dynamics of the system, adding Post-Newtonian (PN) corrections to include effects due to General Relativity. Even though this approximation has been extensively used in the literature and has yield a lot of interesting and fundamental results, it can only be applied when strong General Relativity effects are not dominant in the dynamics of the triple system, namely when the binary system is far away from the third body. However binary black hole mergers can also take place close to the center of galaxies, where usually a supermassive black hole is located. In this scenario General Relativity effects can alter significantly the evolution of the triple system and must be included to have a better estimate for the parameters describing the inner binary system. For example the Doppler and gravitational redshift induced by the presence of a supermassive black hole could lead to an higher (and thus incorrect) estimate for the masses of the two merging objects [150, 151]. There are two main mechanisms for the formation of triple systems where the binary system is close to a supermassive black hole. The first one is by tidal capture, which can lead to binaries that can either merger before completing one orbit around the supermassive black hole or binaries orbiting for several times around the third body before merging. Even though this is a viable mechanism for a binary system to orbit close to a supermassive black hole, its even rate is very low [152, 153]. The other one is a well known mechanism for planetesimals in protoplanetary

discs which can also be applied to black hole binary systems. In particular planetesimals move with a Keplerian velocity while the protoplanetary disc, because of the gas pressure, is moving with a smaller velocity compared to the Keplerian one. A headwind arises from the difference between these two velocities which effectively pushes the planetesimals towards the inner regions of the disc [154–157]. Recently the same mechanism has been used by [52,158] to explain how black holes can be driven towards the supermassive black hole at the center of a galaxy and get trapped on a region close to the Innermost Stable Circular Orbit (ISCO), which is usually called *last migration trap*. This trapping mechanism is due to relativistic effects taking place close to the ISCO of a supermassive black hole which lead to a super-Keplerian motion for the gas [159–161]. On the other hand, compact objects driven into this region will move with a Keplerian velocity and, from the difference between the motion of the gas and the objects, it will arise a tailwind which can counter (in some cases) the negative torque generated by the gravitational wave emitted by the object-supermassive black hole binary, trapping compact objects in a region very close to the ISCO of a supermassive black hole [162–164]. These objects will eventually interact with themselves and form binary systems that can evolve in this region until they merge under the influence of the third body.

In this scenario it is no longer possible to treat the supermassive black hole as a point particle since this approximation only holds when the distance between the binary system and the supermassive black hole is much larger than the Schwarzschild radius of the latter. Moreover we can no longer apply the weak field approximation since binaries in this region of space-time can have a relative velocity comparable to the speed of light and strong gravity can induce effects of the gravitational potential that can be considered non-perturbative in comparison with the PN expansion. Thus in order to understand properly the dynamics of a binary system in a strong gravity regime, it is necessary to describe the supermassive black hole generating the tidal environment in which the two objects are moving using a metric, which encodes all possible General Relativity effects.

It is still possible to treat the interaction between the inner and outer orbit perturbatively by using a more general approximation than the weak field one, called *small-tide approximation* [70]. To introduce this approximation we need first to define two different length scales in our triple system: the first one is associated with the inner binary, and it is related to its total mass $m = m_1 + m_2$, while the second one is related to the outer orbit, more specifically it is the radius of the curvature $\mathcal{R}$ induced by the external supermassive black hole on the position of the binary system. The small-tide approximation assures us that we can always distinguish between the binary system and the external background, treating the last one as a small perturbation to the

dynamics of the binary, when the following condition is satisfied [70]:

$$m \ll \mathcal{R} \implies \frac{m}{\mathcal{R}} \ll 1.^{5} \tag{1.55}$$

Recalling that for a binary system with total mass m orbiting around a supermassive black hole of mass m_3 at a distance r its orbital velocity v and the radius of the curvature induced by the external body can be written as

$$v \sim \sqrt{\frac{m+m_3}{r}}, \quad \text{and} \quad \mathcal{R} \sim \sqrt{\frac{r^3}{m+m_3}}, \tag{1.56}$$

we can rewrite the condition (1.55) as

$$\frac{m}{\mathcal{R}} \sim \frac{m}{m+m_3} v^3 \ll 1. \tag{1.57}$$

There are two different ways of satisfying this condition, the first one is the already mentioned weak-field approximation, placing the binary system far away from the supermassive black hole so that its orbital velocity $v \ll 1$, and we can analyse the system leaving the masses of the three objects unconstrained. The second one instead is the so called *small-hole approximation*, where the total mass of the binary system is assumed to be much smaller than the one of the external supermassive black hole, i.e. $m/(m+m_3) \ll 1$, leaving the mutual distance (and thus the orbital velocity of the binary) unconstrained. Both of these approximations satisfy the most general small-tide condition (1.55), but while the first one breaks down as the binary system gets closer to the supermassive black hole, the second one is still valid even when the binary is at a distance from the third body comparable to the size of the latter one $r \sim m_3$. Note that in this last scenario, as we get closer to supermassive black hole, we need to be careful to still satisfy the stability condition presented in (1.2) to avoid tidal disrupting events and to let the binary system evolve until the merger. In our analysis this is achieved by shrinking the binary system as we place it on an orbit closer to the supermassive black hole, in this way not only the radius of the curvature induced by the external body will always be much larger than the typical scale of the binary itself, allowing us to analyse the problem perturbatively, but also the stability condition will be always satisfied, allowing us to evolve the system for a long time (even up until the merger of the two compact objects in the binary) to study its secular dynamics. It is also worth noticing that the stability condition is satisfied in astrophysical context, in fact for an enough massive black hole the radius of the last stable orbit[6] is of order $10 \div 10^3$ AU depending on its mass and spin,

[5] Here we set $G = c = 1$.

[6] Here we are referring to the last stable circular orbit since for the purpose of this thesis we will restrict ourselves to circular orbits.

while for a binary system typical values for the semi-major axis (especially in the last orbits before they start merging) can be $10^{-1} \div 10$ AU [19, 147, 165].

In what follow we will use the small-hole approximation to study how the ZKL mechanism is modified in the presence of a strong gravitational field, i.e. when the inner binary is placed very close, even on the ISCO, of a supermassive black hole.

1.2.1 Binary system in a tidal force background

In this section, we review the basic concepts regarding the dynamics of a black hole binary system in the context of a general tidal force background up to the quadrupole approximation. The tidal forces arise from the curvature of the spacetime in which the binary system is moving. We will treat the two black holes in the binary system as point particles, using the Newtonian approximation for a simpler analysis. The quadrupole tidal force background on the other hand is kept completely general and it is described using General Relativity. We assume the binary system to be freely falling, hence to leading order its center of mass moves on a geodesic of the background space-time. See [166] for a similar analysis.

The metric in the neighborhood of a geodesic of a background spacetime can be described, in general, using the Thorne-Hartle version of the Fermi-normal coordinates [167], namely

$$\begin{aligned} g_{00} &= -1 - \mathcal{E}_{ij}x^i x^j + \mathcal{O}((x/\mathcal{R})^3) \quad , \\ g_{0i} &= -\frac{2}{3}\epsilon_{ijk}\mathcal{B}^j{}_l x^k x^l + \mathcal{O}((x/\mathcal{R})^3) \quad , \\ g_{ij} &= \delta_{ij}(1 - \mathcal{E}_{kl}x^k x^l) + \mathcal{O}((x/\mathcal{R})^3) \quad , \end{aligned} \tag{1.58}$$

where $i, j = 1, 2, 3$, the square of the geodesic distance to the geodesic is $x^2 = x^i x^i$ and $\mathcal{R}$ is the curvature length scale. In Appendix B we provide a brief review on Fermi normal coordinates.

As already anticipated, to speak meaningfully about the dynamics of the binary system in a tidal field background, we need to require that the curvature length scale $\mathcal{R}$ of the background is significantly larger than the size x of the binary system, hence $x \ll \mathcal{R}$ [70], i.e. we need to satisfy the small-tide approximation (1.55).

The fact that we keep terms up to order $x^2/\mathcal{R}^2$ in (1.58) encaptures the quadrupole approximation of the tidal forces, for which the electric and magnetic tidal moments $\mathcal{E}_{ij}$ and $\mathcal{B}_{ij}$ are related to the Riemann curvature tensor as

$$\mathcal{E}_{ij} = R_{0i0j}|_{x=0} \quad , \quad \mathcal{B}_{ij} = \frac{1}{2}\epsilon_{pq(i}R^{pq}{}_{|j)0}|_{x=0} \quad , \tag{1.59}$$

with $i, j, p, q = 1, 2, 3$. In general, the tidal moments depend on the proper time τ of the geodesic. We assume that the background spacetime has $R_{\mu\nu} = 0$ which is indeed true for the Kerr spacetime. Below in Section 1.2.2 we

will restrict ourselves to tidal moments $\mathcal{E}_{ij}$ and $\mathcal{B}_{ij}$ for geodesics around a Kerr black hole, as computed in [69, 168], but for the moment we keep our considerations general.

We now assume that the center of mass of the binary is located at the geodesic and we model the two black holes in the binary system as two point particles moving in the spacetime described by the metric (1.58). The Lagrangian for particle 1 is

$$L_{(1)} = -m_1 c^2 \sqrt{-G_{00} - 2G_{0i}\frac{v^i_{(1)}}{c} - G_{ij}\frac{v^i_{(1)}v^j_{(1)}}{c^2}} \,. \tag{1.60}$$

Here $v^i_{(1)}$ is the velocity of particle 1. The metric $G_{\mu\nu}$ is evaluated at the position $\vec{x}_1$ of particle 1 and it is given by the background metric $g_{\mu\nu}$ with tidal forces (1.58) plus the gravitational potentials generated by particle 2. For the latter, we use the PN expansion of Sections 5.1.4 and 5.1.5 in the book [16]. Explicitly, we have up to 1PN

$$\begin{aligned} G_{00} &= g_{00} - 2\phi_{(2)} - 2(\phi^2_{(2)} + \psi_{(2)}) + \cdots \\ G_{0i} &= g_{0i} + \zeta^{(2)}_i + \cdots \\ G_{ij} &= g_{ij} - 2\delta_{ij}\phi_{(2)} + \cdots \end{aligned} \tag{1.61}$$

where the standard PN gravitational potentials $\phi_{(2)}$, $\psi_{(2)}$ and $\zeta^{(2)}_i$ arise solely from the gravitational interaction with particle 2, see [16] for details. Notice that here we are neglecting possible terms corresponding to mixed couplings between the tidal forces and the PN expansion. These contributions would appear for the first time as terms of the type $\phi_{(2)}$ times the tidal moments.

We can now perform a PN expansion of the Lagrangian (1.60) for particle 1, where we have to keep in mind that the tidal moments are treated as a small perturbation and thus they should only be included up to the first order. Schematically, this gives

$$\begin{aligned} L_{(1)} =& L_{(1)}|_{\mathcal{E}=\mathcal{B}=0} - \frac{1}{2}m_1 c^2 x^i_{(1)} x^j_{(1)} \mathcal{E}_{ij} \\ & - \frac{2c}{3} m_1 v^i_{(1)} x^k_{(1)} x^l_{(1)} \epsilon_{ijk} \mathcal{B}^j{}_l + \cdots \end{aligned} \tag{1.62}$$

Here the first term $L_{(1)}|_{\mathcal{E}=\mathcal{B}=0}$ is the Lagrangian that arises solely from the gravitational interaction with particle 2, as well as the kinetic energy of particle 1. The second term in (1.62), coupling to $\mathcal{E}_{ij}$, is the leading coupling to the quadrupole tidal moments of the background spacetime. The third term in (1.62), coupling to $\mathcal{B}_{ij}$, is subleading as it is suppressed by $v^i_{(1)}/c$. Note that the coupling between the gravitational potentials and the tidal moments would be of order $v^2_{(1)}/c^2$ or higher, thus not affecting this term.

Considering the Newtonian limit, with respect to the two particles in the binary, of all the terms in the Lagrangian (1.62), and adding the analogous

contributions for the second particle, we get the Lagrangian for the Newtonian limit of the binary system, which can be written as

$$L_{\text{Newton}} = -(m_1+m_2)c^2 + \frac{1}{2}m_1 v_{(1)}^2 + \frac{1}{2}m_2 v_{(2)}^2 + \frac{Gm_1m_2}{r} - \frac{c^2}{2}\Big[m_1 x_{(1)}^i x_{(1)}^j + m_2 x_{(2)}^i x_{(2)}^j\Big]\mathcal{E}_{ij}. \tag{1.63}$$

Introducing now the center of mass quantities

$$\begin{aligned} &M = m_1+m_2, \quad \mu = \frac{m_1m_2}{M} \ , \\ &\vec{X} = \frac{m_1\vec{x}_{(1)}+m_2\vec{x}_{(2)}}{M}, \quad \vec{x} = \vec{x}_{(2)}-\vec{x}_{(1)}, \quad r = |\vec{x}| \ , \\ &\vec{V} = \frac{m_1\vec{v}_{(1)}+m_2\vec{v}_{(2)}}{M}, \quad \vec{v} = \vec{v}_{(2)}-\vec{v}_{(1)} \ , \end{aligned} \tag{1.64}$$

the Lagrangian (1.63) becomes

$$L_{\text{Newton}} = -Mc^2 + \frac{1}{2}MV^2 + \frac{1}{2}\mu v^2 + \frac{GM\mu}{r} - \frac{c^2}{2}\Big[MX^iX^j + \mu x^i x^j\Big]\mathcal{E}_{ij} \ . \tag{1.65}$$

Since the center of mass motion of the binary is decoupled from the relative motion of the binary system we can consistently set

$$\vec{X} = 0, \quad \vec{V} = 0 \ . \tag{1.66}$$

This means that the center of mass of the binary system is placed on the geodesic, which agrees with the fact that at large distance scales the binary system should be seen as one particle of mass M moving along the geodesic. Using moreover the general formula ([70])

$$x^i x^j \mathcal{E}_{ij} = r^2 \mathcal{E}^q \ , \tag{1.67}$$

where $\mathcal{E}^q$ is the quadrupole tidal potential, we get the binary system Lagrangian

$$L_{\text{Newton}} = \frac{1}{2}\mu v^2 + \frac{GM\mu}{r} - \frac{c^2}{2}\mu\, r^2\mathcal{E}^q \ . \tag{1.68}$$

One can now easily Legendre transform this to the Hamiltonian

$$H_{\text{Newton}} = \frac{1}{2\mu}p^2 - \frac{GM\mu}{r} + \frac{c^2}{2}\mu\, r^2\mathcal{E}^q \ , \tag{1.69}$$

with $p^i = \mu v^i$. This Hamiltonian describes the dynamics of a binary system of two particles moving along a geodesic in a background spacetime deformed by the presence of quadrupole tidal forces, arising from the curvature of the spacetime itself. This is valid in a local inertial system as set by the Fermi-normal coordinates (1.58).

1.2.2 Binary system in the background of large Kerr black hole

In this section we analyse the scenario of a black hole triple system. We consider two black holes of masses m_1 and m_2 in a bound motion, forming the BBH system. We will refer to it as the inner binary, and their motion as the inner orbit. We will assume the BBH system to be orbiting around a third supermassive black hole (SMBH), with mass m_3. Moreover the masses of the two companions in the binary system are much smaller than the mass of the external black hole, namely $m_1, m_2 \ll m_3$.

To study analytically the dynamics of the BBH system in a tidal environment, we will assume two independent separations of scales. The first one consists in taking the Schwarzschild radii of the two black holes in the binary to be much smaller than their separations r, which means that the BBH system is in the particle/PN regime:

$$r \gg \frac{2Gm_1}{c^2} \ , \quad \frac{2Gm_2}{c^2} \quad . \tag{1.70}$$

In particular, their relative velocity is much smaller than the speed of light.

Secondly, we work in a regime where the small-tide approximation is satisfied, i.e. we are assuming that the characteristic size of the BBH system r is very small compared to the radius of the curvature $\mathcal{R}$ induced by the SMBH on the position of the binary. This enables us to treat the influence of the SMBH on the BBH via a tidal force approximation, even when the BBH is close to the SMBH. Under these assumptions the motion of the binary system can be described, to leading order, as a geodesic one in the background sourced by the supermassive Kerr black hole. We will refer to this motion as the *outer orbit*. On the geodesic the small-tide approximation $r \ll \mathcal{R}$ can be written explicitly as

$$r \ll \hat{r}\sqrt{\frac{c^2\hat{r}}{Gm_3}} \ , \tag{1.71}$$

with $\hat{r}$ the radial coordinate of the Kerr metric that we introduce below.

We will restrict ourselves in this thesis to the leading quadrupole effect, arising from the Riemann curvature tensor of the Kerr metric evaluated on the geodesic. Below we shall include PN effects in the binary dynamics, in the form of the periastron precession and the GW radiation-reaction, thus we assume that the octupole tidal forces are smaller than these PN effects.

Kerr black hole background

In our setup the SMBH is describe by the Kerr metric, whose line element, represented in Boyer-Lindquist coordinates $\hat{x}^\mu = (\hat{t}, \hat{r}, \hat{\theta}, \hat{\phi})$, reads

$$\begin{aligned} d\hat{s}^2 = &- \Big(1 - \frac{2Gm_3\hat{r}}{c^2\Sigma}\Big)c^2 d\hat{t}^2 - \frac{4Gm_3\hat{r}}{c^2\Sigma} s_3 \sin^2\hat{\theta}\; c\, d\hat{t}\, d\hat{\phi} \\ &+ \frac{\mathcal{A}}{\Sigma}\sin^2\hat{\theta}\; d\hat{\phi}^2 + \frac{\Sigma}{\Delta} d\hat{r}^2 + \Sigma d\hat{\theta}^2 \quad . \end{aligned} \tag{1.72}$$

Where m_3 is the black hole mass, $s_3 = J_3/(c\, m_3)$ is the specific angular momentum and we defined

$$\begin{aligned} \Sigma = \hat{r}^2 + s_3^2\cos^2\hat{\theta}\;, \quad \Delta = \hat{r}^2 - \frac{2Gm_3}{c^2}\hat{r} + s_3^2 \quad , \\ \mathcal{A} = (\hat{r}^2 + s_3^2)^2 - \Delta s_3^2 \sin^2\hat{\theta} \quad . \end{aligned} \tag{1.73}$$

For convenience we introduce the dimensionless spin parameter χ, defined as

$$\chi = \frac{s_3 c^2}{Gm_3} \quad . \tag{1.74}$$

The position of the event horizon can be obtained by solving the equation $\Delta = 0$, which in general gives two roots: the major one represents the event horizon while the other describes a Cauchy horizon. Moreover the cosmic censorship conjecture requires $0 \leq s_3 \leq (Gm_3/c^2)$, *i.e.* $0 \leq \chi \leq 1$.

A generic geodesic $\hat{x}^\mu(\tau)$ in the Kerr spacetime is parametrized by three constants of motion, respectively representing the energy $\hat{E}$, the angular momentum $\hat{L}$ and the Carter constant K per unit of rest energy [169].

In our analysis we will restrict ourselves to circular ($\hat{r}$ constant) and equatorial ($\hat{\theta} = \pi/2$) geodesics in the Kerr background. In this case the tangent vector u^μ, representing the four-velocity of a particle moving along the geodesic, can be written as

$$u^\mu \equiv \frac{d\hat{x}^\mu}{d\tau} = u^t(\delta^\mu_t + \Omega\; \delta^\mu_\phi) \quad , \tag{1.75}$$

where the redshift factor u^t and the coordinate angular velocity Ω are defined as

$$\begin{aligned} u^t \equiv \frac{d\hat{t}}{d\tau} &= \frac{1}{\sqrt{-(g_{tt} + 2\Omega g_{t\phi} + \Omega^2 g_{\phi\phi})}} \quad , \\ \Omega \equiv \frac{d\hat{\phi}}{d\hat{t}} &= \frac{\sigma\,(Gm_3)^{1/2}}{\hat{r}^{3/2} + \sigma s_3 \left(\frac{Gm_3}{c^2}\right)^{1/2}} \quad , \end{aligned} \tag{1.76}$$

and where we use $\sigma = \pm 1$ to respectively distinguish orbits that are co-rotating and counter-rotating relatively to the angular momentum of the Kerr black

hole. [7] We also introduce the orbital angular velocity defined with respect to the proper time, which will be useful later in our analysis. This is given by $\Omega_{\hat{\phi}} = u^t \Omega$, which explicitly reads

$$\Omega_{\hat{\phi}} \equiv \frac{d\hat{\phi}}{d\tau} = \frac{\sigma \left(G m_3\right)^{1/2}}{\hat{r}^{1/2}\sqrt{\hat{r}^2 + 2\sigma s_3 \left(\frac{G m_3}{c^2}\hat{r}\right)^{1/2} - 3\frac{G m_3}{c^2}\hat{r}}} \ . \tag{1.77}$$

In the case of circular and equatorial geodesics, it is possible to obtain explicit expressions for the constants of motion in terms of the orbital radius $\hat{r}$, the black hole mass m_3, and the specific spin value s_3. More specifically, one has the energy, orbital angular momentum, and Carter constant per unit of rest energy

$$\begin{aligned}
\hat{E} &= \frac{\hat{r}^{3/2} - \frac{2Gm_3}{c^2}\hat{r}^{1/2} + \sigma s_3 \left(\frac{Gm_3}{c^2}\right)^{1/2}}{\hat{r}^{3/4}\sqrt{\hat{r}^{3/2} - 3\frac{Gm_3}{c^2}\hat{r}^{1/2} + 2\sigma s_3 \left(\frac{Gm_3}{c^2}\right)^{1/2}}} \ , \\
\hat{L} &= \frac{\sigma \left(\frac{Gm_3}{c^2}\right)^{1/2}\left(\hat{r}^2 + s_3^2 - 2\sigma s_3 \ \left(\frac{Gm_3}{c^2}\hat{r}\right)^{1/2}\right)}{\hat{r}^{3/4}\sqrt{\hat{r}^{3/2} - 3\frac{Gm_3}{c^2}\hat{r}^{1/2} + 2\sigma s_3 \left(\frac{Gm_3}{c^2}\right)^{1/2}}} \ , \\
K &= \left(s_3\hat{E} - \hat{L}\right)^2 = \left(\hat{r} - \sigma s_3\sqrt{\frac{c^2\hat{r}}{Gm_3}}\right)^2 \frac{\hat{r}^2\Omega_{\hat{\phi}}^2}{c^2} \ .
\end{aligned} \tag{1.78}$$

Finally, for later convenience, we also introduce the Innermost Stable Circular Orbit (ISCO). More in detail, in the equatorial plane of a Kerr black holes it is possible to identify two ISCOs: the first one is co-rotating ($\sigma = +1$) with the black hole while the second one is counter-rotating ($\sigma = -1$) with it. The value of the radial coordinate at which the ISCOs are located in the equatorial plane of the Kerr spacetime is given by [170]

$$\hat{r}^{\sigma}_{\rm ISCO} = \frac{Gm_3}{c^2}\left[3 + Z_2 - \sigma\sqrt{(3 - Z_1)(3 + Z_1 + 2Z_2)}\right] \ , \tag{1.79}$$

where

$$\begin{aligned}
Z_1 &= 1 + \left(1 - \chi^2\right)^{\frac{1}{3}}\left[(1+\chi)^{\frac{1}{3}} + (1-\chi)^{\frac{1}{3}}\right] \ , \\
Z_2 &= \sqrt{Z_1^2 + 3\chi^2} \ .
\end{aligned} \tag{1.80}$$

One can see immediately that for $\chi = 0$ eq. (1.79) reduces to $\hat{r}_{\rm ISCO} = 6Gm_3/c^2$, i.e. the usual ISCO position for a Schwarzschild black hole.

[7] In the Schwarzschild limit $\chi = 0$ then σ distinguishes anti-clockwise and clockwise orbits, respectively.

Binary system on a Kerr geodesic

As mentioned above, the two black holes in the BBH system are treated as point particles in the Newtonian limit since we assume the condition (1.70) to hold. We assume that the binary is moving along a circular, equatorial orbit in the background of a supermassive Kerr black hole. As seen in Section 1.2.1, if the binary system is small enough (1.71) we can treat the influence of the SMBH as a small perturbation on the BBH system, and we can approximate its presence through quadrupole tidal forces acting on the binary system, which is moving approximately on a geodesic of the Kerr background. This means we can employ the results of Section 1.2.1.

For the Kerr metric (1.72), we can use the *Marck's tetrad* [69] to describe the local Fermi-normal coordinates (1.58) of Section 1.2.1. Marck's tetrad is given by the four vectors λ^μ_A which provide an orthonormal basis for the vector space at each point of the Kerr-geodesic since $\lambda^\mu_A \lambda^\nu_B g_{\mu\nu} = \eta_{AB}$ and $\lambda^\mu_A \lambda^\nu_B \eta^{AB} = g_{\mu\nu}$, where in particular $\lambda^\mu_0 = u^\mu$ is the four-velocity. Note that $A = 0, 1, 2, 3$ are the flat tetrad indices. One can equivalently represent Marck's tetrad as the orthonormal one-forms $\lambda^A_\mu = \eta^{AB} g_{\mu\nu} \lambda^\nu_B$. One can now employ the standard map of the Fermi-Normal coordinates between vectors on the Kerr geodesic and events in the neighborhood of the geodesic. For Marck's tetrad, we have in addition to the time coordinate $x^0 = \tau$, which is the proper time on the geodesic, also the spatial coordinates x^i parametrizing an orthogonal vector $\sum_{i=1}^3 x^i \lambda^\mu_i$ at the geodesic. In this way the coordinates x^A describe a neighborhood of the geodesic. We will call this coordinate system the *Marck's frame of reference*.

Since Marck's tetrad is parallel-transported along the geodesic, it provides an inertial frame, meaning it is characterized by a vanishing acceleration and vanishing angular velocity of rotation of spatial basis vectors [171] [8]

$$a^i \equiv \lambda^i_\mu \frac{D\lambda^\mu_0}{d\tau} = 0 \quad , \quad \omega^i \equiv -\frac{1}{2}\epsilon^{ij}{}_k \lambda^\mu_j \frac{D\lambda^k_\mu}{d\tau} = 0 \quad . \tag{1.81}$$

For circular geodesics in the equatorial plane ($\hat{\theta} = \pi/2$), Marck's tetrad can be conveniently written in the one-forms basis as

$$\begin{aligned} \lambda^0_\mu &= \left(\hat{E}, 0, 0, \hat{L}\right) \quad , \\ \lambda^1_\mu &= \cos\Psi \ \tilde{\lambda}^1_\mu - \sin\Psi \ \tilde{\lambda}^2_\mu \quad , \\ \lambda^2_\mu &= \sin\Psi \ \tilde{\lambda}^1_\mu + \cos\Psi \ \tilde{\lambda}^2_\mu \quad , \\ \lambda^3_\mu &= (0, 0, -\hat{r}, 0) \quad , \end{aligned} \tag{1.82}$$

[8] Both formulas can be derived starting from the general transport law for an observer's tetrad, $D\lambda^\mu_a/d\tau = -\Omega^\mu{}_\nu \lambda^\nu_a$, with the quantity $\Omega_{\mu\nu} = a_\mu u_\nu - u_\mu a_\nu + u^\alpha \omega^\beta \epsilon_{\alpha\beta\mu\nu}$ [171].

with

$$\begin{aligned}\tilde{\lambda}^1_\mu &= \left(0, \sqrt{\frac{\hat{r}^2}{K+\hat{r}^2}}\frac{(\sqrt{K}s_3+\hat{E}\hat{r}^2)}{\Delta}, 0, 0\right) \quad , \\ \tilde{\lambda}^2_\mu &= \left(\frac{(s_3-\hat{E}\sqrt{K})}{\sqrt{K+\hat{r}^2}}, 0, 0, \frac{\hat{E}\sqrt{K}s_3 - s_3^2 - \hat{r}^2 - K}{\sqrt{K+\hat{r}^2}}\right) \quad ,\end{aligned} \tag{1.83}$$

where $\hat{r}$ is the constant radius of the circular equatorial geodesic and the angle Ψ is introduced to ensure that the tetrad is parallel transported along the geodesic [69, 168], as shown by Eqs. (1.81). The explicit expression for Ψ in terms of the geodesic's proper time τ is given by $\Psi = \Omega_\Psi \tau$, with

$$\Omega_\Psi \equiv \sigma\sqrt{\frac{Gm_3}{\hat{r}^3}} \quad . \tag{1.84}$$

To use the results for the Lagrangian and Hamiltonian of Section 1.2.1, given respectively in Eqs. (1.68) and (1.69), we report the explicit expressions for the electric tidal moments in the equatorial plane of a Kerr black hole, which are given by [69, 168][9]

$$\begin{aligned}\mathcal{E}_{11} &= \left[1 - 3\left(1+\frac{K}{\hat{r}^2}\right)\cos^2\Psi\right]\frac{Gm_3}{c^2\hat{r}^3} \quad , \\ \mathcal{E}_{22} &= \left[1 - 3\left(1+\frac{K}{\hat{r}^2}\right)\sin^2\Psi\right]\frac{Gm_3}{c^2\hat{r}^3} \quad , \\ \mathcal{E}_{33} &= \left(1+3\frac{K}{\hat{r}^2}\right)\frac{Gm_3}{c^2\hat{r}^3} \quad , \\ \mathcal{E}_{12} &= -3\left(1+\frac{K}{\hat{r}^2}\right)\frac{Gm_3}{c^2\hat{r}^3}\cos\Psi\sin\Psi \quad .\end{aligned} \tag{1.85}$$

These results can be used together with Eq. (1.67) to get an explicit expression for the scalar quadrupole electric tidal moment induced by the Kerr black hole, as measured by an observer using Fermi-normal coordinates, namely

$$\begin{aligned}r^2\mathcal{E}^q = \frac{Gm_3}{c^2\hat{r}^3}\Bigg[&r^2 + 3(x^3)^2\frac{K}{\hat{r}^2} \\ &-3\left(1+\frac{K}{\hat{r}^2}\right)(x^1\cos\Psi + x^2\sin\Psi)^2\Bigg] \quad .\end{aligned} \tag{1.86}$$

With this, we can describe the dynamics of the binary system in the approximations (1.70) and (1.71) via the Lagrangian (1.68) and Hamiltonian (1.69) of the BBH system.

[9] See Chapter 2, Section 2.1.1, for a derivation of the quadrupole tidal moments.

1.2.3 Gyroscope precession and the distant-star frame

In this section, we introduce the *gyroscope precession* of Marck's parallel transported reference frame by introducing a non-inertial frame of reference that we dub the *distant-star frame*. [10]

This precession arises from the curvature of the background spacetime, like it happens in the case of the Earth-Moon binary system orbiting around the Sun [172]. More in detail, the BBH system has an angular momentum which is precessing in its motion along an equatorial, circular geodesic in the Kerr background, around the direction identified by the angular momentum of the SMBH. In the Schwarzschild space-time this gyroscope precession is known as the *Fokker-de Sitter precession* [173], whereas in the equatorial plane of a Kerr black hole, it takes the name of *Schiff's precession* [174].

The origin of this precession is the difference between the local and global points of view for our binary system moving on a geodesic. Marck's frame represents the local view point, where we have an approximate inertial system close to the center of mass of the binary that moves on the geodesic. However, there is also a global point of view, in which the global properties of the Kerr spacetime are taken into account. In the case of an equatorial, circular motion this is clear since the only spatial coordinate in the BL coordinates of Kerr that changes is the angle $\hat{\phi}$ as

$$\hat{\phi} = \Omega_{\hat{\phi}} \tau \quad , \tag{1.87}$$

where $\Omega_{\hat{\phi}}$ is given in (1.77). A period of motion is obviously when $\hat{\phi}$ changes with 2π. However, Marck's frame is not the same after one period, since the Ψ angle has changed with $\Delta\Psi = 2\pi(\Omega_\Psi/\Omega_{\hat{\phi}} - 1)$, which gives the gyroscope precession.

Since the precession is not observable in Marck's frame of reference by itself, it is useful to define a non-inertial reference frame in which the gyroscope precession is manifest. Such a frame, here called the *distant-star* frame of reference, is constructed in [175], by simply rotating the Marck's frame with an angle $\hat{\phi} - \Psi$ such that the distant-star frame is periodic under rotations with respect to the $\hat{\phi}$ angle. Specifically, seeing it as a tetrad e^i_μ, it is defined by the following rotation of Marck's tetrad $e^i_\mu = R^i{}_j \lambda^j_\mu$ with

$$R^i{}_j = \begin{pmatrix} \cos(\Omega_{\rm g}\tau) & -\sin(\Omega_{\rm g}\tau) & 0 \\ \sin(\Omega_{\rm g}\tau) & \cos(\Omega_{\rm g}\tau) & 0 \\ 0 & 0 & 1 \end{pmatrix} \quad . \tag{1.88}$$

[10] The gyroscope precession was also considered for a BBH system in orbit around a Schwarzschild black hole in [166].

where we introduced the gyroscope angular velocity $\Omega_{\rm g}$ as

$$\Omega_{\rm g} = \Omega_{\hat{\phi}} - \Omega_\Psi = \Omega_\Psi \left(\frac{1}{\sqrt{1 + 2\frac{s_3}{c}\Omega_\Psi - 3\frac{\hat{r}^2}{c^2}\Omega_\Psi^2}} - 1 \right) \quad , \tag{1.89}$$

such that $\hat{\phi} - \Psi = \Omega_{\rm g}\tau$. It is easy to check that $\Omega_g = 0$ at $\hat{r} = 4/9\ (Gm_3/c^2)\chi^2$, and that this location never corresponds to a stable orbital radius, since $\hat{r}_\star < \hat{r}^\sigma_{\rm ISCO}$ for $0 \leq \chi \leq 1$. For completeness, we report that at the ISCO one has $\Omega_g = (c/\hat{r}_{\rm ISCO})(\sqrt{2}-1)/\sqrt{6}$ in the Schwarzschild case $\chi = 0$, whereas in the extreme Kerr case, $\chi = 1$, the gyroscope precession diverges as $\Omega_g \approx 2c/\sqrt{3}(\hat{r} - \hat{r}^+_{\rm ISCO})^{-1}$ for co-rotating orbits, and $\Omega_g = (c/\hat{r}^-_{\rm ISCO})(1/3 - \sqrt{3}/4)$ for the counter-rotating ones. As we shall see below, the distant-star frame provides a local coordinate system close to the circular equatorial geodesic in which one can directly observe the precession as a fictitious force in the Lagrangian description.

In general, a local observation of a precession angle is not possible, since one cannot compare angles between two events in spacetime in a path-independent manner. However, the construction of the distant-star tetrad is based on the global structure of the Kerr background, being stationary and axisymmetric, which gives a natural definition of angular and radial directions in the equatorial plane through Carter's tetrad [176]. Thus, in this sense, one can meaningfully claim the distant-star frame is fixed with respect to the asymptotic definition of the rotating angle, justifying its name as an angle with respect to distant stars. In other words, the distant-star frame provides a Cartesian frame that keeps a fixed orientation with respect to distant stars [175]. Hence, the non-inertial distant-star frame of reference provides a global point of view, contrary to the local inertial Marck's frame of reference.

Given that the distant-star tetrad e^i_μ is anchored to the geodesic, it has naturally a vanishing acceleration but it is characterized by a non-vanishing angular velocity of rotation relative to the Marck's tetrad [171]

$$a^i \equiv e^i_\mu \frac{De^\mu_0}{d\tau} = 0 \quad , \quad \omega^i \equiv -\frac{1}{2}\epsilon^{ij}{}_k e^\mu_j \frac{De^k_\mu}{d\tau} = \Omega_g \delta^i_3 \quad , \tag{1.90}$$

where we used the vector tetrad basis $e^\mu_i = \lambda^\mu_j (R^T)^j{}_i$ and $e^\mu_0 = \lambda^\mu_0 = u^\mu$.

The spatial coordinates $\boldsymbol{r}^i$ associated with the distant-star tetrad are given by [11]

$$\boldsymbol{r}^i = R^i{}_j x^j \quad . \tag{1.91}$$

In the following, we shall use the Cartesian vector notation

$$\boldsymbol{r} = \boldsymbol{r}^1 \hat{\boldsymbol{x}} + \boldsymbol{r}^2 \hat{\boldsymbol{y}} + \boldsymbol{r}^3 \hat{\boldsymbol{z}} \quad , \tag{1.92}$$

[11] This follows from the fact that for any vector V^μ its spatial components are $\boldsymbol{r}^i = V^\mu e^i_\mu = V^\mu R^i{}_j \lambda^j_\mu$ and $x^i = V^\mu \lambda^i_\mu$.

where we defined the unit vectors

$$\hat{\boldsymbol{x}} = \begin{pmatrix} 1 \\ 0 \\ 0 \end{pmatrix} \quad , \quad \hat{\boldsymbol{y}} = \begin{pmatrix} 0 \\ 1 \\ 0 \end{pmatrix} \quad , \quad \hat{\boldsymbol{z}} = \begin{pmatrix} 0 \\ 0 \\ 1 \end{pmatrix} \quad . \tag{1.93}$$

The consequence of going to this non-inertial frame for the binary system is the introduction of fictitious forces. Indeed, the local Lagrangian now becomes

$$\mathcal{L} = \frac{\mu}{2}(\boldsymbol{v} - \boldsymbol{\Omega}_{\mathbf{g}} \times \boldsymbol{r})^2 + \frac{GM\mu}{r} - \frac{c^2\mu}{2} r^2 \mathcal{E}^q \quad , \tag{1.94}$$

where we introduced the Cartesian vectors $\boldsymbol{v} = d\boldsymbol{r}/d\tau$ and $\boldsymbol{\Omega}_{\mathbf{g}} = \Omega_{\rm g}\hat{\boldsymbol{z}}$ in agreement with Eq. (1.90). Now Eq. (1.67) reads

$$\begin{aligned} r^2\mathcal{E}^q = & \frac{Gm_3}{c^2\hat{r}^3}\left[r^2 + 3(\boldsymbol{r}^3)^2\frac{K}{\hat{r}^2} + \right. \\ & \left. -3\left(1 + \frac{K}{\hat{r}^2}\right)(\boldsymbol{r}^1\cos\hat{\phi} + \boldsymbol{r}^2\sin\hat{\phi})^2\right] \quad . \end{aligned} \tag{1.95}$$

To find the Hamiltonian we define the canonical momentum as

$$\boldsymbol{\pi} = \frac{\partial\mathcal{L}}{\partial\boldsymbol{v}} = \mu\left(\boldsymbol{v} - \boldsymbol{\Omega}_{\rm g} \times \boldsymbol{r}\right) \quad , \tag{1.96}$$

and the canonical angular momentum as

$$\boldsymbol{L}_{\rm in} = \boldsymbol{r} \times \frac{\partial\mathcal{L}}{\partial\boldsymbol{v}} = \boldsymbol{r} \times \boldsymbol{\pi} \quad , \tag{1.97}$$

where we adopt the subscript "in" for later convenience to distinguish the angular momentum of the inner BBH system and the angular momentum associated with the outer orbit. The Hamiltonian, thus, reads

$$\mathcal{H} = \frac{\boldsymbol{\pi}^2}{2\mu} - \frac{G\mu M}{r} + \boldsymbol{\Omega}_{\rm g} \cdot \boldsymbol{L}_{\rm in} + \frac{\mu c^2}{2} r^2 \mathcal{E}^q \quad , \tag{1.98}$$

with $\mathcal{E}^q$ given in Eq.(1.95). The extra term in (1.98) with respect to (1.69) is responsible for the gyroscope precession of $\boldsymbol{L}_{\rm in}$.

1.2.4 Euler angles and action-angle variables

In this section we review standard definitions of angular coordinates and momenta that are highly useful in Celestial mechanics to describe the dynamics of the inner binary, and to derive the secular Hamiltonian in Section 1.2.5. Firstly we define all these quantities with respect to the distant-star reference frame, and secondly we introduce the action-angle formalism in Marck's frame of reference, providing a canonical transformation between the distant-star and Marck's frame Hamiltonians.

Euler angles

During the motion of the inner binary along a circular, equatorial geodesic in the Kerr spacetime, the orientation of the inner orbital plane of the BBH system can vary with respect to the outer orbital plane of the Kerr SMBH.

The vector (1.92) describing the relative position of a body in a Newtonian elliptic orbit can be represented as

$$\boldsymbol{r} = r(\cos\psi\ \hat{\boldsymbol{u}} + \sin\psi\ \hat{\boldsymbol{v}}) \quad , \tag{1.99}$$

where

$$r = \frac{a(1-e^2)}{1+e\cos\psi} \quad , \tag{1.100}$$

where a and e are respectively the *semi-major axis* and the *eccentricity* of the orbit, whereas ψ is the angular coordinate that keeps track of the body motion along the orbit, namely the *true anomaly*.

The two directions $\hat{\boldsymbol{u}}$ and $\hat{\boldsymbol{v}}$ have a precise geometrical meaning, with $\hat{\boldsymbol{u}}$ ($\psi = 0$) identifying the *periapsis direction*, and $\hat{\boldsymbol{v}}$ ($\psi = \pi/2$) lying along the *direction of the ascending nodes*. The space spanned by these two vectors specifies the inner orbital plane. These two vectors, together with the direction of the angular momentum for the inner binary $\hat{\boldsymbol{L}}_{\rm in} = \hat{\boldsymbol{u}} \times \hat{\boldsymbol{v}}$, form a triad of orthonormal vectors.

Since the inner binary is assumed to be in a Newtonian regime, it is possible to unambiguously introduce the *eccentric anomaly* ζ and the *mean anomaly* β, defined by means of

$$\cos\psi = \frac{\cos\zeta - e}{1 - e\cos\zeta} \quad , \quad \beta = \zeta - e\sin\zeta \quad . \tag{1.101}$$

The first relation defines ζ in terms of the true anomaly ψ, whereas the second is the Kepler equation. Kepler's equation is a transcendental equation and no closed-form solution is known that allows to express the eccentric anomaly ζ in terms of the mean anomaly β. The mean anomaly β represents the angle that a fictitious body moving in a circular orbit would span if it had the same orbital frequency as the actual body moving along the elliptic orbit. In other words its motion is uniform in time, $\beta = \sqrt{GM/a^3}\tau$.

One can obtain a generic orientation of the orbit using the Euler angles defined through the following rotation matrices

$$R_\theta = \begin{pmatrix} \cos\theta & -\sin\theta & 0 \\ \sin\theta & \cos\theta & 0 \\ 0 & 0 & 1 \end{pmatrix} \quad , \quad R_I = \begin{pmatrix} 1 & 0 & 0 \\ 0 & \cos I & -\sin I \\ 0 & \sin I & \cos I \end{pmatrix} \quad , \quad R_\gamma = \begin{pmatrix} \cos\gamma & -\sin\gamma & 0 \\ \sin\gamma & \cos\gamma & 0 \\ 0 & 0 & 1 \end{pmatrix} \quad , \tag{1.102}$$

where the angle θ is called the *longitude of ascending nodes*, I is the *orbital inclination*, and γ is the *argument of the periapsis*. We refer the reader to Fig. 1.6 for an illustration of the orbital parameters.

In general to describe a Newtonian orbit with an arbitrary orientation we need to introduce a reference plane. Given that we are working under the assumption $m_3 \gg (m_1 + m_2)$, it is natural to take the equatorial plane of the Kerr black hole as the reference plane. An arbitrary orientation of the inner binary is therefore derived by performing the rotation $\boldsymbol{r} = R_\theta R_I R_\gamma (r\cos\psi\ \hat{\boldsymbol{x}} + r\sin\psi\ \hat{\boldsymbol{y}})$, and by fixing $\psi = 0, \pi/2$ one gets

$$\begin{aligned}\hat{\boldsymbol{u}} =&(\cos\gamma\cos\theta - \cos I\sin\gamma\sin\theta)\ \hat{\boldsymbol{x}} \\ &+ (\cos\gamma\sin\theta + \cos I\sin\gamma\cos\theta)\ \hat{\boldsymbol{y}} \\ &+ \sin I\sin\gamma\ \hat{\boldsymbol{z}}\ ,\end{aligned} \tag{1.103}$$

$$\begin{aligned}\hat{\boldsymbol{v}} =&(-\sin\gamma\cos\theta - \cos I\cos\gamma\sin\theta)\ \hat{\boldsymbol{x}} \\ &+ (-\sin\gamma\sin\theta + \cos I\cos\gamma\cos\theta)\ \hat{\boldsymbol{y}} \\ &+ \sin I\cos\gamma\ \hat{\boldsymbol{z}}\ .\end{aligned} \tag{1.104}$$

For later use, we define in addition the *eccentricity vector* as

$$\boldsymbol{e} = e\ \hat{\boldsymbol{u}}\ , \tag{1.105}$$

which corresponds to the dimensionless version of the *Laplace–Runge–Lenz* vector [177].

The direction of the angular momentum for the inner binary is readily obtained as $\hat{\boldsymbol{L}}_{\rm in} = \hat{\boldsymbol{u}} \times \hat{\boldsymbol{v}}$, yielding

$$\hat{\boldsymbol{L}}_{\rm in} = \sin I\sin\theta\ \hat{\boldsymbol{x}} - \sin I\cos\theta\ \hat{\boldsymbol{y}} + \cos I\ \hat{\boldsymbol{z}}\ . \tag{1.106}$$

The magnitude of the outer orbit angular momentum $\hat{L}$ for a fully relativistic equatorial, circular geodesic in the Kerr background, as the one along which our BBH system is moving, is given in Eq. (1.78), whereas its direction in the distant-star frame is

$$\hat{\boldsymbol{L}}_{\rm out} = \hat{\boldsymbol{z}}\ . \tag{1.107}$$

Notice that, by definition, the inclination angle quantifies the projection of the inner orbit angular momentum on the outer orbit one, $\hat{\boldsymbol{L}}_{\rm in} \cdot \hat{\boldsymbol{L}}_{\rm out} = \cos I$.

Action-angle variables

In Celestial mechanics every time we are working with a periodic motion, it is convenient to analyse the problem by introducing the action-angle formalism, mostly because for any libration of periodic motion, we can introduce action-angle variables to describe the momenta. This is advantageous since they are constants of motion and allow us, in our description of the BBH-SMBH system, to describe the non-tidal part of the Hamiltonian (1.69) purely in

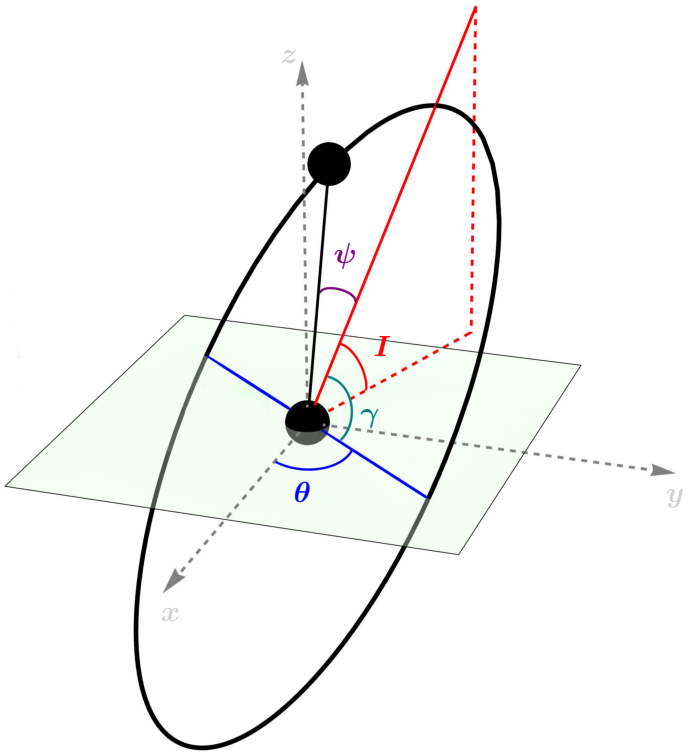

Figure 1.6: Illustration of orbital parameters. The green plane represents the reference plane while the intersection between the red line and the orbit constitutes the periapsis and the intersection between the blue line and the orbital plane provides the ascending node.

terms of constants of motion. We shall use the action-angle variables known as *Delauney variables* which we already introduced in Sec. 1.1 and here recall for convenience, with the position given by the three angles

$$(\beta, \gamma, \theta) \quad , \tag{1.108}$$

each periodic with period 2π, as well as the corresponding action-angle variables

$$\begin{gathered} J_\beta = \mu\sqrt{GMa} \quad , \quad J_\gamma = \mu\sqrt{GMa(1-e^2)} \quad , \\ J_\theta = \mu\sqrt{GMa(1-e^2)}\cos I \quad , \end{gathered} \tag{1.109}$$

with M and μ defined in Eq. (1.64) as the total mass and the reduced mass of the BBH system respectively.

We recall that the Delauney action variables are related to the magnitude and the orientation of the angular momentum of the inner binary with respect to the reference plane. In particular

$$J_\gamma = |\boldsymbol{L}_{\rm in}| \quad , \quad J_\theta = \boldsymbol{L}_{\rm in} \cdot \hat{\boldsymbol{L}}_{\rm out} \quad . \tag{1.110}$$

The total Hamiltonian of the inner binary (1.98) in the distant-star reference frame can therefore be simply expressed, in terms of action-angle variables, as

$$\mathcal{H} = -\left(\frac{GM}{J_\beta}\right)^2 + \Omega_{\rm g} J_\theta + \mathcal{H}_{\rm q} \quad . \tag{1.111}$$

and the quadrupole tidal part is expressed in terms of Euler angles according to

$$\begin{aligned}\mathcal{H}_{\rm q} = \frac{\mu}{2}\frac{Gm_3 r^2}{\hat{r}^3}\Bigg[1 + 3\frac{K}{\hat{r}^2}\sin^2(\gamma+\psi)\sin^2 I \\ - 3\left(1+\frac{K}{\hat{r}^2}\right)\big(\cos(\hat{\phi}-\theta)\cos(\gamma+\psi) \\ + \sin(\hat{\phi}-\theta)\sin(\gamma+\psi)\cos I\big)^2\Bigg] \quad .\end{aligned} \tag{1.112}$$

Action-angle variables for Marck's frame

For later convenience, we also introduce the action-angle variables for the Hamiltonian in Marck's frame of reference given by Eqs. (1.69) and (1.86).

It follows from Section 1.2.3 that the longitude of ascending nodes for Marck's reference frame is

$$\theta' = \theta - \Omega_{\rm g}\tau \quad , \tag{1.113}$$

where θ is the corresponding longitude of ascending nodes in the distant-star frame. This can also be written as $\theta' - \Psi = \theta - \hat{\phi}$. The other angles β and γ remain the same.

The Hamiltonian together with the action-angle variables conjugate to the angles (β, γ, θ') can be found directly by using a canonical transformation of the second type [177]. More precisely, this implies that the momenta $(J_\beta, J_\gamma, J_\theta)$ given in the distant-star frame (1.109) are the same for the Marck's frame, for it to be a canonical transformation. In detail, we have the generating function

$$F_2(q, P, \tau) = \beta\ J_\beta + \gamma\ J_\gamma + (\theta - \Omega_{\rm g}\tau)\ J_\theta \quad , \tag{1.114}$$

with (q, p) and (Q, P) being respectively the distant-star and the Marck phase space variables, which can be identified as

$$\begin{aligned} q_i &= (\beta, \gamma, \theta), \quad Q_i = (\beta, \gamma, \theta')\,, \\ p_i &= P_i = (J_\beta, J_\gamma, J_\theta)\,. \end{aligned} \tag{1.115}$$

This gives $p_i = \partial F_2/q_i$ and $Q_i = \partial F_2/\partial P_i$ as needed. The transformed Hamiltonian therefore becomes

$$H = \mathcal{H} + \partial_\tau F_2 = \mathcal{H} - \Omega_{\rm g} J_\theta \ . \tag{1.116}$$

From this we get the Hamiltonian in Marck's frame as

$$H = -\left(\frac{GM}{J_\beta}\right)^2 + H_{\rm q} \quad . \tag{1.117}$$

with quadrupole tidal part

$$\begin{aligned} H_{\rm q} = \frac{\mu}{2}\frac{Gm_3 r^2}{\hat{r}^3}\Bigg[1 + 3\frac{K}{\hat{r}^2}\sin^2(\gamma+\psi)\sin^2 I \\ - 3\left(1+\frac{K}{\hat{r}^2}\right)\Big(\cos(\Psi-\theta')\cos(\gamma+\psi) \\ + \sin(\Psi-\theta')\sin(\gamma+\psi)\cos I\Big)^2\Bigg] \quad . \end{aligned} \tag{1.118}$$

It is straightforward to check that if one introduces the Delauney variables directly for Marck's frame Hamiltonian given by Eqs. (1.69) and (1.86) one would get the same result as above.

1.2.5 Secular Hamiltonian

In this section we obtain the Hamiltonian describing the secular dynamics of the BBH-SMBH triple system. As already mentioned previously, the secular dynamics describes the binary system at timescales much larger than both the inner and outer orbit periods, namely the timescales respectively associated with the inner motion of the two black holes in the BBH system and the geodesic motion of the binary around the Kerr black hole.

The secular Hamiltonian is obtained by getting rid of the fast-dynamics in the triple system, namely by taking the average over both the inner orbit motion as well as the outer orbit motion. As explained above, these two motions can be separated to leading order in our regime (1.71), in that the outer orbit motion corresponds to the center of mass of the binary system moving on a circular geodesic in the equatorial plane of the supermassive Kerr black hole.

The motion of the two black holes in the inner binary, i.e. the inner orbit, is described as a Newtonian elliptic motion, which is perturbed by tidal forces.[12] To take the average, we need an angle that grows uniformly with time in the elliptic motion. In the Newtonian regime this is provided by the mean anomaly β defined in Eq. (1.101). However, since the tidal part of the Hamiltonian (1.112) is a function of the true anomaly ψ instead, we translate $(2\pi)^{-1}\int_0^{2\pi} d\beta$ into

$$\frac{1}{2\pi}\int_0^{2\pi} d\psi \frac{(1-e^2)^{3/2}}{(1+e\cos\psi)^2} \quad , \tag{1.119}$$

[12] In Section 1.2.7 we shall include the 1PN effect of the periastron precession as well as the leading GW radiation-reaction effect.

since this follows from Eq. (1.101).

The averaging procedure for the outer orbit is more subtle, this is due to the fact that General Relativistic effects play a role. In terms of the action-angle variables introduced in Section 1.2.4, we have found the Hamiltonian in both the non-inertial distant-star frame with Eqs. (1.111)-(1.112) as well as in the inertial Marck's frame with Eqs. (1.117)-(1.118).

We start by discussing the averaging procedure for the outer orbit in the distant-star frame, since this resemble the Newtonian case (see for example [19]), and thus it is more intuitive. In fact, by considering the Hamiltonian (1.111)-(1.112), we notice that it is periodic in the angle $\hat{\phi}$ with period 2π. This periodicity is precisely associated with one outer orbit cycle of motion. Moreover, the angle grows linearly with proper time, as one can infer from Eq. (1.87), making it the relativistic analog of the outer orbit angle, that one for instance uses in [19] for the averaging of the outer orbit. Therefore, the outer orbit average in this frame is simply performed as $(2\pi)^{-1}\int_0^{2\pi} d\hat{\phi}$.

The secular Hamiltonian is thus computed as the following double-average of the Hamiltonian (1.111) in the distant-star frame

$$\langle \mathcal{H} \rangle = -\left(\frac{GM}{J_\beta}\right)^2 + \Omega_{\rm g} J_\theta + \langle \mathcal{H}_{\rm q} \rangle \quad , \tag{1.120}$$

with

$$\langle \mathcal{H}_{\rm q} \rangle \equiv \frac{1}{(2\pi)^2}\int_0^{2\pi} d\hat{\phi}\int_0^{2\pi} d\psi \frac{(1-e^2)^{3/2}}{(1+e\cos\psi)^2}\mathcal{H}_{\rm q} \quad , \tag{1.121}$$

which explicitly reads

$$\begin{aligned}
&\langle \mathcal{H}_{\rm q} \rangle = -\Omega_{\rm ZLK}^{(\rm GR)} J_\gamma \left(\mathcal{W} + \frac{5}{3}\right) \quad , \\
&\mathcal{W} = (1-e^2)(\cos^2 I - 2) - 5e^2 \sin^2 I \sin^2\gamma \quad , \\
&\Omega_{\rm ZLK}^{(\rm GR)} = \Omega_{\rm ZLK}^{(\rm N)}\left(1 + 3\frac{K}{\hat{r}^2}\right) \quad , \\
&\Omega_{\rm ZLK}^{(\rm N)} = \frac{3}{8J_\gamma}\left(\frac{Gm_3\mu}{\hat{r}}\right)\left(\frac{a}{\hat{r}}\right)^2 \quad ,
\end{aligned} \tag{1.122}$$

where the subscript ZLK refers to the ZLK effect which will be extensively discussed in the remaining Sec. 1.2.6 and in Sec. 1.2.7.

From the expressions above we can see that the General Relativistic effects arising from the Kerr perturber are included in the dynamics of the BBH system through the overall prefactor $\Omega_{\rm ZLK}^{(\rm GR)}$ in the averaged tidal Hamiltonian (1.122). It is easy to check from (1.122) that in the weak field regime $\hat{r} \to \infty$ one recovers the Newtonian secular Hamiltonian of Ref. [19]. These General Relativistic effects are completely accounted for by the term in $\Omega_{\rm ZLK}^{(\rm GR)}$ proportional to the Carter constant K.

However, not all the General Relativistic effects are explicitly manifest in the prefactor $\Omega_{\rm ZLK}^{\rm (GR)}$, defined in Eq. (1.122). Some of them are not immediately apparent from the above secular Hamiltonian of Eqs. (1.120) and (1.122). The most obvious one is the gyroscope precession of the binary system introduced in Section 1.2.3, here arising from the term $\Omega_{\rm g} J_\theta$ in the total Hamiltonian (1.120). Another less explicit effect is the time dilation of the proper time used above, relative to the asymptotic time $\hat{t}$. This we shall include later in Section 1.2.7. Both of these effects are related to how an asymptotic observer will view the binary system, i.e. the global point of view, rather than the local point of view. Furthermore, in Section 1.2.7 we shall add further relativistic effects to the binary dynamics, to describe gravitational backreaction due to gravitational waves.

So far we have considered the averaging procedure only in the distant-star frame. It is important to check that one can obtain the same secular average in Marck's frame of reference. We notice immediately that the Hamiltonian (1.117)-(1.118) is periodic in Ψ with period 2π. Also, the angle grows linearly with time $\Psi = \Omega_\Psi \tau$. Therefore, we conclude that, in Marck's frame, one should compute the outer orbit average as $(2\pi)^{-1}\int_0^{2\pi} d\Psi$. Explicitly,

$$\langle H \rangle = -\left(\frac{GM}{J_\beta}\right)^2 + \langle H_{\rm q} \rangle \quad . \tag{1.123}$$

with

$$\langle H_{\rm q} \rangle \equiv \frac{1}{(2\pi)^2}\int_0^{2\pi} d\Psi \int_0^{2\pi} d\psi \frac{(1-e^2)^{3/2}}{(1+e\cos\psi)^2} H_{\rm q} \quad , \tag{1.124}$$

It is now straightforward to see that double-average over the tidal part of the Hamiltonian in the two different frames agree

$$\langle H_{\rm q} \rangle = \langle \mathcal{H}_{\rm q} \rangle \quad . \tag{1.125}$$

This means the only difference between the secular Hamiltonians in the two frames is the constant term $\Omega_{\rm g} J_\theta$, accounting for the fictitious forces.

However, as explained in Section 1.2.3, the gyroscope precession essentially measures the difference between $\hat{\phi}$ and Ψ when they have gone through one cycle in the outer orbit motion. So how can the outer orbit average over the tidal contribution give the same result in the two different frames, as we are averaging over two different angles? The answer lies in the formula $\hat{\phi} - \theta = \Psi - \theta'$. In the distant-star frame one should keep fixed θ in taking the average, as this angle is fixed during the motion. But, for Marck's frame, it is instead the angle θ' that one should keep fixed. Thus, the reason that the outer orbit averages give the same result in the two frames is that the difference between θ and θ' precisely accounts for the difference $\hat{\phi} - \Psi$, which is the gyroscope precession.

Notice that the canonical transformation detailed in Sec. 1.2.4 can also be

directly used to relate the secular Hamiltonian in the distant-star frame with the secular Hamiltonian in Marck's frame. Since neither depend on the respective longitude of ascending nodes angle (θ and θ'), this transformation simply relates the secular Hamiltonians as $\langle H\rangle = \langle \mathcal{H}\rangle - \Omega_{\rm g} J_\theta$.

1.2.6 ZLK mechanism in a strong GR background

In this section, we apply the result for the secular Hamiltonian in the distant-star reference frame, as derived in the previous section, to study the long timescale dynamics of the BBH system moving on an equatorial circular geodesic of the external Kerr SMBH.

An important result of this Section is that we can quantify to what extent the ZLK frequency departs from its Newtonian value when one takes into account strong gravity effects associated to the general relativistic description that we adopt for the outer orbit. Moreover, in this Section we derive the equations of motion for the inner orbital parameters, from which one can study the evolution of the ZLK mechanism. This will be used later to compare the weak-gravity limit of our results to the PN corrections found in the literature. In Section 1.2.7 we build on the results of this section by refining the equations of motion for the inner orbital parameters found in Section 1.2.6 to include the periastron precession and GW emission. This is used to study the ZLK mechanism and its influence on the binary merger time.

ZLK frequency in the vicinity of SMBH

From the distant-star frame secular Hamiltonian, given by Eqs. (1.120) and (1.122), it is immediate to observe that two main effects govern the secular dynamics of the BBH system: the ZLK mechanism, which manifests due to the tidal interaction with the external SMBH, and the gyroscope precession, which is present in the distant-star frame of reference whenever a general relativistic description for the SMBH is adopted.

We begin this section by discussing the ZLK mechanism which in the distant-star secular Hamiltonian is modeled by the quadrupole tidal contribution $\langle \mathcal{H}_q\rangle$ in Eq. (1.122). A well-known result in the literature concerning the ZLK mechanism [20, 27, 123] is that the set of parameters characterizing the outer orbit only enters in $\langle \mathcal{H}_q\rangle$ through the frequency of the eccentricity/inclination oscillations. We observe from (1.122) that this remains true in our case, as all the information concerning the outer orbit enter through the frequency $\Omega_{\rm ZLK}^{\rm (GR)}$. Thus, all new tidal force effects that arise from an exact metric description of the SMBH as a Kerr black hole enters through this frequency. Therefore, the main aim of the following is to show that BBH systems close enough to an external SMBH to probe the strong gravity regime can manifest substantial deviations in the frequency of the ZLK oscillations, com-

pared to the frequency one gets from employing a Newtonian point particle approximation.

We begin by comparing $\Omega_{\rm ZLK}^{\rm (GR)}$ to the Newtonian frequency $\Omega_{\rm ZLK}^{\rm (N)}$, i.e. the frequency that would have resulted from Newtonian quadrupole tidal forces induced by a particle of mass m_3. We find

$$\frac{\Omega_{\rm ZLK}^{\rm (GR)}}{\Omega_{\rm ZLK}^{\rm (N)}} = \frac{1+\frac{3\chi^2}{d^2}-\frac{4\sigma\chi}{d^{3/2}}}{1-\frac{3}{d}+\frac{2\sigma\chi}{d^{3/2}}} \quad , \tag{1.126}$$

where we defined for convenience the dimensionless radius d for the equatorial circular orbit as

$$d = \hat{r}\frac{c^2}{Gm_3} \quad . \tag{1.127}$$

Remarkably, at the ISCO $\hat{r} = \hat{r}_{\rm ISCO}^{\sigma}$ the ratio (1.126) takes the universal value[13]

$$\Omega_{\rm ZLK}^{\rm (GR)} = 2\Omega_{\rm ZLK}^{\rm (N)} \quad . \tag{1.128}$$

This result will be highly important in Section 1.2.7 where we consider the evolution of the BBH-SMBH system in detail. One can check that (1.128) gives the maximal value of the ratio (1.126) that the binary system can attain. Instead, for large d the ratio goes to one. Both of these statements are illustrated in Fig. 1.7. The result (1.128) shows that one has an order one difference between the weak-field Newtonian result $\Omega_{\rm ZLK}^{\rm (N)}$ and our novel strong field result $\Omega_{\rm ZLK}^{\rm (GR)}$ when close to the SMBH.

However, it is important to note here that the frequency $\Omega_{\rm ZLK}^{\rm (GR)}$ is measured with respect to the proper time of the BBH orbit. Thus, this is not the frequency that an asymptotic observer would measure. To find the corresponding asymptotic ZLK frequency we need to incorporate the redshift factor as follows

$$\Omega_{\rm ZLK}^{(\infty)} = \frac{1}{u^t}\Omega_{\rm ZLK}^{\rm (GR)} \tag{1.129}$$

where the redshift factor can be written as

$$u^t = \frac{\Omega_{\hat{\phi}}}{\Omega} = \frac{1+\frac{\sigma\chi}{d^{3/2}}}{\sqrt{1-\frac{3}{d}+\frac{2\sigma\chi}{d^{3/2}}}} \quad , \tag{1.130}$$

which one can check is always greater than 1, and it is a decreasing function of $\sigma\chi$ for fixed d. Using (1.130) we get the following ratio between the asymptotically measured ZLK frequency $\Omega_{\rm ZLK}^{(\infty)}$, which now takes into account all the GR effects, and the corresponding Newtonian frequency $\Omega_{\rm ZLK}^{\rm (N)}$

$$\frac{\Omega_{\rm ZLK}^{(\infty)}}{\Omega_{\rm ZLK}^{\rm (N)}} = \frac{1+\frac{3\chi^2}{d^2}-\frac{4\sigma\chi}{d^{3/2}}}{\left(1+\frac{\sigma\chi}{d^{3/2}}\right)\sqrt{1-\frac{3}{d}+\frac{2\sigma\chi}{d^{3/2}}}} \quad . \tag{1.131}$$

[13] One can derive this using $K = \frac{1}{3}\hat{r}_{\rm ISCO}^2$ at the ISCO, see Ref. [168].

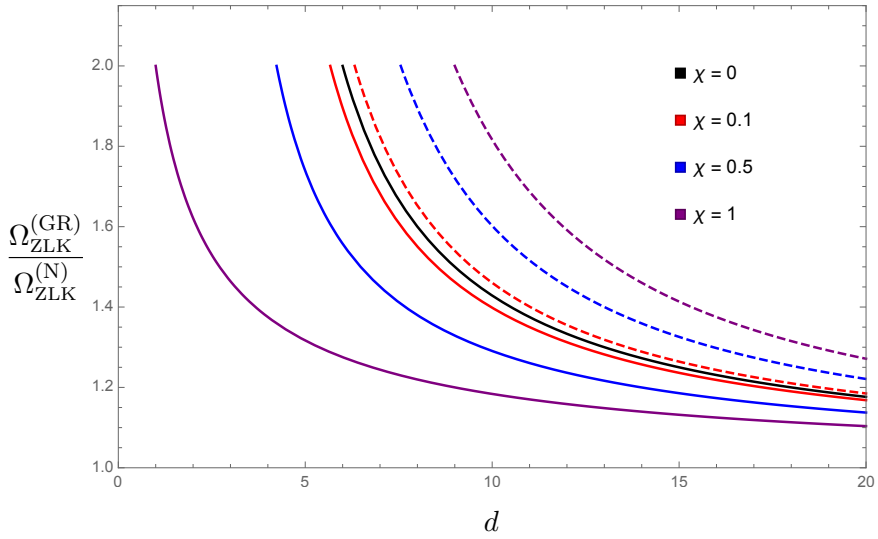

Figure 1.7: Diagram of the ratio $\Omega^{(GR)}_{ZLK}/\Omega^{(N)}_{ZLK}$ versus the distance d from the SMBH. Different colors label various values of the black hole spin χ where the solid and dashed lines represent co-rotating ($\sigma = +1$) and counter-rotating ($\sigma = -1$) orbits, respectively. Each curve terminates at the ISCO.

The inclusion of the redshift factor gives a more refined difference in the ratio of the frequencies. One finds that in the counter-rotating case $\sigma = -1$ the maximal value of the ratio (1.131) is at the ISCO, as illustrated in Fig. 1.8. For the co-rotating case $\sigma = 1$, the same is true for the range $0 \leq \chi \leq 0.69$. However, as illustrated in Fig. 1.9, this behavior starts changing in the range $0.69 \leq \chi \leq 0.7$, so that for $\chi \geq 0.7$ the maximal value of the ratio (1.131) is no longer reached at the ISCO. We see from Fig. 1.10 that for $\chi \geq 0.75$ it is instead the minimal value that one reaches at the ISCO.

For all three Figs. 1.8, 1.9, and 1.10 we note that the ratio (1.131) approaches 1 for d going to infinity, as one would expect. Finally, we have also plotted the value of the ratio (1.131) at the ISCO in Fig. 1.11.

The above results for $\Omega^{(\infty)}_{ZLK}/\Omega^{(N)}_{ZLK}$ show that the GR effects that arise from being in close vicinity to the SMBH are highly significant. This is particularly relevant in the case of bound systems of BBHs situated in the GC. Indeed, we see the importance of including strong-gravity effects as they significantly alter the frequency, and therefore the timescale, of the ZLK oscillations. One can also see that the spin of the SMBH, as modeled by a Kerr black hole, can significantly alter the dynamics.

Evolution equations for ZLK mechanism

Using the secular Hamiltonian (1.122) we can now derive the evolution equations for the orbital variables describing the inner BBH system. It is possible

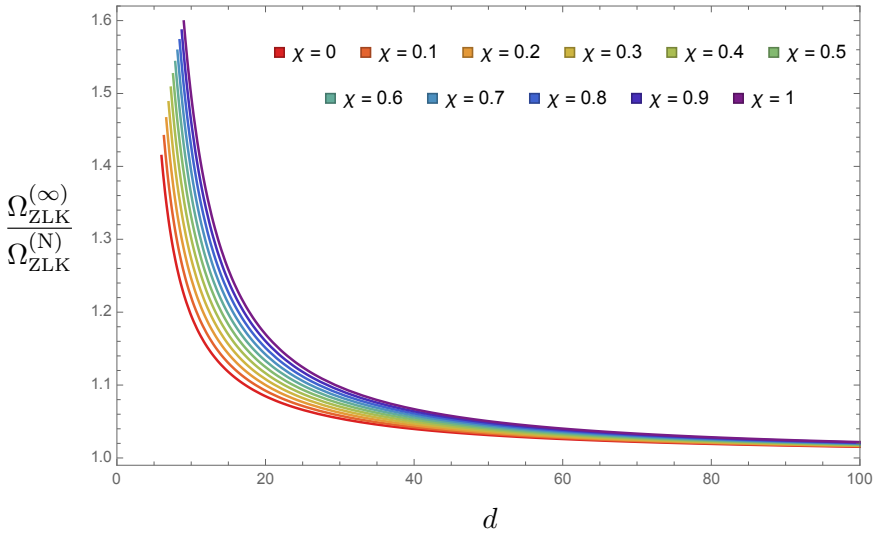

Figure 1.8: The ratio $\Omega^{(\infty)}_{\rm ZLK}/\Omega^{(\rm N)}_{\rm ZLK}$ is plotted in the counter-rotating case $\sigma = -1$ as a function of the dimensionless radius d for several values of the spin. The figure shows that the maximum value for the ratio is always at the ISCO.

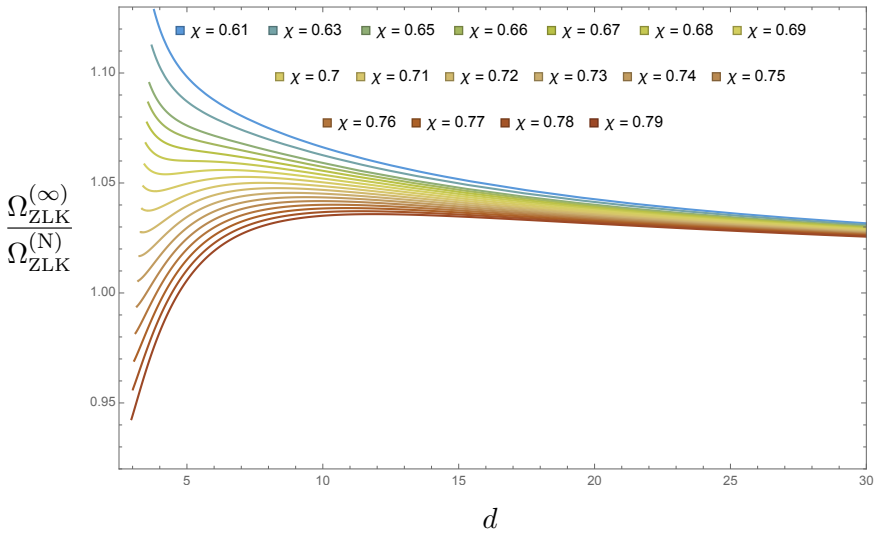

Figure 1.9: The ratio $\Omega^{(\infty)}_{\rm ZLK}/\Omega^{(\rm N)}_{\rm ZLK}$ is plotted in the co-rotating case $\sigma = 1$ as function of the dimensionless radius d for the range $0.61 \leq \chi \leq 0.79$.

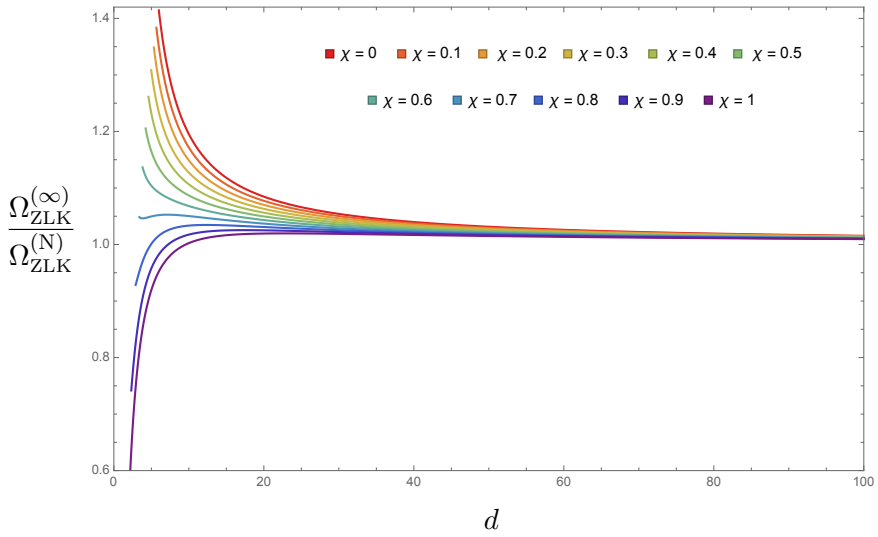

Figure 1.10: The ratio $\Omega^{(\infty)}_{\rm ZLK}/\Omega^{(\rm N)}_{\rm ZLK}$ is plotted in the co-rotating case $\sigma = 1$ as a function of the dimensionless radius d for several values of the spin.

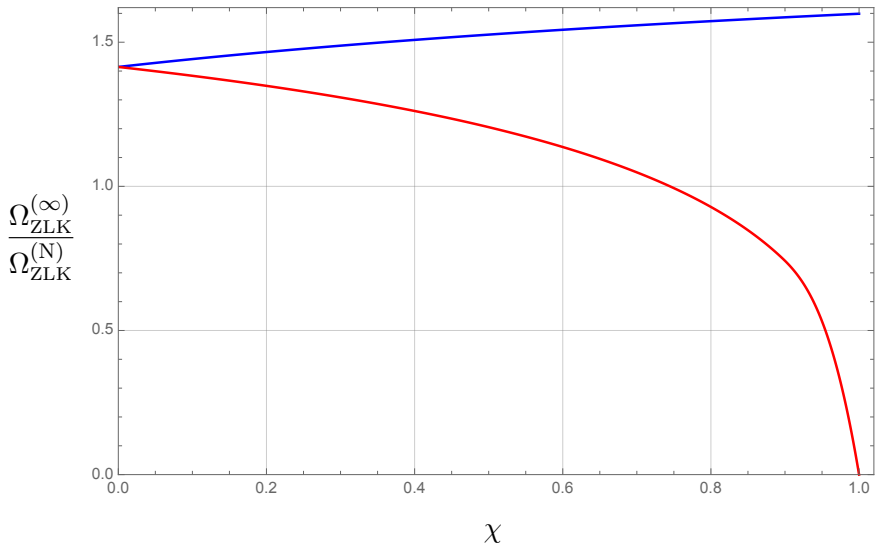

Figure 1.11: Here the binary system is always placed at the ISCO. The blue line describes the counter-rotating case while the red line describes the co-rotating case.

to derive an evolution equation for the orbital inclination I by exploiting the fact that $J_\theta = J_\gamma \cos I$, Eq. (1.109), which yields

$$\frac{dI}{d\tau} = \frac{1}{J_\gamma \sin I}\left(\frac{dJ_\gamma}{d\tau}\cos I - \frac{dJ_\theta}{d\tau}\right) \quad . \tag{1.132}$$

This general equation will be useful when including the loss of angular momentum associated with the emission of GWs, which we postpone to Sec. 1.2.7. In this section instead, we only focus on the effect of tidal deformations resulting in the ZLK mechanism. For the secular Hamiltonian (1.122) the Euler angle θ is a cyclic variable so that its conjugate momentum J_θ is a constant of motion, $dJ_\theta/d\tau = -\partial_\theta \langle \mathcal{H} \rangle = 0$, and the last term in (1.132) does not contribute if we ignore the emission of GWs.

Similarly, the equation of motion for the eccentricity of the inner binary follows from the definition of the Delauney variable J_γ in Eq. (1.109). In the following we use the fact that no variation of the semi-major axis a exists in the absence of GW emission, so that

$$\frac{de}{d\tau} = \frac{dJ_\gamma}{d\tau}\left(\frac{dJ_\gamma}{de}\right)^{-1} = -\frac{1-e^2}{e}\frac{1}{J_\gamma}\frac{dJ_\gamma}{d\tau} \quad . \tag{1.133}$$

Therefore, the evolution equations for the orbital elements can be derived from the equation of motion of J_γ. This follows from Hamilton's equations and only involves the tidal Hamiltonian

$$\frac{dJ_\gamma}{d\tau} = -\frac{\partial \langle \mathcal{H} \rangle}{\partial \gamma} = -5\Omega_{\rm ZLK}^{\rm (GR)} J_\gamma e^2 \sin^2 I \sin 2\gamma \quad . \tag{1.134}$$

From the relations (1.132), (1.133), and (1.134) one can derive the ZLK contributions to the evolution equations for the orbital inclination I and for the eccentricity e

$$\frac{dI}{d\tau} = -\frac{5}{2}\Omega_{\rm ZLK}^{\rm (GR)} e^2 \sin 2I \sin 2\gamma \quad , \tag{1.135}$$

$$\frac{de}{d\tau} = 5\,\Omega_{\rm ZLK}^{\rm (GR)} e(1-e^2)\sin^2 I \sin 2\gamma \quad . \tag{1.136}$$

From these equations of motion, it is immediate to notice that the stationary points for minimum and maximum inclination and eccentricity correspond to $\gamma = 0, \pi/2$. As we mentioned earlier, as long as the gravitational backreaction is neglected, $J_\theta = \boldsymbol{L}_{\rm in} \cdot \hat{\boldsymbol{L}}_{\rm out} = \mu\sqrt{GMa(1-e^2)}\cos I$ is conserved, meaning that the orbital inclination has a maximum $I_{\rm max}$ when the eccentricity is minimal $e_{\rm min}$, and viceversa. In particular, by computing the second derivative in (1.135) and (1.136), it is easy to show that the pair $(I_{\rm max}, e_{\rm min})$ occur for $\gamma = 0$, whereas one has $(I_{\rm min}, e_{\rm max})$ for $\gamma = \pi/2$.

The evolution equation for the longitude of ascending nodes can be derived from Eq. (1.122), upon making in $\langle \mathcal{H} \rangle$ the substitution $\cos I = J_\theta / J_\gamma$. One has

$$\frac{d\theta}{d\tau} = \frac{\partial \langle \mathcal{H} \rangle}{\partial J_\theta} = \Omega_{\rm g} - 2\Omega_{\rm ZLK}^{\rm (GR)} \cos I (1 - e^2 + 5e^2 \sin^2 \gamma) \quad , \tag{1.137}$$

where it is evident the contribution of the gyroscope precession in the distant-star frame. Using the canonical transformation detailed in Sec. 1.2.4 it is immediate to derive an analogous equation for the shifted angle $\theta' = \theta - \Omega_g \tau$ in Marck's frame, which indeed lacks the gyroscope precession contribution. We stress that in passing from the distant-star to Marck's frame of reference only θ changes in θ', and therefore all other equations of motion written before remain unaltered.

Finally, the equation of motion for the argument of the periapsis γ can be found by trading the eccentricity e for the angular momentum J_γ and using again that $\cos I = J_\theta / J_\gamma$. We get

$$\frac{d\gamma}{d\tau} = \frac{\partial \langle \mathcal{H} \rangle}{\partial J_\gamma} = 2\Omega_{\rm ZLK}^{\rm (GR)} [2(1 - e^2) - 5(1 - e^2 - \cos^2 I) \sin^2 \gamma] \quad . \tag{1.138}$$

General-relativistic effects in the ZLK mechanism

The ZLK mechanism is an effect for which a binary system under the influence of the tidal forces of an outer third body can exhibit a periodic exchange of eccentricity and orbital inclination, with a timescale much larger than its orbital period [20, 27, 123].

To understand under which circumstances this mechanism can operate, one can start by recalling that, in the Newtonian approximation for the inner binary, the secularly-averaged Hamiltonian $\langle \mathcal{H} \rangle$ and the angular momentum projection J_θ are conserved quantities. Their values can therefore be estimated by fixing initial conditions for the eccentricity e_0 and the inclination I_0. The corresponding values for $\langle \mathcal{H} \rangle$ and J_θ will be labeled as $\langle \mathcal{H} \rangle_0$ and $(J_\theta)_0$. By restricting to the case in which the inner orbit is initially circular, $e_0 = 0$, from the conservation of energy and angular momentum, explicitly $\langle \mathcal{H} \rangle_0 = \langle \mathcal{H} \rangle_{\gamma = \pi/2}$ and $(J_\theta)_0 = \mu \sqrt{GMa(1 - e_{\rm max}^2)} \cos I_{\rm min}$, one gets

$$e_{\rm max} = \sqrt{1 - \frac{5}{3} \cos^2 I_0} \quad , \quad \cos I_{\rm min} = \pm \sqrt{\frac{3}{5}} \quad . \tag{1.139}$$

Notice that, being $I_{\rm min}$ independent of the initial inclination I_0, it does not only constitute the minimum inclination reached in the ZLK oscillation but also the critical angle for the onset of the ZLK effect [20]. For the ZLK mechanism to work, one has that the initial inclination I_0 should obey $|\cos I_0| < \sqrt{3/5}$. For an initial inclination $I_0 \approx \pi/2$ of the inner binary system in circular orbit ($e_0 = 0$), the system exhibits high eccentricity $e_{\rm max} \approx 1$.

We thus find that including full general relativistic effects for the outer orbit does not alter the way the ZLK mechanism is triggered, it only affects

the frequencies associated with the ZLK oscillations, as discussed in Sec. 1.2.6. In Sec. 1.2.7 we will include PN effects in the inner binary dynamics that will modify the condition (1.139) [178].

A more exhaustive way to see how the ZLK mechanism manifests itself together with the general-relativistic gyroscope precession consists of considering the interchange between the eccentricity vector $\boldsymbol{e}$ of the inner binary and its angular momentum $\boldsymbol{L}_{\rm in}$ relative to the orbital plane of the outer binary. More specifically, from Eqs. (1.105),(1.106) and (1.110), one has

$$\frac{d\boldsymbol{L}_{\rm in}}{d\tau} = \frac{dL_{\rm in}}{d\tau}\hat{\boldsymbol{L}}_{\rm in} + L_{\rm in}\frac{d\hat{\boldsymbol{L}}_{\rm in}}{d\tau} \quad , \quad \frac{d\boldsymbol{e}}{d\tau} = \frac{de}{d\tau}\hat{\boldsymbol{u}} + e\frac{d\hat{\boldsymbol{u}}}{d\tau} \quad . \tag{1.140}$$

These evolution equations can be computed explicitly by recalling that both directions for $\boldsymbol{e}$ and $\boldsymbol{L}_{\rm in}$ are parametrized in terms of Euler angles I, γ, and θ (see Eqs. (1.103), (1.105), and (1.106)) whereas their magnitudes are respectively related to the eccentricity e and the Delauney variable J_γ (see Eqs. (1.110) and (1.133)) so that

$$\frac{d\boldsymbol{L}_{\rm in}}{d\tau} = \frac{dJ_\gamma}{d\tau}\hat{\boldsymbol{L}}_{\rm in} + J_\gamma\left(\frac{d\hat{\boldsymbol{L}}_{\rm in}}{dI}\,\frac{dI}{d\tau} + \frac{d\hat{\boldsymbol{L}}_{\rm in}}{d\theta}\,\frac{d\theta}{d\tau}\right) \quad , \tag{1.141}$$

$$\frac{d\boldsymbol{e}}{d\tau} = \frac{de}{d\tau}\hat{\boldsymbol{u}} + e\left(\frac{d\hat{\boldsymbol{u}}}{dI}\,\frac{dI}{d\tau} + \frac{d\hat{\boldsymbol{u}}}{d\theta}\,\frac{d\theta}{d\tau} + \frac{d\hat{\boldsymbol{u}}}{d\gamma}\,\frac{d\gamma}{d\tau}\right) \quad . \tag{1.142}$$

By exploiting vector identities, Eqs. (1.141) and (1.142) can be rewritten as

$$\begin{aligned}\frac{d\boldsymbol{L}_{\rm in}}{d\tau} = {}& \boldsymbol{\Omega}_g \times \boldsymbol{L}_{\rm in} + 2\Omega_{\rm ZLK}^{\rm (GR)} J_\gamma\Big[(1-e^2)(\hat{\boldsymbol{L}}_{\rm in}\cdot\hat{\boldsymbol{L}}_{\rm out})(\hat{\boldsymbol{L}}_{\rm in}\times\hat{\boldsymbol{L}}_{\rm out}) \\ & - 5(\boldsymbol{e}\cdot\hat{\boldsymbol{L}}_{\rm out})(\boldsymbol{e}\times\hat{\boldsymbol{L}}_{\rm out})\Big] \quad , \end{aligned} \tag{1.143}$$

$$\begin{aligned}\frac{d\boldsymbol{e}}{d\tau} = {}& \boldsymbol{\Omega}_g \times \boldsymbol{e} + 2\Omega_{\rm ZLK}^{(GR)}\Big[(\hat{\boldsymbol{L}}_{\rm in}\cdot\hat{\boldsymbol{L}}_{\rm in})(\boldsymbol{e}\times\hat{\boldsymbol{L}}_{\rm in}) + 2\hat{\boldsymbol{L}}_{\rm in}\times\boldsymbol{e} \\ & - 5(\boldsymbol{e}\cdot\hat{\boldsymbol{L}}_{\rm out})(\hat{\boldsymbol{L}}_{\rm in}\times\hat{\boldsymbol{L}}_{\rm out})\Big] \quad , \end{aligned} \tag{1.144}$$

where we used $\boldsymbol{\Omega_g} = \Omega_g\hat{\boldsymbol{L}}_{\rm out}$ and the results obtained in Eqs. (1.133) and (1.134).

Eqs. (1.143) and (1.144) are written in terms of the proper time τ related to the inner binary system. From the point of view of an asymptotic observer, they become

$$\begin{aligned}\frac{d\boldsymbol{L}_{\rm in}}{d\hat{t}} = {}& \boldsymbol{\Omega}_g^{(\infty)} \times \boldsymbol{L}_{\rm in} + 2\Omega_{\rm ZLK}^{(\infty)} J_\gamma\Big[(1-e^2)(\hat{\boldsymbol{L}}_{\rm in}\cdot\hat{\boldsymbol{L}}_{\rm out})(\hat{\boldsymbol{L}}_{\rm in}\times\hat{\boldsymbol{L}}_{\rm out}) \\ & - 5(\boldsymbol{e}\cdot\hat{\boldsymbol{L}}_{\rm out})(\boldsymbol{e}\times\hat{\boldsymbol{L}}_{\rm out})\Big] \quad , \end{aligned} \tag{1.145}$$

$$\frac{d\boldsymbol{e}}{d\hat{t}} = \boldsymbol{\Omega}_g^{(\infty)} \times \boldsymbol{e} + 2\Omega_{\rm ZLK}^{(\infty)}\Big[(\hat{\boldsymbol{L}}_{\rm in}\cdot\hat{\boldsymbol{L}}_{\rm in})(\boldsymbol{e}\times\hat{\boldsymbol{L}}_{\rm in}) + 2\hat{\boldsymbol{L}}_{\rm in}\times\boldsymbol{e}$$

$$- 5(\boldsymbol{e}\cdot\hat{\boldsymbol{L}}_{\rm out})(\hat{\boldsymbol{L}}_{\rm in}\times\hat{\boldsymbol{L}}_{\rm out})\Big] \quad , \tag{1.146}$$

where we defined

$$\Omega_g^{(\infty)} = \frac{1}{u^t}\Omega_g \ . \tag{1.147}$$

Notice that the redshifted gyroscope precession frequency above is always finite: at the ISCO, for instance, one has $\Omega_g^{(\infty)} = (c/\hat{r}_{\rm ISCO})(\sqrt{2}-1)/(2\sqrt{3})$ in the non-spinning case $\chi = 0$, whereas at extremality, $\chi = 1$, one finds $\Omega_g^{(\infty)} = 1/2(c/r^+_{\rm ISCO})$ and $\Omega_g = (c/\hat{r}^-_{\rm ISCO})(4/\sqrt{3}-9)/26$ respectively for the co-rotating and counter-rotating orbits.

Eq.s (1.145) and (1.146) include the gyroscope precession and extend the results previously known in the literature for the ZLK effect [140, 141, 179] to the case in which the external body, in this case a supermassive Kerr black hole, is described using the Kerr metric (1.72), thus being in a strong GR regime.

In the case of a circular orbit for the inner binary, $\boldsymbol{e} = 0$, which constitutes a solution for the equation for the eccentricity, Eq. (1.145) becomes

$$\frac{d\boldsymbol{L}_{\rm in}}{d\hat{t}} = \left[\Omega_g^{(\infty)} - 2\Omega_{\rm ZLK}^{(\infty)}(\hat{\boldsymbol{L}}_{\rm in}\cdot\hat{\boldsymbol{L}}_{\rm out})\right](\hat{\boldsymbol{L}}_{\rm out}\times\boldsymbol{L}_{\rm in}) \quad , \tag{1.148}$$

which describes the precession of the angular momentum of the inner binary $\boldsymbol{L}_{\rm in}$ around the direction of the angular momentum of the outer binary $\hat{\boldsymbol{L}}_{\rm out}$. In the weak-field limit $\hat{r}\to\infty$, one has

$$\begin{aligned}
&\frac{d\boldsymbol{L}_{\rm in}}{d\hat{t}} = \\
&\left[\frac{3}{2}\frac{(Gm_3)^{\frac{3}{2}}\sigma}{c^2\ \hat{r}^{\frac{5}{2}}} - \frac{GJ_3}{c^2\hat{r}^3} - \frac{3}{4}\frac{m_3}{\hat{r}^3}\sqrt{\frac{Ga^3}{M}}(\hat{\boldsymbol{L}}_{\rm in}\cdot\hat{\boldsymbol{L}}_{\rm out})\right](\hat{\boldsymbol{L}}_{\rm out}\times\boldsymbol{L}_{\rm in}) \\
&+\left[\frac{9}{8}\frac{(Gm_3)^{\frac{5}{2}}\sigma}{c^4\ \hat{r}^{\frac{7}{2}}} - 3\frac{G^2m_3J_3}{c^4\hat{r}^4} - \frac{9}{8}\frac{Gm_3^2}{c^2\hat{r}^4}\sqrt{\frac{Ga^3}{M}}(\hat{\boldsymbol{L}}_{\rm in}\cdot\hat{\boldsymbol{L}}_{\rm out})\right](\hat{\boldsymbol{L}}_{\rm out}\times\boldsymbol{L}_{\rm in}) \\
&+\mathcal{O}\left(\hat{r}^{-9/2}\right) \quad ,
\end{aligned}$$

where in the first line, the first term represents the 1PN contribution due to the gyroscope precession, the second term is a relativistic effect related to the spin of the SMBH and the third term represents the precession generated by the standard ZLK mechanism. This is consistent with the results presented in Ref. [140], in the hierarchical regime for circular outer orbits and where the contribution proportional to the spin of the SMBH comes from the Lense-Thirring precession. The second line is instead a new result and represents higher-order contributions which we predict using the result in Eq. (1.148).

As pointed out in the past literature (see for instance [180], [181] and [140]) the interplay of the ZLK mechanism with additional precessing effects

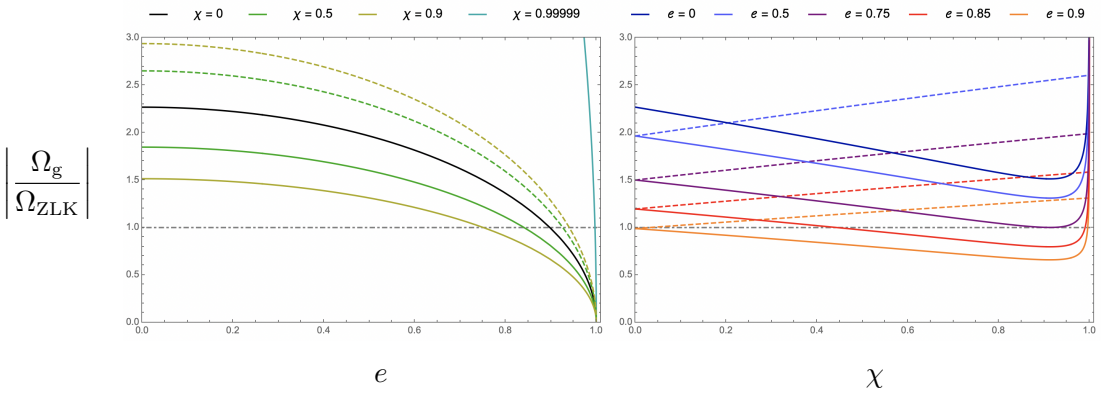

Figure 1.12: In this figure we set $m_1 = m_2 = 10\ M_\odot$, $m_3 = 2 \times 10^9\ M_\odot$ and $a = 0.1$ AU. (Left panel) Absolute value of the ratio between the gyroscope precession frequency and the ZLK frequency as a function of the inner binary eccentricity e. The different curves are obtained for different values of the dimensionless spin parameter χ of the SMBH. (Right panel) Absolute value of the ratio between the gyroscope precession frequency and the ZLK frequency as a function of the dimensionless spin parameter χ of the SMBH, for different values of the eccentricity of the inner binary e. The solid and dashed coloured curves are respectively for co-rotating ($\sigma = +1$) and counter-rotating ($\sigma = -1$) outer geodesics. The value $R = 1$, depicted with the dot-dashed line, marks the trans-adiabatic regime in which $\Omega_g^{(\infty)} \approx \Omega_{\rm ZLK}^{(\infty)}$. The rightmost curve in the left panel, corresponding to $\chi = 0.99999$, is reported to show that $R \to \infty$ for $\chi \to 1$, in agreement with the behaviour presented in the right panel and the discussion made below Eq. (1.89).

can lead to significant alteration in the BBH dynamics and exhibit chaotic features. The dynamical behaviour can be identified by means of an adiabatic parameter, that we define as

$$R \equiv \left|\frac{\Omega_g^{(\infty)}}{\Omega_{\rm ZLK}^{(\infty)}}\right|\Bigg|_{\hat{r}^\sigma_{\rm ISCO}} = \left|\frac{\Omega_g}{\Omega_{\rm ZLK}^{(\rm GR)}}\right|\Bigg|_{\hat{r}^\sigma_{\rm ISCO}}\,, \tag{1.149}$$

where the ratio is evaluated at the ISCO, since $\hat{r}^\sigma_{\rm ISCO}$ marks the scale at which the strong-gravity effects are more relevant in our setup. Fig. 1.12 shows plots for the ratio R in a specific configuration for the BBH-SMBH system as a function of the inner BBH system eccentricity e and the SMBH spin parameter χ. It would be interesting to study the interplay between the gyroscope precession and the ZLK mechanism further.

1.2.7 Binary merger time close to a supermassive BH

In this section, we refine the dynamics of the inner binary system by adding the periastron precession and GW emission, so that we can study the interplay

of these effects together with the ZLK mechanism. This enables us to study how treating the SMBH in strong gravity can alter the dynamics of the BBH system compared to if one included only the Newtonian gravity effect of the SMBH [19, 182].

We recall that to treat the presence of the SMBH as a perturbation of the BBH system the condition (1.71) must be satisfied. After introducing the parametrization for an elliptic orbit as in (1.100), the tidal condition can be rewritten in terms of the semi-major axis a of the binary system as

$$a \ll \hat{r}\sqrt{\frac{c^2\hat{r}}{Gm_3}}\,. \tag{1.150}$$

This ensures that we can safely neglect the GW backreaction of the outer orbit and consider therefore only the GWs emitted by the inner BBH [19].

Post-Newtonian dynamics of the binary system

GWs emitted by the inner BBH system reduce its energy and angular momentum and consequently its semi-major axis a and eccentricity e. Peters's equations [15, 183] keep into account this gravitational backreaction by providing the orbit-averaged evolution of e and a for an isolated binary. The average variations read

$$\begin{aligned}\left\langle \frac{da}{d\tau} \right\rangle_{\rm GW} &= -\frac{64}{5}\frac{G^3\mu M^2}{a^3c^5}\frac{1}{\left(1-e^2\right)^{7/2}}\left(1+\frac{73}{24}e^2+\frac{37}{96}e^4\right)\,, \\ \left\langle \frac{de}{d\tau} \right\rangle_{\rm GW} &= -\frac{304}{15}\frac{G^3\mu M^2}{a^4c^5}\frac{e}{\left(1-e^2\right)^{5/2}}\left(1+\frac{121}{304}e^2\right)\,.\end{aligned} \tag{1.151}$$

These equations were obtained to model the gravitational backreaction for an isolated binary, but one can include the influence of a third external body, that interacts with the binary through the ZLK mechanism, by adding these PN contributions to the system of equations describing the time evolution of the orbital variables (a, e, γ, I), as given in Eqs. (1.135), (1.136), (1.138). In particular, the first of the two PN contributions above is responsible for triggering the inspiral phase for the binary system, by decreasing the relative distance a between the two masses. As opposed to the ZLK mechanism, which can lead to an increase of the orbital eccentricity e, the second equation shows how the emission of GWs tends to circularise the orbit.

We recall that J_γ represents the magnitude of the angular momentum for a Newtonian binary system. Hence, by combining Eqs. (1.151) with the definition of J_γ, according to Eq. (1.109), it is immediate to estimate the loss of angular momentum associated to the GW emission, namely [184]

$$\left\langle \frac{dJ_\gamma}{d\tau} \right\rangle_{\rm GW} = -\frac{32}{5}\frac{G^{7/2}\mu^2M^{5/2}}{a^{7/2}c^5}\frac{1}{(1-e^2)^2}\left(1+\frac{7}{8}e^2\right)\,. \tag{1.152}$$

It is important to stress that the gravitational backreaction only reduces the magnitude of the angular momentum, without affecting its direction. In other words, if we ignore the presence of the SMBH, the binary system remains in the same plane when including the GW emission. Thus, we have $\langle dI/d\tau \rangle_{\rm GW} = 0$ which from Eq. (1.132) gives

$$\left\langle \frac{dJ_\theta}{d\tau} \right\rangle_{\rm GW} = \left\langle \frac{dJ_\gamma}{d\tau} \right\rangle_{\rm GW} \cos I \quad . \tag{1.153}$$

It is immediate to notice, using Eq. (1.152), that the loss of angular momentum (or, analogously, the decreasing of the orbital distance and eccentricity, according to Eq. (1.151)) due to GW emission becomes extremely efficient when the condition $e \approx 1$ is met. As we discuss this in more detail in the following subsection, the enhancement in the eccentricity due to the ZLK mechanism can therefore boost the merger of eccentric binary systems. While such *ZLK-boosted mergers* were already noticed in previous works that analyzed the combined ZLK dynamics with PN effects (see for instance Refs. [19,182]), in the next subsection we show that strong gravity effects associated to the external SMBH can lead to further significant changes in the frequency of the ZLK-oscillations and in the merger time. Finally, following [19], we include also the effect of the periastron precession of elliptic orbits as an additional contribution to the evolution equations, since this 1PN effect plays a significant role in the ZLK mechanism. Indeed, as we shall review later, it is known to limit the range in which the ZLK mechanism is valid. Notice that the periastron precession preserves the angular momentum vector $d\boldsymbol{L}_{\rm in}/d\tau = 0$, meaning for instance that the orbital plane remains unchanged and only manifests itself as an apsidal advance $d\hat{\boldsymbol{e}}_{\rm in}/d\tau = (d\gamma/d\tau)\hat{\boldsymbol{v}}$ (see Eqs. (1.141) and (1.142)). The periastron precession can therefore be written in terms of a first derivative for the argument of periapsis γ, according to

$$\left(\frac{d\gamma}{d\tau}\right)_{PN} = \frac{3}{ac^2\left(1-e^2\right)}\left(\frac{GM}{a}\right)^{3/2} \quad . \tag{1.154}$$

As discussed below, these PN effects alter the dynamics of the ZLK mechanism for BBH systems influenced by the presence of an external mass. We can now write down a closed set of equations by combining the evolution equations Eqs. (1.135), (1.136), (1.138) of Sec. 1.2.6, which considers the strong gravity effects of an external spinning SMBH, with the effects of GW emission and

periastron precession introduced above. This gives the evolution equations

$$\begin{aligned}
\left\langle \frac{da}{d\tau} \right\rangle &= -\frac{64}{5}\frac{G^3\mu M^2}{a^3c^5}\frac{1}{\left(1-e^2\right)^{7/2}}\left(1+\frac{73}{24}e^2+\frac{37}{96}e^4\right) \quad , \\
\left\langle \frac{de}{d\tau} \right\rangle &= 5\Omega_{\rm ZLK}^{\rm (GR)} e(1-e^2)\sin^2 I \sin 2\gamma \\
&\quad -\frac{304}{15}\frac{G^3\mu M^2}{a^4c^5}\frac{e}{\left(1-e^2\right)^{5/2}}\left(1+\frac{121}{304}e^2\right) \quad , \\
\left\langle \frac{d\gamma}{d\tau} \right\rangle &= 2\Omega_{\rm ZLK}^{\rm (GR)}[2(1-e^2)-5(1-e^2-\cos^2 I)\sin^2\gamma] \\
&\quad +\frac{3}{ac^2\left(1-e^2\right)}\left(\frac{GM}{a}\right)^{3/2} \quad , \\
\left\langle \frac{dI}{d\tau} \right\rangle &= -\frac{5}{2}\Omega_{\rm ZLK}^{\rm (GR)} e^2 \sin 2I \sin 2\gamma \quad ,
\end{aligned} \tag{1.155}$$

where the equations have to be supplemented with the definition $J_\gamma = \mu\sqrt{GMa(1-e^2)}$, as in Eq. (1.109), and with the general-relativistic definition of the ZLK frequency $\Omega_{\rm ZLK}^{\rm (GR)}$, that we derived in Eq. (1.126). These evolution equations are written with respect to the proper time τ, being the time associated with the inner binary system. However, one can use $\frac{d}{d\hat{t}} = \frac{1}{u^t}\frac{d}{d\tau}$ to translate these equations into evolution equations with respect to the asymptotic time $\hat{t}$ to obtain the dynamical description as seen by an asymptotic observer. The system of equations (1.155) allows us to study how the orbital parameters (e, a, I, γ) of the inner binary, evolve in time. To solve them, one has to specify initial conditions for the inner BBH system, $(a_0, e_0, \gamma_0, I_0)$, a set of parameters that characterize the outer circular equatorial orbit around the Kerr SMBH $(\hat{r}, s_3, \sigma = \pm 1)$, and the three masses (m_1, m_2, m_3).

In the next subsection, we solve numerically the system of equations (1.155), for some specific case of interest. We will work in astronomical units, i.e. (AU, $M_\odot$ and years), where $G = 4\pi^2$ and $c = 63072$ AU/years.
As previously explained, we need to impose the condition (1.150) for the tidal approximation to be valid. This allows us to neglect the GW backreaction of the outer orbit over the timescale that governs the inner binary dynamics. Furthermore, we are working in the near-Newtonian regime (1.70) in which we can treat the black holes in the inner binary approximately as particles.
The ZLK oscillations take place on a timescale much longer than the orbital period of the binary system around the SMBH. Thus, it becomes important to ensure that the triple system is stable, allowing the ZLK mechanism to enhance the eccentricity of the BBH system. When the binary system is too close to the SMBH, the interaction between the three bodies can result in a tidal breakup.

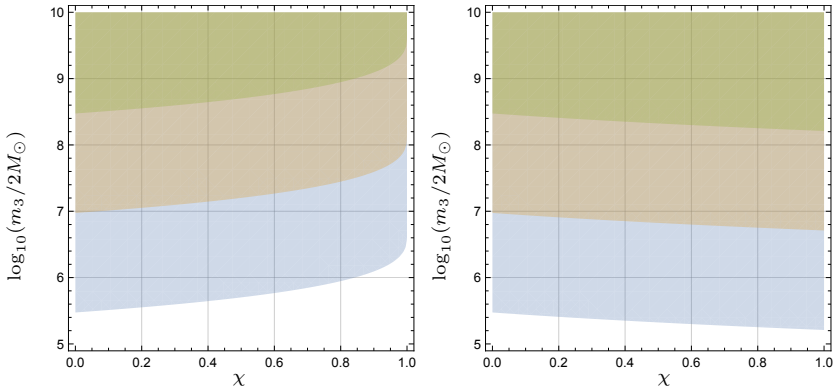

Figure 1.13: The colored regions represent regions of the parameter space for the SMBH which are consistent with the tidal breakup condition $\hat{r}/a > (3m_3/M)^{1/3}$. The green, orange and blue colors respectively identify $\hat{r} = \hat{r}^{\sigma}_{\rm ISCO}$, $\hat{r} = 10\ \hat{r}^{\sigma}_{\rm ISCO}$ and $\hat{r} = 100\ \hat{r}^{\sigma}_{\rm ISCO}$, whereas the left and right panels distinguish co-rotating ($\sigma = +1$) and counter-rotating orbits ($\sigma = -1$). The plots are obtained by fixing $m_1 = m_2 = 10\ M_\odot$ and $a = 0.1$ AU, as representative values for a stellar-mass BBH system.

To ensure that the presence of an SMBH does not lead to a tidal break up of the binary system, the stability condition defined in (1.2) and (1.1) has to be satisfied. In our analysis, we carefully chose the radial distance between the binary system and the SMBH so as to always guarantee the stability of the triple system. As an illustrative example, in Fig. 1.13 we plot the regions of the parameter space for the SMBH which are consistent with the tidal breakup condition (1.2), in the case of a stellar-mass BBH system with masses $m_1 = m_2 = 10\ M_\odot$ and separation $a = 0.1$ AU.

To prepare for the analysis we perform in the remaining of this section, we now briefly introduce respectively the GW and PN timescales at play in our investigation and the peak frequency of GW emitted by the BBH system. These will play a key role in the next subsections where we show how the GR effects in the strong field regime affect the merger time of the binary system and the emission of GW waves.

Time Scales

For an isolated BBH system the merger time due to the emission of GWs is [15, 16]

$$T_{\rm GW} = \frac{5}{256}\frac{c^5 a_0^4}{G^3 m_1 m_2 M} G(e_0)(1-e_0^2)^{7/2} \quad , \tag{1.156}$$

where

$$G(e_0) = \frac{48}{19 g^4(e_0)(1-e_0^2)^{7/2}} \int_0^{e_0} \frac{g^4(\tilde{e})(1-\tilde{e}^2)^{5/2}}{\tilde{e}\left(1+\frac{121}{304}\tilde{e}^2\right)} d\tilde{e} \quad ,$$
$$g(e) = \frac{e^{12/19}}{1-e^2}\left(1+\frac{121}{304}e^2\right)^{870/2299} \quad . \tag{1.157}$$

The function $G(e_0) \in [0.979, 1.81]$ for $e_0 \in [0,1]$, and for an order of magnitude estimate it can be ignored. For all practical purposes, a good approximation for an isolated BBH system merger time is thus given by

$$T_{\rm GW} \approx 1.6\ (1-e_0^2)^{7/2} \times 10^{10}\ {\rm yrs} \times \left(\frac{10M_\odot}{m_1}\right)\left(\frac{10M_\odot}{m_2}\right)\left(\frac{20M_\odot}{M}\right)\left(\frac{a_0}{0.1\ {\rm AU}}\right)^4 \quad . \tag{1.158}$$

The prefactor $(1-e_0^2)^{7/2}$ shows that for very high values of the eccentricity, the merger time can be drastically reduced. Tidal interactions generated by an external SMBH, through the ZLK mechanism, can produce high eccentricities, thus catalyzing the coalescence for highly-inclined BBHs and speeding up the merger to timescales much shorter than those characteristic of isolated binaries with the same masses and relative distance [185].

From Eq.(1.154) we can compute also the time scale associated with the periastron precession as

$$T_{\rm PN} = \frac{ac^2\left(1-e^2\right)}{3}\left(\frac{a}{GM}\right)^{3/2} \equiv \frac{2\pi}{\Omega_{\rm PN}} \quad . \tag{1.159}$$

In this regard, it is interesting to notice that, when the periastron timescale becomes comparable with the ZLK timescale $T_{\rm ZLK} = 2\pi/\Omega_{\rm ZLK}$, the periastron precession destroys the ZLK resonance and the binary system begins to evolve as if it was isolated. To see the competing effects of the periastron precession and the ZLK mechanism, it is convenient to neglect the GW backreaction and analyze under which conditions $\langle d\gamma/d\tau\rangle = 0$ and $\langle de/d\tau\rangle = 0$ in Eq. (1.155), where the second equation is automatically satisfied by setting $\gamma = \pi/2$. One finds

$$\cos^2 I_0 = \frac{3}{5}(1-e^2) - \frac{3}{10}\frac{1}{(1-e^2)}\frac{\left(\frac{GM}{a}\right)^{3/2}}{ac^2\Omega_{\rm ZLK}^{\rm (GR)}} \tag{1.160}$$

which replaces Eq.(1.139) when the periastron precession is taken into account. Due to the presence of $\Omega_{\rm ZLK}^{\rm (GR)}$, this generalizes the Newtonian formula found in [182]. The window of values for the critical inclination that triggers the ZLK resonance is reduced by the presence of the periastron effect. This makes it complicated to find a condition on $\hat{r}$ that would result in the condition

$\cos^2 I_0 > 0$. To illustrate this, consider the simpler case of a non-spinning SMBH for which we find the following condition

$$\frac{\hat{r}^3}{a^3}\left(1-\frac{3Gm_3}{c^2\hat{r}}\right) < \frac{3}{4}(1-e^2)^{3/2}\left(\frac{ac^2}{GM}\right)\frac{m_3}{M} \quad . \tag{1.161}$$

In the limit in which this bound is saturated, the critical inclination value is close to $I_0 \approx 90°$, so that the minimum and maximum values for the inclination almost coincide. It is clear from (1.160) that, consistently, the maximum value of the eccentricity is lowered compared to the case in which the periastron precession is neglected.

Peak Frequency

For eccentric binaries, the GW spectrum is spread across an infinite number of harmonics [183], with frequencies that are integer multiples n of the fundamental Keplerian frequency $1/(2\pi)\sqrt{GM/a^3}$, and peaked approximately at [147]

$$f_{\rm GW} \simeq \frac{\sqrt{GM}}{\pi[a(1-e^2)]^{3/2}}(1+e)^{1.1954} \quad . \tag{1.162}$$

In the evolution of an isolated binary the gravitational backreaction, encoded in Eqs. (1.151), would contribute to circularize the orbit and move the peak frequency towards the usual $n = 2$ harmonic long before the merger takes place [16]. Under the influence of an external body, however, the ZLK mechanism can provide large eccentricity oscillations in highly-inclined binaries and can enhance the peak frequency to values high enough to enter in the sensitivity band of future space-based GW detectors [35].

Binary merger time in the weak field limit

In Sec. 1.2.3 we studied how GR effects induced by the presence of a spinning SMBH can lead to a significant enhancement of the frequency for the ZLK resonance in the case of a Newtonian binary system moving on a circular geodesic. By superimposing the ZLK mechanism with the PN dynamics of the inner BBH system, according to the discussion made in the previous subsection, we are now in a position to study how the BBH merger time is influenced by the presence of an external SMBH.

We will start the study of the evolution equations (1.155) by considering a case in which we are in the weak gravity regime, regarding the influence of the SMBH on the binary system. This regime has already been studied previously, *e.g.* in [19], but here we use it to provide a baseline for the analysis in the strong gravity regime (also described by Eqs. (1.155)), which we will discuss later and where we find novel results.

We investigate the evolution equations (1.155) by solving them numerically. For the weak-field example of this section we choose fixed masses

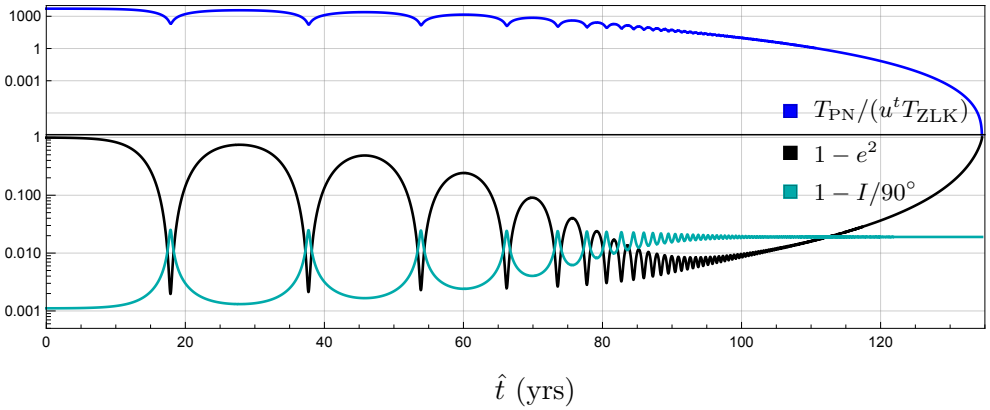

Figure 1.14: We focus on the spinless case for the SMBH, i.e. $\chi = 0$. Here $\hat{r} = 120$ AU, which corresponds to approximately $\hat{r} \approx 500\ \hat{r}_{\rm ISCO}$ for a non-spinning black hole with mass $m_3 = 4 \times 10^6 M_\odot$. We combine the effect of the ZLK mechanism with the periastron precession and GW emission. The picture highlights that the maximum values of the BBH eccentricity e corresponds to the minimum values for its orbital inclination I and viceversa.

$m_1 = m_2 = 10\ M_\odot$ and $m_3 = 4 \times 10^6\ M_\odot$ for the three black holes.[14] We use these values to connect to previous literature (e.g. Ref. [19]) and since m_3 is roughly the mass of Sagittarius A*. Moreover, we choose the initial conditions for the inner binary to be $e_0 = 0.1$, $a_0 = 0.1$ AU , $\gamma_0 = 0^\circ$ and $I_0 = 89.9^\circ$, so that we only need to specify the outer orbit parameters.[15]

For a non-spinning SMBH with the above-mentioned choice for m_3 we have the ISCO radius $\hat{r}_{\rm ISCO} = 6\ Gm_3/c^2 \approx 0.24$ AU. Naturally, the strong gravity effects from the presence of the SMBH are most significant at the ISCO. We choose here the outer orbit radius to be $\hat{r} = 120$ AU $\approx 500\ \hat{\rm r}_{\rm ISCO}$ which means we are within the weak-field regime (concerning the gravitational influence of the SMBH on the binary system). In this regime, the redshift factor is $u^t \approx 1$ according to Eq. (1.76). At the same time, $\hat{r} = 120$ AU ensures we are well below the tidal breakup limit (1.2).

From Eq. (1.158) one can observe that, with our choice for the orbital parameters, it would take approximately $\sim 10^{10}$ years for an isolated binary to coalesce. In Fig. 1.14 we show our numerical solution, which presents the characteristic quasi-periodic behavior of the BBH system influenced by an

[14] Note that the system has the scaling property that if we scale all three masses m_1, m_2, and m_3 with the same factor, along with the initial conditions for the semi-major axis of the inner binary a_0 and radius of the outer orbit $\hat{r}$, the merger time will be rescaled with this factor as well.

[15] The initial value for the inclination angle I is chosen specifically to maximize the ZLK mechanism. The initial value for the semi-major axis a is fixed to be 0.1 AU. This value is small enough to ensure that the binary system does not break up when interacting with the SMBH, according to Eq. (1.2), but it is also sufficiently large to allow the two black holes in the inner binary to evolve without merging too fast [114].

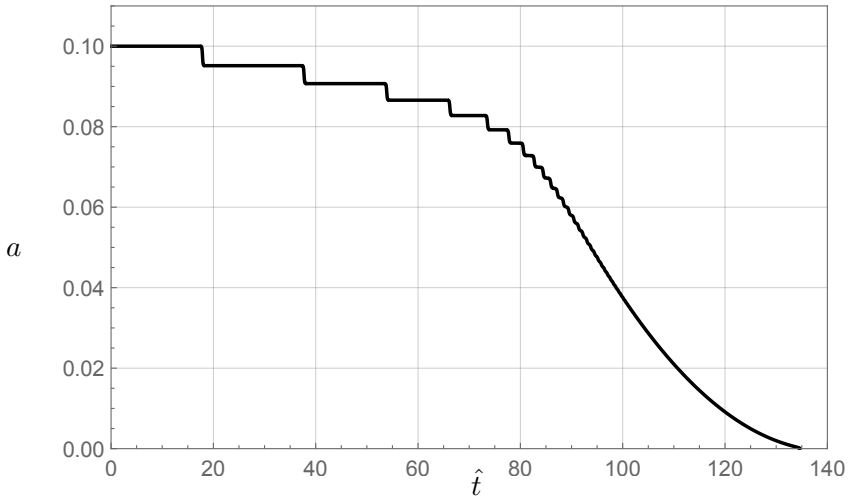

Figure 1.15: Semi-major axis as a function of the asymptotic time $\hat{t}$ in the non-spinning case for $\hat{r} = 500\ \hat{r}_{\rm ISCO} \approx 120$ AU. The step-like behavior is a consequence of the loss of angular momentum, which is maximized when the eccentricity oscillations are close to their maximum values (the minima of the black curve in Fig. 1.14).

external SMBH. From Fig. 1.14 it is immediate to see that the time for the merger to occur is drastically reduced to order $\sim 10^2$ years by the presence of the eccentricity oscillations associated with the weak-gravity ZLK mechanism.

It is possible to distinguish three different phases that characterize the merger process in the example we consider. At earlier stages ($T_{\rm PN} \gg T_{\rm ZLK}$) the ZLK mechanism dominates the dynamics and, due to the inner binary's high initial inclination, leads to large-amplitude oscillations for the eccentricity and inclination. More specifically one can see from Fig. 1.14 that, in agreement with the ZLK mechanism, the maximum eccentricity e (minima of the black curve) corresponds to a minimum of the inclination I (maxima of the cyan curve). The temporary increase of the eccentricity up to $e \approx 0.999$ leads to an efficient loss of angular momentum via GW emission in a small amount of time, which translates into the typical step-like monotonic decreasing of the semi-major axis a (see Fig. 1.15), and in a progressive reduction of the ZLK oscillations amplitude.

In the intermediate stage, the ZLK timescale becomes comparable with the periastron precession timescale ($T_{\rm ZLK} \sim T_{\rm PN}$), and the eccentricity/inclination oscillations are hampered by the PN contributions in the BBH dynamics.
In the final phase ($T_{\rm PN} \ll T_{\rm ZLK}$), the ZLK resonance is suppressed. In other words, the BBH evolves as if the system were isolated and characterized by a high initial eccentricity inherited by the ZLK mechanism. The Peter's contributions in Eqs. (1.155) then become dominant, causing a fast orbital circularisation and a prompt decreasing in the semi-major axis of the BBH system

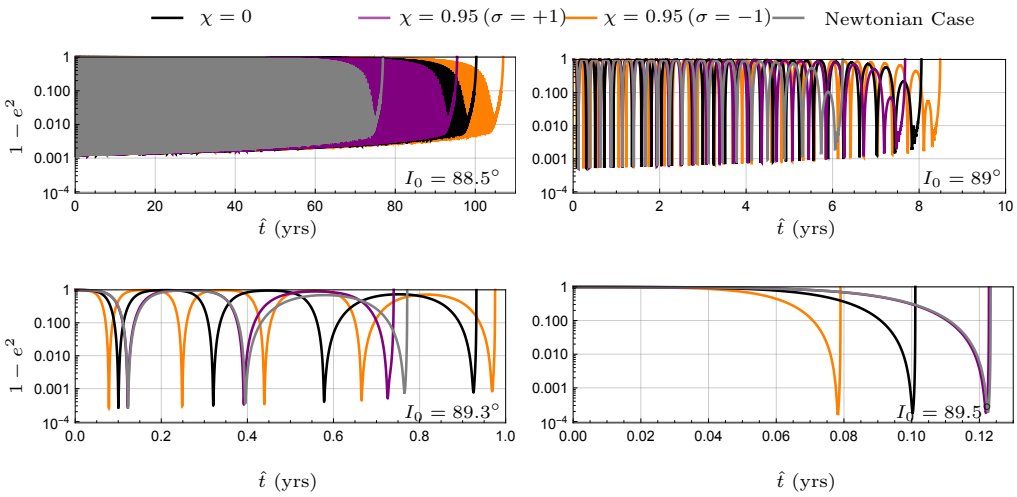

Figure 1.16: The picture shows the evolution of the eccentricity for a BBH system perturbed by an external SMBH of mass $m_3 = 2 \times 10^9\ M_\odot$. The four panels correspond to different values of the initial inclination I_0. The gray curve represents the case in which the external black hole is treated in the Newtonian point particle approximation, the black curve includes general-relativistic effects associated with a non-spinning black hole whereas the purple and orange curves describe a Kerr black hole with spin parameter $\chi = 0.95$ in the co-rotating (purple line) and counter-rotating (orange line) case. Here we choose $\hat{r} = 180$ AU. In terms of the ISCO radius it means $\hat{r} \sim 1.5\ \hat{r}_{\rm ISCO}$ for $\chi = 0$ while for $\chi = 0.95$ we have $\hat{r} \sim 4.7\ \hat{r}^{+}_{\rm ISCO}$ in the co-rotating case and $\hat{r} \sim 1.02\ \hat{r}^{-}_{\rm ISCO}$ in the counter-rotating case. The four panels show that small variations in the initial inclination I_0 correspond to huge variations in the merger time, both for the GR and the Newtonian case. The amplitude of the ZLK oscillations shows that the maximum eccentricity grows as $I_0 \to 90°$. In particular, note that when the the ZLK mechanism is most efficient, i.e. when $I_0 \sim 90°$, strong-gravity effects contribute to accelerate the BBH merger compared to the Newtonian case (bottom right panel). Instead, for smaller values of I_0, the ZLK mechanism is less efficient and the merger time is thus slowed down by the redshift factor (top panels and bottom left panel).

via GW emission. Even though a realistic description of the final stages of the inspiral phase would require much more advanced analytic or numerical frameworks, here we limit to convene that the BBH merger takes place when both a and e vanish.

Binary merger time in the strong field limit

We are now ready to study the evolution equations (1.155) for configurations in which one can see the strong field effects in full, regarding the influence

of the SMBH on the binary system. Indeed, we shall consider configurations for which the radius $\hat{r}$ of the outer orbit is comparable with the ISCO radius $\hat{r}^{\sigma}_{\rm ISCO}$ of the SMBH.

Since we are in a strong-gravity regime, it means that we will also be able to account for the dependence on the spin of the SMBH and in the following we will describe both the case where the BBH system moves on a co-rotating ($\sigma = +1$) circular equatorial orbit or a counter-rotating ($\sigma = -1$) circular equatorial orbit.

For the configurations of this subsection, we choose the mass of the SMBH to be $m_3 = 2 \times 10^9\ M_\odot$ which happens to be roughly the mass of M87*. This choice allows us to explore the situation where a stellar BBH system with masses $m_1 = m_2 = 10\ M_\odot$ and semi-major axis $a = 0.1$ AU is near or at the ISCO of the SMBH, while at the same time being sufficiently far away from the tidal breakup condition (1.2), see Fig. 1.13.

We consider three cases for the spin of the SMBH: the non-spinning case $\chi = 0$, and the highly spinning cases $\chi = 0.95$ with co-rotation ($\sigma = 1$) and counter-rotation ($\sigma = -1$).[16]

Finally, we choose the outer orbit radius to be $\hat{r} = 180$ AU, respectively corresponding to $\hat{r} \approx 4.68\ \hat{r}^{+}_{\rm ISCO}$ for co-rotating and $\hat{r} \approx 1.02\ \hat{r}^{-}_{\rm ISCO}$ for counter-rotating orbits. Notice that this value is also consistent in the case of a non-spinning SMBH of the same mass, since it would correspond to $\hat{r} \approx 1.51\ \hat{r}_{\rm ISCO}$.

We emphasize that the chosen values of the parameters ensure that the BBH system is not subjected to a tidal breakup and can experience strong gravity effects due to the tidal interaction with the external SMBH.

We have solved the evolution equations (1.155) for these choices of configurations. The result is depicted in Fig. 1.16 where we show the evolution of $1-e^2$ as a function of the asymptotic time $\hat{t}$ for four different initial inclination angles $I_0 = 88.5°, 89°, 89.3°, 89.5°$. Moreover, we choose the remaining initial conditions for the inner binary to be $e_0 = 0.1$, $a_0 = 0.1$ AU and $\gamma_0 = 0°$. As one can see, in Fig. 1.16 we compare the BBH eccentricity evolution for the case where the inner binary is moving on a co-rotating and a counter-rotating circular equatorial Kerr geodesic (respectively purple and orange curves), with the case in which the external body is a non-spinning SMBH (black curve) described in the Newtonian point particle approximation (grey curve). This is to highlight the effect of the SMBH spin.

We point out that when the BBH is at the ISCO of the SMBH, or close to it, the GR effects become quite significant and the Newtonian point particle approximation is no longer valid to describe the dynamics of the system. Here we use the point particle description for the SMBH to illustrate the comparison between our novel results valid in the full GR regime and the results obtained in the standard point particle approximation. We can conclude that describing

[16] We choose $\chi = 0.95$ since it is supposed to be close to the value of the spin of M87* as inferred by the Event Horizon Telescope Collaboration [186, 187].

the SMBH with the Kerr metric, instead of as a point particle, leads to effects that significantly impact the dynamics of the BBH system.

The four different panels with four different initial inclination angles in Fig 1.16 aim to illustrate the strong dependence of the merger dynamics on the initial inclination angle I_0: it is possible to observe that the more the BBH system is inclined, the more the ZLK mechanism is effective in reaching high values for the eccentricity and, thus, in reducing the merger time. This feature of the ZLK mechanism remains true regardless of whether the SMBH is described in a Newtonian or in a general-relativistic manner. Indeed, in all cases, one can observe that the maximum eccentricity grows as I_0 increases approaching 90° and, consequently, a smaller number of ZLK oscillations is needed in order to boost the merger.
In particular, by making use of the terminology adopted in Ref. [19], the two top panels and the bottom left panel in Fig. 1.16 describe a *slow-merger dynamics*, i.e. when the BBH system undergoes more than one ZLK cycle before merging, whereas the bottom right panel depicts a *fast-merger dynamics*, in which the BBH system coalesces in just one cycle of the ZLK mechanism, and the merger time $\hat{t}_\star$ is directly given by $\hat{t}_\star \approx u^t T_{\rm ZLK}$ [19].

Another feature associated with strong gravity effects that emerges from Fig. 1.16 is related to the impact of the redshift factor on the merger time. We recall that in the evolution equations of the system, Eqs. (1.155), the details of the description adopted for the SMBH enter through the ZLK frequency $\Omega_{\rm ZLK}^{(\rm GR)}$ which now, from the point of view of an observer in the asymptotic region of the Kerr space-time, translates into the quantity $\Omega_{\rm ZLK}^{(\infty)}$ defined in Eq. (1.129), where the role of the redshift factor is evident.

When the SMBH is described using the Kerr metric (or the Schwarzschild metric for non-spinning black holes), it is the redshift factor which is responsible for slowing down the evolution of the system and causing an increase in the merger time compared to the case where one uses the standard Newtonian point particle description for the SMBH. The effect of the gravitational redshift is particularly evident in the two top panels of Fig. 1.16, where the BBH evolution is characterized by a large number of ZLK cycles. Here one sees that for example the orange curve, with a redshift factor $u^t \approx 1.24$, corresponds to a slower merger time compared to the black curve with redshift factor $u^t \approx 1.22$ and so on.

Finally, Fig. 1.16 highlights another consequence of being in a strong-gravity regime. In Sec. 1.2.6 we discussed how a general-relativistic description of the external SMBH can lead to a significant increase in the local ZLK frequency when compared to the Newtonian description. As opposed to the gravitational redshift, thus, the strong-gravity effects in the ZLK frequency contribute to catalyzing the BBH merger at earlier times than in the Newtonian case. In particular, from Fig. 1.7 it is immediate to see that for a fixed value of the radial coordinate $\hat{r}$ and of the spin parameter χ, the deviation

of $\Omega^{(\mathrm{GR})}_{\mathrm{ZLK}}$ from the Newtonian value $\Omega^{(\mathrm{N})}_{\mathrm{ZLK}}$ is greater for counter-rotating orbits. The interplay between the GR enhancement of the local ZLK frequency, which accelerates the merger, and the gravitational redshift, which instead tends to slow down the merger, is particularly evident in the bottom right panel of Fig. 1.16. For the co-rotating case (purple), the gravitational redshift $u^t \approx 1.2$ almost entirely compensates the GR frequency enhancement $\Omega^{(\mathrm{GR})}_{\mathrm{ZLK}}/\Omega^{(\mathrm{N})}_{\mathrm{ZLK}} \approx 1.21$, so that $\Omega^{(\infty)}_{\mathrm{ZLK}}/\Omega^{(\mathrm{N})}_{\mathrm{ZLK}} \approx 1$. This makes the purple curve almost indistinguishable from the Newtonian one (the gray curve). In the non-spinning (black) and counter-rotating (orange) case, instead, one respectively has $\Omega^{(\mathrm{GR})}_{\mathrm{ZLK}}/\Omega^{(\mathrm{N})}_{\mathrm{ZLK}} \approx 1.49$ and $\Omega^{(\mathrm{GR})}_{\mathrm{ZLK}}/\Omega^{(\mathrm{N})}_{\mathrm{ZLK}} \approx 1.95$, [17] corresponding to $\Omega^{(\infty)}_{\mathrm{ZLK}}/\Omega^{(\mathrm{N})}_{\mathrm{ZLK}} \approx 1.22$ and $\Omega^{(\infty)}_{\mathrm{ZLK}}/\Omega^{(\mathrm{N})}_{\mathrm{ZLK}} \approx 1.57$ respectively so that the strong-gravity effects in the ZLK frequency dominate over the gravitational redshift, thus accelerating the merger.

GW peak frequency at the ISCO

As already remarked, the strong-gravity effects should be maximal when the BBH is closest to the SMBH, which, for equatorial orbits, is when the outer orbit is at the ISCO. In this section we analyze this scenario in detail. As already mentioned at the beginning of Sec. 1.2 this scenario is astrophysically relevant since there are some mechanisms that can lead compact objects to migrate from the outer regions of a galaxy towards the SMBH at its center where they can get trapped on a region close to the ISCO that allow binaries to form and coalesce [52–54].

We begin with the case of a high initial inclination, $I_0 = 89.9°$, which maximizes the ZLK mechanism. We have depicted this in Fig. 1.17, showing the evolution of the BBH eccentricity in terms of the proper time τ (solid black line) and the asymptotic time $\hat{t}$ (red line) compared with the case in which the external SMBH is treated in a Newtonian point particle approximation (dashed curve). The masses are chosen as it follows: $m_1 = m_2 = 10M_\odot$ for the BBH and $m_3 = 2 \times 10^9\ M_\odot$ for the SMBH, ensuring that it is possible to approach the ISCO while avoiding tidal breakup. For simplicity we have chosen to focus on the non-spinning case $\chi = 0$, for which $\hat{r} \approx 119$ AU, and $u^t = \sqrt{2}$.

We see from Fig. 1.17 that the combination of a high initial inclination angle and the strong-gravity effects at the ISCO speeds up the merger, which occurs in just a single ZLK oscillation. Accordingly, Fig. 1.17 also shows that the maximum eccentricity is enhanced when including GR effects, reaching extremely high values $1 - e^2_{\mathrm{max}} < 10^{-4}$, and further contributing to reduce the merger time ($\hat{t} \approx 0.025$ yrs in terms of the asymptotic time) compared to

[17] This value in the counter-rotating case is consistent with the fact that the BBH orbits very close to the SMBH ISCO, $\hat{r} \approx 1.02\ \hat{r}^{-}_{\mathrm{ISCO}}$.

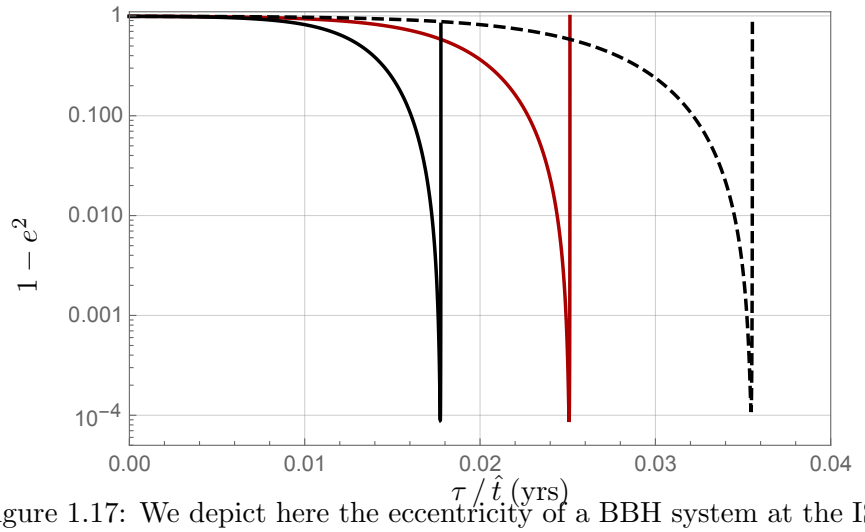

Figure 1.17: We depict here the eccentricity of a BBH system at the ISCO of an SMBH with $\chi = 0$. The solid black and red lines represent the system in terms of the local time τ and the asymptotic time $\hat{t}$, respectively. The masses are chosen as $m_1 = m_2 = 10\ M_\odot$ and $m_3 = 2 \times 10^9\ M_\odot$. In contrast, the dashed black line is the result obtained by using the Newtonian point particle approximation for the SMBH with the same outer orbit radius 119 AU. The initial conditions for the BBH orbital parameters are $e_0 = 0.1$, $a_0 = 0.1$ AU, $\gamma_0 = 0°$ and $I_0 = 89.9°$.

the examples presented before in Fig. 1.14. Finally, it is important to observe that, in terms of the proper time τ (black curve in Fig. 1.14), the merger time is halved, as compared to the merger time when using the Newtonian point particle approximation for the SMBH (dashed curve in Fig. 1.14), in perfect agreement with the analytical prediction we derived in Sec. 1.2.6 that at the ISCO of an SMBH one has $\Omega^{(\mathrm{GR})}_{\mathrm{ZLK}}/\Omega^{(\mathrm{N})}_{\mathrm{ZLK}} = 2$.

Other than the merger time, it is of obvious importance to understand the frequency spectrum of the GWs emitted from the BBH, to see further observational signatures of placing the BBH at the ISCO of the SMBH. A measure of this is the peak frequency f_{GW} of Eq. (1.162) that marks the dominant frequency in the GW spectrum.

As pointed out in previous works [19, 185], an exhaustive characterization of ZLK-boosted triple systems via GW signal observations would require combining future space-based interferometers such as LISA, to probe the earlier phase of the merger when the two black holes are widely separated and the ZLK mechanism dominates, together with current ground-based facilities (such as LIGO-Virgo-KAGRA), which can detect the merger of an already-circularized BBH system at late stages.

As is evidenced by Figs. 1.16 and 1.17, highly inclined ($I_0 > 89.4°$) binaries in the strong-gravity regime are characterized by fast-merger dynamics. The

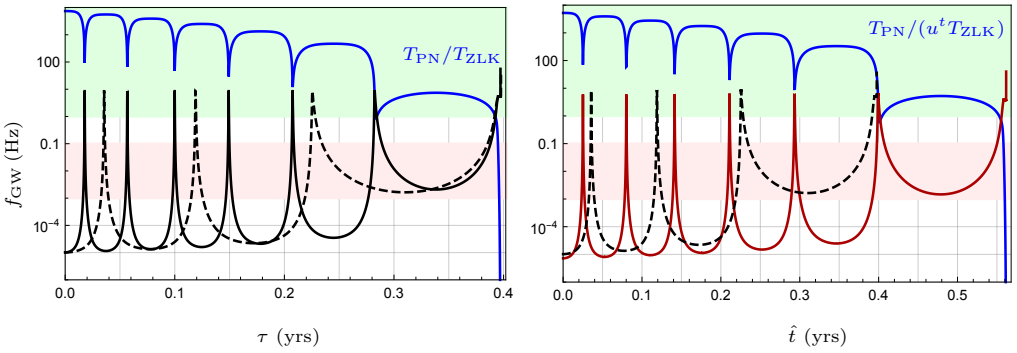

Figure 1.18: GW peak frequency $f_{\rm GW}$ emitted by the BBH system as a function of the proper time τ (left panel) and asymptotic time $\hat{t}$ (right panel). The BBH is placed on the ISCO of a non-spinning SMBH with mass $m_3 = 2 \times 10^9\ M_\odot$, corresponding to $\hat{r} \approx 120$ AU. The two black holes in the binary system have masses of $m_1 = m_2 = 10\ M_\odot$ with an initial separation of $a_0 = 0.1$ AU, an initial inclination angle $I_0 = 89.4°$, initial eccentricity $e_0 = 0.1$ and $\gamma_0 = 0°$.
Left Panel: we compare the peak frequency when treating the SMBH by a full GR description using the Schwarzschild metric (solid black) to what one obtains from a Newtonian point particle description (dashed black). One notices that there is twice the number of peaks in the GR description compared to the Newtonian approximation, consistent with the fact that $\Omega^{\rm (GR)}_{\rm ZLK} = 2\ \Omega^{\rm (N)}_{\rm ZLK}$ at the ISCO. The gravitational redshift is not considered in this plot.
Right Panel: the same comparison as in the left panel, but in terms of the asymptotic time $\hat{t}$ (red curve). This includes the gravitational redshift u^t. Notice that the inclusion of the redshift factor makes the merger time quite different in the two cases (4.8 months in the Newtonian case compared to 6.9 months in the GR case) and reduces the maximum value reached by the frequency.
The blue curve reproduces the ratio between the PN precession and the ZLK timescales. Finally, the pink and green bands in the background respectively show the range of frequency detectable for the upcoming interferometers ET ($1\ {\rm Hz} < f_{\rm GW} < 10\ {\rm kHz}$) and LISA ($0.001\ {\rm Hz} < f_{\rm GW} < 0.1\ {\rm Hz}$) .

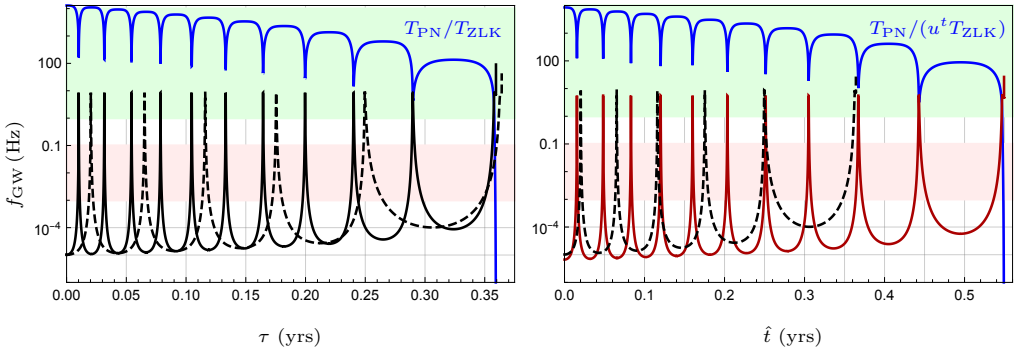

Figure 1.19: Same peak frequency comparison as in Fig. 1.18 between the Newtonian and the GR case but now for a spinning SMBH with $m_3 = 2 \times 10^9\ M_\odot$ and $\chi = 0.3$ (with $\sigma = 1$). In this case, the co-rotating ISCO is located at $\hat{r} \approx 99$ AU. As in Fig. 1.18 the left and the right panels differ for the inclusion of the redshift factor, which in this case amounts to $u^t \approx 1.41$.

GW signal in these cases would result in a single pulse observed by both ET and LISA, promptly followed by a chirp signal detected by LIGO-Virgo-KAGRA.

Lowering the initial inclination angle I_0 should instead provide more ZLK oscillations, as seen in Fig. 1.16, since the ZLK mechanism is less hampered by the periastron precession. This could in turn provide a longer signal to be observed by ET and LISA. Indeed, one would expect the detection of a BBH merger by LIGO-Virgo-KAGRA to be preceded by a series of repeated pulses detected by ET and LISA at earlier times, that mark the presence of the ZLK cycles.

To show this, we plot in Figs. 1.18 and 1.19 the GW peak frequency $f_{\rm GW}$ of the GW emission from the BBH as a function of time given a slightly lower initial inclination angle $I_0 = 89.4°$. We consider two cases, one for zero spin $\chi = 0$ of the SMBH (Fig. 1.18) and one with non-zero co-rotating spin $\chi = 0.3$ (Fig. 1.19). In both cases the BBH moves along the ISCO of the SMBH. In the figures we compare the results of our novel GR description for the SMBH to what one would have obtained by treating the SMBH as a Newtonian point particle. In detail, the black curves in Figs. 1.18 and 1.19 mark the peak frequency $f_{\rm GW}$ measured with proper time τ on the left while the red curve marks the asymptotically measured peak frequency $f_{\rm GW}$ with asymptotic time $\hat{t}$ of the Kerr space-time on the right. These curves are then compared to the peak frequency $f_{\rm GW}$ that one obtains from SMBH as Newtonian point particle, marked by the black dashed curves.

While $\chi = 0$ in Fig. 1.18, we have turned on the spin of the SMBH in Fig. 1.19 with $\chi = 0.3$ corresponding to a co-rotating spin $\sigma = 1$. Turning on the spin parameter for the SMBH allows binary systems to access regions of space-time which would be prohibited in the non-spinning case. More specif-

ically, the co-rotating ISCO for Kerr lies closer to the black hole than in the non-spinning case. Comparing the spinning case to the non-spinning case, we observe that the binary system undergoes a larger number of ZLK cycles before the merger occurs.

For the left panels of Figs. 1.18 and 1.19 we have depicted the evolution of the peak frequency in terms of the proper time, which is the local time of the BBH. These panels highlight the fact that in the early phases of the merger when the period of ZLK oscillations is much shorter than the one of the periastron precession ($T_{\rm PN} \gg T_{\rm ZLK}$, as marked with the blue curve), the future interferometers ET and LISA would detect twice the number of pulses entering their frequency band (depicted with pink and green stripes respectively) compared to a Newtonian point particle description of the SMBH. This is consistent with our analytic prediction that at the ISCO of any SMBH, we have $\Omega^{\rm (GR)}_{\rm ZLK} = 2\Omega^{\rm (N)}_{\rm ZLK}$. While the LISA sensitivity band (10^{-3} Hz $< f_{\rm GW} < 10^{-1}$ Hz) detects GWs emitted only in the earlier phases of the inspiral, it is interesting to notice that the ET frequency band (1 Hz $< f_{\rm GW} <$ 10 kHz) allows to observe GWs up to the final stages of the BBH merger.

In the right panels of Figs. 1.18 and 1.19 we depict instead the evolution of the peak frequency in terms of the asymptotic time $\hat{t}$, *i.e.* the time appropriate for the GW detector. The redshift factor included in the asymptotic time is not only responsible for reducing the maximum peak frequency reached by the GW emitted by the binary, but it also shifts the positions of the pulses and significantly affects the merger time.

Finally, Figs. 1.18 and 1.19 show how in the last part of the merger ($T_{\rm PN} \ll T_{\rm ZLK}$) the GW peak frequency enters the detectable band of LIGO/Virgo/Kagra ($f_{\rm GW} > 10$ Hz).

Chapter 2

Extreme Mass Ratio Inspirals

With the term Extreme Mass Ratio Inspirals (EMRIs) we refer to binary systems where the two companions have masses that are not comparable, i.e. one of the two objects is way heavier than the other. If we denote the mass of the primary object M and the mass of the secondary one m, the mass ratio for an EMRI $p = m/M$ is always much smaller than 1, namely $p \ll 1$, where typical values for the mass ratio are in the range $10^{-8} < p < 10^{-4}$ [50].

There are different formation channels for EMRI systems, but a lot of them have a high uncertainty on the event rates [188]. Here we report the most well-studied yet, which is usually known as the *dry channel* [189], where EMRI systems form in galactic nuclei with a low gas density. In this scenario it is possible for compact objects to form a dense environment close to the galactic nuclei, where stellar mass objects can get gravitationally bounded to the central SMBH, forming an EMRI which usually will have a high eccentricity [188,190]. Another channel proposed in the literature involves the tidal disruption of a binary system in the proximity of a SMBH, where one of the two objects in the binary is ejected during the tidal disrupting event while the other gets gravitationally bounded to the SMBH, forming an EMRI system with usually a low eccentricity [191, 192].

Since in the literature people are also referring to binary systems with a different mass ratio as EMRIs, and given that in the Universe there exist binaries with a mass ratio close to the one of an EMRI, we recall briefly the nomenclature usually implemented in astrophysics for this kind of systems:

- Intermediate Mass Ratio Inspirals (IMRIs) [193, 194] - the mass ratio for these binaries usually lies in the range $10^{-4} < p < 10^{-2}$ and they can be divided in two classes: light and heavy IMRIs. We refer to the former one when an Intermediate Mass Black Hole (IMBH) is orbited by a stellar-mass object, while the latter describes a binary where the primary object is a supermassive black hole (SMBH) and the secondary one an IMBH.

- Extreme Mass Ratio Inspirals (EMRIs) [64,195–197] - these binaries are the ones we are interested in. As already mention above, their mass ratio is usually in the range $10^{-8} < p < 10^{-4}$ and the two companions are a supermassive black hole and a stellar mass compact object or, in some cases, a SMBH and a binary stellar mass compact object. In the latter case the system is usually called b-EMRI [65–68].

- Extremely Large Mass Ratio Inspirals (XMRIs) [198, 199] - The mass ratio for these systems is $p \leq 10^{-8}$ and they usually have a SMBH as the primary companion and a sub-stellar object, such as a brown dwarf, as a secondary one.

In this thesis we will focus our attention on EMRIs and b-EMRIs but it is worth mentioning that IMRIs are widely studied since they represent the link between EMRIs and comparable-masses binaries and the study of their properties can give us a better insight on the how SMBHs can form from IMBHs. On the other hand XMRIs can give us valuable information on what is happening in the inner region of our Galaxy, close to the SMBH at its center. For a more detailed analysis on IMRIs we refer the reader to refs. [64,193–197], while for XMRIs to refs. [198, 199].

All the systems mentioned above, given the large mass of the primary companion in the binary system, are expected to emit gravitational waves in the range of 10^{-4} Hz $\div$ 1 Hz, depending on how massive the SMBH is. Thus, the current ground-based interferometers LIGO, Virgo and KAGRA, are not able to investigate these kind of systems [200–203].[1] On the other hand the future space-based interferometers such as LISA, Taiji or TianQin will be able to investigate the Universe through gravitational waves in the mHz band, making EMRIs the perfect candidates and primary targets for them [58–63]. Thus to investigate the dynamics of EMRIs, their properties and how they are affected by the presence of a tidal environment is of paramount importance, especially for the future of gravitational waves [188].

Given the nature of EMRIs, i.e. the extreme difference between the masses of the two companions forming the binary system, the stellar compact object can spend an extended period of time ($\sim$ years) completing $10^2 \div 10^5$ orbital cycles in the region near the horizon of the SMBH before merging [50, 64], where the dynamics of the system is strongly affected by general relativity effects, making EMRIs probes for strong-field gravity. Moreover the gravitational wave signals emitted by these systems will be extremely sensitive to the parameters characterizing the SMBH [189], making EMRIs the perfect candidates for a more accurate measure of the mass or the spin of a SMBH. Finally it is worth mentioning that EMRIs, thanks to the future space-based interfer-

[1] It might be possible for ground-based interferometers to detect gravitational waves emitted by very light IMRIs, see references in the main text for more details.

ometers, can also be used as dark sirens in the context of cosmology [204,205] and they can be used to investigate theories of fundamental physics [206,207].

2.1 EMRIs in tidal environment

In this section we will focus our attention on how the dynamics of an EMRI system is affected by the presence of an external tidal field, which in our case will arise from the presence of a spinning black hole, i.e. a Kerr black hole, in the proximity of the EMRI system. More specifically we will consider a hierarchical three body system: a thigh inner binary with a non-spinning black hole of mass M (described by the Schwarzschild metric) and a test particle of mass m under the gravitational interaction of a supermassive black hole with mass M_*, see Fig. 2.1 for a schematic representation of the triple system. We also assume the outer orbit around the Kerr black hole to be much wider compared to the orbit of the test particle around the Schwarzschild black hole. Moreover there is also a hierarchy in the masses, namely we consider $m \ll M \ll M_*$, where the condition $m \ll M$ ensures that we can treat the inner binary system as an EMRI, while the second one, i.e. $M \ll M_*$, allows us to analyse the presence of the outer SMBH as a perturbation to the dynamics of the EMRI. In other words the latter condition is necessary to satisfy the small-tide approximation introduced in (1.55) using the small-hole

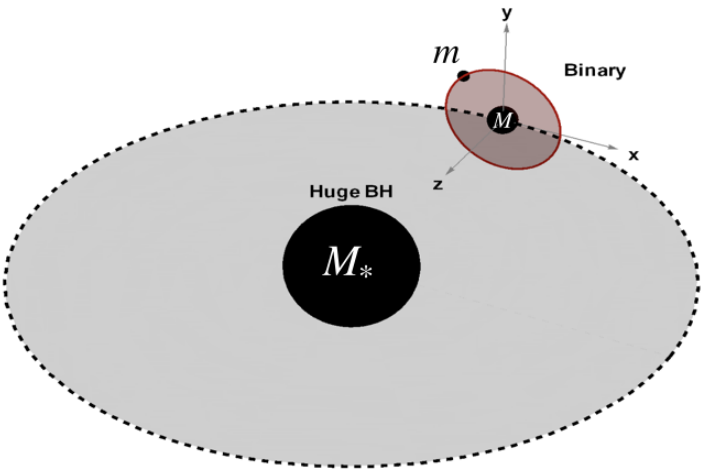

Figure 2.1: Schematic representation of the hierarchical triple system analysed in our problem. M_* represents the supermassive spinning black hole, described by the Kerr metric. The other two masses M and m form together a EMRI system, where M depict a non spinning black hole described by the Schwarzschild metric, while m represents a test particle.

approximation and to analyse how the dynamics of the EMRI is affected by strong gravity effects. Given the hierarchical configuration of our problem we can also treat the SMBH - EMRI binary as an EMRI itself, where we will refer to the Schwarzschild - test particle binary as the *inner* EMRI while to the SMBH - inner EMRI as the *outer* one. Thus the small-tide condition (1.55) (that here we satisfy thanks to the hierarchical configuration) is fundamental to capture the dynamics of the inner binary system since, as we mentioned previously in this chapter, the secondary companion of an EMRI system will spend a lot of orbital cycles near the horizon of the more massive object. This also apply to our problem where the inner EMRI will be orbiting very close to the SMBH, where it is no longer possible to neglect strong gravity effects.

2.1.1 Tidal moments induced by a Kerr black hole

In this section we will follow Refs. [69, 70] to construct the quadrupole tidal moments for a geodesic motion around a Kerr black hole. Some of the topics that we will analyse in this section have already been covered, in a less detailed manner, in Sec. 1.2. Since here we are using a different notation for our triple system, we will repeat some arguments as they will be necessary for our analysis. Moreover in what follow we will work in units with $G = c = 1$.

Carter's tetrad

Here we start by writing the metric for a spinning Kerr black hole of mass M_* and spin J_* in Boyer-Lindquist (BL) coordinates $\hat{x}^\mu = \left(\hat{t}, \hat{r}, \hat{\theta}, \hat{\phi}\right)$, which we already introduced in eq. (1.72) and we here recall for convenience:

$$\begin{aligned} d\hat{s}^2 = -\Big(1-\frac{2M_*\hat{r}}{\Sigma}\Big)d\hat{t}^2 - \frac{4M_*\hat{r}}{\Sigma}a\sin^2\hat{\theta}\; d\hat{t}\, d\hat{\phi} \\ + \frac{\mathcal{A}}{\Sigma}\sin^2\hat{\theta}\; d\hat{\phi}^2 + \frac{\Sigma}{\Delta}d\hat{r}^2 + \Sigma d\hat{\theta}^2 \;, \end{aligned} \tag{2.1}$$

where $a = J_*/M_*$ is the specific angular momentum and

$$\begin{aligned} \Sigma = \hat{r}^2 + a^2\cos^2\hat{\theta}, \quad \Delta = \hat{r}^2 - 2M_*\hat{r} + a^2, \\ \mathcal{A} = (\hat{r}^2 + a^2)^2 - a^2\Delta\sin^2\hat{\theta}\;. \end{aligned} \tag{2.2}$$

The equations of motion for time-like geodesics can be written in terms of three constants of motion, namely the energy per unit mass $\hat{E}$, the angular

momentum per unit mass $\hat{L}$ and the Carter constant K. They read [169]

$$\begin{aligned}
\dot{\hat{t}} &= \frac{\mathcal{A}\hat{E} - 2M_*\hat{r}a\hat{L}}{\Delta\Sigma} \,, \\
\dot{\hat{r}}^2 &= \left[\frac{\hat{E}(\hat{r}^2+a^2) - a\hat{L}}{\Sigma}\right]^2 - \frac{\Delta}{\Sigma^2}(\hat{r}^2+K) \,, \\
\dot{\hat{\theta}}^2 &= \frac{1}{\Sigma^2}\left[K - a^2\cos^2\hat{\theta} - \left(a\hat{E}\sin\hat{\theta} - \frac{\hat{L}}{\sin\hat{\theta}}\right)^2\right] \,, \\
\dot{\hat{\phi}} &= \frac{1}{\Delta}\left[\frac{2M_*\hat{r}a\hat{E}}{\Sigma} + \left(1 - \frac{2M_*\hat{r}}{\Sigma}\right)\frac{\hat{L}}{\sin^2\hat{\theta}}\right] \,,
\end{aligned} \tag{2.3}$$

where the dot denotes differentiation with respect to the proper time τ. The Kerr metric presented in (2.1) can also be written in terms of the so called *Carter's tetrad* [208] as $d\hat{s}^2 = \eta_{(a)(b)}\omega^{(a)}\omega^{(b)}$, where

$$\begin{aligned}
\omega^{(0)} &= \sqrt{\frac{\Delta}{\Sigma}}\left(d\hat{t} - a\sin^2\hat{\theta}d\hat{\phi}\right) \,, \\
\omega^{(1)} &= \sqrt{\frac{\Sigma}{\Delta}}d\hat{r} \,, \\
\omega^{(2)} &= \sqrt{\Sigma}d\hat{\theta} \,, \\
\omega^{(3)} &= \frac{\sin\hat{\theta}}{\sqrt{\Sigma}}\left(ad\hat{t} - (\hat{r}^2+a^2)d\hat{\phi}\right) \,.
\end{aligned} \tag{2.4}$$

In terms of this tetrad, the curvature 2-form can be written as

$$\Omega_{(a)(b)} = \frac{1}{2}C_{(a)(b)(c)(d)}\omega^{(c)} \wedge \omega^{(d)} \,, \tag{2.5}$$

where $C_{(a)(b)(c)(d)}$ are the components of the Weyl tensor (which for the Kerr metric corresponds to the Riemann tensor $R_{\mu\nu\rho\sigma}$) projected along the inverse of Carter's tetrad presented in (2.4), $\omega^{\mu}_{(a)}$, namely

$$C_{(a)(b)(c)(d)} = C_{\mu\nu\rho\sigma}\ \omega^{\mu}_{(a)}\omega^{\nu}_{(b)}\omega^{\rho}_{(c)}\omega^{\sigma}_{(d)}. \tag{2.6}$$

Explicitly the 2-form in (2.5) can be written as [69, 209]

$$\begin{aligned}
\Omega^{(0)(1)} &= 2I_1\ \omega^{(0)} \wedge \omega^{(1)} + 2I_2\ \omega^{(2)} \wedge \omega^{(3)} \,, \\
\Omega^{(0)(2)} &= -I_1\ \omega^{(0)} \wedge \omega^{(2)} + I_2\ \omega^{(1)} \wedge \omega^{(3)} \,, \\
\Omega^{(0)(3)} &= -I_1\ \omega^{(0)} \wedge \omega^{(3)} - I_2\ \omega^{(1)} \wedge \omega^{(2)} \,, \\
\Omega^{(1)(2)} &= -I_1\ \omega^{(1)} \wedge \omega^{(2)} + I_2\ \omega^{(0)} \wedge \omega^{(3)} \,, \\
\Omega^{(1)(3)} &= -I_1\ \omega^{(1)} \wedge \omega^{(3)} - I_2\ \omega^{(0)} \wedge \omega^{(2)} \,, \\
\Omega^{(2)(3)} &= 2I_1\ \omega^{(2)} \wedge \omega^{(3)} - 2I_2\ \omega^{(0)} \wedge \omega^{(1)} \,,
\end{aligned} \tag{2.7}$$

where

$$
\begin{aligned}
I_1 &= \frac{M_* \hat{r}}{\Sigma^3}\left(\hat{r}^2 - 3a^2\cos^2\hat{\theta}\right) \ , \\
I_2 &= \frac{aM_*\cos\hat{\theta}}{\Sigma^3}\left(3\hat{r}^2 - a^2\cos^2\hat{\theta}\right) \ .
\end{aligned}
\tag{2.8}
$$

Marck's tetrad

We now introduce an orthonormal tetrad $\lambda^{(a)} = \left(\lambda_0^{(a)}, \lambda_1^{(a)}, \lambda_2^{(a)}, \lambda_3^{(a)}\right)$ that is parallel-transported along an arbitrary time-like geodesic, following Ref. [69], which we call the *Marck's tetrad*. This tetrad is the same as the one in (1.82), which we here recall for convenience. The first component of the tetrad $\lambda_0^{(a)}$ is a time-like unit vector tangent to the geodesic while the other components $\lambda_i^{(a)}$ are space-like unit vectors. The components of the tetrad satisfy the orthonormal condition

$$
\eta_{(a)(b)}\ \lambda_\alpha^{(a)}\lambda_\beta^{(b)} = \eta_{\alpha\beta} \ , \tag{2.9}
$$

and the parallel-transported condition which guarantees that the tetrad frame is inertial

$$
\lambda_0^\mu \nabla_\mu \lambda_\alpha^\nu = 0 \ , \tag{2.10}
$$

where $\lambda_\alpha^\mu = \omega_{(a)}^\mu \lambda_\alpha^{(a)}$ and $\alpha, \beta = \{0, 1, 2, 3\}$ are the labels of the components of the tetrad.

The explicit expression for the components of the tetrad can be conveniently given in terms of the constant of motion of the Kerr geometry as [69] [2]

$$
\begin{aligned}
\lambda_0^{(a)} &= \left(\frac{\hat{E}(\hat{r}^2+a^2) - a\hat{L}}{\sqrt{\Delta\Sigma}}, \sqrt{\frac{\Sigma}{\Delta}}\dot{\hat{r}}, \sqrt{\Sigma}\dot{\hat{\theta}}, \frac{a\hat{E}\sin^2\hat{\theta} - \hat{L}}{\sin\hat{\theta}\sqrt{\Sigma}}\right) \ , \\
\lambda_1^{(a)} &= \tilde{\lambda}_1^{(a)}\cos\Psi - \tilde{\lambda}_2^{(a)}\sin\Psi \ , \\
\lambda_2^{(a)} &= \tilde{\lambda}_1^{(a)}\sin\Psi + \tilde{\lambda}_2^{(a)}\cos\Psi \ , \\
\lambda_3^{(a)} &= \frac{1}{\sqrt{K}}\left(a\cos\hat{\theta}\lambda_0^{(1)}, a\cos\hat{\theta}\lambda_0^{(0)}, -\hat{r}\lambda_0^{(3)}, \hat{r}\lambda_0^{(2)}\right) \ ,
\end{aligned}
\tag{2.11}
$$

where

$$
\begin{aligned}
\tilde{\lambda}_1^{(a)} &= \sqrt{\frac{T}{KS}}\left(\hat{r}\lambda_0^{(1)}, \hat{r}\lambda_0^{(0)}, \frac{S}{T}a\cos\hat{\theta}\lambda_0^{(3)}, -\frac{S}{T}a\cos\hat{\theta}\lambda_0^{(2)}\right) , \\
\tilde{\lambda}_2^{(a)} &= \sqrt{\frac{T}{S}}\left(\lambda_0^{(0)}, \lambda_0^{(1)}, \frac{S}{T}\lambda_0^{(2)}, \frac{S}{T}\lambda_0^{(3)}\right) \ ,
\end{aligned}
\tag{2.12}
$$

and

$$
S = \hat{r}^2 + K \ , \quad T = K - a^2\cos^2\hat{\theta} \ . \tag{2.13}
$$

[2] We rename $\lambda_2^{(a)}$ and $\tilde{\lambda}_3^{(a)}$ in Ref. [69] with our $\lambda_3^{(a)}$ and $\tilde{\lambda}_2^{(a)}$, respectively.

Notice the identity $\Sigma = S - T$. Here we introduced the Marck's angle Ψ which ensures that the tetrad $\lambda^{(a)} = \left(\lambda_0^{(a)}, \lambda_1^{(a)}, \lambda_2^{(a)}, \lambda_3^{(a)}\right)$ is parallel-transported along the geodesic motion. This angle is a function of the proper time of the Kerr geodesic and satisfies the following differential equation [69]:

$$\dot{\Psi} = \frac{\sqrt{K}}{\Sigma}\left(\frac{\hat{E}(\hat{r}^2 + a^2) - a\hat{L}}{S} + a\frac{\hat{L} - a\hat{E}\sin^2\hat{\theta}}{T}\right) . \tag{2.14}$$

An explicit expression for this angle can be found in ref. [69] and, in terms of the Mino time, in ref. [210].

Tidal tensors

In this subsection we will derive the explicit expressions for the tidal tensors which will be used to build the electric and magnetic tidal potential that contain all the information about the interaction between the inner EMRI and the supermassive Kerr black hole. We start by evaluating the Weyl tensor $C_{\mu\nu\rho\sigma}$ on the parallel-transported tetrad $\lambda^{(a)}$ defined in eq. (2.11). This is the best way to capture tidal effects induced on the test particle moving in the neighborhood of a Kerr geodesic.
In particular in order to compute the quadrupole tidal potential we are interested in the following components of the Weyl tensor projected on the tetrad $\lambda^{(a)}$ [69, 70]

$$\begin{aligned} C_{ij} &\equiv C_{(a)(b)(c)(d)}\lambda_0^{(a)}\lambda_i^{(b)}\lambda_0^{(c)}\lambda_j^{(d)} , \\ C_{ijk} &\equiv C_{(a)(b)(c)(d)}\lambda_0^{(a)}\lambda_i^{(b)}\lambda_j^{(c)}\lambda_k^{(d)} , \end{aligned} \tag{2.15}$$

where the first one is a rank-2 tensor while the second one a rank-3 tensor. We recall that $C_{(a)(b)(c)(d)} = C_{\mu\nu\rho\sigma}\ \omega^{\mu}{}_{(a)}\omega^{\nu}{}_{(b)}\omega^{\rho}{}_{(c)}\omega^{\sigma}{}_{(d)}$. It is worth mentioning that C_{ij} is a STF tensor while C_{ijk} is a trace-free and anti-symmetric in (j,k) tensor which satisfies the condition $C_{ijk} + C_{jki} + C_{kij} = 0$, yielding to the following two relations

$$C_{ijk} - C_{jik} = -C_{kij}, \quad C_{ijk} - Ckji = -C_{jki}. \tag{2.16}$$

We are now ready to give the explicit expressions for the components in (2.16) in terms of the parameters describing the Kerr geodesic. Note that these expressions hold for an arbitrary time-like geodesic in the Kerr background.

Starting with the C_{ij}, the non-zero components are

$$
\begin{aligned}
C_{11} &= \left[1 - \frac{3ST}{K\Sigma^2}(\hat{r}^2 - a^2\cos^2\hat{\theta})\cos^2\Psi\right] I_1 + \frac{6ST}{K\Sigma^2} a\hat{r}\cos\hat{\theta}\cos^2\Psi I_2 \ , \\
C_{12} &= -\frac{3ST}{K\Sigma^2}\left[\left(\hat{r}^2 - a^2\cos^2\hat{\theta}\right) I_1 - 2a\hat{r}\cos\hat{\theta} I_2\right]\sin\Psi\cos\Psi \ , \\
C_{13} &= -\frac{3\sqrt{ST}}{K\Sigma^2}\left[a\hat{r}\cos\hat{\theta}(S+T) I_1 + \left(\hat{r}^2 T - a^2 S\cos^2\hat{\theta}\right) I_2\right]\cos\Psi \ , \\
C_{22} &= \left[1 - \frac{3ST}{K\Sigma^2}(\hat{r}^2 - a^2\cos^2 \hat{theta})\sin^2\Psi\right] I_1 + \frac{6ST}{K\Sigma^2} a\hat{r}\cos\hat{\theta}\sin^2\Psi I_2 \ , \\
C_{23} &= -\frac{3\sqrt{ST}}{K\Sigma^2}\left[a\hat{r}\cos\hat{\theta}(S+T) I_1 + \left(\hat{r}^2 T - a^2 S\cos^2\hat{\theta}\right) I_2\right]\sin\Psi \ , \\
C_{33} &= \left[1 + \frac{3}{K\Sigma^2}(\hat{r}^2 T^2 - a^2 S^2\cos^2\hat{\theta})\right] I_1 - \frac{6ST}{K\Sigma^2} a\hat{r}\cos\hat{\theta} I_2 \ ,
\end{aligned}
\tag{2.17}
$$

where $I_{1,2}$ are defined in (2.8) and S, T in (2.13).
For the rank-3 tensor C_{ijk} the non-vanishing componets are given by

$$
\begin{aligned}
C_{112} &= \frac{3\sqrt{ST}}{K\Sigma^2}\left[\left(\hat{r}^2 T - a^2 S\cos^2\hat{\theta}\right) I_1 - a\hat{r}\cos\hat{\theta}(S+T) I_2\right]\cos\Psi \ , \\
C_{113} &= \frac{3ST}{K\Sigma^2}\left[2a\hat{r}\cos\hat{\theta} I_1 + \left(\hat{r}^2 - a^2\cos^2\hat{\theta}\right) I_2\right]\sin\Psi\cos\Psi \ , \\
C_{123} &= -\frac{6ST}{K\Sigma^2} a\hat{r}\cos\hat{\theta}\cos^2\Psi I_1 + \frac{1}{K\Sigma^2}\left[\left(\hat{r}^2 T + a^2 S\cos^2\hat{\theta}\right)(S-T)\right. \\
&\quad \left. -3ST\left(\hat{r}^2 - a^2\cos^2\hat{\theta}\right)\cos^2\Psi\right] I_2 \ , \\
C_{212} &= \frac{3\sqrt{ST}}{K\Sigma^2}\left[\left(\hat{r}^2 T - a^2 S\cos^2\hat{\theta}\right) I_1 - a\hat{r}\cos\hat{\theta}(S+T) I_2\right]\sin\Psi \ , \\
C_{213} &= \frac{6ST}{K\Sigma^2} a\hat{r}\cos\hat{\theta}\sin^2\Psi I_1 + \frac{1}{K\Sigma^2}\left[\hat{r}^2 T(2S+T) - a^2\cos^2\hat{\theta} S(S+2T)\right. \\
&\quad \left. -3ST\left(\hat{r}^2 - a^2\cos^2\hat{\theta}\right)\cos^2\Psi\right] I_2, \\
C_{312} &= \frac{6ST}{K\Sigma^2} a\hat{r}\cos\hat{\theta} I_1 + \frac{1}{K\Sigma^2}\left[\hat{r}^2 T(S+2T) - a^2\cos^2\hat{\theta} S(2S+T)\right] I_2 \ .
\end{aligned}
\tag{2.18}
$$

Where we observe that $C_{223} = -C_{113}$, $C_{312} = C_{213} - C_{123}$, $C_{313} = -C_{212}$, $C_{323} = C_{112}$. Restricting ourselves to geodesic motion in the equatorial plane of the Kerr spacetime, i.e. fixing $\hat{\theta} = \pi/2$, the tidal tensors simplify greatly and we recover the expressions presented in (1.85), in agreement with Ref. [69,

211, 212]

$$
\begin{aligned}
C_{11} &= \left[1 - 3\left(1 + \frac{K}{\hat{r}^2}\right)\cos^2\Psi\right]\frac{M_*}{\hat{r}^3}\ , \\
C_{22} &= \left[1 - 3\left(1 + \frac{K}{\hat{r}^2}\right)\sin^2\Psi\right]\frac{M_*}{\hat{r}^3}\ , \\
C_{12} &= -3\left(1 + \frac{K}{\hat{r}^2}\right)\frac{M_*}{\hat{r}^3}\cos\Psi\sin\Psi\ , \\
C_{33} &= \left(1 + 3\frac{K}{\hat{r}^2}\right)\frac{M_*}{\hat{r}^3}\ ,
\end{aligned}
\tag{2.19}
$$

while the rank-3 tensor components in the equatorial plane reduce to

$$
\begin{aligned}
C_{121} &= -\frac{3M_*\sqrt{K}}{\hat{r}^4}\sqrt{1 + \frac{K}{\hat{r}^2}}\cos\Psi\ , \\
C_{221} &= -\frac{3M_*\sqrt{K}}{\hat{r}^4}\sqrt{1 + \frac{K}{\hat{r}^2}}\sin\Psi\ ,
\end{aligned}
\tag{2.20}
$$

in agreement with refs. [211,213]. Finally we recall that the explicit expressions for the constant of motion in the Kerr equatorial plane are defined in (1.78)[3] and the equation for the Marck angle reduces to

$$
\dot{\Psi} = \frac{\sqrt{K}}{\hat{r}^2 + K}\left(\hat{E} - \frac{a}{a\hat{E} - \hat{L}}\right) = \sigma\sqrt{\frac{M_*}{\hat{r}^3}},
\tag{2.21}
$$

where $\sigma = \pm 1$ distinguish between co-rotation orbits $(+)$ and counter-rotating orbits $(-)$ in the Kerr spacetime.

Electric and magnetic quadrupole moments

Following ref. [70], the electric and magnetic quadrupole tidal potential can be written as

$$
\mathcal{E}_{ij} \equiv C_{ij}\ , \quad \mathcal{B}_{ij} \equiv -\frac{1}{2}\epsilon_{kl\langle i}C_{j\rangle}{}^{kl}\ ,
\tag{2.22}
$$

with ϵ_{ijk} the three-dimensional Levi-Civita symbol with $\epsilon_{123} = +1$. The Cartesian indices, denoted by Latin letters, are raised and lower with the Kronecker delta δ_{ij}. Both the electric and magnetic tidal potential are STF, meaning that they will have 5 independent components each, accounting for the 10 independent components of the Weyl tensor. To give an example here we report the magnetic quadrupole tidal moments in terms of the C_{ijk} [4]

$$
\begin{aligned}
&\mathcal{B}_{11} = -C_{123}\ , \quad \mathcal{B}_{12} = C_{113}\ , \quad \mathcal{B}_{13} = -C_{112}\ , \\
&\mathcal{B}_{22} = C_{213}\ , \quad \mathcal{B}_{23} = -C_{212}\ , \quad \mathcal{B}_{33} = C_{123} - C_{213}\ ,
\end{aligned}
$$

[3] Where in the notation used in this chapter we have $m_3 \to M_*$ and $s_3 \to a$.

[4] We only report the magnetic tidal potential since this is a new result, while the electric quadrupole tidal moments have already been computed in several works, see for example [69].

where we used that $C_{223} = -C_{113}$, $C_{312} = C_{213} - C_{123}$, $C_{313} = -C_{212}$ and $C_{323} = C_{112}$. For the purpose of our analysis it is more convenient to decompose the electric $\mathcal{E}_{ij}$ and magnetic $\mathcal{B}_{ij}$ tidal potential in terms of their irreducible representation of SO(3). To this end we need to introduce two ingredients: the first one is the radial unit vector

$$\Omega^i = \frac{x^i}{r}, \tag{2.23}$$

where $r = \sqrt{\delta_{ij}x^i x^j}$ is the Euclidean radius which gives us the distance from the geodesic, and the second one is the projector to the space orthogonal to Ω^i, given by

$$\gamma^{ij} = \delta^{ij} - \Omega^i\Omega^j. \tag{2.24}$$

Then the decomposition for the electric quadrupole tidal potential $\mathcal{E}_{ij}$ can be written as

$$\mathcal{E}_{ij} = \mathcal{E}^{\rm q}\left(\Omega_i\Omega_j - \frac{1}{2}\gamma_{ij}\right) + 2\mathcal{E}^{\rm q}_{(i}\Omega_{j)} + \frac{1}{2}\mathcal{E}^{\rm q}_{\langle ij\rangle}\ , \tag{2.25}$$

where the scalar $\mathcal{E}^{\rm q}$, the transverse vector $\mathcal{E}^{\rm q}_i$ (*i.e.* $\Omega^i\mathcal{E}^{\rm q}_i = 0$) and the transverse STF tensor $\mathcal{E}^{\rm q}_{\langle ij\rangle}$ are given by

$$\begin{aligned}
\mathcal{E}^{\rm q} &\equiv\ \Omega^i\mathcal{E}_{ij}\Omega^j = -\gamma^{ij}\mathcal{E}_{ij}\ ,\\
\mathcal{E}^{\rm q}_i &\equiv \gamma_i{}^j\mathcal{E}_{jk}\Omega^k\ ,\\
\mathcal{E}^{\rm q}_{\langle ij\rangle} &\equiv 2\gamma_i{}^k\gamma_j{}^l\mathcal{E}_{kl} - \mathcal{E}_{kl}\gamma^{kl}\gamma_{ij} = 2\gamma_i{}^k\gamma_j{}^l\mathcal{E}_{kl} + \mathcal{E}^q\gamma_{ij}\ .
\end{aligned} \tag{2.26}$$

For the quadrupole magnetic tidal potential $\mathcal{B}_{ij}$, we first write down the decomposition of the rank-3 tidal tensor C_{ijk}

$$C_{ijk} = \mathcal{B}^{\rm q}_k\left(\Omega_i\Omega_j - \gamma_{ij}\right) - \mathcal{B}^{\rm q}_j\left(\Omega_i\Omega_k - \gamma_{ik}\right) + \frac{1}{2}\left(\mathcal{B}^{\rm q}_{\langle ik\rangle}\Omega_j - \mathcal{B}^{\rm q}_{\langle ij\rangle}\Omega_k\right)\ , \tag{2.27}$$

with the inverse relations given by

$$\mathcal{B}^q_i = C_{jki}\Omega^j\Omega^k\ ,\qquad \mathcal{B}^q_{\langle ij\rangle} = 2\Omega^k C_{lk(i}\gamma^l{}_{j)}\ . \tag{2.28}$$

Thus the decomposition for the magnetic tidal potential reads

$$\mathcal{B}_{ij} = \epsilon^{lk}{}_{(i}\left[\mathcal{B}^{\rm q}_l\left(\Omega_{j)}\Omega_k - \gamma_{j)k}\right) + \frac{1}{4}\left(\mathcal{B}^{\rm q}_{\langle j)l\rangle}\Omega_k - \mathcal{B}^{\rm q}_{\langle j)k\rangle}\Omega_l\right)\right]\ , \tag{2.29}$$

with symmetrization with respect to the indices (i, j) and STF with respect to the indices $\langle jl\rangle$ and $\langle jk\rangle$. The transverse vector $\mathcal{B}^{\rm q}_i$ and the transverse STF tensor $\mathcal{B}^{\rm q}_{\langle ij\rangle}$ are

$$\begin{aligned}
\mathcal{B}^{\rm q}_i &\equiv \epsilon_{ijk}\Omega^j\mathcal{B}^k{}_l\Omega^l\ ,\\
\mathcal{B}^{\rm q}_{\langle ij\rangle} &\equiv 2\epsilon_{kl(i}\gamma^m{}_{j)}\Omega^k\mathcal{B}^l{}_m\ .
\end{aligned} \tag{2.30}$$

2.1.2 Hierarchical triple system

In this section we use the explicit results that we got for the quadrupole tidal moments to analyse how the dynamics of the test particle of mass m moving along a circular geodesic around the Schwarzschild black hole of mass M is affected by the presence of the supermassive spinning Kerr black hole of mass M_*. We recall that we are interested in studying the scenario where the inner EMRI is orbiting close to the SMBH black hole, i.e. when strong gravity effects can no longer be neglected. As we mentioned in Sec. 1.2, a way of analysing the dynamics of a binary system in the strong gravity regime is to employ the small-tide approximation introduced in eq. (1.55),which here we satisfy by requiring $M \ll M_*$.

Moreover we will assume that the radius or the orbit along which the test particle m is moving is of order M, namely $r = \mathcal{O}(M)$, with an associated timescale $\tau_{\rm binary} = \mathcal{O}(M)$. For the outer orbit instead we will assume its radius to be of order $\hat{r} = \mathcal{O}(M_*)$, with a timescale $\tau_{\rm Kerr} = \mathcal{O}(M_*)$. From the hierarchy in the masses of the triple system, i.e. $M_* \gg M$, immediately follows that the time scale associated to the outer orbit is much longer than the one associated to the inner orbit, i.e. $\tau_{\rm Kerr} \gg \tau_{\rm binary}$. As a consequence the dynamics of the test particle takes place on a time scale that is much faster then the one associated with the evolution of the orbital parameters of the outer orbit, which means that we can assume that the quadrupole moments and the Marck's angle Ψ do not vary in time[5].

Tidally deformed Schwarzschild spacetime

We can take into account the effects of the tidal field induced by the Kerr SMBH on the dynamics of the test particle by considering that the spacetime where m is moving is described by the Schwarzschild metric induced by M plus a small tidal perturbation due to M_*. We usually refer to this spacetime as the *tidally deformed Schwarzschild spacetime* [70] which can be written as

$$ds^2 = \bar{g}_{\mu\nu}dx^\mu dx^\nu + h_{\mu\nu}dx^\mu dx^\nu \ , \tag{2.31}$$

where the tidal perturbation $h_{\mu\nu}$ is computed up to the first order in the small-tide approximation. The background geometry (in spherical coordinates) is

$$\bar{g}_{\mu\nu}dx^\mu dx^\nu = -f dt^2 + \frac{dr^2}{f} + r^2\Omega_{AB}d\theta^A d\theta^B \ , \tag{2.32}$$

with $f = 1 - 2M/r$ and M being the black hole mass, $\theta^A = (\theta, \phi)$ and $\Omega_{AB}d\theta^A d\theta^B = d\theta^2 + \sin^2\theta d\phi^2$ being the metric of the unit sphere. By only

[5]This is explicit by looking at the expression of $\dot{\Psi}$ in (2.14), where we immediately see that if $\hat{r} = \mathcal{O}(M_*)$, then the rate of change of the angle Ψ is $\dot{\Psi} = \mathcal{O}(1/M_*)$.

retaining the quadrupole order terms in the tidal deformation $h_{\mu\nu}$, one gets

$$\begin{aligned} &h_{\mu\nu}dx^\mu dx^\nu = \\ &-r^2\mathcal{E}^{\rm q}\left(f dt+dr\right)^2-\frac{4}{3}r^3\left(\mathcal{E}^{\rm q}_A-\mathcal{B}^{\rm q}_A\right)\left(f dt+dr\right)d\theta^A \\ &-\frac{1}{3}r^4\left[\left(1-\frac{2M^2}{r^2}\right)\mathcal{E}^{\rm q}_{AB}-\left(1-\frac{6M^2}{r^2}\right)\mathcal{B}^{\rm q}_{AB}\right]d\theta^A d\theta^B. \end{aligned} \tag{2.33}$$

Where here we decomposed the quadrupole tidal potentials in their scalar ($\mathcal{E}^q$), vector $\left(\mathcal{E}^q_A, \mathcal{B}^q_A\right)$ and tensor $\left(\mathcal{E}^q_{AB}, \mathcal{B}^q_{AB}\right)$ components following the decomposition in Eqs. (2.25)-(2.29), and changing coordinates from Cartesian to spherical ones, according to the following relations

$$\begin{aligned} \mathcal{E}^{\rm q}_i dx^i &= \frac{\partial x^i}{\partial x^A}\mathcal{E}^{\rm q}_i dx^A = \mathcal{E}^{\rm q}_\theta(r d\theta)+\mathcal{E}^{\rm q}_\phi(r d\phi)\ , \\ \mathcal{E}^{\rm q}_{\langle ij\rangle}dx^i dx^j &= \frac{\partial x^i}{\partial x^A}\frac{\partial x^j}{\partial x^B}\mathcal{E}^{\rm q}_{\langle ij\rangle}dx^A dx^B = \\ &= \mathcal{E}^{\rm q}_{\theta\theta}(r d\theta)^2+2\mathcal{E}^{\rm q}_{\theta\phi}r^2 d\theta d\phi+\mathcal{E}^{\rm q}_{\phi\phi}(r d\phi)^2\ , \end{aligned} \tag{2.34}$$

and similarly for the magnetic tidal moments $\mathcal{B}^{\rm q}_i, \mathcal{B}^{\rm q}_{\langle ij\rangle}$. The tidally deformed metric for the Schwazrschild spacetime introduced in eq. (2.31) has been derived in ref. [70] and in Appendix C we provide a brief summary of their computation.

As we will see later, how the dynamics of the test particle is affected by the presence of a tidal field depends also on the relative inclination between the inner and the outer orbit[6]. Thus to properly analyse the effects of the Kerr SMBH on the dynamics of the EMRI system we need to introduce the usual three Euler angles which allow us to study all possible configurations for the inner binary. To this end we start by introducing the unit directional vector

$$\Omega^i = (\cos\phi\sin\theta, \sin\phi\sin\theta, \cos\theta)\ , \tag{2.35}$$

centered in the Schwarzschild black hole of mass M, and attached to the reference frame of the EMR system (M, m). Thanks to the spherical symmetry of the Schwarzschild spacetime, we can set without loss of generality $\theta = \pi/2$, restricting the motion of the test particle to the equatorial plane. Therefore any arbitrary orientation of the inner EMRI system is given by

$$\vec{\Omega}' = R_\chi R_\beta R_\alpha \cdot \vec{\Omega}\ , \tag{2.36}$$

[6]Note how this was also clear in the Chapter 1 of this thesis where we analysed the ZLK mechanism, showing how it is highly dependent on the mutual inclination between the inner and outer orbits.

where $R_\alpha, R_\beta, R_\chi$ are the Euler rotational matrices, defined as

$$R_\alpha = \begin{pmatrix} \cos\alpha & \sin\alpha & 0 \\ -\sin\alpha & \cos\alpha & 0 \\ 0 & 0 & 1 \end{pmatrix} \ , \ R_\beta = \begin{pmatrix} 1 & 0 & 0 \\ 0 & \cos\beta & \sin\beta \\ 0 & -\sin\beta & \cos\beta \end{pmatrix} \ , \\ R_\chi = \begin{pmatrix} \cos\chi & \sin\chi & 0 \\ -\sin\chi & \cos\chi & 0 \\ 0 & 0 & 1 \end{pmatrix} \ . \tag{2.37}$$

Moreover we will restrict our analysis to circular orbits for the test particle around the Schwarzschild black hole. In this scenario one of the Euler angles, α in our case, can be reabsorbed by a redefinition of the azimuthal angle $\phi \to \phi + \alpha$. Thus to fully specify any orientation of an orbit in the binary system with respect to the Kerr perturber we only need two angles, namely β and χ [7]. In Fig. 2.2 we show four possible configurations in the case where the SMBH with mass M_* is a Schwarzschild black hole and the binary system is moving on a circular geodesic.

Tidal moments in spherical coordinates

After introducing the three Euler angles it is obvious, by looking at the decomposition of the electric and magnetic quadrupole tidal potentials presented in eq. (2.26) and in eq. (2.30), that they will also depend on the relative configuration between the inner EMRI (M, m) and the Kerr SMBH. More specifically after replacing in the decomposition (2.26) the unit directional vector Ω^i with the new one Ω'^i defined in eq. (2.36), we can write explicitly the components of the electric quadrupole moments as

$$\begin{aligned} \mathcal{E}^{\rm q} &= -\frac{1}{8}\left(C_{33} + \mathcal{T}_2^+ + \mathcal{T}_4^+ - 4\mathcal{T}_3^+ \sin 2\phi\right) \\ &\quad - \frac{1}{8}\left[3(C_{33} + \mathcal{T}_2^+) - \mathcal{T}_4^+\right] \cos 2\phi \ , \\ \mathcal{E}^{\rm q}_\theta &= \frac{1}{4}\left[2\mathcal{T}_3^- \cos\phi - \mathcal{T}_4^- \sin\phi\right] \ , \\ \mathcal{E}^{\rm q}_\phi &= \frac{1}{8}\left[4\mathcal{T}_3^+ \cos 2\phi + \left(3(C_{33} + \mathcal{T}_2^+) - \mathcal{T}_4^+\right) \sin 2\phi\right] \ , \\ \mathcal{E}^{\rm q}_{\theta\theta} &= -\mathcal{E}^{\rm q}_{\phi\phi} = \mathcal{E}^{\rm q} + \frac{1}{2}\left(C_{33} + \mathcal{T}_2^+ + \mathcal{T}_4^+\right) \ , \\ \mathcal{E}^{\rm q}_{\theta\phi} &= -\frac{1}{2}\left(2\mathcal{T}_3^- \sin\phi + \mathcal{T}_4^- \cos\phi\right) \ , \end{aligned} \tag{2.38}$$

[7] Note that these Euler angles are the same introduced in (1.102), with the identifications $\alpha \to \theta$, $\beta \to I$ and $\chi \to \gamma$.

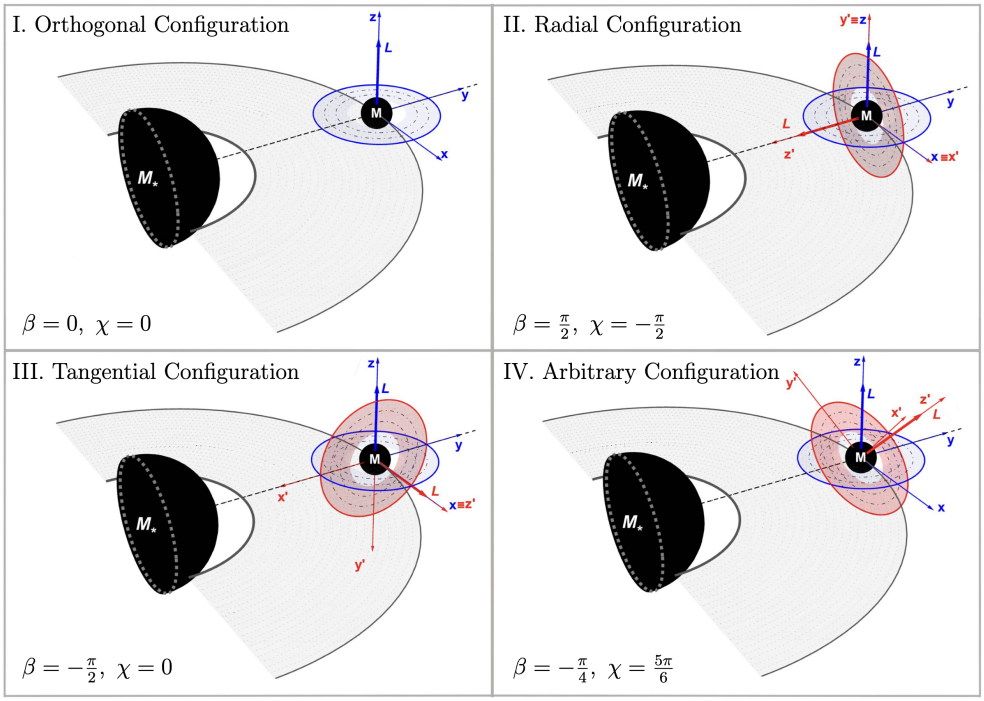

Figure 2.2: For illustrative purposes, we show four possible configurations for a hierarchical three-body system $M_* \gg M \gg m$ in the special case for which the perturber M_* is a Schwarzschild black hole and the EMR binary system (M, m) is parallel-transported around a circular geodesic around M_*, whose orbital plane is depicted in gray and terminates at the ISCO. These configurations are altered significantly in more general cases with a Kerr perturber or non-circular geodesics. The names of the configurations refer to the orientation of the orbital angular momentum L of the binary system with respect to the gray orbital plane. The grey curve represents the orbit around M_*. The blue orbit marks a conventional "initial" orthogonal configuration for the binary system reference frame, with the Cartesian axis oriented according to the parallel transported tetrad (panel I). The red orbits in panels II, III and IV are obtained by Euler rotations with angles written in the bottom-left of each panel.

where we defined the following rotations around χ of the components of C_{ij}

$$\begin{aligned}
\mathcal{T}_1^+ &= C_{23}\cos\chi + C_{13}\sin\chi \ , \\
\mathcal{T}_1^- &= C_{23}\sin\chi - C_{13}\cos\chi \ , \\
\mathcal{T}_2^+ &= 2C_{12}\sin 2\chi + (2C_{22}+C_{33})\cos 2\chi \ , \\
\mathcal{T}_2^- &= 2C_{12}\cos 2\chi - (2C_{22}+C_{33})\sin 2\chi
\end{aligned} \tag{2.39}$$

and the rotations around β of $\mathcal{T}_{1,2}^{\pm}$

$$\begin{aligned}
\mathcal{T}_3^+ &= 2\mathcal{T}_1^-\sin\beta + \mathcal{T}_2^-\cos\beta \ , \\
\mathcal{T}_3^- &= 2\mathcal{T}_1^-\cos\beta - \mathcal{T}_2^-\sin\beta \ , \\
\mathcal{T}_4^+ &= 4\mathcal{T}_1^+\sin 2\beta + (3C_{33}-\mathcal{T}_2^+)\cos 2\beta \ , \\
\mathcal{T}_4^- &= 4\mathcal{T}_1^+\cos 2\beta - (3C_{33}-\mathcal{T}_2^+)\sin 2\beta \, .
\end{aligned} \tag{2.40}$$

Analogously, after the substitution $\Omega^i \to \Omega'^i$, the decomposition for the magnetic quadrupole tidal potential defined in eq. (2.30) yield

$$\begin{aligned}
\mathcal{B}^{\rm q}_{\theta} &= \frac{1}{8}\left[4\mathcal{S}_3^+\cos 2\phi + \left(3(C_{312}-\mathcal{S}_2^+)-\mathcal{S}_4^+\right)\sin 2\phi\right] \ , \\
\mathcal{B}^{\rm q}_{\phi} &= -\frac{1}{4}\left(2\mathcal{S}_3^-\cos\phi - \mathcal{S}_4^-\sin\phi\right) \ , \\
\mathcal{B}^{\rm q}_{\theta\theta} &= -\mathcal{B}^{\rm q}_{\phi\phi} = -\frac{1}{2}\left(2\mathcal{S}_3^-\sin\phi + \mathcal{S}_4^-\cos\phi\right) \ , \\
\mathcal{B}^{\rm q}_{\theta\phi} &= -\frac{3}{8}\left(C_{312}-\mathcal{S}_2^+ + \mathcal{S}_4^+ + \frac{4}{3}\mathcal{S}_3^+\sin 2\phi\right) \\
&\quad + \frac{1}{8}\left[3(C_{312}-\mathcal{S}_2^+)-\mathcal{S}_4^+\right]\cos 2\phi \ ,
\end{aligned} \tag{2.41}$$

where we defined the rotations around χ of the components of C_{ijk}

$$\begin{aligned}
\mathcal{S}_1^+ &= C_{212}\cos\chi + C_{112}\sin\chi \ , \\
\mathcal{S}_1^- &= C_{212}\sin\chi - C_{112}\cos\chi \ , \\
\mathcal{S}_2^+ &= 2C_{113}\sin 2\chi + (C_{123}+C_{213})\cos 2\chi \ , \\
\mathcal{S}_2^- &= 2C_{113}\cos 2\chi - (C_{123}+C_{213})\sin 2\chi
\end{aligned} \tag{2.42}$$

and the rotations around β of $\mathcal{S}_{1,2}^{\pm}$

$$\begin{aligned}
\mathcal{S}_3^+ &= 2\mathcal{S}_1^-\sin\beta - \mathcal{S}_2^-\cos\beta \ , \\
\mathcal{S}_3^- &= 2\mathcal{S}_1^-\cos\beta + \mathcal{S}_2^-\sin\beta \ , \\
\mathcal{S}_4^+ &= 4\mathcal{S}_1^+\sin 2\beta + (3C_{312}+\mathcal{S}_2^+)\cos 2\beta \ , \\
\mathcal{S}_4^- &= 4\mathcal{S}_1^+\cos 2\beta - (3C_{312}+\mathcal{S}_2^+)\sin 2\beta \ .
\end{aligned} \tag{2.43}$$

It is important to stress out that the decomposition for the electric and magnetic quadrupole tidal potential presented in eq. (2.38) and eq. (2.41) is completely general and do not depend on the type of perturber generating the

tidal field, this makes these expressions very useful to model environmental effects also in numerical works. In the particular case we are analysing here, i.e. when the tidal perturber is a Kerr black hole, the tidal tensors C_{ij} and C_{ijk} are given, respectively, in eqs. (2.17) and (2.18).
Moreover it is worth mentioning that in the expressions in eqs. (2.38) and (2.41) the information regarding the tidal deformations induced on the inner binary by the tidal environment are fully captured by the tidal tensors C_{ij} and C_{ijk}, while the two angles β and χ specify the relative orientation between the inner EMRI system and the outer perturber.

2.1.3 Secular dynamics of the inner EMRI

In Sec. 2.1.2 we argued by studying the timescales in play in our problem that the dynamics of the test particle around the Schwarzschild black hole in the inner binary takes place on a timescale that is faster than the one associated with the outer orbit. Practically this means that in our analysis we will neglect the motion of the inner EMRI around the SMBH and we will focus our attention only on the secular dynamics in the binary system, i.e. the dynamics after a large number of orbits of the test particle. This means that we will average only over the inner motion and we will consider all the parameters associated to the outer motion as constants.

Secular Hamiltonian of test particle in binary system

In order to study the secular dynamics of the test particle orbiting around the Schwarzschild black hole we define the four velocity of the test particle as

$$u^{\mu} \simeq \bar{u}^{\mu} + u^{\mu}_{(1)} \,, \tag{2.44}$$

where $\bar{u}^{\mu}$ is the 4-velocity of the unperturbed bound orbit and $u^{\mu}_{(1)}$ is the leading correction due to the tidal perturbation $h_{\mu\nu}$. Here we are interested in circular, equatorial ($\theta = \pi/2$) orbits in the Schawrzschild background metric $\bar{g}_{\mu\nu}$, thus the unperturbed component of the four-velocity can be written as

$$\bar{u}^{\mu} = \left(\bar{E}/f, 0, 0, \bar{L}/r^2\right) , \tag{2.45}$$

where $\bar{E} = -\bar{u}^{\mu}\bar{g}_{\mu\nu}\left(\partial_t\right)^{\nu}$ and $\bar{L} = \bar{u}^{\mu}\bar{g}_{\mu\nu}\left(\partial_{\phi}\right)^{\nu}$ are the conserved energy and angular momentum of the test particle in the unperturbed background. In general the tidal fields induce deformations to all the four components of the four velocity. Specifically they affect the gauge - independent photon redshift measurements [214] $\left(\sim u^{t}_{(1)}\right)$, induce radial deviations $\left(\sim u^{r}_{(1)}\right)$, tilt the orbital plane $\left(\sim u^{\theta}_{(1)}\right)$ and induce a shift on the orbital frequency $\left(\sim u^{\phi}_{(1)}\right)$.
The Hamiltonian of a test particle moving in a tidally deformed Schwarzschild

background can be written as

$$H = \frac{1}{2}u^\mu u^\nu g_{\mu\nu} \simeq \frac{1}{2}\bar{u}^\mu \left(\bar{u}^\nu + 2u^\mu_{(1)}\right)\bar{g}_{\mu\nu} + \frac{1}{2}\bar{u}^\mu\bar{u}^\nu h_{\mu\nu}\,. \tag{2.46}$$

Since we are interested in the quadrupole contributions from the tidal fields, the only deformations of the four-velocity relevant at the quadrupole approximation for our analysis are the $u^t_{(1)}$ and $u^\phi_{(1)}$, while the radial and polar deviations affect the dynamics at higher order [72, 215].

Moreover we are interested in studying the dynamics of the test particle after integrating out the short-term oscillations induced by the tidal fields on the orbit of the particle itself. This procedure is known as the *secular average* and, following Ref. [72], can be understood by considering that the effective dynamics of a test particle, moving on a tidally-deformed geodesic γ' at the leading order in the perturbation $h_{\mu\nu}$, can be analysed by replacing the real physical trajectory γ' with an averaged circular one γ in the perturbed spacetime. The averaged orbit γ can be understood as a *secular orbit* in the full tidally perturbed spacetime.
Given a quantity $\mathcal{A}$, the secular average is defined as

$$\langle\mathcal{A}\rangle = \frac{1}{2\pi}\int_0^{2\pi} \mathcal{A}\big|_\gamma \, d\phi \,, \tag{2.47}$$

where ϕ is the azimuthal angle of the orbit in the Schwarzschild background and γ is the secular orbit on the full metric $g_{\mu\nu}$.
In order to obtain the secular Hamiltonian for the test particle, we compute first the relevant averaged components of the tidal metric $h_{\mu\nu}$. Recalling the explicit expressions for the quadrupole tidal moments in Eqs. (2.38) and (2.41), the relevant averaged components of the tidal part of the metric which will enter the Hamiltonian are

$$\begin{aligned}
\langle h_{tt}\rangle &= -r^2 f^2 \langle\mathcal{E}^{\rm q}\rangle \,, \\
\langle h_{t\phi}\rangle &= 0 \,, \\
\langle h_{\phi\phi}\rangle &= -r^4\left(1 - 2\frac{M^2}{r^2}\right)\langle\mathcal{E}^{\rm q}\rangle \,.
\end{aligned} \tag{2.48}$$

After plugging these expressions in Eq. (2.46) and after using that $\langle u^\mu u^\nu g_{\mu\nu}\rangle \simeq \langle u^\mu\rangle\langle u^\nu\rangle\langle g_{\mu\nu}\rangle$, the averaged Hamiltonian for the test particle can be written as

$$\langle H\rangle \simeq -\frac{1}{2}\left(\frac{\langle E\rangle^2}{f} - \frac{\langle L\rangle^2}{r^2}\right) - \eta\left[\langle E\rangle^2 + \left(1 - 2\frac{M^2}{r^2}\right)\frac{\langle L\rangle^2}{r^2}\right]\frac{r^2}{M^2}\,. \tag{2.49}$$

we recall that E and L represent, respectively, the energy and the angular momentum of the test particle in the full perturbed spacetime and the symbol

$\langle\cdot\rangle$ denotes secular averaged quantities. Moreover we introduced an effective pertubative parameter η which captures all the effects of the tidal deformations at the quadrupole order. This parameter depends only on the orientation of the binary system (on the Euler angles β and χ) and on the tidal deformation induced by the SMBH on the EMRI system (the tidal moments C_{ij}). The explicit expression for this parameter can be written as

$$\begin{aligned}\eta &= -\frac{M^2}{2}\langle\mathcal{E}^{\rm q}\rangle = \\ &= \frac{M^2}{16}\Big\{C_{33}\left(1+3\cos 2\beta\right)+4\left(C_{13}\sin\chi+C_{23}\cos\chi\right)\sin 2\beta \\ &+\left[2C_{12}\sin 2\chi+\left(2C_{22}+C_{33}\right)\cos 2\chi\right]\left(1-\cos 2\beta\right)\Big\}.\end{aligned} \tag{2.50}$$

Note that this expression is completely general and holds for any test particle moving along a circular geodesic on the equatorial plane of a Schwarzschild black hole immersed in a tidal environment when only retaining the quadrupole order in the multipole expansion and when the secular average is applied. In other words the expression for η holds for any source of the tidal fields.
In the specific case analysed here, i.e. when the source of the tidal fields is a Kerr SMBH, we can use the tidal tensors C_{ij} derived in Eq. (2.17) to write explicitly

$$\begin{aligned}\eta = \frac{I_1 M^2}{16K\Sigma^2}&\Big[3ST(\hat{r}^2-a^2\cos^2\hat{\theta})(1-4\sin^2\beta\sin^2\chi)+6\cos 2\beta\left(\hat{r}^2T^2-a^2S^2\cos^2\hat{\theta}\right) \\ &-3a\cos\hat{\theta}\left(aS^2\cos\hat{\theta}+4\hat{r}\sin 2\beta\sqrt{ST}(S+T)\sin\chi\right)+K\Sigma^2+3\hat{r}^2T^2\Big] \\ &+\frac{3I_2M^2\sqrt{ST}}{4K\Sigma^2}\left[\left(a^2S\cos^2\hat{\theta}-\hat{r}^2T\right)\sin 2\beta\sin\chi-2a\hat{r}\sqrt{ST}\cos\hat{\theta}\left(\cos^2\beta-\sin^2\beta\sin^2\chi\right)\right],\end{aligned} \tag{2.51}$$

where K is the Carter constant, while I_1, I_2, S and T are defined in Eqs. (2.8) and (2.13). Note that in the expression (2.51) we reabsorbed the Marck's angle Ψ (which we recall being a constant in our approximation) appearing in the C_{ij} by simply shifting the Euler angle χ as $\chi \to \chi + \Psi$.

In the weak field regime, i.e. when the EMRI binary system is far away from the SMBH ($M_* \ll \hat{r}$), this effective perturbative parameter η reduces to the one already computed in Ref. [72] as expected. To see this explicitly we take the $\hat{r} \to \infty$ limit in the expression (2.51). and after keeping only the leading terms we have

$$\begin{aligned}\eta = &\frac{M^2}{4K}\frac{M_\star}{\hat{r}^3}\Big[3T(\cos^2\beta-\sin^2\beta\sin^2\chi) \\ &-K\left(2-3\sin^2\beta\right)-3a\sqrt{T}\cos\hat{\theta}\sin\chi\sin 2\beta\Big].\end{aligned} \tag{2.52}$$

This expression takes an even simpler form in the equatorial plane of the Kerr black hole ($\hat{\theta} = \pi/2$)

$$\eta = \frac{M^2}{4}\frac{M_\star}{\hat{r}^3}\left(1 - 3\sin^2\beta\sin^2\chi\right) \ , \tag{2.53}$$

where η depends only on the two Euler angles β and χ and not on the spin parameter a. As a consequence, in the weak field limit one cannot distinguish the tidal effects of the SMBH Kerr black hole from the one of a neutral black hole. This comes with no surprise since as we move away from the SMBH, the spin effect becomes less and less significant. Finally after setting $\chi = \pi/2$ and after identifying β as the angle between the tidal symmetry axis, aligned with z, and the orbital plane we have

$$\eta = \frac{M^2 M_*}{4\hat{r}^3}\left(1 - 3\sin^2\beta\right) \tag{2.54}$$

which is the same result obtained in Ref. [72] in the case of an EMRI orbiting around a Schwarzschild SMBH in the weak field regime.

Circular equatorial geodesic in Kerr background

Up until this point both the construction of the quadrupole tidal moments and the analysis of the secular dynamics of the test particle around the Schwarzschild black hole were completely general, meaning that our results can be applyed to any source of tidal fields. Here in this subsection we focus our attention to the special case of an EMRI system moving along a circular geodesic in the equatorial plane of a Kerr black hole. In this scenario, the energy, angular momentum and Carter's constant characterising the outer orbit are given by Eq. (1.78), and they can be used in Eq. (2.51) to get the explicit expression for the perturbative parameter η in the case of a circular equatorial orbit in the Kerr background, namely

$$\eta = \frac{M_* M^2}{4\hat{r}^3}\left\{1 + 3\frac{K}{\hat{r}^2} - 3\left[\frac{K}{\hat{r}^2} + \left(1 + \frac{K}{\hat{r}^2}\right)\sin^2\chi\right]\sin^2\beta\right\} \ . \tag{2.55}$$

Note that this is a general result, valid beyond the weak-field regime ($M_\star \ll \hat{r}$). This expression can be written solely in terms of the Kerr parameters $(a, M_*, \hat{r})$ thanks to the following relation[8]

$$\frac{K}{\hat{r}^2} = -\frac{1}{2}\left(1 - \frac{\hat{r}^2 - \hat{r}M_* - 2\sigma a\sqrt{\hat{r}M_*} + 2a^2}{\hat{r}^2 - 3\hat{r}M_* + 2\sigma a\sqrt{\hat{r}M_*}}\right) \ . \tag{2.56}$$

[8]Note that this relation only holds in the case of a circular equatorial orbit in the Kerr spacetime.

By looking at the expression for the perturbative parameters η in Eq. (2.55) we can notice immediately that for specific configurations for the EMRI system, the effects of the tidal fields on the secular dynamics of the test particle vanish, namely $\eta = 0$. For a fixed χ angle, these configurations are the ones given by $\beta = \beta^*(\chi)$ with

$$\sin^2\beta^*(\chi) = \frac{1 + 3K/\hat{r}^2}{3\left[K/\hat{r}^2 + \left(1 + K/\hat{r}^2\right)\sin^2\chi\right]} \,. \tag{2.57}$$

It is worth mentioning that in the weak-field regime this relation reduces to

$$\sin^2\beta^*(\chi) = \frac{1}{3\sin^2\chi}, \tag{2.58}$$

generalizing the result obtained in Ref. [72], which is only valid for $\chi = \pi/2$.

Given that the closer we are to the SMBH the stronger General Relativity effects become, it is interesting to analyse the scenario where the EMRI binary system is orbiting along the ISCO of the supermassive Kerr black hole. Moreover, as already discussed above, we recall that this scenario is also astrophysically relevant given the existence of migration mechanisms that can lead to binary systems trapped in the region near the ISCO of a SMBH [52–54]. In the Kerr spacetime we can identify two different ISCOs: a co-rotating ISCO ($\sigma = +1$) and a counter-rotating one ($\sigma = -1$). The radial positions of these two orbits are given by Eq. (1.79), which we here recall for convenience

$$\hat{r}^{\sigma}_{\rm ISCO} = M_* \left[3 + Z_2 - \sigma\sqrt{(3 - Z_1)(3 + Z_1 + 2Z_2)}\right] \,, \tag{2.59}$$

where

$$\begin{aligned} Z_1 &= 1 + \left(1 - \frac{a^2}{M_*^2}\right)^{\frac{1}{3}} \left[\left(1 + \frac{a}{M_*}\right)^{\frac{1}{3}} + \left(1 - \frac{a}{M_*}\right)^{\frac{1}{3}}\right] \,, \\ Z_2 &= \sqrt{Z_1^2 + 3\frac{a^2}{M_*^2}} \,. \end{aligned} \tag{2.60}$$

On the ISCO the following relation holds [176]

$$\hat{E}^2_{\rm ISCO} = 1 - \frac{2}{3}\frac{M_*}{\hat{r}^{\sigma}_{\rm ISCO}} \,, \tag{2.61}$$

which can be used in the Carter constant $K = (a\hat{E} - \hat{L})^2$[9] yielding to

$$K = \frac{1}{3\left(\hat{r}^{\sigma}_{\rm ISCO}\right)^2}. \tag{2.62}$$

[9] We recall that this relation between the Carter constant, the energy, the angular momentum and the spin of the Kerr black hole only holds in the equatorial plane, as stated in Eq. (1.78).

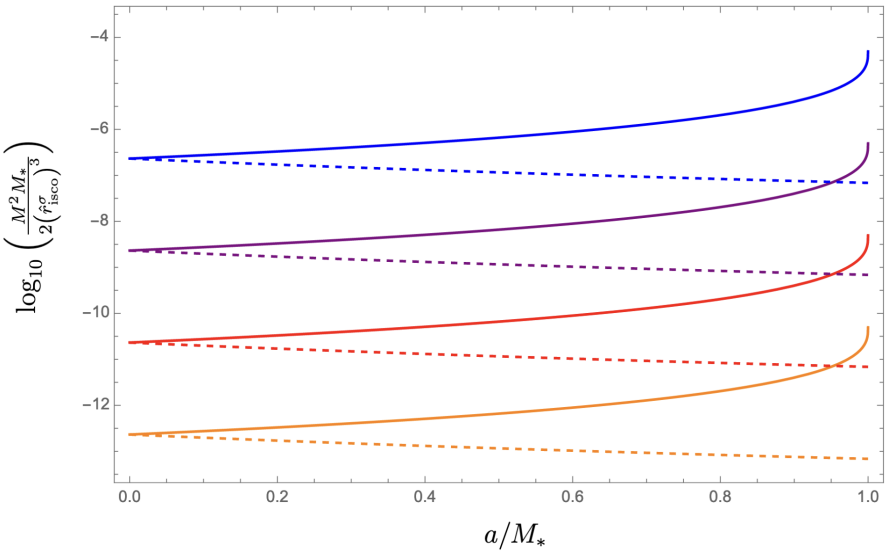

Figure 2.3: The picture represents how η, when evaluated at the ISCO $\hat{r} \equiv \hat{r}^{\sigma}_{\rm isco}$, depends on the black hole spin a. The logarithm of the prefactor in Eq. (2.63) is considered in order to have a clear distinction for the curves. Colors are used to represent different magnitudes for the ratio $\mu = M/M_*$. In particular $\mu = 10^{-2}$ in blue, $\mu = 10^{-3}$ in purple, $\mu = 10^{-4}$ in red and $\mu = 10^{-5}$ in orange. Solid lines are representative for the co-rotating ISCO $\sigma = 1$, whereas dashed lines for counter-rotating ISCO $\sigma = -1$.

With this, we can write the expression for the effective perturbative parameter η on the ISCO as

$$\eta = \frac{M^2 M_*}{2\left(\hat{r}^{\sigma}_{\rm ISCO}\right)^3}\left[1 - \frac{1}{2}(1 + 4\sin^2\chi)\sin^2\beta\right] \ . \tag{2.63}$$

It is worth mentioning that even when $\hat{r}^{\sigma}_{\rm ISCO} \sim \mathcal{O}(M_*)$, which correspond to the co-rotating case $\sigma = +1$ for an extremal Kerr black hole, the small-tide approximation defined in Eq. (1.55) still holds thanks to the hierarchy in the masses $M \ll M_*$. Thus we can legitimately analyse, using the quadrupole approximation, the scenario where the EMRI system is placed on the ISCO of the SMBH. It is possible to distinguish two terms in the η expression in Eq. (2.63): the prefactor $\frac{M^2 M_*}{2\left(\hat{r}^{\sigma}_{\rm ISCO}\right)^3}$, which contains the dependence on the spin parameter of the Kerr perturber and the term in square brackets, which depends on the two Euler angles β and χ, specifying the orientation of the binary system. In Fig. 2.3 we plot the η prefactor in Eq. (2.63) as a function of the spin parameter of the Kerr SMBH for different values of the ratio M/M_*. Note how the effective perturbative parameter η at the ISCO is also well defined in the case of a co-rotating orbit $\sigma = +1$ for an extremal Kerr black hole $a = M_*$, for which the radial position of the ISCO corresponds to

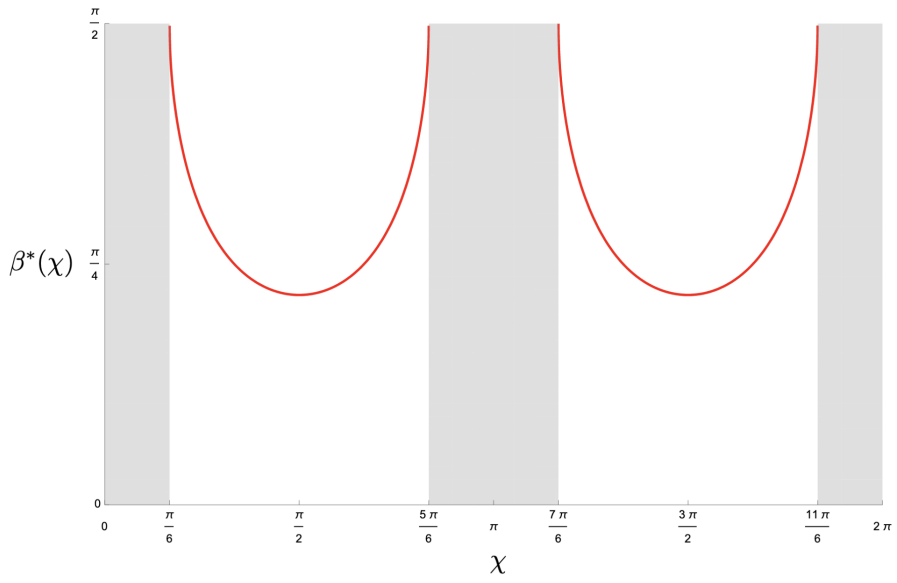

Figure 2.4: The red line identifies the configurations $\beta^*(\chi)$ for which the secular effect of tidal deformations vanishes under the assumption $\hat{r} \equiv \hat{r}^{\sigma}_{\rm ISCO}$. The gray areas represent exclusion zones, namely values of the angle χ in which the relation (2.64) cannot be satisfied. More specifically, these corresponds to values of χ that would lead $|\sin^2\beta^*| > 1$.

$\hat{r}^{+}_{\rm ISCO} = M_*$. In this case the prefactor reduces to $M^2/(2M_*^2)$, which represents also the maximum value of η at the ISCO for a given orientation of the binary system, as can be seen from Fig. 2.3.

On the ISCO the condition (2.57) for which the tidal effects induced by the SMBH on the EMRI system vanish, i.e. $\eta = 0$, simplifies thanks to the relation $K/\left(\hat{r}^{\sigma}_{\rm ISCO}\right)^2$, which allows us to write the condition for $\beta^*(\chi)$ as

$$\sin^2\beta^*(\chi) = \frac{2}{1+4\sin^2\chi}\,. \tag{2.64}$$

In Fig. 2.4 we plot the possible values for $\beta^*(\chi)$ when the EMRI system is moving along the Kerr ISCO.

2.1.4 Secular shifts for the ISCO and the Photon Sphere

In this section we apply the formalism introduced above to study the motion of the test particle along two specific orbits, namely the ISCO of the Schwarzschild black hole and its photon sphere, analysing how the tidal fields generated by the Kerr SMBH deform these two orbits.

The ISCO and the photon sphere represent the closest possible circular orbits for respectively massive and massless particles around black holes. This

makes them two very interesting orbits to analyse since on these orbits it is possible to probe the regime where strong gravity effects emerge. Moreover the ISCO is studied in the context of accretion disks [71, 216], usually associated with the inner edge of the disk [217], while the photon sphere is extremely important in the context of quasi-normal modes [218–220], allowing us to probe with high precision the strong gravity regime [221–223].

Finally we point out that an analysis of the ISCO and the photon sphere in a tidal environment is also carried out in Refs. [71, 72].

Gauge invariance of secular observables

Before we study the effects of the tidal fields on the motion of the test particle, it is useful to briefly discuss the issue of the gauge invariance of these deformations.

We recall that the energy of the test particle can be written in terms of the Killing vector field ∂_t

$$E = -u^\mu g_{\mu\nu} T^\nu , \tag{2.65}$$

where $T = \partial_t$ while $g_{\mu\nu}$ and u^μ are respectively the metric and the four-velocity in the full tidally deformed spacetime. Since the tidal perturbations $h_{\mu\nu}$ do not depend on time, T is still a Killing vector field in the full spacetime $g_{\mu\nu} = \bar{g}_{\mu\nu} + h_{\mu\nu}$, thus the energy is conserved and gauge invariant, namely $dE/d\tau = 0$ in any coordinate system when evaluated on a geodesic.
It is also possible to write the angular momentum in a covariant way

$$L = u^\mu g_{\mu\nu} J^\nu \tag{2.66}$$

where $J = \partial_\phi$. This is a Killing vector field for the Schwarzschild metric $\bar{g}_{\mu\nu}$, however since the tidal perturbation $h_{\mu\nu}$ in general depend on the azimuthal angle ϕ, J is no longer a Killing vector field in the full background $g_{\mu\nu}$ and, as a consequence, L is not conserved along geodesics in the tidally perturbed metric. To address this gauge invariant problem we start by writing the angular momentum L as

$$L \simeq \bar{L} + \eta L_1 \, , \tag{2.67}$$

where $\bar{L}$ is the conserved angular momentum in the unperturbed Schwarzschild background while L_1 is the non-conserved part (in general) arising from the tidal fields. We recall that the secular average is done by averaging over the azimuthal angle ϕ, meaning that the averaged metric $\langle g_{\mu\nu} \rangle$ is ϕ-independent and thus the averaged version of the angular momentum $\langle L \rangle$ is a conserved quantity along the secular geodesic. For a quasi-circular orbit we have

$$\langle L \rangle \simeq \int_0^{2\pi} \left(\bar{L} + \eta L_1 \right) |_\gamma d\phi = 2\pi \bar{L} + \eta \int_0^{2\pi} L_1 |_\gamma d\phi \, . \tag{2.68}$$

We now focus our attention on a class of coordinate transformations such that, at the quadrupole approximation, act on the azimuthal angle according to the

following transformation

$$\phi \to \tilde{\phi} \simeq \phi + \eta\ \chi(r, \theta, \phi)\ , \tag{2.69}$$

where χ is a periodic function of ϕ with a period of 2π ($\chi(\phi) = \chi(\phi + 2\pi)$) while the gauge transformations of the coordinates r and θ are of order $\mathcal{O}(\eta)$, i.e. they are proportional to the quadrupole perturbative parameter η. Under these transformations quasi-circular orbits are always mapped into quasi-circular ones, allowing us to identify the new $\tilde{\phi}$ angle as a rotation angle over which we can average to analyse the secular dynamics. Under the gauge transformations in Eq. (2.69), the first term in the secular average described in Eq. (2.68), transforms as

$$\int_0^{2\pi} \bar{L}|_\gamma d\tilde{\phi} \to \int_0^{2\pi} \bar{L}|_\gamma d\phi + \eta \int_0^{2\pi} \bar{L}|_\gamma d\chi = 2\pi \bar{L}\ , \tag{2.70}$$

where we used the periodicity of χ and the fact that $\bar{L}$ does not depend on ϕ. The second term in Eq. (2.68), under the same gauge transformations (2.69), reads as

$$\int_0^{2\pi} L_1|_\gamma d\tilde{\phi} \to \int_0^{2\pi} L_1|_\gamma d\phi + \eta \int_0^{2\pi} L_1|_\gamma d\chi\ . \tag{2.71}$$

Notice how in general the last integral in the expression above in not zero, given that L_1 depends on ϕ. However we can safely neglect this contribution since, for the specific gauge transformations presented in Eq. (2.69), this would be of order η^2 and thus of higher order compared to the quadrupole approximation.[10]
With these results we can write Eq. (2.68) as

$$\langle L \rangle \simeq \int_0^{2\pi} \left(\bar{L} + \eta L_1\right)|_\gamma d\tilde{\phi} \to 2\pi \bar{L} + \eta \int_0^{2\pi} L_1|_\gamma d\phi\ , \tag{2.72}$$

this relation tells us that $\langle L \rangle$ is gauge invariant under coordinate transformations 2π-periodic in ϕ of order $\mathcal{O}(\eta)$.
Similarly it is possible to prove that also $\langle u^t \rangle$ and $\langle u^\phi \rangle$ are invariant under the gauge transformations described in Eq. (2.69). As a consequence also the averaged orbital frequency for a quasi-circular orbit, defined as

$$\Omega = \frac{u^\phi}{u^t}\ , \tag{2.73}$$

is gauge-invariant under this class of transformations.

[10] This is true since L_1 is already of order η, see Eq. (2.68).

Tidal deformations on the ISCO

The ISCO represents the closest stable circular orbit for a massive particle in a black hole spacetime and it is fully characterized by its radius, energy and angular momentum. We can find these parameters starting from the secular Hamiltonian in Eq. (2.49)and following the reasoning of [215], which yields to three defining conditions for the ISCO, namely

$$\begin{aligned} \langle H\rangle|_{r=r_{\rm ISCO}} &= -\frac{1}{2}\ , \\ \left.\frac{d\langle H\rangle}{dr}\right|_{r=r_{\rm ISCO}} &= 0\ , \\ \left.\frac{d^2\langle H\rangle}{dr^2}\right|_{r=r_{\rm ISCO}} &= 0\ . \end{aligned} \tag{2.74}$$

We assume that secular tidal effects are all proportional, up to the quadrupole order, to the effective perturbative parameter η and we expand the observables around their unperturbed values as[11]

$$\begin{aligned} r_{\rm ISCO} &\simeq r_0 + \eta\, r_1\ , \\ E_{\rm ISCO} &\simeq E_0 + \eta\, E_1\ , \\ L_{\rm ISCO} &\simeq L_0 + \eta\, L_1\ , \end{aligned} \tag{2.75}$$

where (r_0, E_0, L_0) represent the unpertubed values for the radius, energy and angular momentum of the ISCO for a Schawrzschild black hole while (r_1, E_1, L_1) define the corrections induced by the tidal fields at first order in η.

After plugging the expanded expressions for the radius, energy and angular momentum defined in Eq. (2.75) into the ISCO conditions (2.74), at leading order we can find the unperturbed values for the parameters (r_0, E_0, L_0) characterizing the ISCO of a Schwarzschild black hole, namely

$$r_0 = 6\ M\ ,\quad E_0 = \frac{2\sqrt{2}}{3}\ ,\quad L_0 = 2\sqrt{3}\ M\ . \tag{2.76}$$

Analogously by solving Eqs. (2.74) at first order in η we find the corrections to the orbital parameters of the ISCO (r_1, E_1, L_1) induced by the tidal fields generated by the Kerr SMBH, which read

$$r_1 = 3072\ M\ ,\quad E_1 = -\frac{152\sqrt{2}}{3}\ ,\quad L_1 = -348\sqrt{3}\ M\ . \tag{2.77}$$

Another relevant quantity that it is interesting to analyse is the ISCO orbital frequency, which in general for quasi-circular orbits is defined as [72, 214]

$$\Omega^2 = \left(\frac{u^\phi}{u^t}\right)^2 = \frac{M}{r^3} - \frac{(r-3M)}{2r^2} u^\mu u^\nu \partial_r \langle h_{\mu\nu}\rangle\ , \tag{2.78}$$

[11] For ease of notation from now on we will drop the bracket $\langle\cdot\rangle$ notation for the secular averaged quantities.

where u^μ are the components of the four-velocity (2.44). After writing the ISCO orbital frequency as the unpertubed frequency in the Schwarzschild background plus a tidal correction proportional to η, namely

$$\Omega_{\rm ISCO} \simeq \Omega_0 + \eta\ \Omega_1\ , \tag{2.79}$$

we find

$$M\ \Omega_0 = \frac{1}{6\sqrt{6}}, \quad M\ \Omega_1 = -\sqrt{\frac{2}{3}}\frac{491}{6}\ . \tag{2.80}$$

This expression tells us how the orbital frequency of the test particle moving on the ISCO is shifted by the presence of a Kerr SMBH.
Finally we can use the ISCO orbital frequency defined in Eq. (2.78) to introduce a gauge-independent quantity which allows us to measure the radial separation between the two companions in the EMRI system. Following Ref. [214] we introduce

$$R_\Omega = \left(\frac{M}{\Omega^2}\right)^{1/3}\ , \tag{2.81}$$

which combined with Eqs. (2.79) and (2.80) yields

$$R_\Omega \simeq \frac{2^{2/3}M}{\Omega_0^{2/3}}\left(1 - \frac{2}{3}\eta\frac{\Omega_1}{\Omega_0}\right) = 6M + 3928\eta\ M\ . \tag{2.82}$$

The shift induced by the tidal fields on R_Ω is different from the one computed for the radial coordinate $r_{\rm ISCO}$ in Eq. (2.77) as expected since the former is a gauge-invariant quantity while the latter is not.

Tidal deformations on the Photon Sphere

The photon sphere is the analogous of the ISCO for a massless particle, i.e. the last stable circular orbit for photons. This peculiar orbit is uniquely identified by two parameters, namely its radius and the impact parameter defined as $b = L/E$. Given that we need only two parameters to describe the photon sphere, this orbit can be studying by imposing two conditions on the Hamiltonian (2.49)

$$\begin{aligned} \langle H\rangle|_{r=r_{\rm PS}} &= 0\ , \\ \left.\frac{d\langle H\rangle}{dr}\right|_{r=r_{\rm PS}} &= 0\ . \end{aligned} \tag{2.83}$$

By following the same reasoning we used above for the ISCO, we expand the photon sphere parameters in terms of the effective perturbative parameter η, retaining only the leading order, namely

$$\begin{aligned} r_{\rm PS} &\simeq r_0 + \eta\ r_1\ , \\ b_{\rm PS} &\simeq b_0 + \eta\ b_1\ , \end{aligned} \tag{2.84}$$

where by solving the conditions in Eq. (2.83) at leading order in η we obtain the unperturbed values for the photon sphere in the Schwarzschild background:

$$r_0 = 3\ M\ ,\quad b_0 = 3\sqrt{3}\ M\ . \tag{2.85}$$

At first order in η instead we get the tidal corrections induced by the Kerr SMBH:

$$r_1 = -30\ M\ ,\quad b_1 = 30\sqrt{3}\ M\ . \tag{2.86}$$

Finally for completeness we also compute how the orbital frequency of the photon sphere is shifted by the presence of the tidal fields. In general for the orbital frequency we have

$$\Omega = \frac{u^\phi}{u^t} = \frac{1}{b}\ , \tag{2.87}$$

which we write as the unperturbed value plus a tidal correction proportional to η as

$$\Omega_{\rm PS} \simeq \Omega_0 + \eta\ \Omega_1\ . \tag{2.88}$$

Plugging in this expression the results obtained in Eq. (2.85) and (2.86) we can immediately compute the tidal shift induced on the orbital frequency of the photon sphere, which reads

$$M\ \Omega_0 = \frac{1}{3\sqrt{3}}\ ,\quad M\ \Omega_1 = -\frac{10}{3\sqrt{3}}\ . \tag{2.89}$$

Chapter 3

Charged Binary Black Holes

Classically black holes are completely characterized by their mass, spin and charge [224–227]. A charged black hole would attract particles of the opposite charge pulling them into itself and, as a consequence, the charge of the black hole will be quickly neutralized by the surrounding environment and thus generally BHs are considered to be neutral [228, 229]. Although this mechanism seems to work for a non-spinning black hole, the presence of spin can change significantly the neutralization process for a charged BH. This is mostly due to the fact that a spinning black hole could have, in the near-horizon region, a charged separated plasma which can form a force-free magnetosphere [230–233]. This magnetosphere may preserve a global charge in a similar way as it happens for spinning magnetized neutron stars [234,235] under the assumption that BHs posses a magnetosphere in a dipole configuration, for which the conserved charge would be

$$Q \sim \frac{\Omega_* \mu_*}{3c}, \tag{3.1}$$

with μ_* the magnetic moment of the BH dipole and Ω_* the angular velocity of its magnetosphere [234, 235].
Moreover it has been shown in [73] that a rotating black hole immersed in a magnetic field can end up with a net electric charge by swallowing positive charged particles and repelling the negative ones,[1] with a similar mechanism as the one depicted in [236] for a conducting sphere in flat space. The charge of the black hole in this scenario can be estimated by using the injection-energy argument [237], which allow us, by lowering a charged particle along the symmetry axis of the black hole, to write the change in the electrostatic energy of the particle as

$$\epsilon = E_{\text{final}} - E_{\text{initial}} = eA_\mu T^\mu\big|_{\text{horizon}} - eA_\mu T^\mu\big|_\infty, \tag{3.2}$$

[1] This is true if the spin of the black hole is parallel to the magnetic field. If the two are anti-parallel instead then positive charged particle would be repelled and negative ones would be attracted by the black hole.

where T^μ is the timelike Killing vector of the spacetime, A_μ the vector potential of the electromagnetic field and e the charge of the particle falling into the black hole. The latter will keep harvesting charges until the electrostatic injection energy ϵ becomes zero because of the change in A_μ. This yields to

$$\epsilon = e\left(\frac{Q}{2M} - \frac{B_0 J}{M}\right), \tag{3.3}$$

where M is the mass of the black hole, J and Q respectively its angular momentum and charge and B_0 is the strength of the magnetic field. By imposing the condition $\epsilon = 0$ we find that a black hole in a uniform magnetic field can build up a charge given by

$$Q = 2B_0 J.^{2} \tag{3.4}$$

This expression tells us that the charge accumulated by the black hole is proportional to both its spin and the strength of the magnetic field, thus for typical values of the galactic magnetic field ($B_0 \sim 10^{-4} \div 10^{-5}$ Gauss) this mechanism leads to a very small charge-to-mass ratio but nevertheless allows black holes to have a non-zero electric charge.

There are also other astrophysical arguments for which it is relevant to include a small amount of charge in black holes. For example it has been shown that any macroscopic object in the Universe should carry a small amount of charge in order to avoid the separation of electrons and protons in stellar atmosphere [238–241]. We can estimate the charge of a black hole by assuming that celestial bodies in the Universe are neutral, meaning that the electrons and protons densities should be the same $n_p \approx n_e$. We recall that the density distribution can be defined as

$$n(r) = n_0(e)\, \mathrm{e}^{-\Phi(r)/(k_\mathrm{B}T)}, \tag{3.5}$$

where $n_0(r)$ is the density distribution in the absence of external field, k_B the Boltzmann constant, T the temperature and $\Phi(r)$ is the conservative field outside the black hole which we assume to be given by a combination of the gravitational and electromagnetic contribution, namely $\Phi(r) = \Phi_\mathrm{G}(r) + \Phi_\mathrm{E}(r)$. The condition $n_p = n_e$ is satisfied by requiring $\Phi_p \approx \Phi_e$, i.e. we should have the same potential value for both protons and electrons. This condition yields to a constraint for the charge of the black hole, namely

$$\frac{Q_\mathrm{eq}}{M} = \frac{2\pi(m_p + m_e)}{e} \approx 77\,\mathrm{C\,M_\odot^{-1}}, \tag{3.6}$$

where with M we denote the mass of the black hole while m_p and m_e represent the masses of the proton and electron and finally $\mathrm{M}_\odot$ is the Solar mass, i.e. $\mathrm{M}_\odot \sim 2 \times 10^{30}$ kg. If we also include the charge neutralization effects

[2] Here for this brief analysis we worked in geometrized units, i.e. $G = c = 1$.

(Schwinger pair production [242]) to this estimate, the charge of a black hole would reduce to approximately $1\,\mathrm{C}\,\mathrm{M}_{\odot}^{-1}$ [243].

The inclusion of the charge in black hole binaries can also be relevant in the context of gravitational waves since it can help us to build waveform models for signals coming from real astrophysical scenarios [244–248]. Moreover it has been shown in [249] that the presence of the charge in a black hole binary can significantly suppress the merger time. Furthermore on the observational side it is worth mentioning that, with the data that we have at current times, we cannot rule out the presence of a small amount of charge in black holes, see Ref. [241] for an analysis on Sagittarius A* for example.

So far we focused our attention on electrically charged black holes. However lately there has been a great interest in magnetically charged ones because magnetic monopoles[3] are expected to be more massive than electrically charged particles, making the Schwinger pair production less effective and thus leading to more stable magnetically charged black holes than the electrically charged ones [253]. Moreover these objects have drawn a lot of attention in the scientific community since in the near horizon region (usually called *electroweak corona*) the magnetic fields could be so strong that it is possible to restore the electroweak symmetry [254–257]. In particular assuming that the magnetically charged black hole is described by the Reissner-Nordström metric, if the radius of its event horizon is smaller than the monopole radius (assuming a 't Hooft-Polyakov monopole) it is possible to have a hairy black hole with a cloud of electroweak fields in the near horizon region [258, 259], which can enhance the Hawking radiation process and lead on a very short timescale to extremal charged black holes for which the evaporation process is suppress and thus these objects become very stable and can last as long as the age of the Universe [74, 75]. One of the possible formation channel for the production of magnetically charged black holes is to assume that a primordial black hole, in the early Universe, swallows magnetic monopoles building up a net magnetic charge given by $\sqrt{N}$, with N the number of monopoles swallowed [74, 260].

Finally it is also worth mentioning that charged black holes are related to more exotic theories, such as dark matter and mini-charged dark matter scenarios [261,262], where charged black holes could exist thanks to fermions with a fractional electric charge much smaller than the one of an electron which would make the pair production mechanism, usually responsible for neutralization, ineffective. Moreover charged black holes are also related to topological charges [263] and topological stars [264, 265], as well as traversable wormholes [266], superradiant instabilities in AdS spacetime [76], new forces beyond the Standard Model [267] and in the context of the Gertsenshte in- Zel'dovich

[3]Even though we have not detected them yet, they are a key element in the quantisation of the electric charge [250] and they are predicted in all Grand Unified Theories (GUTs) [251, 252].

effect consisting in the conversion, in the presence of a strong magnetic field, of electromagnetic waves into gravitational ones and vice versa [268].

Besides the possible existence of charged black holes in astrophysical scenarios, the presence of an extra parameter in the metric describing a black hole can be used to generalize the ideal Schwarzschild solution, including the possibility to have an extremal black hole and using it as a toy model to study the more realistic scenario of rotating black holes described by the Kerr metric. Thus in this chapter we will analyse how the dynamics of a binary system, an EMRI in particular, changes when we allow one of the two bodies to have a charge in the cases when the binary is isolated and when an external tidal field is present.

3.1 Event horizon of a charged black hole binary merger

In this section we analyse the formation and evolution of the event horizon of a binary black hole system where at least one of the two objects is a charged black hole described by the Reissner-Nordström (RN) metric [269, 270].
To study the evolution of the event horizon during the merger of a binary system is usually, both analytically and numerically, very challenging. However, as shown in [78, 271, 272], the problem simplifies greatly in the Extreme Mass Ratio (EMR) limit, where one of the two objects in the binary system is much smaller than the other. In particular using M and m to describe respectively the masses of the primary and the secondary black hole in the binary, the EMR limit consists in sending $m/M \to 0$. This limit is usually satisfied by taking $m \to 0$ (as we also did in Chapter 2), i.e. considering that one of the two objects in the binary system is a point particle. This approach is ideal if one wants to study the emission and propagation of gravitational waves during the merger of the two companions, using for example a multipolar Regge-Wheeler-Zerilli perturbative approach [273, 274] or the Effective One Body formalism [275–280]. However if we treat the secondary black hole as a point particle we lose all the information about the physics happening on the scale of m and moreover, we lose information about the geometrical structure of the black hole making impossible for us to identify the null hypersurface which defines the event horizon. Then in order to study the physics on the scale of m and to follow the evolution of the event horizon of the small black hole during the merger, we satisfy the EMR limit introduced above by keeping m fixed and sending $M \to \infty$. In this scenario, after placing ourselves in the rest frame of the small black hole, we can neglect the curvature of the spacetime over distances $\ll M$ and moreover we are still able to identify the event horizon of the larger black hole as an accelerated horizon, i.e. a Rindler horizon [78]. With this in mind the procedure that we will use to extract the evolution of the event horizon during the merger, following Ref. [78], is quite

simple. We start by placing ourselves in the rest frame of the small black hole at a distance $\ll M$, in this scenario we can neglect the curvature of the spacetime induced by the primary companion in the spacetime and we can describe the background using the RN metric, i.e. describing the small black hole as a charged one. Furthermore given that $M \gg m$, the event horizon of the binary system at future null infinity $\mathcal{I}^+$ will coincide with the one of the larger black hole in the EMRI system, i.e. it will be an infinite accelerated horizon which corresponds to a congruence of light rays that forms a planar surface. Starting from this surface at $\mathcal{I}^+$ we follow back in time a congruence of null geodesics that, starting from the small, charged black hole, reaches a planar horizon at large distance.
With this formalism we can analyse analytically the evolution of the event horizon during the merger, allowing us to extract some key properties of the merger such as the duration of it, the growth of the area of the small black hole and the presence of a line of caustics. The last one is always present in the event horizon of a black hole merger and it is a consequence of the strong gravitational field causing the light rays to bend towards each other and intersect in caustic points, forming a line of caustics. These points are the first ones to enter the event horizon in the early times of the merger.

Throughout this chapter we use units where $G = c = \epsilon_0 = \mu_0 = 1$, unless otherwise specified.

3.1.1 Analytical solution in $D = 4$

In this section we derive analytically the evolution of the event horizon of a binary black hole merger in the EMR limit where the smaller black hole is a charged one described by the RN metric in 4 dimensions, which in Schwarzschild quasi-spherical coordinates can be written as

$$ds^2 = -\Delta(r)dt^2 + \Delta(r)^{-1}dr^2 + r^2 d\Omega^2, \tag{3.7}$$

with

$$\Delta(r) = 1 - \frac{2m}{r} + \frac{Q^2}{r^2}. \tag{3.8}$$

Here, Q represents the electric or magnetic charge, a combination of the two or, in general, any type of parameter with the same coupling of the charge in the Einstein-Maxwell theory. Moreover, $d\Omega^2 = d\theta^2 + \sin^2\theta d\phi^2$ and m is the mass of the black hole.

The position of the event horizon in the RN background can be found by solving the equation $\Delta(r) = 0$, which has, in general, two different solutions

$$r_\pm = m \pm \sqrt{m^2 - Q^2}, \tag{3.9}$$

which represent the inner (r_-) and outer (r_+) horizon. The latter gives the position of the even horizon while the former is a Cauchy horizon. In the

case of an extremal RN black hole, i.e. when $|Q| = m$, the two solutions in Eq. (3.9) coincide and the location of the event horizon is given by $r_{\rm EH} = m$.

We will analyse separately two different cases: when the charge of the black hole is smaller than its mass $|Q| < m$ and the extremal case where $|Q| = m$. The former one represents the physical and more realistic scenario, where the black hole has a small amount of charge compared to its mass, while the latter describes a black hole with the same amount of charge and mass which corresponds to an unstable configuration since a small amount of charge or mass would lead to a black hole with either $|Q| < m$ or $|Q| > m$ (where the last one corresponds to a naked singularity and thus to a non-physical scenario). Even though extremal black holes are very unlikely to exist in the Universe[4] they are very interesting theoretically speaking. For example, given that the mass of a black hole is related to its dimension, an extremal black hole describes the smallest possible configuration. Moreover they are often used as a tool in supersymmetric theories since they are invariant under supercharges, allowing a microscopic description of the Bekenstein Hawking entropy formula for black holes in terms of D-branes configurations [281–284].

Case $|Q| < m$

We start by studying the evolution of the event horizon of a binary black hole merger when the secondary companion of mass m is a RN black hole with charge $|Q| < m$.

Mathematically an event horizon represents a null hypersurface, which describes a congruence of null geodesics usually called generators. We know that the final configuration of the event horizon, after the merger, at future null infinity is the same as the one of the larger black hole in the binary system in the limit $M \to \infty$, i.e. the generators of the event horizon form a planar horizon. The plan to extract the evolution of the event horizon during the early stages of the merger is then to trace back the null geodesics that define the event horizon at $\mathcal{I}^+$ until they reach the so-called *line of caustics*, which identify the set of points where the generators focus as they enter the event horizon [285–288]. This set of points represents where the event horizon begins in the past since once at the horizon, a null generator can never propagate off it, nor it can ever cross another null geodesic. This means that event horizons are characterized by null geodesics passing through each point of the null hypersurfaces defining them, continuing along the horizon forever into the future, without crossing each other again and in agreement with the cosmic censorship conjecture. Thus in order to extract the evolution of the event horizon during the merger we need to study the geodesic equations describing

[4] Although in general they might be very unstable, there are some scenario in which magnetically charged black holes could exist in a stable configuration, see discussion at the beginning of Chapter 3.

the motion of a congruence of light rays that reach a planar horizon at future null infinity.

We recall that we place ourselves in the rest frame of the RN black hole of mass m and we work in the EMR limit by taking $M \to \infty$. In this way the spacetime in which the merger takes place can be described by the RN metric introduced in Eq. (3.7) which in the $m/M \to 0$ limit still has the usual spherical symmetry and the timelike Killing vector ∂_t[5]. Thanks to the spherical symmetry we can set $\theta = \pi/2$ without loss of generality and we can write the geodesic equations in the RN background for a mass-less particle as

$$\dot{t} = \frac{1}{1 - \frac{2m}{r} + \frac{Q^2}{r^2}}, \tag{3.10}$$

$$\dot{\phi} = -\frac{q}{r^2}, \tag{3.11}$$

$$\dot{r} = \frac{1}{r}\sqrt{r^2 - q^2\left(1 - \frac{2m}{r} + \frac{Q^2}{r^2}\right)}, \tag{3.12}$$

where q represents the ratio between the conserved angular momentum and the energy of the light-ray trajectory and it is called *impact parameter*. Moreover $\dot{t} = \frac{dt}{d\lambda}$, $\dot{\phi} = \frac{d\phi}{d\lambda}$ and $\dot{r} = \frac{dr}{d\lambda}$ with λ the affine parameter.
The impact parameter q has a geometrical interpretation which can be understood by introducing Cartesian-like coordinates

$$x = r\sin(\phi), \quad z = r\cos(\phi). \tag{3.13}$$

In the (x, z) coordinates, asymptotically, all light rays move with $dx = 0$,

$$x|_{r\to\infty} = q + \mathcal{O}(r^{-3}), \tag{3.14}$$

$$z|_{r\to\infty} = r + \mathcal{O}(r^{-1}), \tag{3.15}$$

and the horizon is identified by

$$dt - dz = \mathcal{O}(r^{-3}). \tag{3.16}$$

Fig. 3.1 shows the geometrical meaning of the impact parameter q, that is the distance at future null infinity between the geodesics and the z axis. Moreover in Fig. 3.1, r represents the distance between the geodesics and the center of the RN black hole. Thanks to the spherical symmetry of the RN background we can also bound the collision between the two black holes to happen along the ϕ axis. More precisely the collision axis is defined by the two

[5]This is only true in the exact limit $m/M \to 0$. The inclusion of corrections of order m/M results in breaking these symmetries, making the analysis of the merger way more complicated.

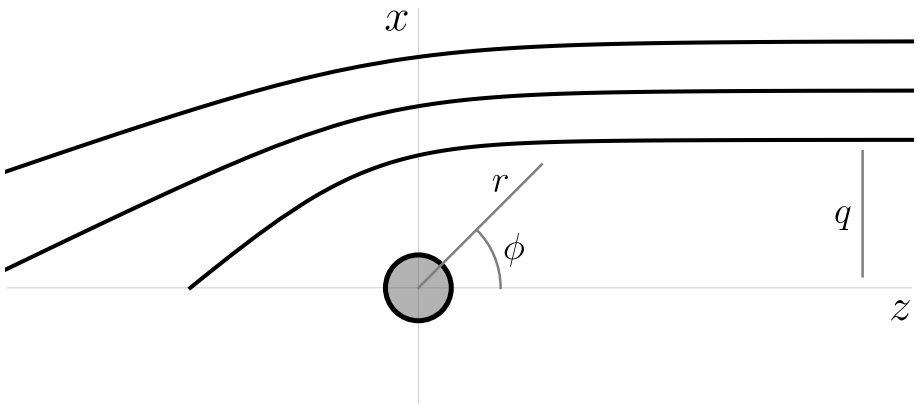

Figure 3.1: Projection of null generators of the event horizon on the spatial plane (x, z). The black lines are the light rays that move towards $\mathcal{I}^+$. At late times, they move along the z direction as the generators of a Rindler horizon $(dt = dz)$. They are labelled by the impact parameter q at future infinity. This graphic representation is the same of Figure 1 from [78], which we reproduce here for convenience.

segments $\phi = 0$ and $\phi = \pi$ in the plane $\theta = \pi/2$ where, after placing ourselves in the rest frame of the small black hole, the former points in the direction away from the large black hole while the latter points in the direction towards the large black hole.

For convenience we rewrite the geodesic equation in (3.10), (3.11) using r as parameter along the geodesics instead of λ. They read

$$\phi_q(r) = \int dr \frac{\dot{\phi}}{\dot{r}}, \quad t_q(r) = \int dr \frac{\dot{t}}{\dot{r}}. \tag{3.17}$$

We now use the fact that at $\mathcal{I}^+$ the null hypersurface defining the event horizon becomes a planar horizon. Thus we take the $r \to \infty$ limit in Eqs. (3.17), which gives us

$$\phi_q(r \to \infty) = \int dr \frac{\dot{\phi}}{\dot{r}}\bigg|_{r\to\infty} = \alpha_q + \frac{q}{r} + \mathcal{O}(r^{-3}), \tag{3.18}$$

and

$$t_q(r \to \infty) = \int dr \frac{\dot{t}}{\dot{r}}\bigg|_{r\to\infty} = r + 2m \log\left(\frac{r}{2m}\right) + \beta_q + \mathcal{O}(r^{-1}). \tag{3.19}$$

We set the two integration constant α_q and β_q by requiring that all the null geodesics move asymptotically in the same direction and that they arrive at future null infinity at the same retarded time. This implies that both α_q and

β_q must be set to some q-independent value, which for simplicity we choose to be zero:

$$\alpha_q = 0, \quad \beta_q = 0. \tag{3.20}$$

By looking at Eqs. (3.17) we can identify immediately the so-called *central generator*, which corresponds to a light ray that starts at $r = r_+$ at $t \to -\infty$ and moves towards infinity in the $\phi = 0$ direction. This generator is characterized by $q = 0$ and, by solving Eqs. (3.17), can be written as

$$\phi_{q=0}(r) = 0, \tag{3.21}$$

$$t_{q=0}(r) = m \log\left(Q^2 + r^2 - 2mr\right) + \frac{\left(2m^2 - Q^2\right) \tan^{-1}\left(\frac{r-m}{\sqrt{Q^2-m^2}}\right)}{\sqrt{Q^2 - m^2}} + r. \tag{3.22}$$

In general to find the other generators of the event horizon we have to solve the q-dependent integrals in Eq. (3.17), which can be written explicitly as

$$\phi_q(r) = -\int \frac{q \;\; dr}{\sqrt{r^4 - q^2 r^2 + 2mq^2 r - q^2 Q^2}}, \tag{3.23}$$

$$t_q(r) = \int \frac{r^4 \;\; dr}{(r^2 - 2mr + Q^2)\sqrt{r^4 - q^2 r^2 + 2mq^2 r - q^2 Q^2}}. \tag{3.24}$$

In order to solve these integrals it is convenient to rewritte them as

$$\phi_q(r) = -\int \frac{q\, dr}{\sqrt{(r - x_1)(r - x_2)(r - x_3)(r - x_4)}}, \tag{3.25}$$

$$t_q(r) = \int \frac{r^4 dr}{(r - r_1)(r - r_2)\sqrt{(r - x_1)(r - x_2)(r - x_3)(r - x_4)}}, \tag{3.26}$$

where x_1, x_2, x_3, x_4 are the solutions of the quartic equation $r^4 - q^2 r^2 + 2mq^2 r - q^2 Q^2 = 0$, and $r_{1,2}$ are the solutions of the quadratic equation $r^2 - 2mr + Q^2 = 0$. We have

$$\begin{aligned} x_{1,2} &= \frac{1}{2\sqrt{6}}\left(\xi_1^{\frac{1}{2}} \mp \xi_2^{\frac{1}{2}}\right), \\ x_{3,4} &= -\frac{1}{2\sqrt{6}}\left(\xi_1^{\frac{1}{2}} \pm \xi_3^{\frac{1}{2}}\right), \\ r_{1,2} &= m \mp \sqrt{m^2 - Q^2}, \end{aligned} \tag{3.27}$$

where

$$\begin{aligned} \xi_1 &= \frac{2\sqrt[3]{2}\gamma}{p} + 2^{2/3} p + 4q^2, \\ \xi_2 &= -\frac{24\sqrt{6} q^2 m}{(\frac{2\sqrt[3]{2}\gamma}{p} + 2^{2/3} p + 4q^2)^{\frac{1}{2}}} - \frac{2\sqrt[3]{2}\gamma}{p} - 2^{2/3} p + 8q^2, \end{aligned}$$

$$\xi_3 = \frac{24\sqrt{6}q^2 m}{(\frac{2\sqrt[3]{2}\gamma}{p} + 2^{2/3}p + 4q^2)^{\frac{1}{2}}} - \frac{2\sqrt[3]{2}\gamma}{p} - 2^{2/3}p + 8q^2,$$
$$p = \left(\sqrt{q^8\left(2q^2+72Q^2-108m^2\right)^2 - 4\left(q^4-12q^2Q^2\right)^3} - q^2\left(2q^2+72Q^2-108m^2\right)\right)^{\frac{1}{3}},$$
$$\gamma = q^4 - 12q^2Q^2. \tag{3.28}$$

Since r_1 and r_2 satisfy $r_1+r_2=2m$, we will use this relation to eliminate r_2 in favor of r_1 when convenient. We will use also the relation $x_1+x_2+x_3+x_4=0$ to simplify the expressions in the integrals.

The solutions to these integrals are given in terms of incomplete elliptic integral of the first, second and third kind[6], namely

$$F(x|\bar{m}) = \int_0^x \frac{d\theta}{\sqrt{1-\bar{m}\sin^2\theta}}, \tag{3.29}$$

$$E(x|\bar{m}) = \int_0^x \sqrt{1-\bar{m}\sin^2\theta}\,d\theta, \tag{3.30}$$

$$\Pi(n;x|\bar{m}) = \int_0^x \frac{d\theta}{(1-n\sin^2\theta)\sqrt{1-\bar{m}\sin^2\theta}}. \tag{3.31}$$

When solving the integrals in Eqs. (3.25) and (3.26) we need to choose carefully the integration constants in order to reproduce the correct asymptotic behaviour depicted in Eqs. (3.18) and (3.19), i.e. we need to fix them to the values we choose in Eq. (3.20). To this end we use the following relation for elliptic integrals [289]

$$\Pi(n;\varphi|\alpha) = -\Pi(N;\varphi|\alpha)+F(\varphi,\alpha)+\frac{1}{2p}\log[(\Delta(\varphi)+p\tan\varphi)(\Delta(\varphi)-p\tan\varphi)^{-1}], \tag{3.32}$$

where

$$N = n^{-1}\sin^2\alpha, \quad p = [(n-1)(1-n^{-1}\sin^2\alpha)]^{\frac{1}{2}}, \quad \Delta(\varphi) = (1-\sin^2\alpha\sin\varphi)^{\frac{1}{2}}. \tag{3.33}$$

Note that this identity can be used to rewrite Eq. (3.31) after identifying $\sin^2\alpha=\bar{m}$ and $\varphi=x$, according to the prescriptions of *Mathematica 12*.
The solutions to Eqs. (3.25) and (3.26), after fixing the integration constants to the values (3.20), can be written as

$$\phi_q(r) = \frac{2q}{\sqrt{bf}}\Big(F(y_1|s) - F(y_2|s)\Big), \tag{3.34}$$

and

$$t_q(r) = \frac{1}{(x_2-r_1)(x_2-r_2)\sqrt{bf}}\Bigg[F(y_2|s)\Big(2ma(r_1-x_2)(2r_2+x_1+x_3)$$

[6]The prescription used here for the square roots of complex numbers and the branch cuts in the elliptic functions is the one implemented in *Mathematica 12*.

$$
\begin{aligned}
&-r_1^2 af - x_2^2(x_3x_2 + x_1x_4)\Big) + x_2\Big(2ma(r_1 - x_2) - ar_1^2 + x_2^2(x_1 + x_2)\Big)\Big] \\
&+\sqrt{\frac{(r-x_1)(r-x_3)(r-x_4)}{r-x_2}} - \sqrt{bf}E(y_2|s) \\
&+ \frac{a}{(m-r_1)\sqrt{bf}}\left[\frac{r_1^4\Pi\left(\frac{(r_1-x_2)c}{(r_1-x_1)f}; y_2|s\right)}{(r_1-x_1)(r_1-x_2)} - \frac{r_2^4\Pi\left(\frac{(x_2-r_2)c}{(x_1-r_2)f}; y_2|s\right)}{(r_2-x_1)(r_2-x_2)}\right] \\
&+ 2m\left[\log\left(\frac{\sqrt{(r-x_1)(r-x_2)} + \sqrt{(r-x_3)(r-x_4)}}{\sqrt{(r-x_3)(r-x_4)} - \sqrt{(r-x_1)(r-x_2)}}\right) - 2\frac{a\Pi\left(\frac{d}{b}; y_2|s\right)}{\sqrt{bf}}\right] \qquad (3.35)
\end{aligned}
$$

where

$$
\begin{aligned}
c_q = &\frac{F(y_1|s)}{(x_2-r_1)(x_2-r_2)\sqrt{bf}}\Big(2ma(r_1-x_2)(2r_2+x_1+x_3) - r_1^2af - x_2^2(x_3x_2+x_1x_4)\Big) \\
&+ x_2\left[\frac{2ma(r_1-x_2) - ar_1^2 + x_2^2(x_1+x_2)}{(x_2-r_1)(x_2-r_2)\sqrt{bf}} + 1\right] - \sqrt{bf}E(y_1|s) + 2m\left[\log\left(\frac{2}{x_1+x_2}\right) - 2\frac{a\Pi\left(\frac{d}{b}; y_1|s\right)}{\sqrt{bf}}\right] \\
&+ \frac{a}{(m-r_1)\sqrt{bf}}\left[\frac{r_1^4\Pi\left(\frac{(r_1-x_2)c}{(r_1-x_1)f}; y_1|s\right)}{(r_1-x_1)(r_1-x_2)} - \frac{r_2^4\Pi\left(\frac{(x_2-r_2)c}{(x_1-r_2)f}; y_1|s\right)}{(r_2-x_1)(r_2-x_2)}\right] \qquad (3.36)
\end{aligned}
$$

and where we introduced the notation

$$
\begin{aligned}
&a = x_1 - x_2, \quad b = x_1 - x_3, \quad c = x_1 - x_4, \quad d = x_2 - x_3, \quad f = x_2 - x_4, \\
&y_1 = \sin^{-1}\left(\sqrt{\frac{f}{c}}\right), \quad y_2 = \sin^{-1}\left(\sqrt{\frac{(r-x_1)f}{(r-x_2)c}}\right), \quad s = \frac{cd}{bf}. \qquad (3.37)
\end{aligned}
$$

Note that these expressions for $t_q(r)$ and $\phi_q(r)$ reproduce the correct asymptotic behaviour, namely for $r \to \infty$ we have

$$
\phi_q(r) \xrightarrow[r\to\infty]{} \frac{q}{r} + \mathcal{O}(r^{-3}), \qquad (3.38)
$$

and

$$
t_q(r) \xrightarrow[r\to\infty]{} r + 2m\log\left(\frac{r}{2m}\right) + \mathcal{O}(r^{-1}). \qquad (3.39)
$$

With the explicit expressions for $t_q(r)$ and $\phi_q(r)$ derived in Eqs. (3.34) and (3.35), we can compute the numerical values for the most relevant parameters describing the event horizon of a charged black hole binary merger in the EMR

limit. To this end we need to fix a value for the charge Q of the RN black hole which we choose to be $Q = 4/5\, m$.

To carry out our analysis we divide the generators of the event horizon in two different classes: the *non-caustic generators* and the *caustic generators*, separated by the impact parameter $q = q_c$. The former ones are characterized by an impact parameter $q \leq q_c$ and going back in time, starting from future null infinity, these generators will not leave the horizon at a caustic point, meaning that they do not have past endpoints. The latter instead are the ones with an impact parameter $q < q_c$, they enter the horizon through the line of caustics and thus, going back in time, they do have endpoints. Among the caustic generators we can identify the ones characterized by an impact parameters $q = q_*$, which are the last to enter the event horizon at the caustic line. See Fig. 3.2 for a graphic representation of the two classes of generators.

The generators characterized by the impact parameter $q = q_c$ play a key role in our analysis, being the ones that separate the two classes of generators described above. They correspond to null geodesics that originate from the event horizon of the small black hole r_+ and move towards the large black hole, i.e. along the $\phi = \pi$ direction. This is the same as the central generator which starts from $r = r_+$ as well but moves in the direction $\phi = 0$. The generators with $q = q_c$ instead do not extend back to infinitely early times (as the central generator does) since they have past endpoints. This can only happen if they are moving towards the large black hole, thus we can find the numerical value for the impact parameter $q = q_c$ by solving the following equation

$$\phi_{q_c}(r_+) = \pi. \tag{3.40}$$

Solving this equation numerically we find

$$q_c = 3.73166\, m. \tag{3.41}$$

It is interesting to compute the growth in the area of the event horizon of the RN black hole due to the non-caustic generators. We recall that the initial area of the event horizon for a charged black hole can be written as

$$\mathcal{A}_{in} = 4\pi r_+^2, \tag{3.42}$$

while, as a consequence of the three dimensional event horizon at future null infinity where the generators that define the event horizon lie on a S^1 of radius q, the contribution of the non-caustic generators to the area of the event horizon is the one of a disk of area πq_c^2. Thus, the growth in the area of the event horizon of the RN black hole due to the non-caustic generators can be written as

$$\Delta\mathcal{A}_{\text{non}-\text{caustic}} = \left(\left(\frac{q_c}{2r_+}\right)^2 - 1\right) 4\pi r_+^2. \tag{3.43}$$

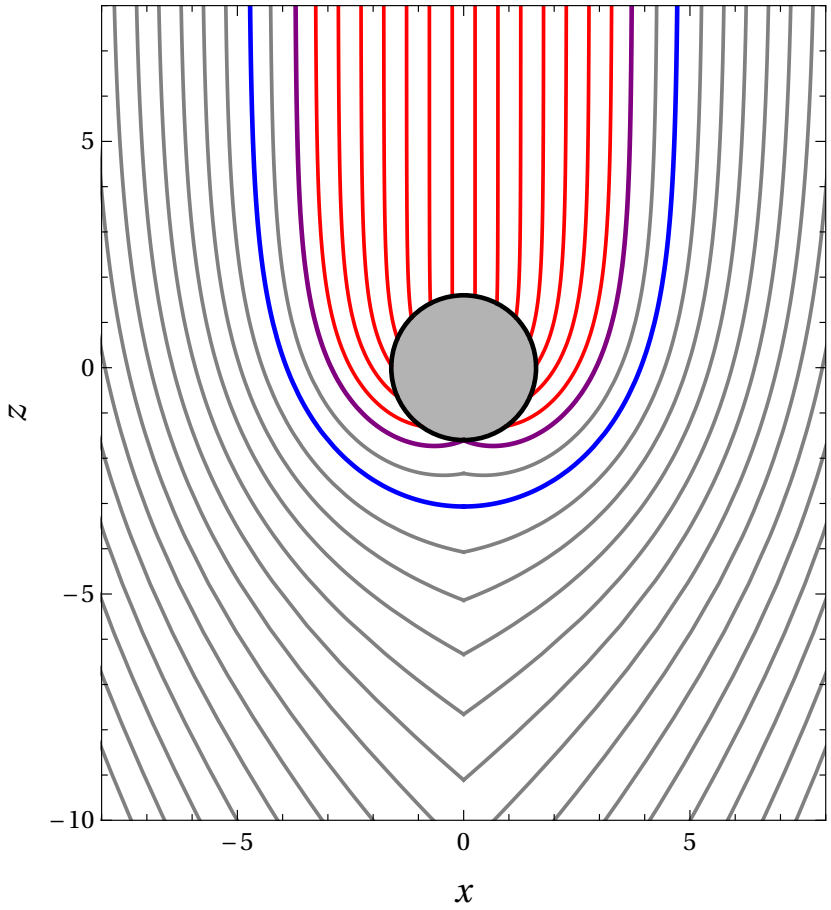

Figure 3.2: Representation in the (x, z) plane of the event horizon. The grey circle is the RN black hole, the red lines represent the non-caustic generators, the purple ones are the generators with $q = q_c$ and the blue curves are the null geodesics with $q = q_*$. The light rays with $q_c < q < q_*$ enter the event horizon through the small black hole while the generators with $q > q_*$ are able to move away from it. The last generators enter the event horizon through the large black hole. All the curves move towards positive z direction. Note that this representation is analogous to the one obtained for the neutral case studied in [78] (see Fig. 5 therein).

Using this, we obtain

$$\Delta\mathcal{A}_{\text{non-caustic}} = 0.35989\ \mathcal{A}_{in}. \tag{3.44}$$

Note that the non-caustic generators are the null geodesics defining the event horizon of the charged black holes at early times, meaning that in the growth of the area of the event horizon analysed in Eq. (3.43), no new generators are added.

We can also analyse the caustic generators, characterized by an impact parameter $q_c < q < \infty$. Among them, we single out the last ones to enter the event horizon at a caustic point at finite time, with an impact parameter $q = q_*$. The value $q = q_*$, together with $t = t_*$ and $r = r_*$, describes the moment when the two event horizons touch each other and merge, usually called the pinch-on instant. Following back from $\mathcal{I}^+$ the generators with an impact parameter $q = q_*$, we see that they remain "still" on the collision axis $\phi = \pi$: they reach the caustic line but they neither approach the small RN black hole nor they leave it. Thus this set of null geodesics is characterized by $\dot{r}|_{\phi=\pi} = 0$.

It is worth mentioning that generators with an impact parameter $q > q_*$ are far away enough from the small black hole to escape its gravitational attraction and, as a consequence, they will not contribute to the evolution of the event horizon of the RN black hole during the merger. In the EMR limit with $M \to \infty$ the event horizon of the large black hole becomes infinite, meaning that the actual number of generators defining the event horizon at future null infinity is infinite. Thus also the null geodesics with an impact parameter $q > q_*$ will enter the final horizon, i.e. the one which will form at the end of the merger, but they will do it through the large black hole instead of the RN one. On the other hand generators with $q < q_*$ are close enough to the small black hole to get pulled towards it because of its gravitational attraction and are forced to enter the event horizon through the RN black hole. It is clear that the last null geodesics to enter the event horizon of the merger through the small RN black hole are exactly the ones characterized by the impact parameter $q = q_*$: they cannot escape the gravitational attraction of the small black hole but they are also not forced to move towards it.

Recalling that for these last generators $\dot{r}|_{\phi=\pi} = 0$, according to Eqs. (3.12) we can find the values for r_* and q_* by solving

$$r_*^4 - q_*^2 r_*^2 + 2q_*^2 m r_* - q_*^2 Q^2 = 0, \quad \phi_{q_*}(r_*) = \pi. \tag{3.45}$$

Once again we solve these equations numerically and we get

$$r_* = 3.0643\, m, \quad q_* = 4.75396\, m. \tag{3.46}$$

After plugging these results in the expression for $t_q(r)$ defined in Eq. (3.35) we can find the numerical value for t_*, which reads

$$t_* = -8.10602\, m. \tag{3.47}$$

We can compare the parameters (3.41), (3.46) and (3.47) that we just obtained in the case of a charged black hole merger with the ones extracted in the neutral case analysed in Ref. [78]. We can notice how in the charged case they are always smaller, meaning that the two event horizon merge closer to the center of the small black hole. Moreover, given that r_* can be interpreted as a measure of how strongly the RN black hole is deformed by the larger one during the merger, the fact that in the charged case r_* is smaller compared to the one obtained in the neutral case means that a RN black hole is less distorted during the merger than a Schwarzschild one.

Furthermore in the EMR limit we can also estimate the duration of the merger. This can be done by considering the difference Δ_* between the retarded time at $\mathcal{I}^+$ of the event horizon in the direction $\phi = 0$ and the retarded time associated to the light rays emitted when the two black holes merge in the direction of the large black hole ($\phi = \pi$). The latter is simply t_*, the former is given by the central generator in Eq. (3.22) evaluated in $r = r_*$[7]. The duration of the merger Δ_* is defined as

$$\Delta_* = t_{q=0}(r_*) - t_*. \tag{3.48}$$

After plugging in Δ_* the expression for $t_{q=0}$ defined in Eq. (3.22) together with the values for r_* and t_* we found in Eqs. (3.46) and (3.47), we have

$$\Delta_* = 10.4669m. \tag{3.49}$$

Again, we can compare this result with the one obtained in the neutral case in Ref [78], which reads $\Delta_* = 11.89352\, m$. We can see that the merger happens faster when one of the two black holes in the binary system is a charged one. In our framework this can be explained by observing that a charged black hole is smaller than its neutral counterpart, leading to a quicker absorption by the larger black hole. This was to be expected since it is already known in the literature that a small amount of electric or magnetic charge in black hole binary systems can lead to faster mergers in the cases of both circular and elliptic orbits [23, 249, 290][8].

The growth in the area of the event horizon of the small charged black hole including also the generators with $q_c < q < q_*$ can be written as

$$\Delta\mathcal{A}_{\text{smallbh}} = \left(\left(\frac{q_*}{2r_+}\right)^2 - 1\right) 4\pi r_+^2, \tag{3.50}$$

where after plugging in the numerical value for q_* found in Eq. (3.46) we have

$$\Delta\mathcal{A}_{\text{smallbh}} = 1.20705\ \mathcal{A}_{in}. \tag{3.51}$$

[7] See Figure 6 in Ref. [78] for a graphical interpretation of Δ_* as the duration of the merger.

[8] See also Ref. [291] for a discussion on the effect of the presence of charge in binaries on the merger rate of primordial black holes.

By comparing our results in Eqs. (3.44) and (3.51) with the ones in the neutral black hole binary obtained in Ref. [78], we can see that the growth in the area of the event horizon of the small black hole during the merger is larger in the charged case. This can be understood by recalling that the more charge is present in a black hole and the smaller the black hole becomes. As a consequence the initial area of a RN black hole will always be smaller than the one of a Schwarzschild black hole with the same mass m, this leads to a greater contribution of the null geodesics to the growth of the area of the event horizon in the charged case. Moreover notice how in both Eqs. (3.44) and (3.51) the $\Delta\mathcal{A}$ for the small black hole is positive, meaning that the area of the event horizon of the RN black hole is bigger after the merger compared to its initial value, satisfying the second law of black hole mechanics.

So far we extracted the parameters of the merger by keeping fixed the charge of the small black hole to a specific value, i.e. $Q = 4/5\,m$, for an illustrative purpose. However it is interesting to analyse how the parameters q_c, q_*, t_*, r_* and Δ_* behave for a general value of the charge Q. To this end, in Figs. 3.3a, 3.3b, 3.3c, 3.3d and 3.3e we plot how the parameters of the merger cited above behave as the charge of the RN black hole grows larger until it reaches its maximum value, i.e. $Q = m$. From these plots we can immediately notice how the more charge is added in the small black hole and the smaller the parameters describing the merger become, reaching their minimum value in the extremal case $Q = m$. In particular Fig. 3.3c tells us that as the charge in the binary system grows larger the small black hole becomes less and less distorted during the merger. From Fig. 3.3e instead, we can see that the merger happens faster as the charge of the RN black hole increases, as expected. Finally the fact that all the parameters become smaller when more charge is added in the binary system simply tells us that the merger between the two black holes is happening closer to the center of the small one.

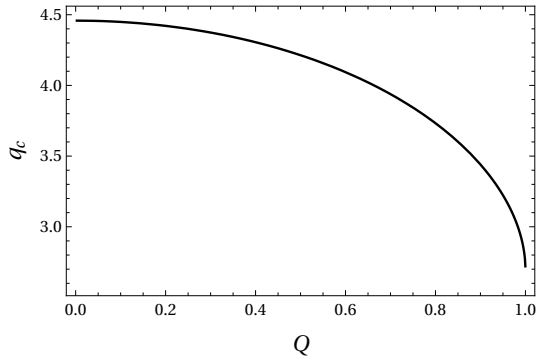

(a) Threshold impact parameter q_c that separates the caustic generators $q > q_c$ and the non-caustic generators $q \leq q_c$, as a function of Q. The axes are measured in units of m.

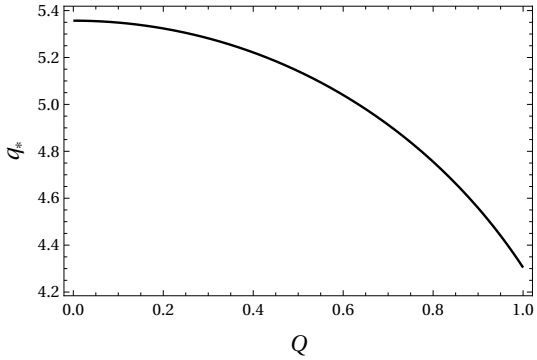

(b) Impact parameter q_* of the last generator to enter the horizon at the caustic line as a function of the charge Q of the small black hole. The axes are measured in units of m.

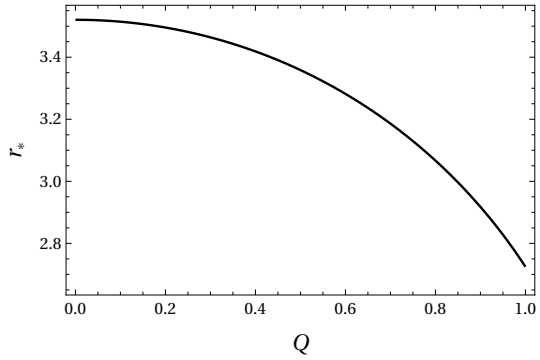

(c) Value of the radial coordinate r_* of the pinch-instant, as a function of Q. r_* measures the distorsion of the RN black hole during the merger. The axes are measured in units of m.

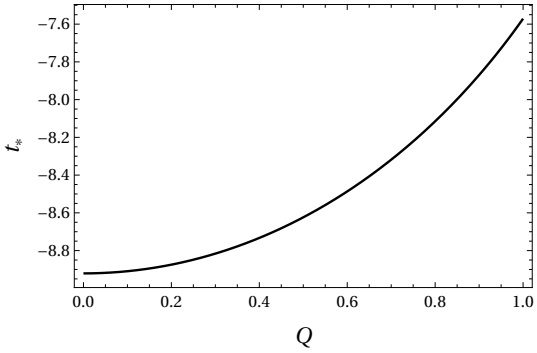

(d) Value of the time coordinate t_* of the pinchon (according to the time origin imposed by (3.39)), as a function of Q. The axes are measured in units of m.

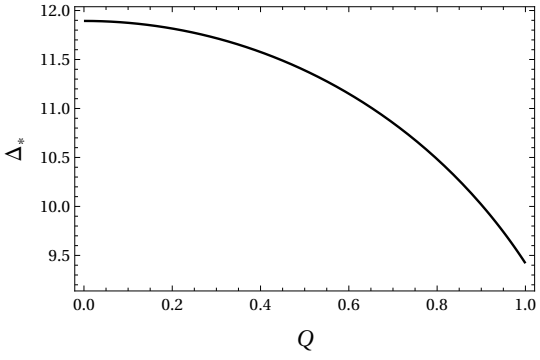

(e) Difference Δ_* between the retarded time at $\mathcal{I}^+$ of the event horizon in the direction $\phi = 0$ and the retarded time associated to the light rays emitted when the two black holes merge in the direction of the large black hole ($\phi = \pi$), as a function of Q. The value of Δ_* can be taken as a measure of the duration of the merger. The axes are measured in units of m.

Extremal case: $|Q| = m$

Here we analyse the case where the small black hole in the binary system is an extremal one, namely it has the same amount of charge and mass $|Q| = m$. As already mentioned at the beginning of this Chapter, extremal black holes are particularly interesting in supersymmetric theories and moreover they also represent the smallest possible configuration for a black hole.

To analyse the extremal case we can take the $Q \to m$ limit either in the Eqs. (3.21)-(3.24) or directly in the results obtained in Eqs. (3.34)-(3.36) in the $|Q| < m$ case. Starting with the expression for $t_q(r)$, in the extremal case this takes the following expression[9]

$$
\begin{aligned}
t_q(r) &= 2m \log\left(\frac{q}{2}\frac{\sqrt{(r-x_1)(r-x_2)}+\sqrt{(r-x_3)(r-x_4)}}{\sqrt{(r-x_3)(r-x_4)}-\sqrt{(r-x_1)(r-x_2)}}\right) - x_2 \\
&+\sqrt{\frac{(r-x_1)(r-x_3)(r-x_4)}{r-x_2}} + \sqrt{bf}\left(E\left(y_1|s\right) - E\left(y_2|s\right)\right) \\
&+\frac{am^4}{\sqrt{bf}(m-x_1)^2(m-x_2)^2}\Bigg\{\left(\frac{x_1x_3f-2qm^2+x_2x_4b}{(m-x_4)(m-x_3)}-2(m-q)\right)\Pi\left(\frac{c(m-x_2)}{f(m-x_1)};y_2|s\right) \\
&+\left(2(m-q)(m-x_3)+\frac{bc(m-x_2)^2-df(m-x_1)^2}{2a(m-x_4)}\right)\Pi\left(\frac{c(m-x_2)}{f(m-x_1)};y_1|s\right) \\
&+\frac{b(m-x_1)(m-x_2)}{a(m-x_3)(m-x_4)}\Bigg[f\left(\frac{E(y_1|s)}{2}-E(y_2|s)\right) \\
&+\frac{c(m-x_2)}{\sqrt{ab}}\left(4\sin(2y_1)+\frac{\sqrt{(r-x_3)(r-x_2)}}{2(m-r)}\sin(2y_2)\right)\Bigg]\Bigg\} \\
&+\frac{ma}{\sqrt{bf}}\Bigg[\frac{m^3f}{(m-x_1)(m-x_2)^2(m-x_4)}\left(F(y_2|s)-\frac{F(y_1|s)}{2}\right)+4\left(\Pi\left(\frac{d}{b};y_1|s\right)-\Pi\left(\frac{d}{b};y_2|s\right)\right)\Bigg] \\
&+\frac{\left(\left(x_1x_4+x_2x_3\right)x_2^2-am\left(4m^2+(x_1-6x_2+x_3)m+2x_2(x_1+x_3)\right)\right)}{\sqrt{bf}(m-x_2)^2}\left(F\left(y_1|s\right)-F\left(y_2|s\right)\right) \\
&+\frac{m^4}{(m-x_1)^2(m-x_2)^2}\left(\frac{a(2m+q)}{\sqrt{bf}}+\frac{\left(x_1x_3f-2m^2q+x_2x_4b\right)}{2(m-x_3)(m-x_4)}\right)\Pi\left(\frac{c(m-x_2)}{f(m-x_1)};y_1|s\right) \\
&+\frac{m^4}{2(m-x_1)(m-x_4)}\left(\frac{b}{a(m-x_3)}\left(\frac{fE\left(y_1|s\right)}{m-x_2}+\frac{c\sin(2y_1)}{2\sqrt{ab}}\right)-\frac{fF\left(y_1|s\right)}{(m-x_2)^2}\right)
\end{aligned}
\tag{3.52}
$$

where we now have that

$$
x_{1,2} = \frac{1}{2}\left(q \mp \sqrt{q(q-4m)}\right), \qquad x_{3,4} = \frac{1}{2}\left(-q \mp \sqrt{q(q+4m)}\right), \tag{3.53}
$$

[9] Here we already explicitly subtracted the integration constant c_q.

and we used the definitions in (3.37). Formally $\phi_q(r)$ in the extremal case has the same expression as the one computed in the $|Q| < m$ case in Eq. (3.34), but with x_1, x_2, x_3 and x_4 given by Eq. (3.53).

We can now follow the exact same procedure used in the $|Q| < m$ case to compute the parameters characterizing the merger of the charged binary black hole in the EMR limit when the small black hole is an extremal one. Starting with the central generator we have

$$t_{q=0}(r) = r + \frac{Q^2 - 2m^2}{r - m} + m \log(Q^2 + r^2 - 2mr). \tag{3.54}$$

While after using the expressions for $t_q(r)$, $t_{q=0}(r)$ and $\phi_q(r)$ defined in respectively (3.52), (3.54) and (3.34) together with Eqs. (3.40), (3.45) and (3.48), we can compute the parameters describing the merger of the two black holes in the extremal case. They read

$$\begin{aligned} q_c &= 2.69128\, m, \quad & q_* &= 4.30440\, m, \\ r_* &= 2.72454\, m, \quad & t_* &= -7.54738\, m, \\ \Delta_* &= 9.39568\, m. \end{aligned} \tag{3.55}$$

The values of q_c and q_* can be used to compute the growth in the area of the event horizon of the small black hole due respectively to the non-caustic generators and the caustic ones. By using Eqs. (3.44) and (3.50), the growth in the area of the event horizon in the extremal case can be written as

$$\Delta\mathcal{A}_{\text{non-caustic}} = 0.81075\ \mathcal{A}_{in}, \quad \Delta\mathcal{A}_{\text{caustic}} = 3.63196\ \mathcal{A}_{in}. \tag{3.56}$$

Comparing these results with the one obtained in the regular case $|Q| < m$, we can immediately notice that the parameters q_c, q_*, r_*, t_* and Δ_*, are smaller in the extremal case, as already shown in Figs. 3.3a, 3.3b, 3.3c, 3.3d and 3.3e. Given that an extremal black hole is the smallest possible configuration for a charged black hole, it will be swallowed more quickly by the large black hole in the binary system while being less distorted during the merger, compared to the regular case where the small black hole has a charge $|Q| < m$. This is well described by the smaller numerical values obtained in the extremal case for respectively Δ_* and r_*. Finally this also explain why the growth in the area of the event horizon is larger in the extremal case compared to the regular case. Being the $|Q| = m$ black hole smaller than the regular $|Q| < m$ one, the contribution of the generators to the growth in the area of its event horizon will be more significant.

Orbit, spin and charge of the large black hole

So far we carried out our computation and analysed the merger of the two black holes in the EMR limit without mentioning the charge or the spin of the large black hole or the orbital properties of the binary system, which in

general are not necessary negligible. However we can argue that for a merger in the EMR limit is always possible to neglect those contributions and that the case of a radial in-fall in a non-charged, non-spinning large black hole describes every possible merger in the EMR limit.

Starting from the orbital properties of the binary, we can write any relative motion between the two black holes in the EMR limit as a linear combination of perpendicular and parallel contributions with respect the event horizon of the large black hole. The asymptotic surface, from which we trace back the event horizon of the merger in the EMR limit, is invariant under boosts along the collision axis and this guarantees the invariance under perpendicular motion, while we can fix to zero the parallel motion without loss of generality by using a similar argument [78,271], where a change in the parallel motion would simply result in a different value for the integration constants in Eqs. (3.18) and (3.19).

Moreover we can also prove that the charge of the large black hole plays no role in the merger the EMR limit. This is due to the fact that the charge would scale as r^{-2}, where on the other hand the mass scales as r^{-1}, see Eq. (3.7). The steeper r-dependence makes it so that the contribution of the charge becomes irrelevant outside the event horizon in the $M \to \infty$, even when the large black hole is an extremal one.

3.1.2 Numerical solution in 4 dimensions

In this section we use a numerical approach to analyse the merger of a charged black hole binary system in the EMR limit. The numerical computation is based on the Hamiltonian formalism for the geodesic equations and it has the advantage of leading to easier differential equations to solve numerically mainly because avoids working with incomplete elliptic integrals.

To carry on the numerical computation we start by rewriting the equations of motion derived already in Ref. [271][10]

$$\frac{dt}{d\lambda} = \Delta(r)^{-1} \tag{3.57}$$

$$\frac{dr}{d\lambda} = \Delta(r) p_r \tag{3.58}$$

$$\frac{d\phi}{d\lambda} = \frac{q}{r^2} \tag{3.59}$$

$$\frac{dp_r}{d\lambda} = -\frac{\Delta'(r)}{2\Delta(r)^2} - \frac{\Delta'(r)}{2} p_r^2 + \frac{q^2}{r^3} \tag{3.60}$$

where λ is the affine parameter, q the impact parameter at infinity, $\Delta(r) = 1 - \frac{2m}{r} + \frac{Q^2}{r^2}$ and $\Delta'(r) = \frac{d\Delta(r)}{dr}$.

[10] The authors in Ref. [271] work in the plane $\theta = 0$, where the geodesics lie in the constant ϕ planes. Thanks to the spherical symmetry of the RN background we are free to change the non-trivial angular variable $\theta \leftrightarrow \phi$ and get the same form of the geodesic equations.

The first step to solve these differential equations is to find a set of integration constants, which can be done by requiring that at future null infinity the null hypersurface defining the event horizon of the merger becomes a planar horizon. Next, by evaluating $p^\mu p_\mu = 0$, we compute the explicit expression for $p^r(r)$, which reads

$$p_r = \frac{\sqrt{1-\left(1-\frac{2m}{r}+\frac{Q^2}{r^2}\right)\frac{q^2}{r^2}}}{1-\frac{2m}{r}+\frac{Q^2}{r^2}} \tag{3.61}$$

We use this result to decouple the inverse equation $d\lambda/dr$. This allows us to work with the inverse equations where we can perform a series expansion around $r \to \infty$, integrate and inverse the series. This procedure yields

$$r(\lambda) = r_\infty + \lambda + \frac{q^2}{2\lambda} - \frac{mq^2}{2\lambda^2} + \frac{\left(4Q^2-3q^2\right)q^2}{24\lambda^3} + \mathcal{O}\left(\lambda^{-4}\right), \tag{3.62}$$

where r_∞ is the integration constant, which we can set to zero by λ reparametrisation. We can then use Eq. (3.62) to solve (3.58), (3.59) and (3.61) around $\mathcal{I}^+$. We get

$$\begin{aligned} t(\lambda) = t_\infty + \lambda + 2m\log\frac{\lambda}{2m} + \frac{Q^2-4m^2}{\lambda} - \frac{m(8m^2-q^2-4Q^2)}{2\lambda^2} \\ - \frac{16m^4+Q^2(q^2+Q^2)-3m^2(q^2+4Q^2)}{3\lambda^3} + \mathcal{O}\left(\lambda^{-4}\right) \end{aligned} \tag{3.63}$$

$$\phi(\lambda) = \phi_\infty - \frac{q}{\lambda} + \frac{q^3}{3\lambda^3} + \mathcal{O}\left(\lambda^{-4}\right) \tag{3.64}$$

$$p_r(\lambda) = 1 + \frac{2m}{\lambda} + \frac{8m^2-q^2-2Q^2}{2\lambda^2} + \frac{m\left(8m^2-q^2-4Q^2\right)}{\lambda^3} + \mathcal{O}\left(\lambda^{-4}\right) \tag{3.65}$$

where the integration constants t_∞ and ϕ_∞ can be set to zero without loss of generality by shifting the time origin and orientation of the null plane.

Now that we have determined all the integration constants needed for our computation, we can solve numerically the set of coupled differential equations in Eqs. (3.57), (3.58), (3.59) and (3.60). Solving these equations yields to three independent functions, namely $t(\lambda)$, $r(\lambda)$ and $\phi(\lambda)$, which means that all the information about the merger can be summarized in a three-dimensional plot[11]. For convenience we plot the evolution of the generators of the event horizon during the merger in the (x, z, t) space, where x and z are the Cartesian-like coordinates introduced in (3.13). The results are shown in Fig. 3.4 for the regular case $|Q| = 4/5\, m$, and in Fig. 3.5 for the extremal case $|Q| = m$, while in Fig. 3.6 we show constant-time slices of these two plots, showing the evolution of the merger.

[11] Note that the parameter λ is physically irrelevant and moreover $p_r(\lambda)$ can be computed from $r(\lambda)$ using Eq. (3.61)

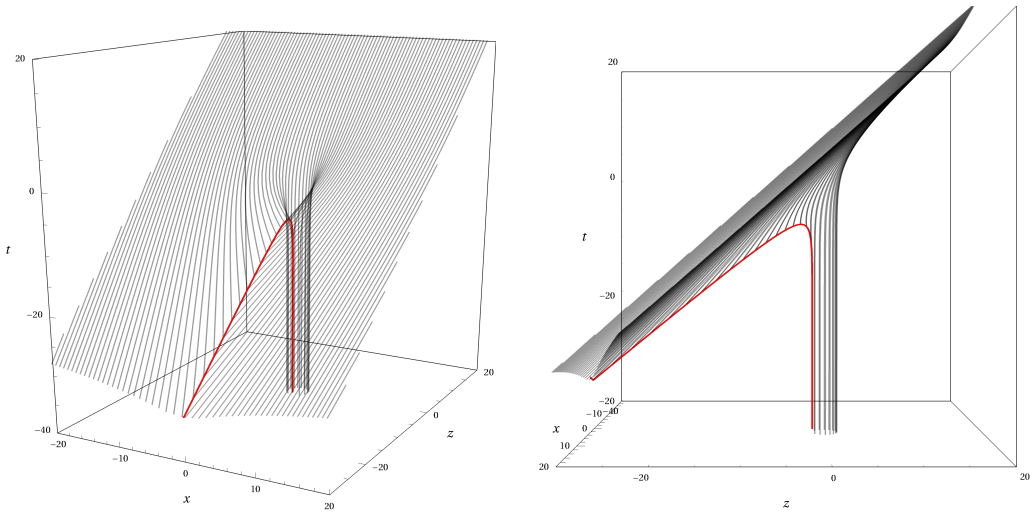

(a) (b)

Figure 3.4: Event horizon in a merger of a supermassive black hole with a charged black hole of $|Q| = 4/5\,m$. The red curve represents the caustic line. The axes are measured in units of m.

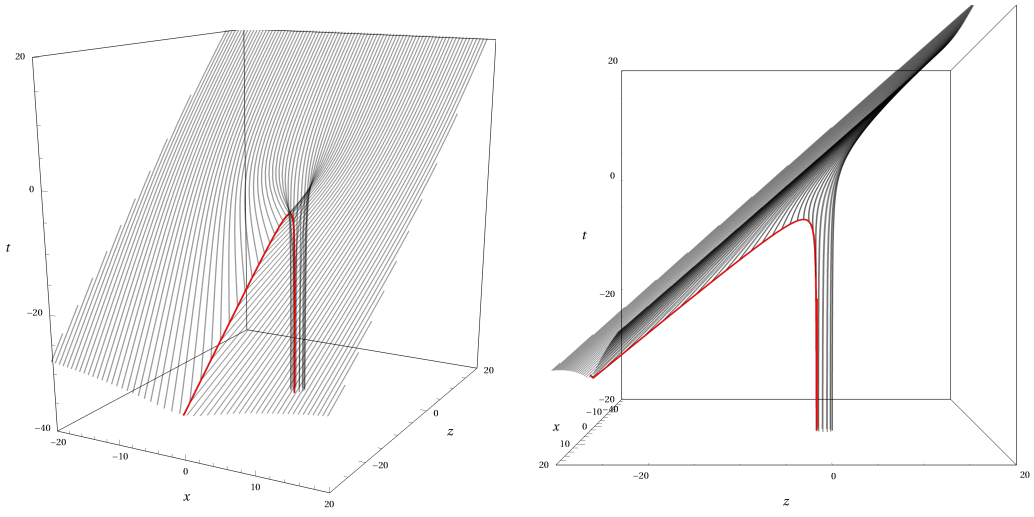

(a) (b)

Figure 3.5: Event horizon in a merger of a supermassive black hole with an extremal charged black hole of $|Q| = m$. The red curve represents the caustic line. The axes are measured in units of m.

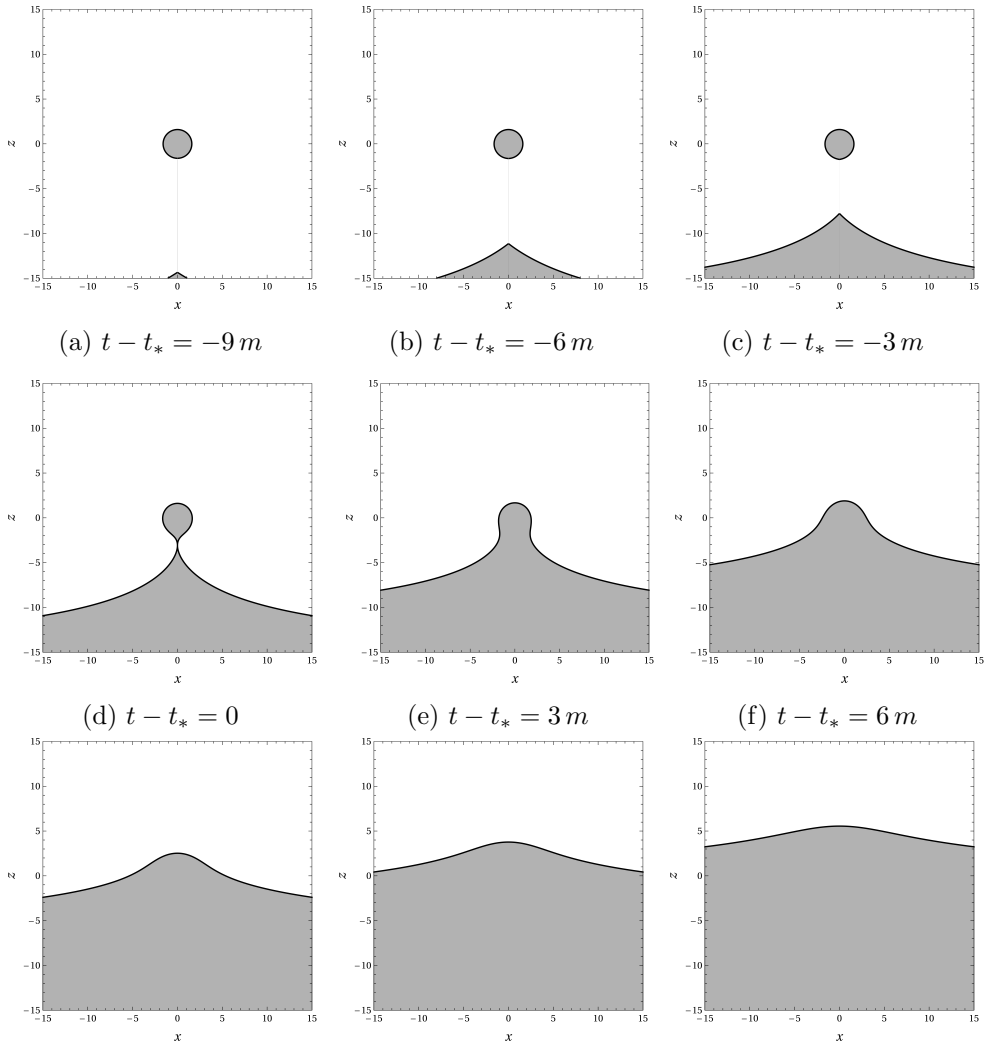

(a) $t - t_* = -9\,m$ (b) $t - t_* = -6\,m$ (c) $t - t_* = -3\,m$

(d) $t - t_* = 0$ (e) $t - t_* = 3\,m$ (f) $t - t_* = 6\,m$

(g) $t - t_* = 9\,m$ (h) $t - t_* = 12\,m$ (i) $t - t_* = 15\,m$

Figure 3.6: Constant-time slices of the event horizon in a merger of a supermassive black hole (down) with a charged black hole of $|Q| = 4/5m$ (centre) in the latter's centre-of-mass reference frame. The event horizon is plotted with a black line, the grey area represents the inside of the black holes. The axes are measured in units of m. The time slices are taken at regular time intervals.

Finally we can also compute the same parameters characterizing the merger that we obtained with the analytical procedure in Eqs. (3.41), (3.46), (3.47) and (3.55). With the numerical approach, in the regular case where the RN black hole as a charge fixed to $|Q| = 4/5\, m$, we find

$$q_c = 3.73m, \quad r_* = 3.07m, \quad q_* = 4.76m, \quad t_* = -8.12m, \tag{3.66}$$

while in the extremal case where $|Q| = m$ we have

$$q_c = 2.71m, \quad r_* = 2.71m, \quad q_* = 4.30m, \quad t_* = -7.57m. \tag{3.67}$$

The two methods agree as expected, with very small discrepancies of the order $\mathcal{O}(0.01m)$.

3.1.3 Generalisation to $D > 4$ dimensions

The numerical procedure we introduced in the previous section allows us to generalise our analysis to more general setups for the binary system, including the case where the merger happens in $D > 4$ dimensions. Note that it only makes sense to analyse our problem in $D \geq 4$ since in lower dimensions black holes, without a cosmological constant, do not exist. Here we analyse the merger in dimensions higher than 4 since string theory or holographic models, such as the AdS/CFT correspondence [292], work in dimension higher than 4. Moreover the study of the problem in generic D dimensions allow us to understand which properties are characteristic of General Relativity and which one are due to the choice $D = 4$.

In generic D dimensions, the metric of a RN black hole is formally the same as the one defined in Eq. (3.7), where the function $\Delta(r)$ has now the following form

$$\Delta(r) = 1 - \frac{2m}{r^{D-3}} + \frac{Q^2}{r^{2(D-3)}} \tag{3.68}$$

As we did in the $D = 4$ case, we now need the asymptotic conditions to be able to integrate the equations of motion, however it is not possible to find these integration constants in generic D dimensions. What we can do instead is to perform the asymptotic expansion for each fixed value of D. Just to give an illustrative example, from now on we will work in $D = 5$ dimensions, where we can write the asymptotic conditions at $\mathcal{I}^+$ as

$$r(\lambda) = \lambda + \frac{q^2}{2\lambda} - \frac{mq^2}{2\lambda^2} + \frac{\left(4Q^2 - 3q^2\right) q^2}{24\lambda^3} + \mathcal{O}\left(\lambda^{-4}\right) \tag{3.69}$$

$$t(\lambda) = \lambda + \frac{Q^2}{\lambda} - \frac{2m + Q^2\left(q^2 + Q^2\right)}{3\lambda^3} + \mathcal{O}\left(\lambda^{-4}\right) \tag{3.70}$$

$$\phi(\lambda) = -\frac{q}{\lambda} + \frac{q^3}{3\lambda^3} + \mathcal{O}\left(\lambda^{-4}\right) \tag{3.71}$$

$$p_r(\lambda) = 1 + \frac{4m - q^2}{2\lambda^2} + \mathcal{O}\left(\lambda^{-4}\right) \tag{3.72}$$

With these asymptotic conditions we can solve the equations of motion introduced in Eqs. (3.57), (3.58), (3.59) and (3.60) by following the same procedure enlightened in the $D = 4$ case, but this time using for $\Delta(r)$ the definition in Eq. (3.68). In Figs. 3.7 and 3.8 we show our results for $D = 5$ and for a fixed value of the charge of the small black hole which, coherently with our previous analysis, we choose to be $|Q| = 4/5\, m$.

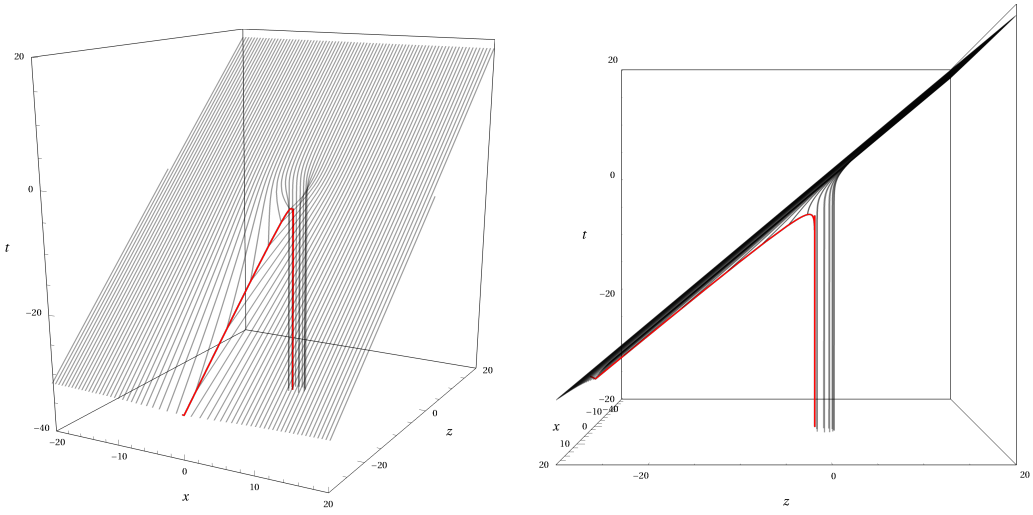

Figure 3.7: Event horizon in a merger of a supermassive black hole with a charged black hole of $|Q| = 4/5\, m$ in $D = 5$ dimensions. The red curve represents the caustic line. The axes are measured in units of m.

Finally, for completeness, we also compute the parameters characterizing the merger in $D = 5$ dimensions and for a charged black hole with charge $|Q| = 4/5\, m$. They read

$$q_c^{D=5} = 2.50\, m, \quad r_*^{D=5} = 1.98\, m, \quad D = 5_*^D = 2.72\, m, \quad \Delta_*^{D=5} = 6.26\, m. \tag{3.73}$$

By comparing these results with the ones obtained in $D = 4$ dimensions we can notice two main differences: the first one is that in $D = 5$ the small black hole is less distorted during the merger, as can be seen from $r_*^{D=5} < r_*$, while the second one is the relation $\Delta_*^{D=5} < \Delta_*$ which implies a shorter merger time in higher dimensions. This can be explained by looking at the expression in generic D dimensions for $\Delta(r)$ in (3.68). In particular the higher the dimensions the steeper becomes the r-dependence and thus the timescale and the length scale for decaying become much shorter in $D > 4$ dimensions. Along these lines we can also explain the relations $q_*^{D=5} < q_*$ and $q_c^{D=5} < q_c$. One final comment worth making is that the parameters $(q_c, q_*, r_*, \Delta_*)$ characterizing the merger become smaller and smaller as the number of dimensions

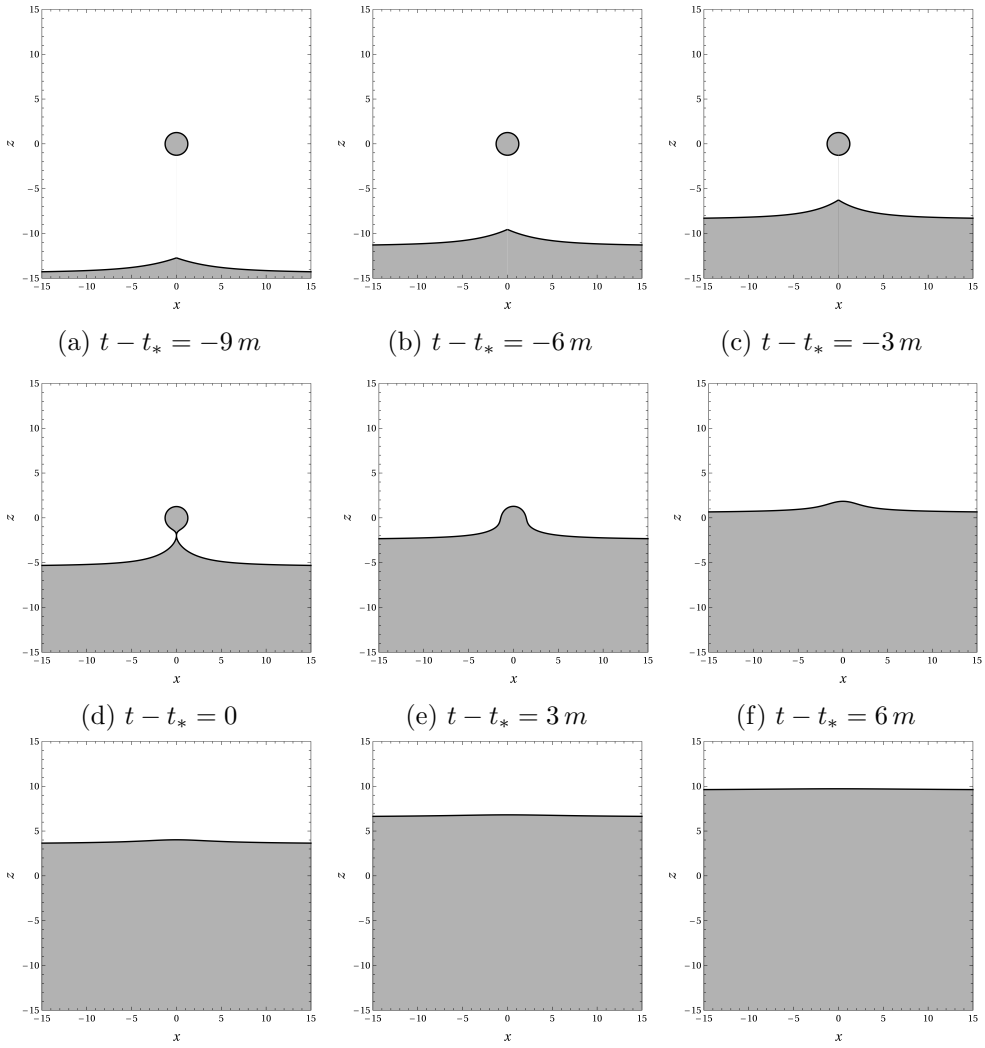

(a) $t - t_* = -9\,m$ (b) $t - t_* = -6\,m$ (c) $t - t_* = -3\,m$

(d) $t - t_* = 0$ (e) $t - t_* = 3\,m$ (f) $t - t_* = 6\,m$

(g) $t - t_* = 9\,m$ (h) $t - t_* = 12\,m$ (i) $t - t_* = 15\,m$

Figure 3.8: Constant-time slices of the event horizon in a merger of a supermassive black hole (down) with a charged black hole of $|Q| = 4/5m$ (centre) in the latter's centre-of-mass reference frame and in $D = 5$ dimensions. The event horizon is plotted with a black line, the grey area represents the inside of the black holes. The axes are measured in units of m. The time slices are taken at regular time intervals.

increases. More precisely they are monotonously decreasing functions of D and they asymptotically approach zero as D goes to infinity.

3.2 Tidal effects on charged binaries

In this section we analyse how the dynamics of a test particle moving around a RN black hole is affected by the presence of an external tidal field. We will follow the same procedure enlightened in Chapter 2, where we studied the motion of a test particle around a Schwarzschild black hole in the proximity of a supermassive Kerr black hole, but this time the primary companion in the inner EMRI will be a charged black hole instead of a neutral one. Our goal is to first write down the metric for a tidally deformed RN black hole and second to analyse how the presence of the charge can alter the effects of the tidal fields on the dynamics of the test particle. We will not specify the source of the tidal fields, keeping our computation completely general in terms of tidal multipole moments, up to the quadrupole order in their expansion. Just to give an example, the tidal field could be generated by a supermassive Kerr black hole around which the EMRI system with a charged black hole and a test particle is orbiting. See Fig. 3.9 for a graphical representation of this setup.

The effects of tidal fields on a RN black hole have been recently studied in the context of Tidal Love numbers [293–295] and in higher dimensions than 4 [296, 297].

Throughout this section we will work in geometric units, i.e. $G = c = 1$.

3.2.1 Tides on Reissner–Nordström Black Holes

The first step in our analysis is to compute the metric of a tidally deformed RN black hole. The spacetime around a spherically symmetric, asymptotically flat charged black hole, solution of the Einstein - Maxwell theory, is the one already pointed out in Eq. (3.7), which here we rewrite for convenience as

$$\begin{aligned} ds^2 &= -f(r)dt^2 + \frac{dr^2}{f(r)} + r^2 d\Omega^2\,, \quad f(r) = 1 - \frac{2M}{r} + \frac{\mathcal{Q}^2}{r^2}\,, \\ \mathcal{F} &= -\frac{Q}{r^2} dt \wedge dr + P\epsilon\,, \end{aligned} \tag{3.74}$$

where we introduced the Maxwell field strength $\mathcal{F}$, M is the mass of the black hole while $d\Omega^2$ and ϵ represent, respectively, the metric and the volume form of the 2-sphere, which in generic coordinates z^A (with $A = 1, 2$) and spherical coordinates (θ, ϕ) take the following expressions

$$d\Omega^2 = \Omega_{AB} dz^A dz^B = d\theta^2 + \sin^2\theta d\phi^2\,, \quad \epsilon = \frac{1}{2!}\epsilon_{AB} dz^A \wedge dz^B = \sin\theta d\theta \wedge d\phi\,. \tag{3.75}$$

Finally in (3.74), we also introduced the electric charge Q, magnetic charge P, and "total" charge $\mathcal{Q}$, which are defined by

$$Q = \frac{1}{4\pi}\int_{S^2} \star F\,, \quad P = \frac{1}{4\pi}\int_{S^2} F\,, \quad \mathcal{Q} = \sqrt{Q^2 + P^2}\,, \tag{3.76}$$

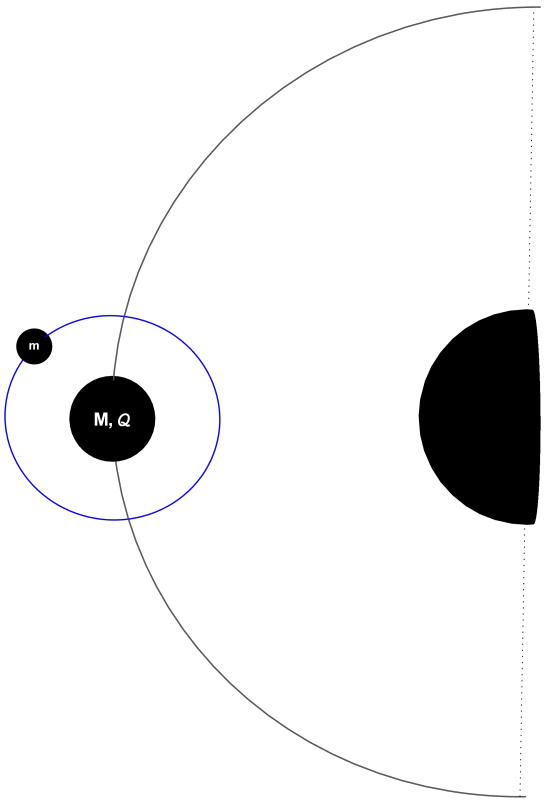

Figure 3.9: Graphical representation of a hierarchical triple system with a test particle m orbiting around a RN black hole of mass M and charge $\mathcal{Q}$.

where S^2 is any 2-sphere enclosing the hole. For completeness we also recall that in the RN geometry two Killing horizons are present, namely

$$r_\pm = M \pm \sqrt{M^2 - Q^2 - P^2}, \tag{3.77}$$

where under the assumption $M^2 \geq Q^2 + P^2$, r_+ corresponds to the event horizon of the black hole while r_- to a Cauchy horizon.

Moreover to compute the metric of a tidally deformed RN black hole we will work with advanced Eddington–Finkelstein (EF) coordinates (v, r, θ, ϕ), where

$$dv = dt + \frac{dr}{f(r)}\,. \tag{3.78}$$

This set of coordinates is regular at both horizons $r_\pm$ and allows us to work in the *light-cone gauge*, which is convenient in the computation of the metric according to Appendix C and Ref. [70].

3.2.2 Stationary Gravitational Tides

The metric of a tidally deformed RN black hole in the presence of a stationary tidal source can be written as

$$g_{\mu\nu} = g^{\rm RN}_{\mu\nu} + h_{\mu\nu}\,, \quad \mathcal{F}_{\mu\nu} = \mathcal{F}^{\rm RN}_{\mu\nu} + \delta\mathcal{F}_{\mu\nu}\,, \tag{3.79}$$

where $(g^{\rm RN}_{\mu\nu}, \mathcal{F}^{\rm RN}_{\mu\nu})$ is the unperturbed RN solution while $(h_{\mu\nu}, \delta\mathcal{F}_{\mu\nu})$ is a stationary solution to the linearised Einstein–Maxwell equations. Note that even if we consider a neutral source for the tidal fields, the strength of the Maxwell field would still be excited with $\delta\mathcal{F}_{\mu\nu}$ since the background spacetime is charged.

The metric for a tidally deformed RN black hole can be derived by following the steps presented in Ref. [77], which we refer the reader to for more details. Here for the purpose of this thesis, we are only interested in the final result which, in Schwarzschild coordinates and in the Regge–Wheeler gauge, can be written as

$$\begin{aligned} h = {} & \mathcal{X}_{\ell m}(r) Y^{\ell m} \left(dt \otimes dt + \frac{dr \otimes dr}{f(r)^2} \right) + r^2 \mathcal{U}_{\ell m}(r) Y^{\ell m} d\Omega^2 \\ & + r^2 \mathcal{V}_{\ell m}(r) \left(dt \otimes X^{\ell m} + X^{\ell m} \otimes dt \right)\,, \end{aligned} \tag{3.80}$$

$$\begin{aligned} \delta\mathcal{F} = {} & \left(Q \frac{\mathcal{U}_{\ell m}(r)}{r^2} - \frac{\mathcal{E}_{\ell m}(r)}{r^2} \right) Y^{\ell m} dt \wedge dr + \left(P \mathcal{V}_{\ell m}(r) - \frac{f(r)}{\ell(\ell+1)} \frac{d\mathcal{E}_{\ell m}(r)}{dr} \right) dt \wedge Z^{\ell m} \\ & + \frac{f(r)}{\ell(\ell+1)} \frac{d\mathcal{B}_{\ell m}(r)}{dr} dr \wedge X^{\ell m} + \mathcal{B}_{\ell m}(r) Y^{\ell m} \epsilon\,, \end{aligned} \tag{3.81}$$

where here we introduced the usual spherical harmonics $Y^{\ell m}$ and the associated even and odd vector harmonics $Z^{\ell m}_A = D_A Y^{\ell m}$ and $X^{\ell m}_A = \epsilon_{AB} D^B Y^{\ell m}$, where D_A denotes the covariant derivative on the 2-sphere. Moreover we also introduced the functions [12]

$$\mathcal{E}_{\ell m}(r) \equiv Q \Phi^+_{\ell m}(r) + P \Phi^-_{\ell m}(r)\,, \quad \mathcal{B}_{\ell m}(r) \equiv P \Phi^+_{\ell m}(r) - Q \Phi^-_{\ell m}(r)\,. \tag{3.82}$$

The radial functions $\mathcal{X}_{\ell m}(r), \mathcal{U}_{\ell m}(r), \mathcal{V}_{\ell m}(r)$ and $\Phi^\pm_{\ell m}(r)$ appearing in Eqs. (3.80)-(3.81) can be written as finite power series in r, namely

$$\mathcal{X}_{\ell m}(r) = r^\ell \sum_{n=0}^{\ell+3} a^\ell_n r^{-n}\,, \quad \mathcal{U}_{\ell m}(r) = r^\ell \sum_{n=0}^{\ell+1} b^\ell_n r^{-n}\,, \quad \Phi^+_{\ell m}(r) = r^\ell \sum_{n=0}^{\ell} c^\ell_n r^{-n}\,, \tag{3.83}$$

[12] For completeness we mention that in comparison with Ref. [77], here for convenience Φ^+ and Φ^- are defined with an extra multiplicative factor given by $1/(2\mathcal{Q}^2)$ and $i/(2\mathcal{Q}^2)$ respectively.

$$\mathcal{V}_{\ell m}(r) = r^{\ell-1}\sum_{n=0}^{2\ell} d_n^\ell r^{-n}\,, \quad \Phi^-_{\ell m}(r) = r^{\ell}\sum_{n=0}^{\ell+1} e_n^\ell r^{-n}\,, \tag{3.84}$$

where the constant coefficients $a_n^\ell, b_n^\ell, c_n^\ell, d_n^\ell, e_n^\ell$ can be obtained immediately from the equations of motion. In Appendix D we show some of them explicitly as an example. Notice that the two sets of functions $\{\mathcal{V}_{\ell m}(r), \Phi^-_{\ell m}(r)\}$ and $\{\mathcal{X}_{\ell m}(r), \mathcal{U}_{\ell m}(r), \Phi^+_{\ell m}(r)\}$ are independent from each other and they represent, respectively, the generalised odd and the even sectors of the fluctuations [13], using Ref. [77] formalism. Moreover in order to extract the solutions in Eqs. (3.80) and (3.81), we choose the boundary conditions in such a way that fluctuations are regular at the horizon, while at infinity we assume that the electromagnetic master variables $\Phi^\pm_{\ell m}$ grow as $\sim r^\ell$. In general the latter variables would evolve as $\Phi^\pm_{\ell m} \sim r^{\ell+1}$, but since here we are only interested in purely gravitational tides (thus neglecting the electromagnetic ones), we assume that at infinity they grow slower, namely $\Phi^\pm_{\ell m} \sim r^\ell$ (see Refs. [293, 295, 296] for a similar analysis). These boundary conditions allow us to identify uniquely the solutions (3.80) and (3.81), up to a global amplitude per sector which is usually determined by matching them with the source of the tidal fields. Finally it is worth mentioning that since we are only considering gravitational tides, if the charge $\mathcal{Q}$ of the RN black hole vanishes, then $\delta\mathcal{F} = 0$ as expected. Moreover the dipolar $\ell = 1$ degrees of freedom of the tidal contribution are not present in our solutions since they are completely related to the electromagnetic sector of the tides and here in this analysis we focus, again, only on the gravitational contribution.

To apply this formalism in the analysis of the dynamics of a charged EMRI system in a tidal environment, we will restrict ourselves only to the case of an electrically charged black hole, focusing only on the quadrupolar modes $\ell = 2$ of the tidal fields. Moreover we will follow Refs. [70, 77] to write the solutions presented in Eqs. (3.80) and (3.81) in terms of multipole tidal moments and in the light-cone gauge, this yields to the following non-vanishing components of the tidal fluctuations

$$\begin{aligned} h_{vv} &= -r^2 f^2 \mathcal{E}^{\mathsf{q}}\,, \\ h_{vA} &= -\frac{2}{3} r^3 f \left(\mathcal{E}^{\mathsf{q}}_A - \mathcal{B}^{\mathsf{q}}_A\right)\,, \\ h_{AB} &= -\frac{1}{3} r^2 \left(Q^2 + r^2 - 2M^2\right)\mathcal{E}^{\mathsf{q}}_{AB} + \frac{r^2}{3}\left(r^2 - r_+^2\right)\mathcal{B}^{\mathsf{q}}_{AB}\,, \end{aligned} \tag{3.85}$$

[13] In general, for a non-vanishing magnetic charge $P \neq 0$, the traditional even and odd sectors would mix, see Ref. [298] for a more general discussion.

and

$$\begin{aligned}
\delta\mathcal{F}_{vr} &= \frac{Q}{2r^2}(r^2-Q^2)\mathcal{E}^{\mathfrak{q}}\,,\\
\delta\mathcal{F}_{vA} &= Qrf\mathcal{E}^{\mathfrak{q}}_{A}\,,\\
\delta\mathcal{F}_{rA} &= -\frac{r}{3}Q\left(\mathcal{E}^{\mathfrak{q}}_{A}-\mathcal{B}^{\mathfrak{q}}_{A}\right)\,,\\
\delta\mathcal{F}_{AB} &= \frac{Q}{2}\left(r^2-Q^2\right)\mathcal{B}^{\mathfrak{q}}\epsilon_{AB}\,,
\end{aligned} \tag{3.86}$$

where $\mathcal{E}^{\mathfrak{q}}, \mathcal{E}^{\mathfrak{q}}_{A}, \mathcal{E}^{\mathfrak{q}}_{AB}$ and $\mathcal{B}^{\mathfrak{q}}, \mathcal{B}^{\mathfrak{q}}_{A}, \mathcal{B}^{\mathfrak{q}}_{AB}$ are the electric and magnetic tidal multipole potentials as introduced in [70]. The solutions presented in Eqs. (3.85) and (3.86) represent the tidal contributions to the metric of a deformed RN black hole and, together with the metric (3.74), they describe the spacetime where the test particle in the EMRI system is moving.

3.2.3 Secular Dynamics

Here we analyse the dynamics of a test particle moving in a RN deformed spacetime, which is given by (at the quadrupolar order in the tides' modes), by the usual RN background (3.74) plus the tidal corrections defined in Eq. (3.85). We will neglect the contribution of the self-force by assuming that the ratio between the mass m of the test particle and the mass M of the charged black hole is small enough, namely $m/M \ll 1$, allowing us to describe the motion of the test particle with the geodesic equations. Moreover, in order to treat the presence of the tidal environment as a small perturbation on the dynamics of the EMRI system, we also implement the small-tide approximation introduced in Eq. (1.55), which here we recall for convenience

$$\frac{M}{\mathcal{R}} \ll 1, \tag{3.87}$$

where $\mathcal{R}$ represents the radius of the curvature of the spacetime on the position of the binary system. Finally we recall that we will consider only an electrically charged black hole, where in this case the tidal perturbations of the spacetime metric are exactly given by Eqs. (3.85) and (3.86).

Secular Hamiltonian of the test particle

The first step to study the dynamics of a test particle moving in a deformed RN spacetime is to introduce the Hamiltonian describing the EMRI system, which can be written as[14]

$$H = \frac{1}{2}\bar{u}_\mu\bar{u}^\mu + \bar{u}_\mu u^\mu_{(1)} + \frac{1}{2}\bar{u}^\mu\bar{u}^\nu h_{\mu\nu}\,. \tag{3.88}$$

Here we introduced the four-velocity of the test particle, defined as

$$u^\mu = \bar{u}^\mu + u^\mu_{(1)}\,, \tag{3.89}$$

[14]Indexes are lowered and raised with the unperturbed RN metric.

where $\bar{u}^\mu$ is tangent to a geodesic of the unperturbed background, and $u^\mu_{(1)}$ is a correction due to the tidal deformation $\sim h_{\mu\nu}$. In our computation we will consider circular unperturbed orbits, which are described by $\bar{u}^\mu$. The explicit expression for the unperturbed component of the four-velocity, in the case of a circular and equatorial orbit, can be written as

$$\bar{u}^\mu = \left(\frac{\bar{E}}{f}, 0, 0, \frac{\bar{L}}{r^2}\right), \quad \bar{u}^\mu = \left(\frac{\bar{E} - \frac{qQ}{mr}}{f}, 0, 0, \frac{\bar{L}}{r^2}\right), \tag{3.90}$$

where the left one describes the case of a neutral test particle while the right one depicts the scenario of a charged test particle, where q and m represent respectively its charge and mass while the constants $\bar{E}$ and $\bar{L}$ denote the specific energy and angular momentum. In the presence of an external tidal field the unperturbed orbits get deformed and, in general, they are no longer circular. As a result the trajectories in the full spacetime, i.e. the unperturbed RN background plus the tidal environment, can be written as a mean circular orbit plus some small oscillatory corrections [72]. Here we are interested in studying the secular effects induced by the tidal environment on the dynamics of the test particle, thus we focus our analysis on the mean circular part of the orbits in the perturbed spacetime. This is done by integrating out the oscillatory terms in the full trajectories by using the secular averaging procedure, which we recall that for a mean circular orbit γ and a arbitrary quantity $\mathcal{A}$ can be written as

$$\langle \mathcal{A} \rangle \equiv \frac{1}{2\pi} \int_0^{2\pi} \mathcal{A} \,|_\gamma \, d\phi \,. \tag{3.91}$$

With this formalism, we can compute the secular Hamiltonian describing the EMRI system by applying this averaging procedure to the expression in Eq. (3.88). In the case of a neutral test particle this yields to

$$\langle H \rangle = -\frac{1}{2}\left(\frac{\langle E \rangle^2}{f} - \frac{\langle L \rangle^2}{r^2}\right) - \eta \left[\langle E \rangle^2 + f\frac{\langle L \rangle^2}{r^2}\right]\frac{r^2}{M^2}\,, \tag{3.92}$$

where $E \equiv -u \cdot \partial_t$ and $L \equiv u \cdot \partial_\phi$ denote the specific energy and angular momentum of the trajectory, η is an effective perturbative parameter proportional to the mean amplitude of the tidal field $\langle \mathcal{E}^q \rangle$, defined as

$$\eta = -\frac{M^2}{2}\langle \mathcal{E}^q \rangle, \tag{3.93}$$

[15]

and we used that, form the solution (3.85), the metric components average to

$$\langle h_{vv} \rangle = -r^2 f^2 \langle \mathcal{E}^{\mathrm{q}} \rangle \,, \quad \langle h_{v\phi} \rangle = 0, \quad \langle h_{\phi\phi} \rangle = -r^4 f \langle \mathcal{E}^{\mathrm{q}} \rangle \,. \tag{3.94}$$

[15] Note that this is the same definition provided in Eq. (2.50), but here we keep it completely general without specifying the source of the tidal environment.

For a charged test particle instead, the averaged Hamiltonian takes the following form

$$\langle H\rangle = -\frac{1}{2}\left(\frac{\left(\frac{\tilde{q}Q}{r}-\langle E\rangle\right)^2}{f}-\frac{\langle L\rangle^2}{r^2}\right)-\eta\left[\left(\frac{\tilde{q}Q}{r}-\langle E\rangle\right)^2+f\frac{\langle L\rangle^2}{r^2}\right]\frac{r^2}{M^2}, \quad (3.95)$$

where we introduced, for later convenience, the charge-to-mass ratio $\tilde{q}=q/m$ for the test particle.

In what follows we will use the secular or averaged Hamiltonians defined in Eqs. (3.92) and (3.95) to compute how the ISCO and the light ring of the RN black hole are deformed by the presence of an external tidal field, in both cases of a neutral and charged test particle. We remind the reader that these two orbits are key elements in the propagation of matter, light and gravity in the vicinity of a black hole.

3.2.4 Tidal Effects on the ISCO and the Light Ring - Neutral Test Particle

We start by considering the case of a neutral test particle orbiting around the tidally deformed RN black hole. We recall that the mean ISCO is characterized by the following conditions in terms of the secular Hamiltonian (3.92) [215]

$$\langle H\rangle|_{r=r_{\rm ISCO}} = -\frac{1}{2}\ , \quad \left.\frac{d\langle H\rangle}{dr}\right|_{r=r_{\rm ISCO}} = 0\ , \quad \left.\frac{\partial^2\langle H\rangle}{\partial r^2}\right|_{r=r_{\rm ISCO}} = 0\ . \quad (3.96)$$

Given that the RN black hole is immersed in a tidal environment, the parameters characterizing the ISCO should be given by their usual unperturbed values plus a small deviation proportional to the mean amplitude of the tidal field $\sim\eta$, namely the radial coordinate, the energy and the angular momentum of the ISCO can be written as

$$r_{\rm ISCO}\simeq r_0+\eta\, r_1\,, \qquad L_{\rm ISCO}\simeq L_0+\eta\, L_1\,, \qquad E_{\rm ISCO}\simeq E_0+\eta\, E_1\,, \quad (3.97)$$

where (r_0, E_0, L_0) denote the unperturbed ISCO parameters, and attempt to solve (3.96) for the deformations (r_1, E_1, L_1). For completeness, we also recall that the ISCO's orbital frequency can be written as [72, 214]

$$\Omega^2=\left(\frac{u^\phi}{u^t}\right)^2=\frac{1}{2r^2}\left[\frac{2M}{r}-(r-3M)\,u^\mu u^\nu\partial_r\langle h_{\mu\nu}\rangle\right]\ , \quad (3.98)$$

and search for solutions of the form

$$\Omega_{\rm ISCO}\simeq\Omega_0+\eta\ \Omega_1\,. \quad (3.99)$$

The unpertubed values for the ISCO's parameters can be obtained by solving (3.96) at zeroth order in η. In terms of the mass and charge of the RN black hole, they can be written as

$$\begin{aligned} r_0 &= 2M + \left(\frac{\mathcal{W}}{M}\right)^{1/3} + \left(\frac{M}{\mathcal{W}}\right)^{1/3}(4M^2 - 3Q^2)\,, \\ L_0 &= r_0\sqrt{\frac{Mr_0 - Q^2}{r_0^2 - 3Mr_0 + 2Q^2}}\,, \\ E_0 &= \frac{r_0^2 - 2Mr_0 + Q^2}{r_0\sqrt{r_0^2 - 3Mr_0 + 2Q^2}}\,, \\ \Omega_0 &= \frac{\sqrt{Mr_0 - Q^2}}{r_0^2}\,, \end{aligned} \tag{3.100}$$

where we introduced the quantity

$$\mathcal{W} = \left(8\,M^4 - 9\,M^2Q^2 + 2\,Q^4 + Q^2\sqrt{5\,M^4 - 9\,M^2Q^2 + 4\,Q^4}\right). \tag{3.101}$$

These are the usual known values characterizing the ISCO of a charged black hole [299–302]. By solving the ISCO conditions presented in Eq (3.96) at the first order in η, we can find analogous expressions also for the tidal corrections $(r_1, E_1, L_1, \Omega_1)$, which can be written as

$$\begin{aligned} r_1 &= \frac{2r_0^2(r_0^2 - 2Mr_0 + Q^2)}{M^2C}\Big(2M^3\left(44Q^2r_0^2 + 63r_0^4\right) - M^2\left(52Q^4r_0 + 199Q^2r_0^3 + 101r_0^5\right) \\ &\quad - 48M^4r_0^3 + M\left(10Q^6 + 99Q^4r_0^2 + 111Q^2r_0^4 + 34r_0^6\right) - 4\left(4Q^6r_0 + 7Q^4r_0^3 + 5Q^2r_0^5 + r_0^7\right)\Big)\,, \\ L_1 &= \frac{1}{2M^2\sqrt{Mr_0 - Q^2}(r_0^2 - 3Mr_0 + 2Q^2))^{3/2}}\Big(6M^4r_0^2(2r_0 - r_1) \\ &\quad + M^3r_0\left(Q^2(9r_1 - 20r_0) + r_0^2(4r_0 + r_1)\right) + 2M^2\left(Q^4(4r_0 - 2r_1) - 5Q^2r_0^3 - 9r_0^5\right) \\ &\quad + 2M\left(6Q^4r_0^2 + 9Q^2r_0^4 + 5r_0^6\right) - 2r_0\left(Q^2 + r_0^2\right)\left(2Q^4 + Q^2r_0^2 + r_0^4\right)\Big)\,, \\ E_1 &= -\frac{1}{2M^2r_0^2\left(r_0^2 - 3Mr_0 + 2Q^2\right)^{3/2}}\Big(M^2r_1\left(Mr_0^2(6M - r_0) + 4Q^4 - 9MQ^2r_0\right) \\ &\quad + 2r_0\left(r_0^2 - 2Mr_0 + Q^2\right)\left(r_0^2\left(8M^2 - 7Mr_0 + 2r_0^2\right) + Q^2r_0(3r_0 - 8M) + 2Q^4\right)\Big)\,, \\ \Omega_1 &= \frac{4M^2Q^2(r_1 - r_0) + M^3r_0(4r_0 - 3r_1) - 6MQ^2r_0^2 + 4Q^2r_0^3 + 4Q^4r_0 - 2r_0^5}{2M^2r_0^3\sqrt{Mr_0 - Q^2}}\,, \end{aligned} \tag{3.102}$$

where, for the ease of notation, all the expressions are written in terms of r_0 given in Eq. (3.100) and some expressions are implicitly given in terms of r_1.

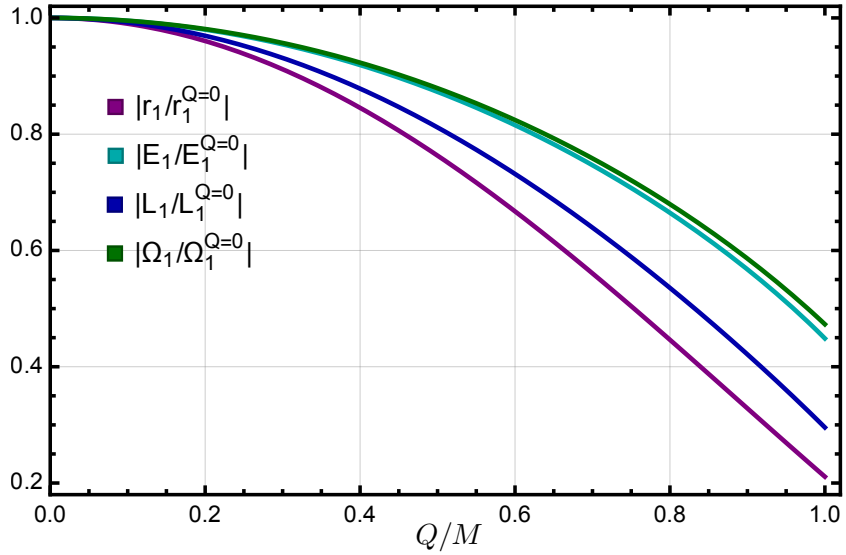

Figure 3.10: Tidal corrections to the ISCO's position, energy, angular momentum and orbital frequency as a function of the black hole's charge-to-mass ratio Q/M. We represent the absolute value of the tidal correction normalised to their value in the case that the black hole is neutral.

Moreover we defined

$$C = Q^4 r_0^2 \left(179 M r_0 - 222 M^2 - 24 r_0^2\right) + 6 Q^6 r_0 (17 M - 8 r_0) - 16 Q^8 + 12 M Q^2 r_0^3 \left(17 M^2 - 18 M r_0 + 4 r_0^2\right) + M r_0^4 \left(96 M^2 r_0 - 72 M^3 - 34 M r_0^2 + 3 r_0^3\right). \tag{3.103}$$

However, since their expressions are not very illuminating, we prefer to represent them in Fig. 3.10 as a function of the charge-to-mass ratio Q/M of the RN black hole. From our results we can see that the magnitude of all the tidal corrections decreases as the charge of the black hole grows larger. This is exactly what we could have guessed from the beginning since as the charge increases, the throat of the black hole elongates dragging the ISCO closer to its center, washing away the tidal effects induced by an external field. It is particularly interesting to notice that the tidal corrections reach their minimum values in the extremal limit $Q/M = 1$, where the throat of the black hole becomes infinitely long and they read

$$r_1 = 648 M, \quad L_1 = -126\sqrt{2} M, \quad E_1 = -\sqrt{\frac{3}{2}}\frac{105}{4}, \quad \Omega_1 = -\frac{73\sqrt{3}}{4M}. \tag{3.104}$$

Thus, in our analysis, we have found that the tidal corrections induced by the external environment on the ISCO of a RN black hole are suppressed as the charge approaches extremality (as expected), but in the extremal limit they do not vanish and they converge to finite values.

Next we carry out a similar analysis for the light ring of the RN black hole, which is defined by its position $r_{\rm LR}$ and impact parameter $b_{\rm LR} = L/E$. These two parameters can be found by using the averaged Hamiltonian (3.92) and by solving the following conditions [303, 304]

$$\langle H\rangle|_{r=r_{\rm LR}} = 0\ , \quad \left.\frac{d\langle H\rangle}{dr}\right|_{r=r_{\rm LR}} = 0\ . \tag{3.105}$$

Analogously with the ISCO case, we search for solutions of the form

$$r_{\rm LR} \simeq r_0 + \eta\, r_1\ , \quad b_{\rm LR} \simeq b_0 + \eta\, b_1\ , \quad \Omega_{\rm LR} \simeq \Omega_0 + \eta\, \Omega_1\ . \tag{3.106}$$

At the zeroth order in η they define the unperturbed parameters for the light ring of a RN black hole, which can be written as [305]

$$r_0 = \frac{3M+\sqrt{9M^2-8Q^2}}{2},\ b_0 = \frac{(3M+\sqrt{9M^2-8Q^2})^2}{2[2M(3M+\sqrt{9M^2-8Q^2})-4Q^2]^{1/2}},\ \Omega_0 = \frac{1}{b_0}, \tag{3.107}$$

while by solving Eqs. (3.105) at first order in η we find the tidal corrections induced by the external environment on the light ring parameters, which read

$$r_1 = -15M + 9\frac{Q^2}{M} + \frac{Q^2}{M^2}\sqrt{9M^2-8Q^2} - \frac{45M^2-38Q^2}{\sqrt{9M^2-8Q^2}}\,,$$

$$b_1 = \frac{\sqrt{2M(3M+\sqrt{9M^2-8Q^2})-4Q^2}}{2M^2}(5M(3M+\sqrt{9M^2-8Q^2})-4Q^2)\,,$$

$$\Omega_1 = \frac{4(Q^2-M(\sqrt{9M^2-8Q^2}+2M))\sqrt{2M(\sqrt{9M^2-8Q^2}+3M)-4Q^2}}{M^2(\sqrt{9M^2-8Q^2}+3M)^2}\,. \tag{3.108}$$

We represent them in Fig. 3.11. From these results we can notice how, similarly to the ISCO case, the tidal corrections are decreasing functions of the charge-to-mass ratio of the RN black hole, reaching their minimum, but still non-zero, values once again at extremality. For completeness, the values of the parameters characterizing the light ring in the extremal limit can be written as

$$\begin{aligned} &r_0 = 2M\,, \qquad b_0 = 4M\,, \qquad \Omega_0 = \frac{1}{4M}\,,\\ &r_1 = -12M\,, \quad b_1 = 16M\,, \quad \Omega_1 = -\frac{1}{M}. \end{aligned} \tag{3.109}$$

3.2.5 Tidal Effects on the ISCO - Charged Test Particle

Here we analyse the scenario where the test particle possesses an electric charge q. In this case the dynamics is richer than the one of a neutral test

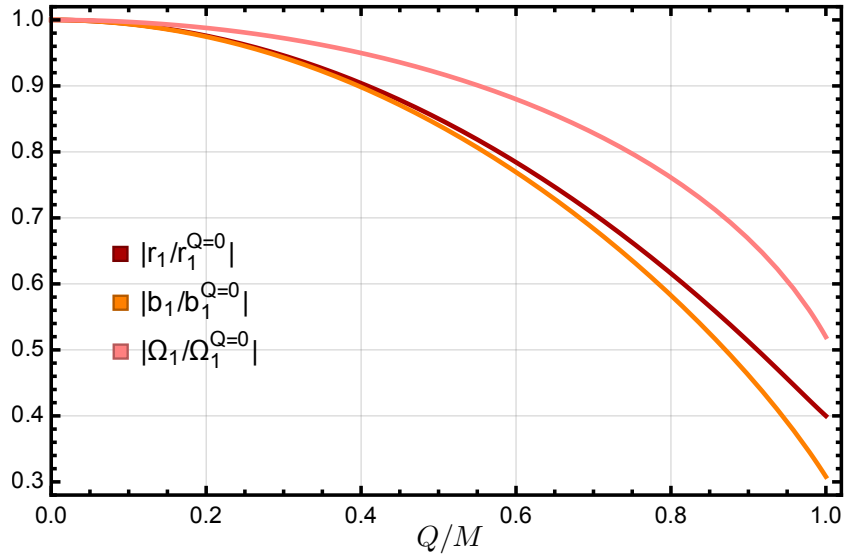

Figure 3.11: Tidal corrections to the light ring's position, impact parameter and orbital frequency as a function of the black hole's charge-to-mass ratio Q/M. The corrections are normalised to their values in the neutral black hole case.

particle since now the secondary companion in the EMRI system interacts both gravitationally and electromagnetically with the tidally deformed background. Note that even if we are considering only gravitational tides, the Maxwell field strength is coupled with the gravitational deformations thanks to the charge Q of the RN black hole. Thus, in the case of a charged test particle, the tidal corrections contain both a gravitational and electromagnetic contribution.

The Hamiltonian describing the EMRI system with a charged test particle is given by Eq. (3.95), which we expand in terms of the dimensionless parameter $\tilde{q}$, which we assume to be small ($\tilde{q} \ll 1$) in order to carry out the computation analytically. After retaining only terms up to the first order in the expansion, the Hamiltonian takes the following form

$$\begin{aligned}\langle H\rangle &= -\frac{1}{2}\left(\frac{\left(\frac{\tilde{q}Q}{r}-\langle E\rangle\right)^2}{f}-\frac{\langle L\rangle^2}{r^2}\right)-\eta\left[\left(\frac{\tilde{q}Q}{r}-\langle E\rangle\right)^2+f\frac{\langle L\rangle^2}{r^2}\right]\frac{r^2}{M^2}\\ &\sim -\frac{1}{2}\left(\frac{\langle E\rangle\left(\langle E\rangle-\frac{2\tilde{q}Q}{r}\right)}{f}-\frac{\langle L\rangle^2}{r^2}\right)-\eta\left[\langle E\rangle\left(\langle E\rangle-\frac{2\tilde{q}Q}{r}\right)+f\frac{\langle L\rangle^2}{r^2}\right]\frac{r^2}{M^2}\,.\end{aligned} \tag{3.110}$$

Even though the assumption $\tilde{q} \ll 1$ is not valid for elementary particles, for which the charge-to-mass ratio is very large $\sim 10^{21}$,[16] it captures very well

[16] We recall that we are working in geometric units, with $G = c = 1$.

the scenario where the test particle in the EMRI is actually a macroscopic body, for which the charge-to-mass ratio should be instead very small [243]. Following the same steps presented previously in the case of a neutral test particle, we write the ISCO parameters as their unperturbed values in the RN spacetime (for a charged test particle this time) plus a tidal correction proportional to η, namely

$$\begin{aligned} r_{\rm ISCO} &\simeq r_0 + \tilde{q} r_0^q + \eta \left(r_1 + \tilde{q} r_1^q\right), \\ L_{\rm ISCO} &\simeq L_0 + \tilde{q} L_0^q + \eta \left(L_1 + \tilde{q} L_1^q\right), \\ E_{\rm ISCO} &\simeq E_0 + \tilde{q} E_0^q + \eta \left(E_1 + \tilde{q} E_1^q\right), \\ \Omega_{\rm ISCO} &\simeq \Omega_0 + \tilde{q} \Omega_0^q + \eta \left(\Omega_1 + \tilde{q} \Omega_1^q\right), \end{aligned} \tag{3.111}$$

where $(r_\alpha, E_\alpha, L_\alpha, \Omega_\alpha)$, with $\alpha = 0, 1$, are the gravitational contributions to respectively the unperturbed parameters and the tidal corrections computed in the neutral test particle case. More in detail, the unpertubed values (denoted by the subscript 0) can be obtained by solving at leading order the ISCO conditions presented in Eq. (3.96) with the Hamiltonian (3.110), where E_0, L_0, r_0 and Ω_0 denote the ISCO parameters for a RN black hole in the absence of tidal deformation for $q = 0$, and their expressions are given in Eqs.(3.100), while r_0^q, L_0^q, E_0^q and Ω_0^q are the first order corrections due to the charge q and can be written as

$$\begin{aligned} r_0^q &= -\frac{Q r_0 \sqrt{r_0^2 - 3Mr_0 + 2Q^2}\left(r_0^2 - 6Mr_0 + 6Q^2\right)\left(r_0^2 - 2Mr_0 + Q^2\right)^2}{C}, \\ L_0^q &= \frac{2Qr_0\left(r_0^2 - 2Mr_0 + Q^2\right)}{C\sqrt{Mr_0 - Q^2}}\Big(5Q^6 + MQ^2 r_0^2(27M - 14r_0) + 7Q^4 r_0(r_0 - 3M) \\ &\quad - Mr_0^3\left(12M^2 - 9Mr_0 + r_0^2\right)\Big), \\ E_0^q &= \frac{Q}{r_0 C}\Big(2MQ^2 r_0^3\left(36M^2 - 44Mr_0 + 9r_0^2\right) - Q^4 r_0^2\left(84M^2 - 81Mr_0 + 10r_0^2\right) \\ &\quad + Mr_0^4\left(36M^2 r_0 - 24M^3 - 12Mr_0^2 + r_0^3\right) + 8Q^6 r_0(5M - 3r_0) - 6Q^8\Big), \\ \Omega_0^q &= \frac{2Q\left(r_0^2 - 3Mr_0 + 2Q^2\right)^{3/2}\left(M^2 r_0^4 - Q^2 r_0^2\left(3M^2 - Mr_0 + r_0^2\right) + 3MQ^4 r_0 - Q^6\right)}{C r_0^2\sqrt{Mr_0 - Q^2}}, \end{aligned} \tag{3.112}$$

where C is defined in Eq. (3.103) and, to avoid heavy notation, we chose to give the various expressions in terms of r_0 which is given in Eq. (3.100). Notice how by sending the charge of the test particle to zero $q \to 0$ (or equivalently $\tilde{q} \to 0$) the parameters (3.111) reduce to those given in Eq.(3.100) for a neutral test particle, as expected. Moreover by setting the charge of the RN black hole to zero, i.e. $Q = 0$, we recover the parameters describing the ISCO of a Schwarzschild black hole, which obviously do not depend on the charge of

the test particle, while for an extremal charged black hole ($Q = M$) the ISCO parameters, up to the first order in $\tilde{q}$, takes the following expressions

$$\begin{aligned} r_0 + \tilde{q}\, r_0^q &= 4M - \tilde{q}\sqrt{\frac{2}{3}}M, \qquad & L_0 + \tilde{q}\, L_0^q &= 2\sqrt{2}M - \tilde{q}\sqrt{3}M, \\ E_0 + \tilde{q}\, E_0^q &= \sqrt{\frac{3}{2}}\frac{3}{4} + \tilde{q}\frac{1}{16}, \qquad & \Omega_0 + \tilde{q}\, \Omega_0^q &= \frac{\sqrt{3}}{16\, M} - \tilde{q}\frac{\sqrt{2}}{96\, M}. \end{aligned} \tag{3.113}$$

Here we can see explicitly that the position of the ISCO depends on the charge-to-mass ratio $\tilde{q}$ of the test particle. In particular when the charge of the test particle and the one of the RN black hole have the same sign, the ISCO is closer to the black hole itself, while if the two charges have opposite signs the ISCO is pushed far away compared to the case of a neutral test particle.

Finally by solving the ISCO conditions (3.96) at first order in η with the Hamiltonian (3.110), we find the tidal corrections to the ISCO parameters of a RN black hole in the case of a charged test particle, namely the ones with the subscript 1 defined in Eq. (3.111). Here $(r_1, L_1, E_1, \Omega_1)$ denote the tidal contributions to the gravitational field, which do not depend on the charge of the test particle and they correspond to the ones computed for a neutral test particle, while with the superscript q we represent the tidal contributions to the electromagnetic field, which are always proportional (in our approximation $\tilde{q} \ll 1$) to the charge of the test particle. They read

$$\begin{aligned} r_1^q &= \frac{r_0}{C^2 M^2 \sqrt{\mathcal{K}}} \Bigg\{ \xi_2 \Big[-2M^3 \left(44Q^2 r_0^2 + 63 r_0^4\right) + M^2 \left(199 Q^2 r_0^3 + 52 Q^4 r_0 + 101 r_0^5\right) \\ &\quad + 48 M^4 r_0^3 - M \left(99 Q^4 r_0^2 + 111 Q^2 r_0^4 + 10 Q^6 + 34 r_0^6\right) + 4 \left(5 Q^2 r_0^5 + 7 Q^4 r_0^3 + 4 Q^6 r_0 + r_0^7\right) \Big] \\ &\quad - CQ \left(r_0^2 - 2Mr_0 + Q^2\right) \xi_1 \Bigg\}, \\ L_1^q &= \frac{Q}{4C\mathcal{K}^2 M^2 r_0 \left(Mr_0 - Q^2\right)^{3/2} \left(r_0^2 - 2Mr_0 + Q^2\right)} \left(\xi_3 + \frac{2}{\sqrt{\mathcal{K}}}\xi_4\right), \\ E_1^q &= \frac{Q\left(\xi_5 + \sqrt{\mathcal{K}}\xi_6\right)}{4 r_0^3 \left(r_0^2 - 2Mr_0 + Q^2\right)}, \\ \Omega_1^q &= \frac{\xi_7}{CM^2 r_0^4 \sqrt{Mr_0 - Q^2} \left(r_0^2 - 2Mr_0 + Q^2\right)^2}, \end{aligned} \tag{3.114}$$

where again C is defined in Eq. (3.103), $\mathcal{K} = r_0^2 - 3Mr_0 + 2Q^2$ and the explicit expression for $\xi_1, .., \xi_7$ is relegated to App. E.

In the extremal limit ($Q = M$), the ISCO parameters up to first order in

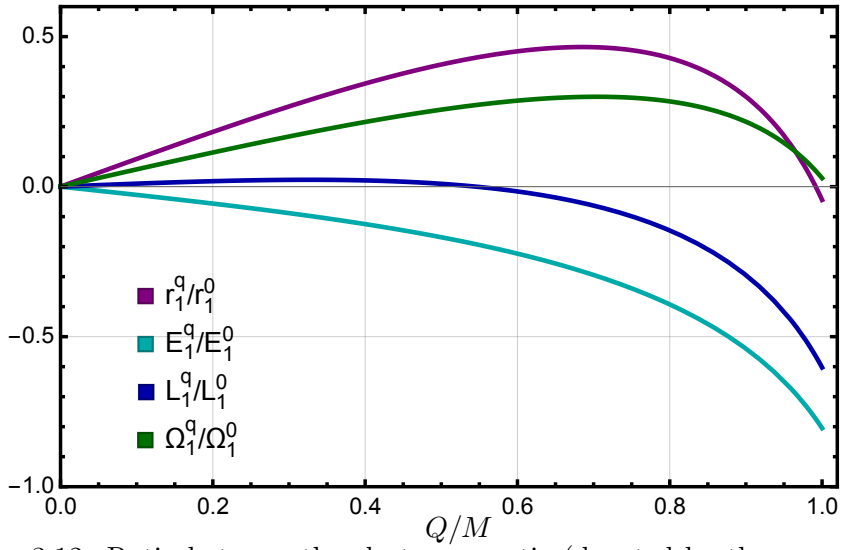

Figure 3.12: Ratio between the electromagnetic (denoted by the superscript q) and gravitational (denoted by the superscript 0) contributions to the tidal corrections of the ISCO parameters in the case of a charged test particle, as a function of Q/M.

$\tilde{q}$, including also the tidal contributions, simplify to

$$\begin{aligned} r_{\rm ISCO}^{\rm extremal} &\simeq 4M - \sqrt{\frac{2}{3}}\tilde{q}M + \eta\,(648 - \tilde{q}\,35\sqrt{\frac{2}{3}})\,M, \\ L_{\rm ISCO}^{\rm extremal} &\simeq 2\sqrt{2}M - \sqrt{3}\tilde{q}M - \eta\,(126\sqrt{2} - \tilde{q}\,62\sqrt{3})\,M, \\ E_{\rm ISCO}^{\rm extremal} &\simeq \sqrt{\frac{3}{2}}\frac{3}{4} + \frac{\tilde{q}}{16} - \eta\,(\frac{105}{4}\sqrt{\frac{3}{2}} - \tilde{q}\,\frac{207}{8})\,, \\ \Omega_{\rm ISCO}^{\rm extremal} &\simeq \frac{\sqrt{3}}{16\,M} - \tilde{q}\frac{\sqrt{2}}{96\,M} - \eta\,(\frac{73}{4}\sqrt{3} + \tilde{q}\frac{61}{96}\sqrt{2})\frac{1}{M}. \end{aligned} \tag{3.115}$$

Similarly to the neutral test particle case, the explicit expressions for the tidal corrections are not very useful. Given that all tidal corrections carry a gravitational and an electromagnetic contribution, as shown in Eq. (3.111), in Fig. 3.12 we plot the ratio of these two contributions as a function of the charge-to-mass Q/M ratio of the RN black hole for each parameter characterizing the ISCO, assessing the relative importance of these two effects as the charge of the black hole grows.

The electromagnetic contribution of course vanishes for $Q = 0$, and it is activated as Q increases. While the behaviour is slightly different for each quantity, in all cases the gravitational correction dominates in magnitude over the electromagnetic one for all Q. This may have been anticipated given that we are only considering a gravitational tidal source. It is also worth noticing that, for some values of Q, the electromagnetic corrections to the ISCO's position and angular momentum vanish. Such a non-monotonic behaviour

reveals a nontrivial balance of forces governing the particle's dynamics, which is much richer than in the neutral case.

Chapter 4

Conclusions

In this thesis we analysed how the dynamics of a black hole binary system is affected by the presence of a tidal environment, which in our analysis is usually sourced by a supermassive spinning black hole forming a triple system with the binary. We focused our attention on the scenarios where strong gravity effects emerge, i.e. when the binary system is orbiting along a geodesic very close to the supermassive black hole. We described the interaction between the tidal environment and the binary system perturbatively, treating the presence of the supermassive black hole as a perturbation on the binary system, thanks to the small-tide approximation introduced in Eq. (1.55), i.e. by requiring that the characteristic scale of the binary system is much smaller compared to the radius of the curvature induced by the tidal environment on the position of the binary itself. The effects of the tidal field are entirely captured by the multipole tidal moments $\mathcal{E}_{a_1,a_2,\dots,a_j}$ and $\mathcal{B}_{a_1,a_2,\dots,a_j}$, which are functions of solely the parameters characterizing the supermassive black hole. Strong gravity effects can significantly modify the dynamics of a binary system, potentially affecting also the gravitational wave signals emitted by the binary during the merger of the two companions. This, together with the fact that the new interferometers such as LISA and the Einstein Telescope will allow us to investigate regions of the Universe where strong gravity effects dominate the evolution of a binary system [50, 207], motivates us to analyse carefully black hole triple systems using General Relativity instead of the usual astrophysical approach relying on the weak field approximation.

More in detail, in Chapter 1 we analysed the evolution of a black hole binary system orbiting around a supermassive Kerr black hole along a circular and equatorial geodesic. We used the small tide approximation to treat the interaction between the binary system and the Kerr black hole as a small perturbation and we also assumed that the distance between the two companions in the binary was much bigger than the characteristic scales of the two black holes, allowing us to describe them as point particles and thus to describe

the binary using a Newtonian approach. In other words, the supermassive black hole generating the tidal field is described with the Kerr metric, using General Relativity, while the binary system is depicted as a Newtonian binary. We analysed how the description of the von Zeipel-Lidov-Kozai (ZLK) mechanism changes with our new approach, showing how with a relativistic description the characteristic frequency of the ZLK mechanism is enhanced by an extra factor depending of the parameters describing the source of the tidal field which becomes extremely relevant when the binary system is orbiting in the near horizon region of the supermassive Kerr black hole. This extra term in the frequency leads to faster mergers in the binary system and to a different signal for the peak frequency of the gravitational waves emitted by the two companions compared to the one predicted in the weak field limit. Moreover our approach allow us to incorporate new effects in the dynamics of the binary system that the usual point particle description cannot include, such as the gravitational redshift arising from the fact that the outer spacetime is now curved. This effect slows down the merger between the two objects, competing with the ZLK mechanism which, on the other hand, speeds up the merger. A General Relativistic description of the tidal environment captures also all possible effects of the spin of the supermassive Kerr black hole in the evolution of the binary system, allowing us to recover with a post-Newtonian (PN) expansion the usual spin-related contributions to the dynamics of the two companions included in the weak field approximation but also to extend the previously known results with new terms. Finally by describing the triple system in two different reference frames, i.e. the local inertial frame dubbed *Marck's frame* and the non-inertial one called *distant stars frame*, we were able to study the gyroscope precession of the angular momentum of the binary system around the direction identified by the angular momentum of the Kerr black hole. This precession is known in literature as the *Fokker - de Sitter precession* [173] or the *Schiff's precession* [174], depending on whereas it happens respectively in the Schwarzschild spacetime or in the Kerr one. As we did for the spin contribution, we used the PN expansion to recover the results already known in the literature [140], adding to them higher order corrections that so far were not taken into account.

In Chapter 2 we focused our attention on Extreme Mass Ratio Inspirals (EMRIs), i.e. binary systems where one of the two companions is much bigger than the other. Because of this large difference in the masses of the two objects, the lighter one is expected to undergo several orbital cycles in the near horizon region of the heavier one, where strong gravity effects play a crucial role in the dynamics of the system [50, 64]. This makes them the perfect candidates for the future interferometers to investigate regions of the Universe which can possibly give us an invaluable insight in the strong gravity regime, potentially leading to new physics [189, 206, 207, 306]. Their key role in the future of gravitational wave physics has motivated the scientific community to

study them in great details in different contexts [64,195–197]. They have been used as probes to investigate the properties of black holes [307–311], for the detection of scalar and vector fields [312, 313] and to analysed astrophysical environments [314]. They have been studied in relation with the self-force theory [315, 316], and they are particularly relevant in the context of resonances [317–323]. Furthermore it has been shown that a fraction of EMRIs might actually be b-EMRIs, i.e. binary Extreme Mass Ratio Inspirals, where the secondary companion is a binary system, instead of a single compact object [65, 324, 325]. This had lead to an increasing interest in EMRI systems in tidal environments, where the binary is orbiting around an external supermassive black hole, analysing how the latter affects the dynamics of the former [46, 71, 72]. For all of the reasons mentioned above, in Chapter 2 we studied how the dynamics of an EMRI system is affected by the presence of a tidal environment, which in our analysis will be generated by a supermassive Kerr black hole, in a strong gravity regime when the binary and the external black hole are close to each other. We started by computing the explicit expressions for the multipole electric ($\mathcal{E}_{a_1,a_2,\dots,a_j}$) and magnetic ($\mathcal{B}_{a_1,a_2,\dots,a_j}$) tidal moments at their leading order, i.e. the quadrupole one, generated by the Kerr black hole. The electric ones were already computed in previous works in the literature [69,71,72] while the magnetic quadrupole moments are a novelty that has never been computed before.[1] These tidal moments encode all the information about the source of the tidal field where the EMRI systems is moving, and we use them to study how the dynamics of the secondary companion in the binary system is affected by the presence of a supermassive Kerr black hole. In particular we focused our attention on two specific orbits, the ISCO of the primary companion and its light ring, computing the tidal shifts induced on their orbital parameters by the tidal environment on a secular timescale, i.e. on a timescale much longer than the orbital period of the test particle in the EMRI system. We encoded all the information about the tidal environment in an effective perturbative parameter η introduced in Eq. (2.50) and we showed how depending on the orientation of the binary system with respect to the plane where the outer orbit lies, the external tidal field can either push far away the radial position of both the ISCO and the light ring or can get them closer to the event horizon of the primary companion in the EMRI. Moreover we showed how it exists a particular configuration for the binary system, identified by the β_* parameter defined in Eq. (2.57), for which the EMRI system does not feel the presence of the tidal field and thus both the ISCO and the light ring remain unperturbed.

In Chapter 3 we include the presence of the charge in binary systems. Although it is widely believed that electrically charged black hole do not exist

[1] Note that the magnetic quadrupole tidal moments have also been computed, in a less general scenario compared to the one analysed in this thesis, in Ref. [211].

in the Universe because of the neutralization with the surrounding environment [229], it is still reasonable to include the charge in binary systems for different reasons. First of all there are some mechanisms capable of electrically charge a black hole, which usually lead to a very small - but non zero - charge for this astrophysical objects [73, 234, 235, 238–241, 243]. Secondly to include the electric charge in black hole mergers can potentially lead to a more accurate waveform models in the case of mergers happening in astrophysical environments [244–249]. Moreover the charge introduced in our analysis can also be a magnetic one. Magnetically charged black holes are more stable compared to their electrically charged counterpart, mostly because magnetic charges are expected to be way more heavier than the electric ones, making the pair-production neutralization ineffective [253]. Besides their stability [74, 75], magnetically charged black holes have drawn a lot of attention in the scientific community because of the corona forming in the near horizon region of the charged black hole where the electroweak symmetry is restored [254–257]. Finally the inclusion of an extra parameter in the description of a black hole allows us to analyse a more general scenario compared to the one where we only consider spherically symmetric and neutral objects, which can be used as a toy model for the more realistic astrophysical scenario of a spinning black hole or for some theories beyond General Relativity that predict the presence of an extra parameter in the metric describing a black hole [326–328]. Lastly it is also theoretically interesting to analyse charged black holes since they can also become extremal, i.e. when it has the same amount of charge and mass, scenario that is not achievable for a neutral black hole since it is only described by one parameter (its mass). Extremal black holes are a key element in supersymmetric theories [329] and in the context of theories in dimensions higher than four [281–284], making charged black holes perfect tools for investigating these theories.

In the first part of Chapter 3 we analysed the formation and the evolution of the event horizon of a charged black hole binary system, where one of the two objects is much smaller than the other, making the binary an EMRI system. Denoting with M and m the masses of respectively the primary and the secondary companion in the binary system, EMRIs are studied by taking the EMR limit $m/M \to 0$ which is usually satisfied by assuming that one of the two objects is a test particle, i.e. $m \to 0$. However in this limit we lose all the information about the geometry of the small object, including also the radial position of the event horizon, thus making this limit ineffective for the aim of our analysis. For this reason we choose to satisfy the EMR limit by sending $M \to \infty$, which means that the event horizon of the primary companion becomes a planar horizon. To extract the evolution of the event horizon during the merger we start from its final configuration at future null infinity, i.e. the one at the end of the merger, which corresponds to the one of the larger black hole in the EMRI system and we trace back in time the generators of the event horizon until they reach the line of caustics. We find

that, even though the geometry of the problem is the same as the one analysed in the case of a neutral EMRI system [78], the presence of the charge in the binary can significantly affect the merger of the two black holes. In particular we find that as the charge of the small black hole in the EMRI grows larger, the merger happens closer to its event horizon, the black hole is less distorted during the merger and the time required for the two companions to merge is shorter. This is a consequence of the fact that as the black hole reaches extremality, it becomes smaller in size meaning that it will be swallowed more quickly by the large black hole leading to a faster merger.

In the second part of Chapter 3 instead we analysed how the dynamics of an EMRI system with a charged black hole described by the RN metric as the primary companion is affected by the presence of an external tidal field. We started by writing down the metric for a tidally deformed RN black hole, following Refs. [70, 77] which we then used to study how the ISCO and the light-ring of a RN black hole are deformed by the presence of an external tidal field, comparing our results with the one obtained in Chapter 2 for a neutral EMRI. We carried out the computation in two different scenarios, when the test particle orbiting around the charged black hole in the binary system is a neutral one and when it is charged, under the assumption that the charge of the test particle is small compared to its mass, i.e. $\tilde{q} = q/m \ll 1$. In the case of a neutral test particle we found that as the RN black hole reaches extremality, the shifts induced by the external tidal fields on the parameters characterizing the orbits of the test particle become smaller, reaching their minimum finite values exactly when $Q = M$, with Q and M respectively the charge and the mass of the RN black hole. This can be interpreted by considering that the more charge is added to the black hole, the smaller it becomes in size and as a consequence the ISCO and the light-ring get closer to its event horizon, resulting in a less effective deformation induced by the external tidal fields. In the case of a charged test particle instead the tidal effects have both a gravitational and an electromagnetic contribution, where the latter is proportional to the product of the two charges q and Q, respectively the charge of the test particle and of the RN black hole. We found that both contributions become smaller as the RN black hole approaches extremality, reaching again their minimum (but finite) value when $Q = M$ as expected. It is interesting to notice how the gravitational part of the tidal deformations is larger than the electromagnetic counterpart. This is a consequence of the fact that in our analysis we still considered only gravitational tides.

What has been discussed in this thesis can be seen as a starting point for possible future analysis in the context of triple systems in a strong gravity regime. In this last part of the thesis we mention some, but not all, possible future directions which might be (in our opinion) astrophysically relevant.

The first natural extension to our work would be to study how the dynamics of a binary system moving in an external tidal environment is affected by

the multipole magnetic tidal moments $\mathcal{B}_{a_1,a_2,\ldots,a_j}$. This is motivated by the fact that in contrast with the electric ones, they do not have a Newtonian counterpart, meaning that any astrophysical effect arising from their contribution to the dynamics of a binary system would be purely relativistic. As enlightened in Eq. (C.7), they are proportional to the orbital velocity of the binary system and thus, assuming that the tidal environment is sourced by a supermassive black hole, magnetic tidal moments become extremely relevant when the binary system is very close to the third object. A straightforward way of including them in the dynamics of a triple system would be to analyse the case where the binary system is moving along an eccentric, non-equatorial orbit around a Kerr black hole. In this scenario, they should survive the secular average procedure which, as we saw in Chapter 2, was responsible for suppressing their contribution to the evolution of the binary in the case of a circular outer orbit.

In this thesis we always took into account only the leading contribution in the multipole tidal moments expansion, i.e. the quadrupole order, in the dynamics of a binary system moving in a tidal environment. However it would be extremely important to include also the next order contribution (the octupole order), especially in the context of the ZLK mechanism since, as we have mentioned at the beginning of Chapter 1, new effects (such as the orbital flip) arise when including the octupole order in the multipole expansion. In light of the results of this thesis, specifically the fact that the ZLK mechanism is enhanced in the strong gravity regime, it is particularly interesting to include the octupole tidal potentials in the computation and to study if and how the orbital flip is affected by strong gravity effects.

It is also worth mentioning that non-secular effects, such as resonances, can play a huge role in the dynamics of a binary system. In this context another possible extension of this thesis would be to analyse resonances in triple systems using a General Relativistic approach. First of all, analogously to what happens in the context of ZLK mechanism, strong gravity effects can enhance resonances that in the point particle approximation might be suppressed. Secondly in General Relativity we usually have more frequencies compared to the Newtonian description. Just to give an example, in the weak-field regime (described by Newtonian physics) the azimuthal and radial frequency Ω_ϕ and Ω_r of a binary system orbiting a supermassive black hole are the same, but in the strong gravity regime (described by General Relativity) they split, leading to $\Omega_\phi \neq \Omega_r$. As a consequence, in the strong gravity regime we could have more frequencies resonating with each other, yielding possibly to new resonances that are not captured by the Newtonian description.

Finally tidal effects are not only relevant in the context of gravitational waves, but they might also play a significant role in some high-energy astrophysical phenomena such as for example the emission of electromagnetic jets from black holes. The latter phenomena is still an open question in astrophysics and one possible answer lies in the Blandford–Znajek mecha-

nism [330–332], i.e. the equivalent of the Penrose process [333] for the electromagnetic field. As we also mentioned in Chapter 3, the tidal fields generated by a supermassive black hole, or a tidal environment in general, also affect the field lines of the electromagnetic field around a black hole, potentially changing the emission of jets.

Appendix

Appendix A

Secular evolution equations

Here we write explicitly the evolution equations for the orbital parameters for both the inner and outer orbit up to the octupole approximation in the Hamiltonian (1.3). Here we use the notation presented in Refs. [20,124], which we follow in this Appendix, and we define

$$\begin{aligned} A &= 4 + 3e_1^2 - \frac{5}{2} B \sin^2 i_{\rm tot}, \\ B &= 2 + 5e_1^2 - 7e_1^2 \cos(2g_1) \\ \cos\phi &= -\cos g_1 \cos g_2 - \cos i_{\rm tot} \sin g_1 \sin g_2. \end{aligned} \tag{A.1}$$

For completeness we recall also the definition of the constants C_2 and C_3 defined in (1.18) and (1.36), namely

$$\begin{aligned} C_2 &= \frac{G^2}{16} \frac{\big[(m_1+m_2)m_3\big]^7}{\big[(m_1+m_2+m_3)m_1m_2\big]^3} \frac{L_1^4}{L_2^3 J_2^3}, \\ C_3 &= -\frac{15}{16}\frac{G^2}{4} \frac{\big[(m_1+m_2)m_3\big]^9}{\big[(m_1+m_2+m_3)m_1m_2\big]^4} \frac{m_1-m_2}{m_1m_2} \frac{L_1^6}{L_2^3 J_2^5}. \end{aligned} \tag{A.2}$$

The Hamiltonian up to the octupole order can be written using the elimination of nodes $h_1 - h_2 = \pi$ since the equations of motion for the orbital parameters are not affected by this relation. This is true as long as one uses the conservation of the total angular momentum $\mathbf{J}_{\rm tot}$ to derive the evolution equations for $J_{1,z}$ and $J_{2,z}$ or, given their definition in (1.7) equivalently i_1 and i_2, and not the canonical relation in (1.14) since now we eliminated the angle variables h_1 and h_2. The secular Hamiltonian can then be written (after averaging over the mean anomalies l_1 and l_2) as

$$\begin{aligned} H = C_2 &\Big[(2+3e_1^2)(3\cos^2 i_{\rm tot} - 1) + 15 e_1^2 \sin^2 i_{\rm tot} \cos(2g_1)\Big] \\ &+ C_3 e_1 e_2 \Big[A\cos\phi + 10 \cos i_{\rm tot} \sin^2 i_{\rm tot} (1-e_1^2) \sin g_1 \sin g_2\Big]. \end{aligned} \tag{A.3}$$

For the evolution equations for the arguments of periapsis g_1 and g_2 we can use the canonical relation defined in (1.14) with the Hamiltonian we just defined above. This yields to

$$\begin{aligned}\frac{dg_1}{dt} &= 6C_2\left[\frac{1}{J_1}\left(4\cos^2 i_{\rm tot} + (5\cos(2g_1)-1)(1-e_1^2-\cos^2 i_{\rm tot})\right)\right.\\ &\left.+\frac{\cos i_{\rm tot}}{J_2}\left(2+e_1^2(3-5\cos(2g_1))\right)\right]\\ &- C_3e_2\left[e_1\left(\frac{1}{J_2}+\frac{\cos i_{\rm tot}}{J_1}\right)\left(\sin g_1\sin g_2(10(3\cos^2 i_{\rm tot}-1)(1-e_1^2)+A)\right.\right.\\ &\left.-5B\cos i_{\rm tot}\cos\phi\right) - \frac{1-e_1^2}{e_1J_1}\left(10\sin g_1\sin g_2\cos i_{\rm tot}\sin^2 i_{\rm tot}(1-3e_1^2)\right.\\ &\left.\left.+\cos\phi(3A-10\cos^2 i_{\rm tot}+2)\right)\right],\end{aligned} \tag{A.4}$$

and

$$\begin{aligned}\frac{dg_2}{dt} &= 3C_2\left[\frac{2\cos i_{\rm tot}}{J_1}\left(2+e_1^2(3-5\cos(2g_1))\right)\right.\\ &\left.+\frac{1}{J_2}\left(4+6e_1^2+(5\cos^2 i_{\rm tot}-3)(2+e_1^2(3-5\cos(2g_1)))\right)\right]\\ &+ C_3e_1\left[\sin g_1\sin g_2\left(10\frac{4e_2^2+1}{e_2J_2}\cos i_{\rm tot}\sin^2 i_{\rm tot}(1-e_1^2)\right.\right.\\ &\left.-e_2\left(\frac{1}{J_1}+\frac{\cos i_{\rm tot}}{J_2}\right)\left(A+10(3\cos^2 i_{\rm tot}-1)(1-e_1^2)\right)\right)\\ &\left.+\cos\phi\left(5B\cos i_{\rm tot}e_2\left(\frac{1}{J_1}+\frac{\cos i_{\rm tot}}{J_2}\right)+\frac{4e_2^2+1}{e_2J_2}A\right)\right].\end{aligned} \tag{A.5}$$

For the evolution equations for the inner (e_1) and outer (e_2) eccentricities we can use eqs. (1.15) which explicitly read

$$\begin{aligned}\frac{de_1}{dt} &= C_2\frac{1-e_1^2}{J_1}\left(30e_1\sin^2 i_{\rm tot}\sin(2g_1)\right)\\ &+ C_3e_2\frac{1-e_1^2}{J_1}\left[35\cos\phi\sin^2 i_{\rm tot}e_1^2\sin(2g_1)\right.\\ &-10\cos i_{\rm tot}\sin^2 i_{\rm tot}\cos g_1\sin g_2(1-e_1^2)\\ &\left.-A(\sin g_1\cos g_2-\cos i_{\rm tot}\cos g_1\sin g_2)\right],\end{aligned} \tag{A.6}$$

and

$$\frac{de_2}{dt} = -C_3 e_1 \frac{1-e_2^2}{J_2}\Big[10\cos i_{\rm tot}\sin^2 i_{\rm tot}(1-e_1^2)\sin g_1\cos g_2 \\ +A(\cos g_1\sin g_2 - \cos i_{\rm tot}\sin g_1\cos g_2)\Big]\,. \tag{A.7}$$

We can use again the canonical relation to find the equations describing the time evolution of the angular momenta for the inner (J_1) and outer (J_2) orbit, namely

$$\frac{dJ_1}{dt} = -C_2 30 e_1^2\sin(2g_1)\sin^2 i_{\rm tot} \\ + C_3 e_1 e_2\Big[A\left(\sin g_1\cos g_2 - \cos i_{\rm tot}\cos g_1\sin g_2\right) - 35e_1^2\sin^2 i_{\rm tot}\sin(2g_1)\cos\phi \\ +10\cos i_{\rm tot}\sin^2 i_{\rm tot}(1-e_1^2)\cos g_1\sin g_2\Big]\,, \tag{A.8}$$

and

$$\frac{dJ_2}{dt} = C_3 e_1 e_2\left[A\left(\cos g_1\sin g_2 - \cos i_{\rm tot}\sin g_1\cos g_2\right)\right. \\ \left.+10\cos i_{\rm tot}\sin^2 i_{\rm tot}(1-e_1^2)\sin g_1\cos g_2\right]\,. \tag{A.9}$$

We can derive the evolution equations for the longitude of ascending nodes h_1 and h_2, which can be written as

$$\frac{dh_1}{dt} = -\frac{3C_2}{J_1\sin i_1}\left(2+3e_1^2-5e_1^2\cos(2g_1)\right)\sin(2i_{\rm tot}) \\ - C_3 e_1 e_2\frac{\sin i_{\rm tot}}{J_1\sin i_1}\left[5B\cos i_{\rm tot}\cos\phi\right. \\ \left.-A\sin g_1\sin g_2 + 10(1-e\cos^2 i_{\rm tot})(1-e_1^2)\sin g_1\sin g_2\right]\,, \tag{A.10}$$

where the geometrical relation

$$\sin i_1 = \frac{J_2}{J_{\rm tot}}\sin i_{\rm tot} \tag{A.11}$$

has been implemented. For the evolution equation of h_2 we can simply recall the relation $h_1 - h_2 = \pi$ which immediately tell us that $\dot{h}_1 = \dot{h}_2$.

Finally from the conservation of the total angular momentum we can write the evolution equations for the z component of the angular momenta of the inner ($J_{1,z}$) and outer ($J_{2,z}$) orbits. Moreover by recalling that $J_{\rm tot} = J_{1,z} + J_{2,z} = \text{const.}$ we can write $\dot{J}_{1,z} = -\dot{J}_{2,z}$. Explicitly we have

$$\frac{dJ_{1,z}}{dt} = \frac{J_1}{J_{\rm tot}}\frac{dJ_1}{dt} - \frac{J_2}{J_{\rm tot}}\frac{dJ_2}{dt}, \tag{A.12}$$

which can be re-written using the relation (A.11) as

$$\frac{dJ_{1,z}}{dt} = \frac{\sin i_2}{\sin i_{\rm tot}} \frac{dJ_1}{dt} - \frac{\sin i_1}{\sin i_{\rm tot}} \frac{dJ_2}{dt}. \tag{A.13}$$

It is conveniently to write this equations in terms of the inclinations for the inner and outer orbits i_1 and i_2, using the definitions in (1.7) we have

$$\frac{di_1}{dt} = -\frac{1}{\sin i_1} \left(\frac{\dot{J}_{1,z}}{J_1} - \frac{\dot{J}_1}{J_1} \cos i_1 \right), \tag{A.14}$$

and

$$\frac{di_2}{dt} = -\frac{1}{\sin i_2} \left(\frac{\dot{J}_{2,z}}{J_2} - \frac{\dot{J}_2}{J_2} \cos i_2 \right). \tag{A.15}$$

Appendix B

Fermi normal coordinates

This Appendix is based on Chapter 8 of Ref. [334], which here we slightly reformulate.

We introduce a generic geodesic γ, parametrized in a coordinate system x^μ by $x^\mu(\tau)$, with τ the proper time on the geodesic. The relativistic velocity on γ is given by

$$u^\mu = \frac{dx^\mu}{d\tau}, \tag{B.1}$$

where, for a time-like geodesic

$$g_{\mu\nu} u^\mu u^\nu \tag{B.2}$$

with $g_{\mu\nu}$ the metric describing the spacetime background.

We construct an orthonormal tetrad on the time-like geodesic γ by introducing four vector fields e^a_μ on γ such that they obey the following conditions

$$e^\mu_0 = u^\mu, \quad \frac{D}{d\tau} e^\mu_a = 0, \quad e^\mu_a e^\nu_b g_{\mu\nu} = \eta_{ab}, \tag{B.3}$$

with $a, b = 0, 1, 2, 3$ and where η_{ab} is the usual Minkowski metric. The dual tetrad is defined as

$$e^a_\mu = \eta^{ab} g_{\mu\nu} e^\nu_b. \tag{B.4}$$

Given an event p in the neighborhood of γ, we introduce the unique space-like geodesic β that intersects γ orthogonally ending up at p, where we denote q the intersection point between γ and β. Moreover we demand the tangent vector v^μ of β to be orthogonal, at q, to the tangent vector u^μ of γ, namely

$$g_{\mu\nu} u^\mu v^\nu = 0 \quad \text{at} \quad q. \tag{B.5}$$

Notice that v^μ is the tangent vector at q that points in the direction towards p.

The Fermi normal coordinates $\tilde{x}^\mu$ for p are defined as

$$\tilde{x}^0 = \tau, \quad \tilde{x}^i = e^i_\mu v^\mu, \tag{B.6}$$

where $i = 1, 2, 3$. The geodesic distance between q and p, as measured with the space-like curve β, is denoted s, which can be written as

$$s^2 = \delta_{ij}\tilde{x}^i\tilde{x}^j. \tag{B.7}$$

In terms of Fermi normal coordinates $\tilde{x}^\mu$, we can write the metric in the neighborhood of the time-like geodesic γ as

$$\begin{aligned}
\tilde{g}_{00} &\simeq -1 - \tilde{R}_{0i0j}\tilde{x}^i\tilde{x}^j + \mathcal{O}\left(s^3\right), \\
\tilde{g}_{0i} &\simeq -\frac{2}{3}\tilde{R}_{0jik}\tilde{x}^j\tilde{x}^k + \mathcal{O}\left(s^3\right), \\
\tilde{g}_{ij} &\simeq \delta_{ij} - \frac{1}{3}\tilde{R}_{ikjl}\tilde{x}^k\tilde{x}^l + \mathcal{O}\left(s^3\right),
\end{aligned} \tag{B.8}$$

where $\tilde{R}_{0i0j}$, $\tilde{R}_{0jik}$ and $\tilde{R}_{ikjl}$ represent the components of the Riemann curvature tensor evaluated on γ.

If the background (at least on γ) obeys the equations

$$R_{\mu\nu} = 0, \tag{B.9}$$

then we can write the components of the Riemann curvature tensor as

$$\tilde{R}_{ikjl} = \delta_{ij}\mathcal{E}_{kl} + \delta_{kl}\mathcal{E}_{ij} - \delta_{il}\mathcal{E}_{jk} - \delta_{jk}\mathcal{E}_{il}, \tag{B.10}$$

where we introduce the *electric quadrupole moments* $\mathcal{E}_{ij}$, defined as

$$\mathcal{E}_{ij} = \tilde{R}_{0i0j}. \tag{B.11}$$

Note that from the equation $R_{00} = 0$ (which follows from Eq. (B.9)), together with the general result $R_{0000} = 0$, the following relations hold

$$\mathcal{E}_{ij} = \mathcal{E}_{ji}, \quad \delta^{ij}\mathcal{E}_{ij} = 0. \tag{B.12}$$

Moreover from Eq. (B.9) follows

$$\delta^{ik}\tilde{R}_{0ijk} = 0, \tag{B.13}$$

which implies

$$\tilde{R}_{0ijk} = -\epsilon_{jkl}\mathcal{B}^l_i, \tag{B.14}$$

where we introduce the Levi-Civita tensor ϵ_{jkl} and the *magnetic quadrupole moment* $\mathcal{B}_{ij}$, which obeys

$$\mathcal{B}_{ij} = \mathcal{B}_{ji}, \quad \delta^{ij}\mathcal{B}_{ij} = 0. \tag{B.15}$$

We can now write the metric in the neighborhood of the time-like geodesic γ, in the case where the Ricci tensor vanishes on γ ($R_{\mu\nu} = 0$), in terms of

Thorne-Hartle coordinates, which are related to the Fermi normal ones by the following transformation

$$\hat{x}^a = \tilde{x}^a + \xi^a, \quad \xi^a = \frac{-}{1}6\left(\tilde{x}_c\tilde{x}^c\right)\mathcal{E}_{ab}\tilde{x}^b - \frac{1}{3}\tilde{x}_a\mathcal{E}_{bc}\tilde{x}^b\tilde{x}^c + \mathcal{O}\left(s^3\right). \tag{B.16}$$

Thus, the metric in Thorne-Hartle coordinates can be written as [167]

$$\begin{aligned}
\hat{g}_{00} &\simeq -1 - \mathcal{E}_{ij}\hat{x}^i\hat{x}^j + \mathcal{O}\left(s^3\right), \\
\hat{g}_{0i} &\simeq -\frac{2}{3}\epsilon_{ijk}\mathcal{B}^j_l\hat{x}^k\hat{x}^l + \mathcal{O}\left(s^3\right), \\
\hat{g}_{ij} &\simeq \delta_{ij}\left(1 - \mathcal{E}_{kl}\hat{x}^k\hat{x}^l\right) + \mathcal{O}\left(s^3\right).
\end{aligned} \tag{B.17}$$

Finally, for a more detailed review on Fermi normal coordinates we refer the reader to Refs. [334, 335].

Appendix C

Tidally deformed Schwarzschild spacetime

In this Appendix we briefly review the basic steps needed for the construction of the metric of a tidally deformed Schwarzschild black hole. This metric was derived for the first time in Ref. [70][1], which here we strictly follow and review. Throughout this Appendix we will work in relativistic units, where $G = c = 1$.

The first step is to introduce the two length scales in play in the problem, namely the mass of the tidally deformed black hole M, and the radius of the curvature $\mathcal{R}$ of the external spacetime generated by the source of the tidal fields, evaluated on the position of the black hole. To meaningfully analyse the motion of the black hole in the external spacetime, the tidal interaction between the two must be small, meaning that

$$M \ll \mathcal{R}. \tag{C.1}$$

This allows us to treat the problem perturbatively, with $M/\mathcal{R} \ll 1$, in the so-called *small-tide approximation*. As already mentioned in Chapter 1, if the source of the tidal fields is a supermassive black hole of mass M', the radius $\mathcal{R}$ induced on the position of a black hole of mass M, placed at a distance of b from the former can be written as

$$\mathcal{R} \sim \sqrt{\frac{b^3}{M * M'}}. \tag{C.2}$$

In this scenario, the small-tide approximation takes the following expression

$$\frac{M}{\mathcal{R}} \sim \frac{M}{M + M'} V^3, \tag{C.3}$$

where V^3 is the orbital velocity of tha black hole of mass M, defined as

$$V \sim \sqrt{\frac{M + M'}{b}}. \tag{C.4}$$

[1]Note that a first step in the study of black holes in a tidal environment was already been made in Refs. [336–344].

From the condition (C.3), it is clear that there are two different ways of satisfying the small-tide approximation: by requiring that the orbital velocity of the black hole of mass M is small, i.e. $V \ll 1$, or by assuming that there is a hierarchy in the masses of the two bodies, namely $M \ll M'$. We refer to the first one as the *weak-field limit*, where the two bodies can have comparable masses but they must be far away from each other, while the second one is usually called *small-hole limit*, and requires the supermassive black hole of mass M' to be much bigger than the one of mass M without any limitation on the relative distance between the two objects.

C.1 Tidal Moments and Tidal Potentials

The information about the tidal environment can be completely be encoded in symmetric tracefree (STF) tensors $\mathcal{E}_{a_1a_2\ldots a_l}$ and $\mathcal{B}_{a_1a_2\ldots a_l}$ [345], which are called *tidal multipole moments* and are the most general terms describing the tidal environment compatible with the Einstein field equations [346, 347]. In order to find explicit expressions for these tidal moments, we need to introduce a smooth timelike geodesic γ in a vacuum spacetime, parametrized by the proper time τ in an arbitrary set of coordinates x^α. We can build a vectorial basis by using the velocity u^α tangent to the worldline and an orthonormal triad of vectors $e^\alpha_a(\tau)$, orthogonal to u^α and parallel transported along γ. With this basis we can project the components of the Weyl tensor on the timelike geodesic γ, namely

$$\begin{aligned} C_{a0b0} &= C_{\alpha\mu\beta\nu}e^\alpha_a u^\mu e^\beta_b u^\nu, \\ C_{abc0} &= C_{\alpha\beta\gamma\mu}e^\alpha_a e^\beta_b e^\gamma_c u^\mu, \\ C_{abcd} &= C_{\alpha\beta\gamma\delta}e^\alpha_a e^\beta_b e^\gamma_c e^\delta_d. \end{aligned} \tag{C.5}$$

We can use these decompositions to introduce the leading terms in the multipole expansion for the tidal moments, which are usually referred as *quadrupole tidal moments* and are defined as

$$\mathcal{E}_{ab} = \left(C_{a0b0}\right)^{\mathrm{STF}}, \quad \mathcal{B}_{ab} = \frac{1}{2}\left(\epsilon_{apq}C^{pq}_{\ b}0\right)^{\mathrm{STF}}, \tag{C.6}$$

where ϵ_{abc} is the permutation symbol. For the purpose of our analysis we will only consider the quadrupole order in the multipole expansion of the tidal moments, since in these thesis we will always carry our computations up to this order of approximation, neglecting higher order terms. The quadrupole tidal moments can be expressed in terms of two scales [167]: the length scale given by the radius of the curvature $\mathcal{R}$ and the velocity scale $\mathcal{V}$:

$$\mathcal{E}_{ab} \sim \frac{1}{\mathcal{R}^2}, \quad \mathcal{B}_{ab} \sim \frac{\mathcal{V}}{\mathcal{R}^2}. \tag{C.7}$$

To have a physical understanding of these scales, we consider again the situation where the source of the tidal fields is a supermassive black hole of mass

M', and we place ourselves on a circular orbit at a distance b from this object. In this scenario the two timescales have the following expressions

$$\mathcal{R} \sim \sqrt{\frac{b^3}{M'}}, \quad \mathcal{V} \sim \sqrt{\frac{M'}{b}}, \tag{C.8}$$

which yield

$$\mathcal{E}_{ab} \sim \frac{1}{b^3}, \quad \mathcal{B}_{ab} \sim \frac{1}{b^{7/2}}. \tag{C.9}$$

The next ingredient needed for the construction of the metric of a tidally deformed black hole is the introduction of *tidal potentials*. To this end we introduce the radial unit vector

$$\Omega^a = \frac{x^a}{r}, \tag{C.10}$$

where $r := \sqrt{\delta_{ab} x^a x^b}$, and a projector to the transverse space orthogonal to Ω^a

$$\gamma^a_b = \delta^a_b - \Omega^a \Omega_b. \tag{C.11}$$

We can now combine the tidal moments with Ω^a and γ^a_b to form scalar, vector and tensor tidal potentials. They read

$$\begin{aligned} &\mathcal{E}^{\rm q} = \mathcal{E}_{cd}\Omega^c\Omega^d, \quad \mathcal{E}^{\rm q}_a = \gamma^c_a \mathcal{E}_{cd}\Omega^d, \quad \mathcal{E}^{\rm q}_{ab} = 2\gamma^c_a\gamma^d_b\mathcal{E}_{cd} + \gamma_{ab}\mathcal{E}^{\rm q}, \\ &\mathcal{B}^{\rm q}_a = \epsilon_{apq}\Omega^p\mathcal{B}^q_c\Omega^c, \quad \mathcal{B}^{\rm q}_{ab} = \epsilon_{apq}\Omega^p\mathcal{B}^q_d\gamma^d_b + \epsilon_{bpq}\Omega^p\mathcal{B}^q_c\gamma^c_a, \end{aligned} \tag{C.12}$$

where the superscript q stands for quadrupole order.
To convert this quantities in spherical coordinates (r, θ, ϕ), we redefine

$$x^a = r\Omega^a\left(\theta^A\right), \tag{C.13}$$

where we defined $\Omega^a = (\sin\theta\cos\phi, \sin\theta\sin\phi, \cos\theta)$ and $\theta^A = (\theta, \phi)$. Moreover the relation in Eq. (C.13) implies

$$\frac{\partial x^a}{\partial r} = \Omega^a, \quad \frac{\partial x^a}{\partial \theta^A} = r\Omega^a_A, \tag{C.14}$$

with

$$\Omega^a_A = \frac{\partial \Omega^a}{\partial \theta^A}. \tag{C.15}$$

Finally the following identities hold

$$\Omega_a\Omega^a_A = 0, \quad \Omega_{AB} = \gamma_{ab}\Omega^a_A\Omega^b_B, \quad \Omega^{AB}\Omega^a_A\Omega^b_B = \gamma^{ab}, \tag{C.16}$$

where we introduced the metric on the unit two-sphere defined as $\Omega_{AB} = \mathrm{diag}\left(1, \sin^2\theta\right)$. We make use of the transformation matrix defined in Eq. (C.15) to convert the tidal potentials from Cartesian coordinates into spherical ones by means of the following relations

$$\begin{aligned} &\mathcal{E}^{\rm q}_A = \mathcal{E}^{\rm q}_a\Omega^a_A, \quad \mathcal{E}^{\rm q}_{AB} := \mathcal{E}^{\rm q}_{ab}\Omega^a_A\Omega^b_B, \\ &\mathcal{B}^{\rm q}_A = \mathcal{B}^{\rm q}_a\Omega^a_A, \quad \mathcal{B}^{\rm q}_{AB} := \mathcal{B}^{\rm q}_{ab}\Omega^a_A\Omega^b_B. \end{aligned} \tag{C.17}$$

C.2 Tidally deformed metric

We will now construct the metric of a tidally deformed black hole in two steps. Firstly we compute the metric in the neighborhood of a timelike geodesic γ in a vacuum spacetime, and secondly we place a black hole of mass M on the worldline γ, computing the tidally deformed metric we are seeking.

The metric is obtained by solving the Einstein field equations in vacuum in the local neighborhood of the worldline γ, under the assumption that the size of the neighborhood is smaller than the radius of the curvature induced by the tidal fields on γ, namely

$$r \ll \mathcal{R}, \tag{C.18}$$

where r is the radial coordinate in the background measuring the distance from the worldline. When we place a black hole on the null geodesic γ, the condition (C.18) translates in

$$M \ll \mathcal{R}, \tag{C.19}$$

where M is the mass of the black hole. Note that in the derivation of the metric, the tidal moments introduced above are kept completely general but they must be specified once this metric used to describe astrophysical scenarios.

To derive the expression of the metric it is convenient to work in *light-cone coordinates* (v, r, θ, ϕ). This set of coordinates is suited to analyse light-cone surfaces, which can be thought as a congruence of null geodesics called generators. In particular, we are interested in past light-cone converging on the worldine γ. The reason why it is convenient to work with light-cone coordinates is because the following properties hold

- the advanced-time coordinate v is constant along each light-cone;
- the coordinates (θ, ϕ) are constants on the generators of each light-cone;
- the radial coordinate r can be thought has an affine parameter on the null geodesics defining each light-cone.

The metric in the neighborhood of the worldline γ can be written, in light-cone coordinates (v, x^a), as an expansions in powers of the small parameter $r/\mathcal{R} \ll 1$. Up to the quadrupole order in the multipole expansion for the tidal moments, the metric reads

$$\begin{aligned} g_{vv} &= -1 - r^2 \mathcal{E}^{\mathrm{q}} + \mathcal{O}\left(r/\mathcal{R}\right)^3, \\ g_{va} &= \Omega_a - \frac{2}{3} r^2 \left(\mathcal{E}^{\mathrm{q}}_a - \mathcal{B}^{\mathrm{q}}_a\right) + \mathcal{O}\left(r/\mathcal{R}\right)^3, \\ g_{ab} &= \gamma_{ab} - \frac{1}{3} r^2 \left(\mathcal{E}^{\mathrm{q}}_{ab} - \mathcal{B}^{\mathrm{q}}_{ab}\right) + \mathcal{O}\left(r/\mathcal{R}\right)^3. \end{aligned} \tag{C.20}$$

We can rewrite this metric in quasispherical coordinates $\left(v, r, \theta^A\right)$ as

$$\begin{aligned} g_{vv} &= -1 - r^2\mathcal{E}^{\mathrm{q}} + \mathcal{O}\left(r/\mathcal{R}\right)^3, \\ g_{vr} &= 1, \\ g_{vA} &= -\frac{2}{3}r^3\left(\mathcal{E}^{\mathrm{q}}_A - \mathcal{B}^{\mathrm{q}}_A\right) + \mathcal{O}\left(r/\mathcal{R}\right)^3, \\ g_{AB} &= r^2\Omega_{AB} - \frac{1}{3}r^4\left(\mathcal{E}^{\mathrm{q}}_{AB} - \mathcal{B}^{\mathrm{q}}_{AB}\right) + \mathcal{O}\left(r/\mathcal{R}\right)^3. \end{aligned} \tag{C.21}$$

When a black hole is placed on the worldline γ, the procedure to extract the metric in its neighborhood is exactly the same described in the case of a timelike geodesic in vacuum spacetime but this time the past light-cone will converge on the horizon of the black hole and not on the worldline γ.

Without carrying out explicitly the computation, the metric of a tidally deformed Schwarzschild black hole in quasi-Cartesian coordinates (v, x^a) and up to the quadrupole order in the multipole expansion for the tidal moments can be written as [2]

$$\begin{aligned} g_{vv} &= -f - r^2 e^{\mathrm{q}}_1\mathcal{E}^{\mathrm{q}} + \mathcal{O}\left(r/\mathcal{R}\right)^3, \\ g_{va} &= \Omega_a - \frac{2}{3}r^2\left(e^{\mathrm{q}}_4\mathcal{E}^{\mathrm{q}}_a - b^{\mathrm{q}}_4\mathcal{B}^{\mathrm{q}}_a\right) + \mathcal{O}\left(r/\mathcal{R}\right)^3, \\ g_{ab} &= \gamma_{ab} - \frac{1}{3}r^2\left(e^{\mathrm{q}}_7\mathcal{E}^{\mathrm{q}}_{ab} - b^{\mathrm{q}}_7\mathcal{B}^{\mathrm{q}}_{ab}\right) + \mathcal{O}\left(r/\mathcal{R}\right)^3, \end{aligned} \tag{C.22}$$

where here we have introduced the radial functions

$$\begin{aligned} &e^{\mathrm{q}}_1 = f^2, \quad e^{\mathrm{q}}_4 = f, \quad e^{\mathrm{q}}_7 = 1 - \frac{1}{2x^2}, \\ &b^{\mathrm{q}}_4 = f, \quad b^{\mathrm{q}}_7 = 1 - \frac{3}{2x^2}, \end{aligned} \tag{C.23}$$

with

$$f = 1 - \frac{1}{x}, \quad x = \frac{r}{2M}. \tag{C.24}$$

We recall that this metric has been derived under the assumption that $M \ll \mathcal{R}$ and it is valid in the spacetime region where $r \ll \mathcal{R}$. Note that in the $M \to 0$ limit the metric reduces to the one in the neighborhood of a timelike geodesic in vacuum spacetime, depicted in Eq (C.20). Moreover by sending $\mathcal{R}$ to infinity and consequently by putting the tidal moments to zero, which corresponds to turning off the tidal fields, we recover the usual Schwarzschild metric in light-cone coordinates for the spacetime, i.e.

$$g_{vv} = -f, \quad g_{va} = \Omega_a, \quad g_{ab} = \gamma_{ab}. \tag{C.25}$$

[2] The fully detailed computation for extracting the metric of a tidally deformed black hole can be found in Ref [70], which in this Appendix we strictly follow and quickly review.

In quasi-spherical coordinates $\left(v, r, \theta^A\right)$ the black hole metric becomes

$$\begin{aligned} g_{vv} &= -f - r^2 e_1^{\mathrm{q}} \mathcal{E}^{\mathrm{q}} + \mathcal{O}\left(r/\mathcal{R}\right)^3, \\ g_{vr} &= 1, \\ g_{vA} &= -\frac{2}{3} r^3 \left(e_4^{\mathrm{q}} \mathcal{E}_A^{\mathrm{q}} - b_4^{\mathrm{q}} \mathcal{B}_A^{\mathrm{q}}\right) + \mathcal{O}\left(r/\mathcal{R}\right)^3, \\ g_{AB} &= r^2 \Omega_{AB} - \frac{1}{3} r^4 \left(e_7^{\mathrm{q}} \mathcal{E}_{AB}^{\mathrm{q}} - b_7^{\mathrm{q}} \mathcal{B}_{AB}^{\mathrm{q}}\right) + \mathcal{O}\left(r/\mathcal{R}\right)^3, \end{aligned} \tag{C.26}$$

where the radial functions are the same as the ones defined in Eq. (C.23). Thus the line element for a tidally deformed Schwarzschild black hole reads

$$\begin{aligned} ds^2 = &-\left(f + r^2 f^2 \mathcal{E}^{\mathrm{q}}\right) dv^2 + 2 dv dr - \frac{4}{3} r^3 f \left(\mathcal{E}_A^{\mathrm{q}} - \mathcal{B}_A^{\mathrm{q}}\right) dv d\theta^A \\ &+ \left\{ r^2 \Omega_{AB} - \frac{1}{3} r^4 \left[\left(1 - \frac{4M^2}{2r^2}\right) \mathcal{E}_{AB}^{\mathrm{q}} - \left(1 - \frac{12M^2}{2r^2}\right) \mathcal{B}_{AB}^{\mathrm{q}} \right] \right\} d\theta^A d\theta^B, \end{aligned} \tag{C.27}$$

where we note again that by sending $\mathcal{R} \to \infty$ we get back the usual Schwarzschild metric in Eddington-Finkelstein coordinates, namely

$$ds^2 = f dv^2 + 2 dv dr + r^2 d\Omega^2. \tag{C.28}$$

Finally we recall that it is possible to rewrite the metric (C.27) in the usual set of coordinates (t, r, θ, ϕ) by using the relation

$$v = t + r + 2M \log f, \tag{C.29}$$

where $f = 1 - 2M/r$.

For a more detailed analysis on the metric of a tidally deformed Schwarzschild black hole we refer the reader to Ref. [70], where this metric was derived for the first time and which we strictly followed in this Appendix.

Appendix D

Explicit solutions for radial functions

In this Appendix we give the explicit expressions for the radial functions $\mathcal{X}_{\ell m}(r), \mathcal{U}_{\ell m}(r), \mathcal{V}_{\ell m}(r)$ and $\Phi^{\pm}_{\ell m}(r)$ appearing in Eqs. (3.80)-(3.81) as an example.

We set the scale to $M = 1$ and, without loss of generality, we choose the normalisations $\mathcal{X} = r^{\ell}\left(1 + O(r^{\ell-1})\right)$ and $\mathcal{V} = r^{\ell-1}\left(1 + O(r^{\ell-2})\right)$. The solutions for $\ell = 2, 3, 4$ read:

- $\ell = 2$:

$$\mathcal{X}_{2,m}(r) = \frac{\left(\mathcal{Q}^2 + r^2 - 2r\right)^2}{r^2} \tag{D.1}$$

$$\mathcal{U}_{2,m}(r) = \mathcal{Q}^2 + r^2 - 2 \tag{D.2}$$

$$\mathcal{V}_{2,m}(r) = \frac{\mathcal{Q}^2}{r} + r - 2 \tag{D.3}$$

$$\Phi^{+}_{2,m}(r) = \frac{1}{2}\left(\mathcal{Q}^2 + 3r^2 - 4\right) \tag{D.4}$$

$$\Phi^{-}_{2,m}(r) = -\frac{3}{2}\left(r^2 - \mathcal{Q}^2\right) \tag{D.5}$$

- $\ell = 3$:

$$\mathcal{X}_{3,m}(r) = \frac{\left(\mathcal{Q}^2 + r^2 - 2r\right)^2\left(\mathcal{Q}^2 + 5r^2 - 5r\right)}{5r^3} \tag{D.6}$$

$$\mathcal{U}_{3,m}(r) = \frac{1}{5}\left(-6\mathcal{Q}^2 + 5r^3 - 10r^2 + \frac{\mathcal{Q}^4}{r} + 6\mathcal{Q}^2 r + 4\right) \tag{D.7}$$

$$\mathcal{V}_{3,m}(r) = \frac{-\mathcal{Q}^6 + 15r^6 - 50r^5 + \left(21\mathcal{Q}^2 + 40\right)r^4 - 32\mathcal{Q}^2 r^3 + 5\mathcal{Q}^4 r^2 + 2\mathcal{Q}^4 r}{15r^4} \tag{D.8}$$

$$\Phi^{+}_{3,m}(r) = \frac{2}{5}\left(5r^3 - 9r^2 + \mathcal{Q}^2(3r-1) + 2\right) \tag{D.9}$$

$$\Phi^{-}_{3,m}(r) = -\frac{4\left(-\mathcal{Q}^4 + 5r^4 - 8r^3 + 4\mathcal{Q}^2 r\right)}{5r} \tag{D.10}$$

- $\ell = 4$:

$$\mathcal{X}_{4,m}(r) = \frac{\left(\mathcal{Q}^2 + r^2 - 2r\right)^2\left(-2\mathcal{Q}^2 + 7r^3 - 14r^2 + 3\left(\mathcal{Q}^2+2\right)r\right)}{7r^3} \tag{D.11}$$

$$\mathcal{U}_{4,m}(r) = \frac{-6\mathcal{Q}^4 + 21r^5 - 70r^4 + 30\left(\mathcal{Q}^2+2\right)r^3 - 60\mathcal{Q}^2 r^2 + \left(9\mathcal{Q}^4 + 24\mathcal{Q}^2 - 8\right)r}{21r} \tag{D.12}$$

$$\mathcal{V}_{4,m}(r) = \frac{\mathcal{Q}^6}{14r^4} - \frac{\mathcal{Q}^4}{7r^3} + r^3 - \frac{9\mathcal{Q}^4}{14r^2} - \frac{9r^2}{2} + \frac{5\left(\mathcal{Q}^2+4\right)\mathcal{Q}^2}{7r} + \frac{3}{7}\left(4\mathcal{Q}^2 + 15\right)r - \frac{5}{14}\left(13\mathcal{Q}^2 + 8\right) \tag{D.13}$$

$$\Phi^{+}_{4,m}(r) = \frac{1}{42}\left(9\mathcal{Q}^4 + 12\mathcal{Q}^2 + 105r^4 - 320r^3 + 30\left(3\mathcal{Q}^2+8\right)r^2 - 120\mathcal{Q}^2 r - 16\right) \tag{D.14}$$

$$\Phi^{-}_{4,m}(r) = -\frac{5\left(4\mathcal{Q}^4 + 21r^5 - 60r^4 + 10\left(\mathcal{Q}^2+4\right)r^3 - 3\mathcal{Q}^2\left(\mathcal{Q}^2+4\right)r\right)}{14r} \tag{D.15}$$

Similar solutions are found for $\ell > 4$.

Appendix E

Explicit expressions for $\xi_1, ..., \xi_7$

Here we write explicitly the expressions for $\xi_1, ..., \xi_7$ introduced in Eqs. (3.114). Their expressions are given in terms of r_0, r_0^q, r_1, L_1 and E_1 (see Eqs. (3.100) (3.102) and (3.112)). In detail we have

$$
\begin{aligned}
\xi_1 = \frac{8\mathcal{K} r_0 \left(r_0^2 - 2Mr_0 + Q^2\right)}{C} \Big\{ & 24M^5 \left(23Q^2 r_0^4 + 21 r_0^6\right) - 6M^4 \left(295 Q^2 r_0^5 + 144 Q^4 r_0^3 + 85 r_0^7\right) \\
& + M^3 \left(1512 Q^2 r_0^6 + 2531 Q^4 r_0^4 + 660 Q^6 r_0^2 + 201 r_0^8\right) - 144 M^6 r_0^5 \\
& - 2M^2 \left(219 Q^2 r_0^7 + 900 Q^4 r_0^5 + 870 Q^6 r_0^3 + 118 Q^8 r_0 + 17 r_0^9\right) \\
& + M \left(543 Q^8 r_0^2 + 956 Q^6 r_0^4 + 371 Q^4 r_0^6 + 42 Q^2 r_0^8 + 30 Q^{10} + 2 r_0^{10}\right) \\
& - 4Q^4 r_0 \left(46 Q^4 r_0^2 + 27 Q^2 r_0^4 + 14 Q^6 + 5 r_0^6\right) \Big\} \\
& + 2\sqrt{\mathcal{K}} \frac{r_0^q}{Q} \Big[-8M^3 \left(61 Q^2 r_0^2 + 102 r_0^4\right) + M^2 \left(1187 Q^2 r_0^3 + 272 Q^4 r_0 + 709 r_0^5\right) + 288 M^4 r_0^3 \\
& - M \left(549 Q^4 r_0^2 + 723 Q^2 r_0^4 + 50 Q^6 + 254 r_0^6\right) + 8 \left(17 Q^2 r_0^5 + 22 Q^4 r_0^3 + 10 Q^6 r_0 + 4 r_0^7\right) \Big] \\
& + \left(r_0^2 - 2Mr_0 + Q^2\right) \Big[Q^2 r_0^2 \left(158 M r_0 - 60 M^2 - 45 r_0^2\right) \\
& + r_0^3 \left(48 M^3 - 122 M^2 r_0 + 61 M r_0^2 - 8 r_0^3\right) - 44 Q^4 r_0^2 + 12 Q^6 \Big] ,
\end{aligned}
$$

$$
\begin{aligned}
\xi_2 = \frac{4Qr_0}{C} \Bigg\{ & 2\mathcal{K} \left(5Q^6 - Mr_0^3 \left(12M^2 - 9Mr_0 + r_0^2 \right) + MQ^2 r_0^2 (27M - 14r_0) + 7Q^4 (r_0^2 - 3Mr_0) \right) \\
& \times \left(r_0^2 \left(24M^2 - 16Mr_0 + 3r_0^2 \right) + 3Q^2 r_0 (3r_0 - 10M) + 10Q^4 \right) \left(r_0^2 - 2Mr_0 + Q^2 \right)^3 \\
& + \mathcal{K} \Big[Q^4 r_0^2 \left(84M^2 - 81Mr_0 + 10r_0^2 \right) - 2MQ^2 r_0^3 \left(36M^2 - 44Mr_0 + 9r_0^2 \right) \\
& + Mr_0^4 \left(24M^3 - 36M^2 r_0 + 12Mr_0^2 - r_0^3 \right) + 8Q^6 r_0 (3r_0 - 5M) + 6Q^8 \Big] \\
& \times \Big[4Q^4 r_0^2 \left(22M^2 - 24Mr_0 + 3r_0^2 \right) - Q^2 r_0^3 \left(72M^3 - 96M^2 r_0 + 14Mr_0^2 + 3r_0^3 \right) \\
& + 4M^2 r_0^4 \left(6M^2 - 10Mr_0 + 3r_0^2 \right) + Q^6 r_0 (29r_0 - 42M) + 6Q^8 \Big] \Bigg\} \\
& - Q^7 r_0^2 \left(2\sqrt{\mathcal{K}} \frac{r_0^q}{Q} \left(468M^2 - 625Mr_0 + 72r_0^2 \right) + r_0 \left(54M^2 + 9Mr_0 + 80r_0^2 \right) \right) \\
& + Q^5 r_0^3 \Big[2\sqrt{\mathcal{K}} \frac{r_0^q}{Q} \left(864M^3 - 1400M^2 r_0 + 361Mr_0^2 - 12r_0^3 \right) \\
& + r_0 \left(420M^3 - 676M^2 r_0 + 645Mr_0^2 - 148r_0^3 \right) \Big] \\
& + Q^3 r_0^4 \Big[2\sqrt{\mathcal{K}} M \frac{r_0^q}{Q} \left(1524M^2 r_0 - 792M^3 - 668Mr_0^2 + 87r_0^3 \right) \\
& + r_0 \left(1068M^3 r_0 - 1094M^2 r_0^2 - 504M^4 + 413Mr_0^3 - 48r_0^4 \right) \Big] \\
& + MQr_0^5 \Big[2\sqrt{\mathcal{K}} \frac{r_0^q}{Q} \left(412M^2 r_0^2 - 648M^3 r_0 + 288M^4 - 104Mr_0^3 + 9r_0^4 \right) \\
& + r_0 \left(376M^2 r_0^2 - 336M^3 r_0 + 144M^4 - 168Mr_0^3 + 25r_0^4 \right) \Big] \\
& + 2Q^9 r_0 \left(2\sqrt{\mathcal{K}} \frac{r_0^q}{Q} (59M - 58r_0) + 3r_0 (10r_0 - 7M) \right) + 8Q^{11} \left(r_0 - 2\sqrt{\mathcal{K}} \frac{r_0^q}{Q} \right), \\
\xi_3 = Cr_0 \left(Q^2 - Mr_0 \right) \Bigg\{ & M^2 r_1 \Big[r_0^3 \left(12M^3 - 20M^2 r_0 + 17Mr_0^2 - 4r_0^3 \right) \\
& + 6MQ^2 r_0^2 (2M - 3r_0) + Q^4 r_0 (16r_0 - 19M) + 4Q^6 \Big] \\
& - 2r_0 \left(r_0^2 - 2Mr_0 + Q^2 \right)^2 \left(r_0^2 \left(8M^2 - 13Mr_0 + 4r_0^2 \right) + Q^2 r_0 (5r_0 - 2M) - 2Q^4 \right) \Bigg\},
\end{aligned}
$$

$$\xi_4 = \left(Q^2 - Mr_0\right)\mathcal{K}\Bigg\{Cr_0\left(r_0^2 - 2Mr_0 + Q^2\right)\Bigg[2(3r_0 - 2M)\left(Mr_0 - Q^2\right)\frac{r_0^q}{Q}r_1M^2$$
$$-\left(Q^4 + r_0(3r_0 - 4M)Q^2 + 2M(M - r_0)r_0^2\right)\frac{r_1^q}{Q}M^2 - 2(2M - 3r_0)r_0\left(r_0^2 - 2Mr_0 + Q^2\right)^2\frac{r_0^q}{Q}$$
$$+8(M - r_0)^2r_0^2\left(r_0^2 - 2Mr_0 + Q^2\right)\frac{r_0^q}{Q}\Bigg] - Cr_0\left(Q^2 - Mr_0\right)\left(r_0^2 - 2Mr_0 + Q^2\right)$$
$$\times\Bigg[8(r_0^qr_1 + r_0(r_1^q - 3r_0^q))\frac{M^3}{Q} + \left((8r_0^q - 5r_1^q)Q + 3\frac{r_0}{Q}(4r_0r_0^q - 2r_1r_0^q - r_0r_1^q)\right)M^2$$
$$+4r_0\left(3Q^2 + 2r_0^2\right)\frac{r_0^q}{Q}M - 4Q\left(Q^2 + 3r_0^2\right)r_0^q\Bigg] + 2\Bigg[\left(Q^4 + r_0(3r_0 - 4M)Q^2 + 2M(M - r_0)r_0^2\right)r_1M^2$$
$$+2(M - r_0)r_0^2\left(r_0^2 - 2Mr_0 + Q^2\right)^2\Bigg]\Bigg[2r_0\Big(6Q^8 + 8r_0(3r_0 - 5M)Q^6 + r_0^2\left(84M^2 - 81r_0M + 10r_0^2\right)Q^4$$
$$-2Mr_0^3\left(36M^2 - 44r_0M + 9r_0^2\right)Q^2 + Mr_0^4\left(24M^3 - 36r_0M^2 + 12r_0^2M - r_0^3\right)\Big)\sqrt{\mathcal{K}}$$
$$-3C\left(r_0^2 - 2Mr_0 + Q^2\right)\frac{r_0^q}{Q}\Bigg] - 2\Bigg[4r_0(3r_0 - 2r_1)M^3 + \left((5r_1 - 8r_0)Q^2 + r_0^2(3r_1 - 4r_0)\right)M^2$$
$$-2\left(r_0^4 + 3Q^2r_0^2\right)M + 4Q^2r_0\left(Q^2 + r_0^2\right)\Bigg]\Bigg[r_0\Big(16Q^{10} + 2r_0(29r_0 - 64M)Q^8$$
$$+r_0^2\left(386M^2 - 313r_0M + 48r_0^2\right)Q^6 + r_0^3\left(631r_0M^2 - 564M^3 - 184r_0^2M + 14r_0^3\right)Q^4$$
$$+Mr_0^4\left(408M^3 - 572r_0M^2 + 240r_0^2M - 33r_0^3\right)Q^2$$
$$+Mr_0^5\left(204r_0M^3 - 120M^4 - 116r_0^2M^2 + 27r_0^3M - 2r_0^4\right)\Big)\sqrt{\mathcal{K}}$$
$$-C\left(Q^2 - Mr_0\right)\left(Q^2 + r_0(3r_0 - 4M)\right)\frac{r_0^q}{Q}\Bigg]\Bigg\} - \Big\{6r_0^2(r_1 - 2r_0)M^4$$
$$-r_0\left((9r_1 - 20r_0)Q^2 + r_0^2(4r_0 + r_1)\right)M^3 + 2\left(9r_0^5 + 5Q^2r_0^3 + 2Q^4(r_1 - 2r_0)\right)M^2$$
$$-2\left(5r_0^6 + 9Q^2r_0^4 + 6Q^4r_0^2\right)M + 2r_0\left(Q^2 + r_0^2\right)\left(2Q^4 + r_0^2Q^2 + r_0^4\right)\Big\}\Big\{2r_0\Big[r_0(87M - 41r_0)Q^8 - 11Q^{10}$$
$$+r_0^2\left(-255M^2 + 209r_0M - 29r_0^2\right)Q^6 + r_0^3\left(360M^3 - 400r_0M^2 + 106r_0^2M - 7r_0^3\right)Q^4$$
$$+Mr_0^4\left(-252M^3 + 348r_0M^2 - 135r_0^2M + 17r_0^3\right)Q^2$$
$$+Mr_0^5\left(72M^4 - 120r_0M^3 + 64r_0^2M^2 - 14r_0^3M + r_0^4\right)\Big]\mathcal{K}^{3/2} - C\left(Mr_0 - Q^2\right)\frac{r_0^q}{Q}\Big[r_0(2r_0 - 3M)$$
$$\times\left(r_0^2 - 2Mr_0 + Q^2\right) + \left(3Q^2 + r_0(7r_0 - 10M)\right)\mathcal{K}\Big]\Bigg\},$$

$$\xi_5 = 4\Bigg\{\frac{r_0}{CM^2}\Bigg[C+Q^4r_0^2\left(84M^2-81Mr_0+10r_0^2\right)-2MQ^2r_0^3\left(36M^2-44Mr_0+9r_0^2\right)$$
$$+Mr_0^4\left(24M^3-36M^2r_0+12Mr_0^2-r_0^3\right)+8Q^6r_0(3r_0-5M)+6Q^8\Bigg]\Bigg[L_1M^2\sqrt{\mathcal{K}\left(Mr_0-Q^2\right)}$$
$$+Q^2\left(M^2(r_1-2r_0)-Mr_0^2+r_0^3\right)-Mr_0\left(M^2(r_1-2r_0)+r_0^3\right)+Q^4r_0\Bigg]+\frac{r_0r_1}{C}\Big[Cr_0(M-r_0)$$
$$+Q^6r_0^2\left(124M^2-105Mr_0+10r_0^2\right)+MQ^4r_0^3\left(169Mr_0-156M^2-28r_0^2\right)$$
$$+MQ^2r_0^4\left(96M^3-124M^2r_0+30Mr_0^2-r_0^3\right)+M^2r_0^5\left(36M^2r_0-24M^3-12Mr_0^2+r_0^3\right)$$
$$+2Q^8r_0(12r_0-23M)+6Q^{10}\Big]+\frac{r_0^2}{CM^2}\left(r_0^2-2Mr_0+Q^2\right)^2\Big[Q^4r_0^2\left(84M^2-81Mr_0+10r_0^2\right)$$
$$+C-2MQ^2r_0^3\left(36M^2-44Mr_0+9r_0^2\right)+Mr_0^4\left(-36M^2r_0+24M^3+12Mr_0^2-r_0^3\right)$$
$$+8Q^6r_0(3r_0-5M)+6Q^8\Big]+\frac{1}{\sqrt{\mathcal{K}}M^2Q}\Big[M^2r_0^qr_1\left(Q^2r_0(3r_0-4M)+2Mr_0^2(M-r_0)+Q^4\right)$$
$$-M^2r_0r_1^q\left(Q^2-Mr_0\right)\left(r_0^2-2Mr_0+Q^2\right)+2r_0^2r_0^q(M-r_0)\left(r_0^2-2Mr_0+Q^2\right)^2\Big]\Bigg\},$$

$$\xi_6 = \frac{4}{M^2}\Bigg\{\frac{\left(Mr_0-Q^2\right)}{\mathcal{K}Q}\Big[r_0^2M^2(4r_0r_0^q+r_0r_1^q-3r_0^qr_1)-M^2Q^2(8r_0r_0^q+r_0r_1^q-5r_0^qr_1)$$
$$+2M^3r_0(r_0(6r_0^q+r_1^q)-4r_0^qr_1)-2Mr_0^2r_0^q\left(3Q^2+r_0^2\right)+4Q^2r_0r_0^q\left(Q^2+r_0^2\right)\Big]$$
$$-\frac{2r_0\left(r_0^2-2Mr_0+Q^2\right)^2}{C\sqrt{(Mr_0-Q^2)\mathcal{K}}}\Big[MQ^2r_0^2(27M-14r_0)-Mr_0^3\left(12M^2-9Mr_0+r_0^2\right)$$
$$+7Q^4r_0(r_0-3M)+5Q^6\Big]\Big[2r_0\left(Q^2+r_0^2\right)\sqrt{Mr_0-Q^2}-M^2\left(\sqrt{\mathcal{K}}L_1$$
$$+2(2r_0-r_1)\sqrt{Mr_0-Q^2}\right)\Big]\Bigg\}-\frac{8L_1r_0^q\sqrt{\mathcal{K}\left(Mr_0-Q^2\right)}}{Q}$$
$$-\frac{1}{M^2\mathcal{K}^2}\Bigg\{\frac{r_0}{\sqrt{\mathcal{K}}}\Big[M^2\left(4Q^6+r_0(16r_0-19M)Q^4+6Mr_0^2(2M-3r_0)Q^2\right.$$
$$\left.+r_0^3\left(12M^3-20r_0M^2+17r_0^2M-4r_0^3\right)\right)r_1-2r_0\left(Q^2+r_0(r_0-2M)\right)^2$$
$$\times\left(r_0(5r_0-2M)Q^2-2Q^4+r_0^2\left(8M^2-13r_0M+4r_0^2\right)\right)\Big]+\frac{2}{CQ}\Big\{Cr_0\left(Q^2+r_0^2-2Mr_0\right)$$
$$\times\Big[2(2M-3r_0)\left(Q^2-Mr_0\right)r_0^qr_1M^2-\left(Q^4+r_0(3r_0-4M)Q^2+2M(M-r_0)r_0^2\right)r_1^qM^2$$

$$
\begin{aligned}
&-2(2M-3r_0)r_0\left(Q^2+r_0(r_0-2M)\right)^2 r_0^q+8(M-r_0)^2r_0^2\left(Q^2+r_0(r_0-2M)\right)r_0^q\Big]\\
&-Cr_0\left(Q^2-Mr_0\right)\left(Q^2+r_0(r_0-2M)\right)\Big[8(r_0^q r_1+r_0(r_1^q-3r_0^q))M^3\\
&+\left((8r_0^q-5r_1^q)Q^2+3r_0(4r_0r_0^q-2r_1r_0^q-r_0r_1^q)\right)M^2+4r_0\left(3Q^2+2r_0^2\right)r_0^qM-4Q^2\left(Q^2+3r_0^2\right)r_0^q\Big]\\
&+\frac{1}{\left(Q^2-Mr_0\right)\mathcal{K}}\Big[6r_0^2(r_1-2r_0)M^4-r_0\left((9r_1-20r_0)Q^2+r_0^2(4r_0+r_1)\right)M^3\\
&+2\left(9r_0^5+5Q^2r_0^3+2Q^4(r_1-2r_0)\right)M^2-2\left(5r_0^6+9Q^2r_0^4+6Q^4r_0^2\right)M+2r_0\left(Q^2+r_0^2\right)\left(2Q^4\right.\\
&\left.+r_0^2Q^2+r_0^4\right)\Big]\Big[2Qr_0\left(11Q^{10}+r_0(41r_0-87M)Q^8+r_0^2\left(255M^2-209r_0M+29r_0^2\right)Q^6\right.\\
&+r_0^3\left(7r_0^3-360M^3+400r_0M^2-106r_0^2M\right)Q^4+Mr_0^4\left(252M^3-348r_0M^2+135r_0^2M-17r_0^3\right)Q^2\\
&\left.-Mr_0^5\left(72M^4-120r_0M^3+64r_0^2M^2-14r_0^3M+r_0^4\right)\right)\mathcal{K}^{3/2}+C\left(Mr_0-Q^2\right)r_0^q\left((2r_0^2-3Mr_0)\right.\\
&\left.\times\left(Q^2+r_0(r_0-2M)\right)+\left(3Q^2+r_0(7r_0-10M)\right)\mathcal{K}\right)\Big]+2\Big[4r_0(3r_0-2r_1)M^3\\
&+\left((5r_1-8r_0)Q^2+r_0^2(3r_1-4r_0)\right)M^2-2\left(r_0^4+3Q^2r_0^2\right)M+4Q^2r_0\left(Q^2+r_0^2\right)\Big]\\
&\times\Big[C\left(Q^2-Mr_0\right)\left(Q^2+r_0(3r_0-4M)\right)r_0^q+Qr_0\left(2r_0(64M-29r_0)Q^8-16Q^{10}\right.\\
&+r_0^2\left(313r_0M-386M^2-48r_0^2\right)Q^6+r_0^3\left(564M^3-631r_0M^2+184r_0^2M-14r_0^3\right)Q^4\\
&+Mr_0^4\left(-408M^3+572r_0M^2-240r_0^2M+33r_0^3\right)Q^2\\
&\left.+Mr_0^5\left(120M^4-204r_0M^3+116r_0^2M^2-27r_0^3M+2r_0^4\right)\right)\sqrt{\mathcal{K}}\Big]\\
&-2\Big[\left(Q^4+r_0(3r_0-4M)Q^2+2M(M-r_0)r_0^2\right)r_1M^2+2(M-r_0)r_0^2\left(r_0^2-2Mr_0+Q^2\right)^2\Big]\\
&\times\Big[3C\left(r_0^2-2Mr_0+Q^2\right)r_0^q-2Qr_0\left(6Q^8+8r_0(3r_0-5M)Q^6+r_0^2\left(84M^2-81r_0M+10r_0^2\right)Q^4\right.\\
&\left.\left.-2Mr_0^3\left(36M^2-44r_0M+9r_0^2\right)Q^2+Mr_0^4\left(24M^3-36r_0M^2+12r_0^2M-r_0^3\right)\right)\sqrt{\mathcal{K}}\Big]\right\}\Bigg\},
\end{aligned}
$$

$$
\begin{aligned}
\xi_7 = {} & 2E_1M^2Q\left(Q^2-Mr_0\right)\Big[6Q^8+8r_0(3r_0-5M)Q^6+r_0^2\left(84M^2-81r_0M+10r_0^2\right)Q^4 \\
& -2Mr_0^3\left(36M^2-44r_0M+9r_0^2\right)Q^2+C+Mr_0^4\left(24M^3-36r_0M^2+12r_0^2M-r_0^3\right)\Big]\mathcal{K}r_0^3 \\
& -M^2Q\left(r_0^2-2Mr_0+Q^2\right)\Big\{2E_1r_0^2\left(r_0^2-2Mr_0+Q^2\right)\Big[5Q^6+7r_0(r_0-3M)Q^4 \\
& +Mr_0^2(27M-14r_0)Q^2-Mr_0^3\left(12M^2-9r_0M+r_0^2\right)\Big]-L_1\sqrt{Mr_0-Q^2}\Big[6Q^8+C \\
& +8r_0(3r_0-5M)Q^6+r_0^2\left(84M^2-81r_0M+10r_0^2\right)Q^4-2Mr_0^3\left(36M^2-44r_0M+9r_0^2\right)Q^2 \\
& +Mr_0^4\left(24M^3-36r_0M^2+12r_0^2M-r_0^3\right)\Big]\Big\}\mathcal{K}r_0 \\
& +\left(Q^2-Mr_0\right)\Big\{CQ\left(5Q^2+r_0(3r_0-8M)\right)r_1M^2 \\
& +Cr_0\Big[\left(r_0^2-2Mr_0+Q^2\right)\left((E_1^qr_0-4Q)M^2-4Qr_0M+4Q\left(Q^2+r_0^2\right)\right) \\
& -2E_1M^2\mathcal{K}r_0^q\Big]+2Q\Big[6Q^8+8r_0(3r_0-5M)Q^6+r_0^2\left(84M^2-81r_0M+10r_0^2\right)Q^4 \\
& -2Mr_0^3\left(36M^2-44r_0M+9r_0^2\right)Q^2+Mr_0^4\left(24M^3-36r_0M^2+12r_0^2M-r_0^3\right)\Big]\Big[\mathcal{K}r_1M^2 \\
& +2r_0\left(Q^2-M^2-r_0M+r_0^2\right)\left(r_0^2-2Mr_0+Q^2\right)\Big]\Big\}\sqrt{\mathcal{K}}r_0+\left(r_0^2-2Mr_0+Q^2\right) \\
& \times\Big\{2C\left(Mr_0-Q^2\right)\left(10Q^2+3r_0(r_0-4M)\right)r_0^qr_1M^2-2Cr_0\left(Mr_0-Q^2\right)\mathcal{K}r_1^qM^2 \\
& +CL_1^qr_0\left(r_0^2-2Mr_0+Q^2\right)\sqrt{Mr_0\mathcal{K}-Q^2\mathcal{K}}M^2-4Qr_0\left(r_0^2-2Mr_0+Q^2\right) \\
& \times\Big[5Q^6+7r_0(r_0-3M)Q^4+Mr_0^2(27M-14r_0)Q^2-Mr_0^3\left(12M^2-9r_0M+r_0^2\right)\Big]\sqrt{\mathcal{K}} \\
& \times\left(r_1\mathcal{K}M^2+2r_0\left(Q^2-M^2-r_0M+r_0^2\right)\left(r_0^2-2Mr_0+Q^2\right)\right) \\
& +2Cr_0^q\sqrt{Mr_0-Q^2}\Big[3r_0\left(4r_0\sqrt{Mr_0-Q^2}+L_1\sqrt{\mathcal{K}}\right)M^3 \\
& -\left(2\left(4r_0\sqrt{Mr_0-Q^2}+L_1\sqrt{\mathcal{K}}\right)Q^2+r_0^2\left(L_1\sqrt{\mathcal{K}}-4r_0\sqrt{Mr_0-Q^2}\right)\right)M^2 \\
& -6r_0^2\sqrt{Mr_0-Q^2}\left(3Q^2+r_0^2\right)M+8Q^2r_0\left(Q^2+r_0^2\right)\sqrt{Mr_0-Q^2}\Big]\Big\}.
\end{aligned}
$$

In the above expressions, C is given in Eq. (3.103) and for convenience we introduced $\mathcal{K} = r_0^2 - 3Mr_0 + 2Q^2$.

Bibliography

[1] L. collaboration and V. collaboration, *Observation of gravitational waves from a binary black hole merger*, Physical Review Letters **116** (Feb., 2016).

[2] S. Kuroyanagi, T. Chiba and T. Takahashi, *Probing the universe through the stochastic gravitational wave background*, Journal of Cosmology and Astroparticle Physics **2018** (Nov., 2018) 038–038.

[3] R. Roshan and G. White, *Using gravitational waves to see the first second of the universe*, 2024.

[4] T. Kahniashvili, "Gravitational Waves as a Probe of the Early Universe." NASA Proposal id. 21-ATP21-141, Jan., 2021.

[5] J. M. Ezquiaga and M. Zumalacárregui, *Dark energy in light of multi-messenger gravitational-wave astronomy*, Frontiers in Astronomy and Space Sciences **5** (Dec., 2018).

[6] E. Maggio, *Probing the Horizon of Black Holes with Gravitational Waves*, p. 333–346. Springer International Publishing, 2023.

[7] E. Maggio, *Probing new physics on the horizon of black holes with gravitational waves*, 2022.

[8] **LIGO Scientific, Virgo** Collaboration, B. P. Abbott *et. al.*, *GWTC-1: A Gravitational-Wave Transient Catalog of Compact Binary Mergers Observed by LIGO and Virgo during the First and Second Observing Runs*, Phys. Rev. X **9** (2019), no. 3 031040 [1811.12907].

[9] M. Mapelli, *Binary black hole mergers: Formation and populations*, Frontiers in Astronomy and Space Sciences **7** (July, 2020).

[10] M. Mapelli, *Formation Channels of Single and Binary Stellar-Mass Black Holes*, p. 1–65. Springer Singapore, 2021.

[11] M. Zevin, *Deciphering the Landscape of Binary Black Hole Formation Channels*, in *American Astronomical Society Meeting Abstracts #235*,

vol. 235 of *American Astronomical Society Meeting Abstracts*, p. 253.06, Jan., 2020.

[12] C. L. Rodriguez, S. Chatterjee and F. A. Rasio, *Binary black hole mergers from globular clusters: Masses, merger rates, and the impact of stellar evolution*, **93** (Apr., 2016) 084029 [1602.02444].

[13] K. Belczynski, V. Kalogera and T. Bulik, *A Comprehensive Study of Binary Compact Objects as Gravitational Wave Sources: Evolutionary Channels, Rates, and Physical Properties*, **572** (June, 2002) 407–431 [astro-ph/0111452].

[14] M. Dominik, K. Belczynski, C. Fryer, D. E. Holz, E. Berti, T. Bulik, I. Mandel and R. O'Shaughnessy, *Double Compact Objects. I. The Significance of the Common Envelope on Merger Rates*, **759** (Nov., 2012) 52 [1202.4901].

[15] P. C. Peters, *Gravitational Radiation and the Motion of Two Point Masses*, Physical Review **136** (Nov., 1964) 1224–1232.

[16] M. Maggiore, *Gravitational Waves. Vol. 1: Theory and Experiments*. Oxford University Press, 2007.

[17] K. Silsbee and S. Tremaine, *Lidov–kozai cycles with gravitational radiation: Merging black holes in isolated triple systems*, The Astrophysical Journal **836** (Feb., 2017) 39.

[18] F. Antonini, S. Chatterjee, C. L. Rodriguez, M. Morscher, B. Pattabiraman, V. Kalogera and F. A. Rasio, *Black hole mergers and blue stragglers from hierarchical triples formed in globular clusters*, The Astrophysical Journal **816** (jan, 2016) 65.

[19] L. Randall and Z.-Z. Xianyu, *An Analytical Portrait of Binary Mergers in Hierarchical Triple Systems*, Astrophys. J. **864** (2018), no. 2 134 [1802.05718].

[20] S. Naoz, *The eccentric kozai-lidov effect and its applications*, Annual Review of Astronomy and Astrophysics **54** (2016), no. Volume 54, 2016 441–489.

[21] M. Dall'Amico, M. Mapelli, S. Torniamenti and M. Arca Sedda, *Eccentric black hole mergers via three-body interactions in young, globular, and nuclear star clusters*, **683** (Mar., 2024) A186 [2303.07421].

[22] M. A. S. Martinez, C. L. Rodriguez and G. Fragione, *On the mass ratio distribution of black hole mergers in triple systems*, The Astrophysical Journal **937** (sep, 2022) 78.

[23] L. Liu and S. P. Kim, *Gravitational and electromagnetic radiations from binary black holes with electric and magnetic charges*, in *5TH INTERNATIONAL CONFERENCE ON EARTH SCIENCE, MINERALS, AND ENERGY (ICEMINE)*, vol. 3019, p. 020001, AIP Publishing, 2024.

[24] M. Arca Sedda, G. Li and B. Kocsis, *Order in the chaos. Eccentric black hole binary mergers in triples formed via strong binary-binary scatterings*, **650** (June, 2021) A189 [1805.06458].

[25] H. V. Zeipel, *Sur l'application des séries de m. lindstedt à l'étude du mouvement des comètes périodiques*, Astronomische Nachrichten **183** (1909), no. 22-24 345–418 [https://onlinelibrary.wiley.com/doi/pdf/10.1002/asna.19091832202].

[26] M. Lidov, *The evolution of orbits of artificial satellites of planets under the action of gravitational perturbations of external bodies*, Planetary and Space Science **9** (1962), no. 10 719–759.

[27] Y. Kozai, *Secular perturbations of asteroids with high inclination and eccentricity*, **67** (Nov., 1962) 591–598.

[28] B.-M. Hoang, S. Naoz, B. Kocsis, F. A. Rasio and F. Dosopoulou, *Black Hole Mergers in Galactic Nuclei Induced by the Eccentric Kozai–Lidov Effect*, Astrophys. J. **856** (2018), no. 2 140 [1706.09896].

[29] F. Antonini, S. Toonen and A. S. Hamers, *Binary black hole mergers from field triples: properties, rates and the impact of stellar evolution*, Astrophys. J. **841** (2017), no. 2 77 [1703.06614].

[30] Y. Lithwick and S. Naoz, *The eccentric kozai mechanism for a test particle*, The Astrophysical Journal **742** (nov, 2011) 94.

[31] F. A. Rasio, S. McMillan and P. Hut, *Binary-Binary interactions and the formation of the PSR B1620-26 triple system in M4*, Astrophys. J. Lett. **438** (1995) L33 [astro-ph/9409056].

[32] D. Mar´in Pina and M. Gieles, *Demographics of three-body binary black holes in star clusters: implications for gravitational waves*, Monthly Notices of the Royal Astronomical Society **527** (12, 2023) 8369–8381 [https://academic.oup.com/mnras/article-pdf/527/3/8369/54580464/stad3777.pdf].

[33] S. Naoz, T. Fragos, A. Geller, A. P. Stephan and F. A. Rasio, *Formation of black hole low-mass x-ray binaries in hierarchical triple systems*, The Astrophysical Journal Letters **822** (May, 2016) L24.

[34] J. M. O. Antognini and T. A. Thompson, *Dynamical formation and scattering of hierarchical triples: cross-sections, Kozai–Lidov oscillations, and collisions*, Mon. Not. Roy. Astron. Soc. **456** (2016), no. 4 4219–4246 [1507.03593].

[35] F. Antonini and H. B. Perets, *Secular evolution of compact binaries near massive black holes: Gravitational wave sources and other exotica*, The Astrophysical Journal **757** (aug, 2012) 27.

[36] H. Lim and C. L. Rodriguez, *Relativistic three-body effects in hierarchical triples*, Phys. Rev. D **102** (2020), no. 6 064033 [2001.03654].

[37] S. Naoz, W. M. Farr, Y. Lithwick, F. A. Rasio and J. Teyssandier, *Secular dynamics in hierarchical three-body systems*, Monthly Notices of the Royal Astronomical Society **431** (03, 2013) 2155–2171 [https://academic.oup.com/mnras/article-pdf/431/3/2155/4890577/stt302.pdf].

[38] E. Michaely and H. B. Perets, *Secular dynamics in hierarchical three-body systems with mass loss and mass transfer*, Astrophys. J. **794** (2014) 122 [1406.3035].

[39] C. M. Will, *Higher-order effects in the dynamics of hierarchical triple systems. Quadrupole-squared terms*, Phys. Rev. D **103** (2021), no. 6 063003 [2011.13286].

[40] Y. Fang and Q.-G. Huang, *Three body first post-Newtonian effects on the secular dynamics of a compact binary near a spinning supermassive black hole*, Phys. Rev. D **102** (2020), no. 10 104002 [2004.09390].

[41] C. M. Will, *Orbital flips in hierarchical triple systems: relativistic effects and third-body effects to hexadecapole order*, Phys. Rev. D **96** (2017), no. 2 023017 [1705.03962].

[42] C. M. Will, *Post-Newtonian effects in N-body dynamics: conserved quantities in hierarchical triple systems*, Class. Quant. Grav. **31** (2014), no. 24 244001 [1404.7724].

[43] S. Naoz, B. Kocsis, A. Loeb and N. Yunes, *Resonant Post-Newtonian Eccentricity Excitation in Hierarchical Three-body Systems*, Astrophys. J. **773** (2013) 187 [1206.4316].

[44] M. Bonetti, F. Haardt, A. Sesana and E. Barausse, *Post-Newtonian evolution of massive black hole triplets in galactic nuclei – II. Survey of the parameter space*, Mon. Not. Roy. Astron. Soc. **477** (2018), no. 3 3910–3926 [1709.06088].

[45] B. Liu, D. Lai and Y.-H. Wang, *Black Hole and Neutron Star Binary Mergers in Triple Systems: II. Merger Eccentricity and Spin-Orbit Misalignment*, 1905.00427.

[46] Z. Pan, H. Yang, L. Bernard and B. Bonga, *Resonant dynamics of extreme mass-ratio inspirals in a perturbed Kerr spacetime*, Phys. Rev. D **108** (2023), no. 10 104026 [2306.06576].

[47] H. Yang, B. Bonga, Z. Peng and G. Li, *Relativistic mean motion resonance*, Phys. Rev. D **100** (Dec, 2019) 124056.

[48] W. Hao, R. Spurzem, T. Naab, L. Wang, M. B. N. Kouwenhoven, P. Amaro-Seoane and R. A. Mardling, *Resonant motions of supermassive black hole triples*, IAU Symp. **312** (2016) 101–104.

[49] A. Kuntz, *Precession resonances in hierarchical triple systems*, Physical Review D **105** (Jan., 2022).

[50] **LISA** Collaboration, P. A. Seoane *et. al.*, *Astrophysics with the Laser Interferometer Space Antenna*, Living Rev. Rel. **26** (2023), no. 1 2 [2203.06016].

[51] M. Punturo *et. al.*, *The Einstein Telescope: A third-generation gravitational wave observatory*, Class. Quant. Grav. **27** (2010) 194002.

[52] P. Peng and X. Chen, *The last migration trap of compact objects in AGN accretion disc*, Mon. Not. Roy. Astron. Soc. **505** (2021), no. 1 1324–1333 [2104.07685].

[53] J. M. Bellovary, M.-M. M. Low, B. McKernan and K. E. S. Ford, *MIGRATION TRAPS IN DISKS AROUND SUPERMASSIVE BLACK HOLES*, The Astrophysical Journal **819** (mar, 2016) L17.

[54] A. Secunda, B. Hernandez, J. Goodman, N. W. C. Leigh, B. McKernan, K. E. S. Ford and J. I. Adorno, *Evolution of retrograde orbiters in an active galactic nucleus disk*, The Astrophysical Journal Letters **908** (feb, 2021) L27.

[55] A. Santini, D. Gerosa and R. Cotesta, *Migration traps in AGN disks and hierarchical mergers as promising origin of the observed q-ef$_f$ correlation*, in *APS April Meeting Abstracts*, vol. 2023 of *APS Meeting Abstracts*, p. M14.001, Jan., 2023.

[56] H. Tagawa, Z. Haiman and B. Kocsis, *Formation and Evolution of Compact-object Binaries in AGN Disks*, **898** (July, 2020) 25 [1912.08218].

[57] Z. Zhang and X. Chen, *The Dynamics and Gravitational-wave Signal of a Binary Flying Closely by a Kerr Supermassive Black Hole*, Astrophys. J. **968** (2024), no. 2 122 [2402.02178].

[58] P. Amaro-Seoane, H. Audley, S. Babak, J. Baker, E. Barausse, P. Bender, E. Berti, P. Binetruy, M. Born, D. Bortoluzzi, J. Camp, C. Caprini, V. Cardoso, M. Colpi, J. Conklin, N. Cornish, C. Cutler, K. Danzmann, R. Dolesi, L. Ferraioli, V. Ferroni, E. Fitzsimons, J. Gair, L. Gesa Bote, D. Giardini, F. Gibert, C. Grimani, H. Halloin, G. Heinzel, T. Hertog, M. Hewitson, K. Holley-Bockelmann, D. Hollington, M. Hueller, H. Inchauspe, P. Jetzer, N. Karnesis, C. Killow, A. Klein, B. Klipstein, N. Korsakova, S. L. Larson, J. Livas, I. Lloro, N. Man, D. Mance, J. Martino, I. Mateos, K. McKenzie, S. T. McWilliams, C. Miller, G. Mueller, G. Nardini, G. Nelemans, M. Nofrarias, A. Petiteau, P. Pivato, E. Plagnol, E. Porter, J. Reiche, D. Robertson, N. Robertson, E. Rossi, G. Russano, B. Schutz, A. Sesana, D. Shoemaker, J. Slutsky, C. F. Sopuerta, T. Sumner, N. Tamanini, I. Thorpe, M. Troebs, M. Vallisneri, A. Vecchio, D. Vetrugno, S. Vitale, M. Volonteri, G. Wanner, H. Ward, P. Wass, W. Weber, J. Ziemer and P. Zweifel, *Laser Interferometer Space Antenna*, arXiv e-prints (Feb., 2017) arXiv:1702.00786 [1702.00786].

[59] W.-R. Hu and Y.-L. Wu, *The Taiji Program in Space for gravitational wave physics and the nature of gravity*, National Science Review **4** (10, 2017) 685–686 [https://academic.oup.com/nsr/article-pdf/4/5/685/31566708/nwx116.pdf].

[60] W.-H. Ruan, Z.-K. Guo, R.-G. Cai and Y.-Z. Zhang, *Taiji program: Gravitational-wave sources*, International Journal of Modern Physics A **35** (2020), no. 17 2050075 [https://doi.org/10.1142/S0217751X2050075X].

[61] J. Luo, L.-S. Chen, H.-Z. Duan, Y.-G. Gong, S. Hu, J. Ji, Q. Liu, J. Mei, V. Milyukov, M. Sazhin, C.-G. Shao, V. T. Toth, H.-B. Tu, Y. Wang, Y. Wang, H.-C. Yeh, M.-S. Zhan, Y. Zhang, V. Zharov and Z.-B. Zhou, *Tianqin: a space-borne gravitational wave detector*, Classical and Quantum Gravity **33** (jan, 2016) 035010.

[62] J. Mei, Y.-Z. Bai, J. Bao, E. Barausse, L. Cai, E. Canuto, B. Cao, W.-M. Chen, Y. Chen, Y.-W. Ding, H.-Z. Duan, H. Fan, W.-F. Feng, H. Fu, Q. Gao, T. Gao, Y. Gong, X. Gou, C.-Z. Gu, D.-F. Gu, Z.-Q. He, M. Hendry, W. Hong, X.-C. Hu, Y.-M. Hu, Y. Hu, S.-J. Huang, X.-Q. Huang, Q. Jiang, Y.-Z. Jiang, Y. Jiang, Z. Jiang, H.-M. Jin, V. Korol, H.-Y. Li, M. Li, M. Li, P. Li, R. Li, Y. Li, Z. Li, Z. Li, Z.-X. Li, Y.-R. Liang, Z.-C. Liang, F.-J. Liao, Q. Liu, S. Liu, Y.-C. Liu,

L. Liu, P.-B. Liu, X. Liu, Y. Liu, X.-F. Lu, Y. Lu, Z.-H. Lu, Y. Luo, Z.-C. Luo, V. Milyukov, M. Ming, X. Pi, C. Qin, S.-B. Qu, A. Sesana, C. Shao, C. Shi, W. Su, D.-Y. Tan, Y. Tan, Z. Tan, L.-C. Tu, B. Wang, C.-R. Wang, F. Wang, G.-F. Wang, H. Wang, J. Wang, L. Wang, P. Wang, X. Wang, Y. Wang, Y.-F. Wang, R. Wei, S.-C. Wu, C.-Y. Xiao, X.-S. Xu, C. Xue, F.-C. Yang, L. Yang, M.-L. Yang, S.-Q. Yang, B. Ye, H.-C. Yeh, S. Yu, D. Zhai, C. Zhang, H. Zhang, J.-d. Zhang, J. Zhang, L. Zhang, X. Zhang, X. Zhang, H. Zhou, M.-Y. Zhou, Z.-B. Zhou, D.-D. Zhu, T.-G. Zi and J. Luo, *The TianQin project: Current progress on science and technology*, Progress of Theoretical and Experimental Physics **2021** (08, 2020) 05A107 [https://academic.oup.com/ptep/article-pdf/2021/5/05A107/37953035/ptaa114.pdf].

[63] Y. Gong, J. Luo and B. Wang, *Concepts and status of chinese space gravitational wave detection projects*, Nature Astronomy **5** (2021), no. 9 881–889.

[64] C. Berry, S. Hughes, C. Sopuerta, A. Chua, A. Heffernan, K. Holley-Bockelmann, D. Mihaylov, C. Miller and A. Sesana, *The unique potential of extreme mass-ratio inspirals for gravitational-wave astronomy*, **51** (May, 2019) 42 [1903.03686].

[65] X. Chen and W.-B. Han, *A New Type of Extreme-mass-ratio Inspirals Produced by Tidal Capture of Binary Black Holes*, Communications Physics **1** (2018) 53 [1801.05780].

[66] Y. Yin, J. Mathews, A. J. K. Chua and X. Chen, *A relativistic model of b-EMRI systems and their gravitational radiation*, 2410.09796.

[67] K. Meng, H. Zhang, X.-L. Fan and Y. Yong, *Distinguish the EMRI and B-EMRI system by gravitational waves*, 2405.07113.

[68] Y. Jiang, W.-B. Han, X.-Y. Zhong, P. Shen, Z.-R. Luo and Y.-L. Wu, *Distinguishability of binary extreme-mass-ratio inspirals in low frequency band*, Eur. Phys. J. C **84** (2024), no. 5 478.

[69] J.-A. Marck, *Solution to the equations of parallel transport in Kerr geometry; tidal tensor*, Proc. R. Soc. Lond. A **385** (1983) 431–438.

[70] E. Poisson and I. Vlasov, *Geometry and dynamics of a tidally deformed black hole*, Phys. Rev. D **81** (2010) 024029 [0910.4311].

[71] V. Cardoso and A. Foschi, *Geodesic structure and quasinormal modes of a tidally perturbed spacetime*, Phys. Rev. D **104** (2021), no. 2 024004 [2106.06551].

[72] H. Yang and M. Casals, *General Relativistic Dynamics of an Extreme Mass-Ratio Binary interacting with an External Body*, Phys. Rev. D **96** (2017), no. 8 083015 [1704.02022].

[73] R. M. Wald, *Black hole in a uniform magnetic field*, Phys. Rev. D **10** (Sep, 1974) 1680–1685.

[74] J. Maldacena, *Comments on magnetic black holes*, Journal of High Energy Physics **2021** (Apr., 2021).

[75] D. Ghosh, A. Thalapillil and F. Ullah, *Astrophysical hints for magnetic black holes*, Physical Review D **103** (Jan., 2021).

[76] B. McInnes, *About magnetic ads black holes*, 2020.

[77] D. Pereñiguez, *Black hole perturbations and electric-magnetic duality*, 2023.

[78] R. Emparan and M. Mart´inez, *Exact event horizon of a black hole merger*, Classical and Quantum Gravity **33** (June, 2016) 155003.

[79] J. Kormendy and D. Richstone, *Inward bound—the search for supermassive black holes in galactic nuclei*, Annual Review of Astronomy and Astrophysics **33** (1995), no. Volume 33, 1995 581–624.

[80] J. Kormendy and L. C. Ho, *Coevolution (or not) of supermassive black holes and host galaxies*, Annual Review of Astronomy and Astrophysics **51** (2013), no. Volume 51, 2013 511–653.

[81] T. J. Herczeg, *A survey of third components in spectroscopic and eclipsing systems*, Astrophysics and Space Science **142** (1988), no. 1 89–95.

[82] A. A. Tokovinin, *On the multiplicity of spectroscopic binary stars*, Astronomy Letters **23** (Nov., 1997) 727–730.

[83] P. P. Eggleton, L. Kisseleva-Eggleton and X. Dearborn, *The Incidence of Multiplicity Among Bright Stellar Systems*, in *Binary Stars as Critical Tools & Tests in Contemporary Astrophysics* (W. I. Hartkopf, P. Harmanec and E. F. Guinan, eds.), vol. 240 of *IAU Symposium*, pp. 347–355, Aug., 2007.

[84] A. Tokovinin, *From binaries to multiples. ii. hierarchical multiplicity of f and g dwarfs*, The Astronomical Journal **147** (mar, 2014) 87.

[85] A. Tokovinin, *Comparative statistics and origin of triple and quadruple stars*, Monthly Notices of the Royal Astronomical Society **389** (09, 2008) 925–938 [https://academic.oup.com/mnras/article-pdf/389/2/925/17319921/mnras0389-092

[86] A. Tokovinin, *From binaries to multiples. i. data on f and g dwarfs within 67 pc of the sun*, The Astronomical Journal **147** (2014).

[87] P. P. Eggleton and A. A. Tokovinin, *A catalogue of multiplicity among bright stellar systems*, **389** (Sept., 2008) 869–879 [0806.2878].

[88] J. E. Grindlay, C. D. Bailyn, H. Cohn, P. M. Lugger, J. R. Thorstensen and G. Wegner, *Discovery of a Possible X-Ray Triple: 4U 1915-05*, **334** (Nov., 1988) L25.

[89] S. Prodan and N. Murray, *On the dynamics and tidal dissipation rate of the white dwarf in 4u 1820-30*, The Astrophysical Journal **747** (feb, 2012) 4.

[90] H. A. Knutson, B. J. Fulton, B. T. Montet, M. Kao, H. Ngo, A. W. Howard, J. R. Crepp, S. Hinkley, G. Bakos, K. Batygin, J. A. Johnson, T. D. Morton and P. S. Muirhead, *Friends of hot jupiters. i. a radial velocity search for massive, long-period companions to close-in gas giant planets*, The Astrophysical Journal **785** (apr, 2014) 126.

[91] S. N. Quinn, R. J. White, D. W. Latham, L. A. Buchhave, G. Torres, R. P. Stefanik, P. Berlind, A. Bieryla, M. C. Calkins, G. A. Esquerdo, G. Fűrész, J. C. Geary and A. H. Szentgyorgyi, *Hd 285507b: An eccentric hot jupiter in the hyades open cluster*, The Astrophysical Journal **787** (apr, 2014) 27.

[92] H. Ngo, H. A. Knutson, S. Hinkley, J. R. Crepp, E. B. Bechter, K. Batygin, A. W. Howard, J. A. Johnson, T. D. Morton and P. S. Muirhead, *Friends of hot jupiters. ii. no correspondence between hot-jupiter spin–orbit misalignment and the incidence of directly imaged stellar companions*, The Astrophysical Journal **800** (feb, 2015) 138.

[93] J. Wang, D. A. Fischer, E. P. Horch and J.-W. Xie, *Influence of stellar multiplicity on planet formation. iii. adaptive optics imaging of kepler stars with gas giant planets*, The Astrophysical Journal **806** (jun, 2015) 248.

[94] N. M. Law, T. Morton, C. Baranec, R. Riddle, G. Ravichandran, C. Ziegler, J. A. Johnson, S. P. Tendulkar, K. Bui, M. P. Burse, H. K. Das, R. G. Dekany, S. Kulkarni, S. Punnadi and A. N. Ramaprakash, *Robotic Laser Adaptive Optics Imaging of 715 Kepler Exoplanet Candidates Using Robo-AO*, **791** (Aug., 2014) 35 [1312.4958].

[95] D. Polishook and N. Brosch, *Many binaries among NEAs*, astro-ph/0607128.

[96] D. Polishook and N. Brosch, *Photometry and spin rate distribution of small-sized main belt asteroids*, Icarus **199** (2009), no. 2 319–332.

[97] D. Nesvorný, D. Vokrouhlický, W. F. Bottke, K. Noll and H. F. Levison, *Observed binary fraction sets limits on the extent of collisional grinding in the kuiper belt*, The Astronomical Journal **141** (apr, 2011) 159.

[98] J. L. Margot, P. Pravec, P. Taylor, B. Carry and S. Jacobson, *Asteroid Systems: Binaries, Triples, and Pairs*, in *Asteroids IV* (P. Michel, F. E. DeMeo and W. F. Bottke, eds.), pp. 355–374. 2015.

[99] t. V. C. R. Abbott et al. (The LIGO Scientific Collaboration and the KAGRA Collaboration), *Open data from the third observing run of ligo, virgo, kagra, and geo*, The Astrophysical Journal Supplement Series **267** (jul, 2023) 29.

[100] J. Samsing, *Eccentric black hole mergers forming in globular clusters*, Phys. Rev. D **97** (May, 2018) 103014.

[101] J. Samsing and E. Ramirez-Ruiz, *On the assembly rate of highly eccentric binary black hole mergers*, The Astrophysical Journal Letters **840** (may, 2017) L14.

[102] J. Samsing, M. MacLeod and E. Ramirez-Ruiz, *Dissipative evolution of unequal-mass binary–single interactions and its relevance to gravitational-wave detections*, The Astrophysical Journal **853** (feb, 2018) 140.

[103] J. Samsing, M. MacLeod and E. Ramirez-Ruiz, *Formation of tidal captures and gravitational wave inspirals in binary-single interactions*, The Astrophysical Journal **846** (aug, 2017) 36.

[104] J. Samsing and T. Ilan, *Topology of black hole binary–single interactions*, Monthly Notices of the Royal Astronomical Society **476** (01, 2018) 1548–1560 [https://academic.oup.com/mnras/article-pdf/476/2/1548/24282700/sty197.pdf].

[105] J. Samsing, M. MacLeod and E. Ramirez-Ruiz, *The formation of eccentric compact binary inspirals and the role of gravitational wave emission in binary–single stellar encounters*, The Astrophysical Journal **784** (mar, 2014) 71.

[106] M. J. Valtonen, *Triple black hole systems formed in mergers of galaxies*, Monthly Notices of the Royal Astronomical Society **278** (01, 1996) 186–190 [https://academic.oup.com/mnras/article-pdf/278/1/186/3459899/278-1-186.pdf].

[107] T. Di Matteo, V. Springel and L. Hernquist, *Energy input from quasars regulates the growth and activity of black holes and their host galaxies*, **433** (Feb., 2005) 604–607 [astro-ph/0502199].

[108] F. M. Khan, I. Berentzen, P. Berczik, A. Just, L. Mayer, K. Nitadori and S. Callegari, *Formation and hardening of supermassive black hole binaries in minor mergers of disk galaxies*, The Astrophysical Journal **756** (aug, 2012) 30.

[109] G. Kulkarni and A. Loeb, *Formation of galactic nuclei with multiple supermassive black holes at high redshifts*, Monthly Notices of the Royal Astronomical Society **422** (04, 2012) 1306–1323 [https://academic.oup.com/mnras/article-pdf/422/2/1306/3477162/mnras0422-1306.pdf].

[110] A. Generozov and H. B. Perets, *A Triple Scenario for the Formation of Wide Black Hole Binaries Such as Gaia BH1*, **964** (Mar., 2024) 83 [2312.03066].

[111] S. Toonen, T. C. N. Boekholt and S. Portegies Zwart, *Stellar triples on the edge. Comprehensive overview of the evolution of destabilised triples leading to stellar and binary exotica*, **661** (May, 2022) A61 [2108.04272].

[112] T. Hayashi, A. A. Trani and Y. Suto, *Dynamical Disruption Timescales and Chaotic Behavior of Hierarchical Triple Systems*, **939** (Nov., 2022) 81 [2207.12672].

[113] R. A. Mardling and S. J. Aarseth, *Tidal interactions in star cluster simulations*, Monthly Notices of the Royal Astronomical Society **321** (03, 2001) 398–420 [https://academic.oup.com/mnras/article-pdf/321/3/398/3830910/321-3-398.pdf].

[114] M. C. Miller, M. Freitag, D. P. Hamilton and V. M. Lauburg, *Binary encounters with supermassive black holes: Zero-eccentricity lisa events*, The Astrophysical Journal **631** (sep, 2005) L117.

[115] H. B. Perets and S. Naoz, *Kozai Cycles, Tidal Friction, and the Dynamical Evolution of Binary Minor Planets*, **699** (July, 2009) L17–L21 [0809.2095].

[116] B. G. Marsden, *The Kozai Resonance in the Motions of Asteroids and Other Bodies*, **525C** (Nov., 1999) 934.

[117] C. Marchal, *The three-body problem*, 1990.

[118] R. S. Harrington, *Dynamical evolution of triple stars.*, **73** (Apr., 1968) 190–194.

[119] M. Delaunay, *Théorie du Mouvement de la Lune*, **21** (Jan., 1861) 80.

[120] H. Lei, C. Circi and E. Ortore, *Modified double-averaged Hamiltonian in hierarchical triple systems*, **481** (Dec., 2018) 4602–4620.

[121] D. Brouwer, *Solution of the problem of artificial satellite theory without drag*, **64** (Nov., 1959) 378.

[122] H. Goldstein, C. Poole and J. Safko, *Classical Mechanics*. Addison Wesley, 2002.

[123] M. L. Lidov and S. L. Ziglin, *Non-restricted double-averaged three body problem in Hill's case*, Celestial Mech. **13** (1976), no. 4 471–489.

[124] W. H. Jefferys and J. Moser, *Quasi-periodic Solutions for the three-body problem*, **71** (Sept., 1966) 568.

[125] F. Farago and J. Laskar, *High-inclination orbits in the secular quadrupolar three-body problem*, Monthly Notices of the Royal Astronomical Society **401** (01, 2010) 1189–1198 [https://academic.oup.com/mnras/article-pdf/401/2/1189/3966087/mnras0401-118

[126] J. Laskar and G. Boué, *Explicit expansion of the three-body disturbing function for arbitrary eccentricities and inclinations*, **522** (Nov., 2010) A60 [1008.2947].

[127] R. A. Mardling, *The determination of planetary structure in tidally relaxed inclined systems*, Monthly Notices of the Royal Astronomical Society **407** (2010), no. 2 1048–1069 [https://onlinelibrary.wiley.com/doi/pdf/10.1111/j.1365-2966.2010.16814.x].

[128] B. Katz and S. Dong, *Exponential growth of eccentricity in secular theory*, 1105.3953.

[129] K. A. Innanen, J. Q. Zheng, S. Mikkola and M. J. Valtonen, *The Kozai Mechanism and the Stability of Planetary Orbits in Binary Star Systems*, **113** (May, 1997) 1915.

[130] H. Kinoshita and H. Nakai, *General solution of the Kozai mechanism*, Celestial Mechanics and Dynamical Astronomy **98** (May, 2007) 67–74.

[131] M. Valtonen and H. Karttunen, *The Three-Body Problem*. 2006.

[132] Yokoyama, T., Santos, M. T., Cardin, G. and Winter, O. C., *On the orbits of the outer satellites of jupiter*, AA **401** (2003), no. 2 763–772.

[133] B. Katz, S. Dong and R. Malhotra, *Long-term cycling of kozai-lidov cycles: Extreme eccentricities and inclinations excited by a distant eccentric perturber*, Phys. Rev. Lett. **107** (Oct, 2011) 181101.

[134] S. Naoz, W. M. Farr, Y. Lithwick, F. A. Rasio and J. Teyssandier, *Hot jupiters from secular planet–planet interactions*, Nature **473** (2011), no. 7346 187–189.

[135] G. Li, S. Naoz, M. Holman and A. Loeb, *Chaos in the test particle eccentric kozai–lidov mechanism*, The Astrophysical Journal **791** (jul, 2014) 86.

[136] D. Fabrycky and S. Tremaine, *Shrinking binary and planetary orbits by kozai cycles with tidal friction**, The Astrophysical Journal **669** (nov, 2007) 1298.

[137] G. Li, S. Naoz, B. Kocsis and A. Loeb, *Eccentricity growth and orbit flip in near-coplanar hierarchical three-body systems*, The Astrophysical Journal **785** (apr, 2014) 116.

[138] W. D. Cochran, A. P. Hatzes, R. P. Butler and G. W. Marcy, *Detection of a planetary companion to 16 Cygni B.*, in *Bulletin of the American Astronomical Society*, vol. 28, p. 1111, Sept., 1996.

[139] F. Baron, J. D. Monnier, E. Pedretti, M. Zhao, G. Schaefer, R. Parks, X. Che, N. Thureau, T. A. ten Brummelaar, H. A. McAlister, S. T. Ridgway, C. Farrington, J. Sturmann, L. Sturmann and N. Turner, *Imaging the algol triple system in the h band with the chara interferometer*, The Astrophysical Journal **752** (may, 2012) 20.

[140] B. Liu, D. Lai and Y.-H. Wang, *Binary mergers near a supermassive black hole: Relativistic effects in triples*, The Astrophysical Journal Letters **883** (sep, 2019) L7.

[141] B. Liu, D. J. Muñoz and D. Lai, *Suppression of extreme orbital evolution in triple systems with short-range forces*, **447** (Feb., 2015) 747–764 [1409.6717].

[142] C. W. Misner, K. S. Thorne and J. A. Wheeler, *Gravitation*. 1973.

[143] J. M. O. Antognini, *Timescales of Kozai-Lidov oscillations at quadrupole and octupole order in the test particle limit*, **452** (Oct., 2015) 3610–3619 [1504.05957].

[144] E. B. Ford, B. Kozinsky and F. A. Rasio, *Secular Evolution of Hierarchical Triple Star Systems*, **535** (May, 2000) 385–401.

[145] M. C. Miller and D. P. Hamilton, *Four-Body Effects in Globular Cluster Black Hole Coalescence*, **576** (Sept., 2002) 894–898 [astro-ph/0202298].

[146] O. Blaes, M. H. Lee and A. Socrates, *The Kozai Mechanism and the Evolution of Binary Supermassive Black Holes*, **578** (Oct., 2002) 775–786 [astro-ph/0203370].

[147] L. Wen, *On the eccentricity distribution of coalescing black hole binaries driven by the Kozai mechanism in globular clusters*, Astrophys. J. **598** (2003) 419–430 [astro-ph/0211492].

[148] N. Seto, *Highly Eccentric Kozai Mechanism and Gravitational-Wave Observation for Neutron Star Binaries*, Phys. Rev. Lett. **111** (2013) 061106 [1304.5151].

[149] J. M. Antognini, B. J. Shappee, T. A. Thompson and P. Amaro-Seoane, *Rapid eccentricity oscillations and the mergers of compact objects in hierarchical triples*, Monthly Notices of the Royal Astronomical Society **439** (02, 2014) 1079–1091 [https://academic.oup.com/mnras/article-pdf/439/1/1079/5629347/stu039.pdf].

[150] X. Chen, S. Li and Z. Cao, *Mass–redshift degeneracy for the gravitational-wave sources in the vicinity of supermassive black holes*, Monthly Notices of the Royal Astronomical Society: Letters **485** (04, 2019) L141–L145 [https://academic.oup.com/mnrasl/article-pdf/485/1/L141/56977202/mnrasl_485_1

[151] X. Chen, *Distortion of Gravitational-Wave Signals by Astrophysical Environments*, in *Handbook of Gravitational Wave Astronomy* (C. Bambi, S. Katsanevas and K. D. Kokkotas, eds.), p. 39. 2021.

[152] E. Addison, P. Laguna and S. Larson, *Busting Up Binaries: Encounters Between Compact Binaries and a Supermassive Black Hole*, 1501.07856.

[153] X. Chen and W.-B. Han, *Extreme-mass-ratio inspirals produced by tidal capture of binary black holes*, Communications Physics **1** (2018), no. 1 53.

[154] I. Adachi, C. Hayashi and K. Nakazawa, *The Gas Drag Effect on the Elliptic Motion of a Solid Body in the Primordial Solar Nebula*, Progress of Theoretical Physics **56** (12, 1976) 1756–1771 [https://academic.oup.com/ptp/article-pdf/56/6/1756/5174571/56-6-1756.pdf].

[155] W. R. Ward, *Protoplanet migration by nebula tides*, Icarus **126** (1997), no. 2 261–281.

[156] E. H. E. H. Levy and J. I. Lunine, *Protostars and planets III*. Space science series. University of Arizona Press, Tucson, 1993.

[157] A. N. Youdin and F. H. Shu, *Planetesimal formation by gravitational instability*, The Astrophysical Journal **580** (nov, 2002) 494.

[158] Z. Pan and H. Yang, *Formation rate of extreme mass ratio inspirals in active galactic nuclei*, **103** (May, 2021) 103018 [2101.09146].

[159] M. Abramowicz, M. Jaroszynski and M. Sikora, *Relativistic, accreting disks.*, **63** (Feb., 1978) 221–224.

[160] M. A. Abramowicz, B. Czerny, J. P. Lasota and E. Szuszkiewicz, *Slim Accretion Disks*, **332** (Sept., 1988) 646.

[161] D. Lancová, D. Abarca, W. Kluźniak, M. Wielgus, A. Sadowski, R. Narayan, J. Schee, G. Török and M. Abramowicz, *Puffy accretion disks: Sub-eddington, optically thick, and stable*, The Astrophysical Journal Letters **884** (oct, 2019) L37.

[162] S. K. Chakrabarti, *Binary Black Holes in Stationary Orbits and a Test of the Active Galactic Nucleus Paradigm*, **411** (July, 1993) 610.

[163] S. K. Chakrabarti, *Gravitational wave emission from a binary black hole system in the presence of an accretion disk*, Phys. Rev. D **53** (Mar, 1996) 2901–2907.

[164] D. Molteni, G. Gerardi and S. K. Chakrabarti, *Simulation of Interactions of an Orbiting Compact Star with an Accretion Disk by Smoothed Particle Hydrodynamics*, **436** (Nov., 1994) 249.

[165] M. Gröbner, W. Ishibashi, S. Tiwari, M. Haney and P. Jetzer, *Binary black hole mergers in AGN accretion discs: gravitational wave rate density estimates*, **638** (June, 2020) A119 [2005.03571].

[166] K.-i. Maeda, P. Gupta and H. Okawa, *Dynamics of a binary system around a supermassive black hole*, Phys. Rev. D **107** (2023), no. 12 124039 [2303.16553].

[167] K. S. Thorne and J. B. Hartle, *Laws of motion and precession for black holes and other bodies*, Phys. Rev. D **31** (Apr, 1985) 1815–1837.

[168] F. Camilloni, G. Grignani, T. Harmark, R. Oliveri, M. Orselli and D. Pica, *Tidal deformations of a binary system induced by an external Kerr black hole*, Phys. Rev. D **107** (2023), no. 8 084011 [2301.04879].

[169] B. Carter, *Global structure of the kerr family of gravitational fields*, Phys. Rev. **174** (Oct, 1968) 1559–1571.

[170] J. M. Bardeen, W. H. Press and S. A. Teukolsky, *Rotating Black Holes: Locally Nonrotating Frames, Energy Extraction, and Scalar Synchrotron Radiation*, **178** (Dec., 1972) 347–370.

[171] C. W. Misner, K. S. Thorne and J. A. Wheeler, *Gravitation*. 1973.

[172] W. Rindler and V. Perlick, *Rotating coordinates as tools for calculating circular geodesics and gyroscopic precession*, General Relativity and Gravitation **22** (Sept., 1990) 1067–1081.

[173] W. de Sitter, *Einstein's theory of gravitation and its astronomical consequences. Third paper*, Mon. Not. Roy. Astron. Soc. **78** (Nov., 1917) 3–28.

[174] L. I. Schiff, *Possible new experimental test of general relativity theory*, Phys. Rev. Lett. **4** (Mar, 1960) 215–217.

[175] D. Bini, A. Geralico and R. T. Jantzen, *Gyroscope precession along bound equatorial plane orbits around a Kerr black hole*, Phys. Rev. D **94** (2016), no. 6 064066 [1607.08427].

[176] J. M. Bardeen, W. H. Press and S. A. Teukolsky, *Rotating black holes: Locally nonrotating frames, energy extraction, and scalar synchrotron radiation*, Astrophys. J. **178** (1972) 347.

[177] H. Goldstein, *Classical Mechanics*. Addison-Wesley, 1980.

[178] C. M. Will, *Incorporating post-newtonian effects in n-body dynamics*, Phys. Rev. D **89** (Feb, 2014) 044043.

[179] A. Kuntz, F. Serra and E. Trincherini, *Effective two-body approach to the hierarchical three-body problem: Quadrupole to 1PN*, Phys. Rev. D **107** (2023), no. 4 044011 [2210.13493].

[180] C. Petrovich and F. Antonini, *Greatly enhanced merger rates of compact-object binaries in non-spherical nuclear star clusters*, Astrophys. J. **846** (2017), no. 2 146 [1705.05848].

[181] B. Liu and D. Lai, *Spin–Orbit Misalignment of Merging Black Hole Binaries with Tertiary Companions*, Astrophys. J. Lett. **846** (2017), no. 1 L11 [1706.02309].

[182] O. Blaes, M. H. Lee and A. Socrates, *The kozai mechanism and the evolution of binary supermassive black holes*, Astrophys. J. **578** (2002) 775–786 [astro-ph/0203370].

[183] P. C. Peters and J. Mathews, *Gravitational radiation from point masses in a keplerian orbit*, Phys. Rev. **131** (Jul, 1963) 435–440.

[184] L. D. Landau and E. M. Lifschits, *The Classical Theory of Fields*, vol. Volume 2 of *Course of Theoretical Physics*. Pergamon Press, Oxford, 1975.

[185] F. Antonini and H. B. Perets, *Secular evolution of compact binaries near massive black holes: Gravitational wave sources and other exotica*, Astrophys. J. **757** (2012) 27 [1203.2938].

[186] F. Tamburini, B. Thidé and M. Della Valle, *Measurement of the spin of the M87 black hole from its observed twisted light*, Mon. Not. Roy. Astron. Soc. **492** (2020), no. 1 L22–L27 [1904.07923].

[187] **Event Horizon Telescope** Collaboration, K. Akiyama *et. al.*, *First M87 Event Horizon Telescope Results. V. Physical Origin of the Asymmetric Ring*, Astrophys. J. Lett. **875** (2019), no. 1 L5 [1906.11242].

[188] A. Cárdenas-Avendaño and C. F. Sopuerta, *Testing Gravity with Extreme-Mass-Ratio Inspirals*, pp. 275–359. Springer Nature Singapore, Singapore, 2024.

[189] S. Babak, J. Gair, A. Sesana, E. Barausse, C. F. Sopuerta, C. P. L. Berry, E. Berti, P. Amaro-Seoane, A. Petiteau and A. Klein, *Science with the space-based interferometer lisa. v. extreme mass-ratio inspirals*, Phys. Rev. D **95** (May, 2017) 103012.

[190] P. Amaro-Seoane, C. F. Sopuerta and M. D. Freitag, *The role of the supermassive black hole spin in the estimation of the EMRI event rate*, Monthly Notices of the Royal Astronomical Society **429** (01, 2013) 3155–3165 [https://academic.oup.com/mnras/article-pdf/429/4/3155/3304923/sts572.pdf].

[191] M. C. Miller, M. Freitag, D. P. Hamilton and V. M. Lauburg, *Binary Encounters with Supermassive Black Holes: Zero-Eccentricity LISA Events*, **631** (Oct., 2005) L117–L120 [astro-ph/0507133].

[192] Y. Raveh and H. B. Perets, *Extreme mass-ratio gravitational-wave sources: mass segregation and post binary tidal-disruption captures*, Monthly Notices of the Royal Astronomical Society **501** (12, 2020) 5012–5020 [https://academic.oup.com/mnras/article-pdf/501/4/5012/35924284/staa4001.pdf].

[193] M. Giersz, N. Leigh, A. Hypki, N. Lützgendorf and A. Askar, *MOCCA code for star cluster simulations - IV. A new scenario for intermediate mass black hole formation in globular clusters*, **454** (Dec., 2015) 3150–3165 [1506.05234].

[194] M. Arca-Sedda, P. Amaro-Seoane and X. Chen, *Merging stellar and intermediate-mass black holes in dense clusters: implications for LIGO, LISA, and the next generation of gravitational wave detectors*, Astron. Astrophys. **652** (2021) A54 [2007.13746].

[195] P. Amaro-Seoane, *Relativistic dynamics and extreme mass ratio inspirals*, Living Rev. Rel. **21** (2018), no. 1 4 [1205.5240].

[196] P. Amaro-Seoane, *The gravitational capture of compact objects by massive black holes*, 2011.03059.

[197] P. Amaro-Seoane, J. R. Gair, M. Freitag, M. Coleman Miller, I. Mandel, C. J. Cutler and S. Babak, *Astrophysics, detection and science applications of intermediate- and extreme mass-ratio inspirals*, Class. Quant. Grav. **24** (2007) R113–R169 [astro-ph/0703495].

[198] L. J. Rubbo, K. Holley-Bockelmann and L. S. Finn, *Event rate for extreme mass ratio burst signals in the laser interferometer space antenna band*, The Astrophysical Journal **649** (sep, 2006) L25.

[199] P. Amaro-Seoane, *Extremely large mass-ratio inspirals*, Phys. Rev. D **99** (Jun, 2019) 123025.

[200] J. R. Gair, I. Mandel, M. C. Miller and M. Volonteri, *Exploring intermediate and massive black-hole binaries with the einstein telescope*, General Relativity and Gravitation **43** (2011), no. 2 485–518.

[201] S. Konstantinidis, P. Amaro-Seoane and K. D. Kokkotas, *Investigating the retention of intermediate-mass black holes in star clusters using N-body simulations*, **557** (Sept., 2013) A135 [1108.5175].

[202] C.-J. Haster, Z. Wang, C. P. L. Berry, S. Stevenson, J. Veitch and I. Mandel, *Inference on gravitational waves from coalescences of stellar-mass compact objects and intermediate-mass black holes*, Monthly Notices of the Royal Astronomical Society **457** (02, 2016) 4499–4506 [https://academic.oup.com/mnras/article-pdf/457/4/4499/18514495/stw233.pdf].

[203] P. Amaro-Seoane, *Detecting intermediate-mass ratio inspirals from the ground and space*, Phys. Rev. D **98** (Sep, 2018) 063018.

[204] **LISA Cosmology Working Group** Collaboration, P. Auclair *et. al.*, *Cosmology with the Laser Interferometer Space Antenna*, Living Rev. Rel. **26** (2023), no. 1 5 [2204.05434].

[205] D. Laghi, N. Tamanini, W. Del Pozzo, A. Sesana, J. Gair, S. Babak and D. Izquierdo-Villalba, *Gravitational-wave cosmology with extreme mass-ratio inspirals*, Mon. Not. Roy. Astron. Soc. **508** (2021), no. 3 4512–4531 [2102.01708].

[206] E. Barausse *et. al.*, *Prospects for Fundamental Physics with LISA*, Gen. Rel. Grav. **52** (2020), no. 8 81 [2001.09793].

[207] **LISA** Collaboration, K. G. Arun *et. al.*, *New horizons for fundamental physics with LISA*, Living Rev. Rel. **25** (2022), no. 1 4 [2205.01597].

[208] B. Carter, *Hamilton-Jacobi and Schrödinger separable solutions of Einstein's equations*, Communications in Mathematical Physics **10** (1968), no. 4 280 – 310.

[209] B. Carter, *Black holes equilibrium states*, in *Les Houches Summer School of Theoretical Physics: Black Holes*, pp. 57–214, 1973.

[210] M. van de Meent, *Analytic solutions for parallel transport along generic bound geodesics in Kerr spacetime*, Class. Quant. Grav. **37** (2020), no. 14 145007 [1906.05090].

[211] K. Alvi, *An Approximate binary black hole metric*, Phys. Rev. D **61** (2000) 124013 [gr-qc/9912113].

[212] E. Poisson, *Retarded coordinates based at a world line, and the motion of a small black hole in an external universe*, Phys. Rev. D **69** (2004) 084007 [gr-qc/0311026].

[213] E. Poisson, *The Motion of point particles in curved space-time*, Living Rev. Rel. **7** (2004) 6 [gr-qc/0306052].

[214] S. L. Detweiler, *A Consequence of the gravitational self-force for circular orbits of the Schwarzschild geometry*, Phys. Rev. D **77** (2008) 124026 [0804.3529].

[215] S. Isoyama, L. Barack, S. R. Dolan, A. Le Tiec, H. Nakano, A. G. Shah, T. Tanaka and N. Warburton, *Gravitational Self-Force Correction to the Innermost Stable Circular Equatorial Orbit of a Kerr Black Hole*, Phys. Rev. Lett. **113** (2014), no. 16 161101 [1404.6133].

[216] S. Chandrasekhar, *The Mathematical Theory of Black Holes*. International series of monographs on physics. Clarendon Press, 1998.

[217] M. A. Abramowicz, M. Jaroszynski, S. Kato, J.-P. Lasota, A. Rozanska and A. Sadowski, *Leaving the ISCO: the inner edge of a black-hole accretion disk at various luminosities*, Astron. Astrophys. **521** (2010) A15 [1003.3887].

[218] V. Cardoso, A. S. Miranda, E. Berti, H. Witek and V. T. Zanchin, *Geodesic stability, Lyapunov exponents and quasinormal modes*, Phys. Rev. D **79** (2009), no. 6 064016 [0812.1806].

[219] V. Cardoso, E. Franzin and P. Pani, *Is the gravitational-wave ringdown a probe of the event horizon?*, Phys. Rev. Lett. **116** (2016), no. 17 171101 [1602.07309]. [Erratum: Phys.Rev.Lett. 117, 089902 (2016)].

[220] H. Yang, *Relating Black Hole Shadow to Quasinormal Modes for Rotating Black Holes*, Phys. Rev. D **103** (2021), no. 8 084010 [2101.11129].

[221] M. D. Johnson *et. al.*, *Universal interferometric signatures of a black hole's photon ring*, Sci. Adv. **6** (2020), no. 12 eaaz1310 [1907.04329].

[222] S. E. Gralla, *Measuring the shape of a black hole photon ring*, Phys. Rev. D **102** (2020), no. 4 044017 [2005.03856].

[223] S. E. Gralla, A. Lupsasca and D. P. Marrone, *The shape of the black hole photon ring: A precise test of strong-field general relativity*, Phys. Rev. D **102** (Dec, 2020) 124004.

[224] B. Carter, *Axisymmetric Black Hole Has Only Two Degrees of Freedom*, Phys. Rev. Lett. **26** (1971) 331–333.

[225] W. Israel, *Event horizons in static electrovac space-times*, Commun. Math. Phys. **8** (1968) 245–260.

[226] S. W. Hawking, *Black holes in general relativity*, Communications in Mathematical Physics **25** (June, 1972) 152–166.

[227] D. C. Robinson, *Classification of black holes with electromagnetic fields*, Phys. Rev. D **10** (Jul, 1974) 458–460.

[228] Y. Gong, Z. Cao, H. Gao and B. Zhang, *On neutralization of charged black holes*, Mon. Not. Roy. Astron. Soc. **488** (2019), no. 2 2722–2731 [1907.05239].

[229] R. Narayan, *Black holes in astrophysics*, New J. Phys. **7** (2005) 199 [gr-qc/0506078].

[230] I. Contopoulos, D. Kazanas and D. B. Papadopoulos, *The force-free magnetosphere of a rotating black hole*, The Astrophysical Journal **765** (Feb., 2013) 113.

[231] A. Tchekhovskoy, R. Narayan and J. C. McKinney, *Efficient generation of jets from magnetically arrested accretion on a rapidly spinning black hole*, Monthly Notices of the Royal Astronomical Society: Letters **418** (11, 2011) L79–L83 [https://academic.oup.com/mnrasl/article-pdf/418/1/L79/56939896/mnrasl_418_1_

[232] X. Li, F.-W. Zhang, Q. Yuan, Z.-P. Jin, Y.-Z. Fan, S.-M. Liu and D.-M. Wei, *Implications of the tentative association between gw150914 and a fermi-gbm transient*, The Astrophysical Journal Letters **827** (Aug., 2016) L16.

[233] R. Perna, D. Lazzati and B. Giacomazzo, *Short gamma-ray bursts from the merger of two black holes*, The Astrophysical Journal Letters **821** (apr, 2016) L18.

[234] B. Zhang, *Mergers of charged black holes: Gravitational-wave events, short gamma-ray bursts, and fast radio bursts*, The Astrophysical Journal Letters **827** (aug, 2016) L31.

[235] F. C. Michel, *Theory of pulsar magnetospheres*, Rev. Mod. Phys. **54** (Jan, 1982) 1–66.

[236] R. Ruffini and A. Treves, *On a Magnetized Rotating Sphere*, **13** (Feb., 1973) 109.

[237] B. Carter, *Black hole equilibrium states*. Gordon and Breach, Science Publishers, Inc, United States, 1973.

[238] A. S. Eddington, *The Internal Constitution of the Stars*. Cambridge Science Classics. Cambridge University Press, 1988.

[239] M. Zajacek and A. Tursunov, *Electric charge of black holes: Is it really always negligible?*, 2019.

[240] J. Bally and E. R. Harrison, *The electrically polarized universe.*, **220** (Mar., 1978) 743.

[241] M. Zajacek, A. Tursunov, A. Eckart, S. Britzen, E. Hackmann, V. Karas, Z. Stuchl´ik, B. Czerny and J. A. Zensus, *Constraining the charge of the galactic centre black hole*, Journal of Physics: Conference Series **1258** (Oct., 2019) 012031.

[242] J. Schwinger, *On Gauge Invariance and Vacuum Polarization*, Physical Review **82** (June, 1951) 664–679.

[243] G. W. Gibbons, *Vacuum Polarization and the Spontaneous Loss of Charge by Black Holes*, Commun. Math. Phys. **44** (1975) 245–264.

[244] O. J. C. Dias, M. Godazgar, J. E. Santos, G. Carullo, W. Del Pozzo and D. Laghi, *Eigenvalue repulsions in the quasinormal spectra of the Kerr-Newman black hole*, Phys. Rev. D **105** (2022), no. 8 084044 [2109.13949].

[245] G. Carullo, D. Laghi, N. K. Johnson-McDaniel, W. Del Pozzo, O. J. C. Dias, M. Godazgar and J. E. Santos, *Constraints on Kerr-Newman black holes from merger-ringdown gravitational-wave observations*, Phys. Rev. D **105** (2022), no. 6 062009 [2109.13961].

[246] C. A. Benavides-Gallego and W.-B. Han, *Gravitational waves and electromagnetic radiation from charged black hole binaries*, Symmetry **15** (Feb., 2023) 537.

[247] G. Bozzola and V. Paschalidis, *General relativistic simulations of the quasicircular inspiral and merger of charged black holes: Gw150914 and fundamental physics implications*, Physical Review Letters **126** (Jan., 2021).

[248] Christiansen, J. B. Jiménez and D. F. Mota, *Charged black hole mergers: orbit circularisation and chirp mass bias*, Classical and Quantum Gravity **38** (Mar., 2021) 075017.

[249] L. Liu, Christiansen, Z.-K. Guo, R.-G. Cai and S. P. Kim, *Gravitational and electromagnetic radiation from binary black holes with electric and magnetic charges: Circular orbits on a cone*, Physical Review D **102** (Nov., 2020).

[250] P. A. M. Dirac, *Quantised singularities in the electromagnetic field,*, Proceedings of the Royal Society of London. Series A, Containing Papers of a Mathematical and Physical Character **133** (1931), no. 821 60–72 [https://royalsocietypublishing.org/doi/pdf/10.1098/rspa.1931.0130].

[251] G. 't Hooft, *Magnetic Monopoles in Unified Gauge Theories*, Nucl. Phys. B **79** (1974) 276–284.

[252] A. M. Polyakov, *Particle Spectrum in Quantum Field Theory*, JETP Lett. **20** (1974) 194–195.

[253] R. S. Hanni, *Limits on the charge of a collapsed object*, Phys. Rev. D **25** (May, 1982) 2509–2514.

[254] J. Ambjorn and P. Olesen, *On electroweak magnetism*, Nuclear Physics B **315** (1989), no. 3 606–614.

[255] J. Ambjorn and P. Olesen, *Electroweak Magnetism: Theory and Application*, Int. J. Mod. Phys. A **5** (1990) 4525–4558.

[256] J. Ambjorn and P. Olesen, *A condensate solution of the electroweak theory which interpolates between the broken and the symmetric phase*, Nuclear Physics B **330** (1990), no. 1 193–204.

[257] J. Ambjorn and P. Olesen, *Electroweak magnetism, w-condensation and anti-screening*, 1993.

[258] K. Lee and E. J. Weinberg, *Nontopological magnetic monopoles and new magnetically charged black holes*, Physical Review Letters **73** (Aug., 1994) 1203–1206.

[259] Y. Bai, J. Berger, M. Korwar and N. Orlofsky, *Phenomenology of magnetic black holes with electroweak-symmetric coronas*, Journal of High Energy Physics **2020** (Oct., 2020).

[260] J. Garc´ia-Bellido, A. Linde and D. Wands, *Density perturbations and black hole formation in hybrid inflation*, Physical Review D **54** (Nov., 1996) 6040–6058.

[261] V. Cardoso, C. F. Macedo, P. Pani and V. Ferrari, *Black holes and gravitational waves in models of minicharged dark matter*, Journal of Cosmology and Astroparticle Physics **2016** (May, 2016) 054–054.

[262] A. De Rújula, S. Glashow and U. Sarid, *Charged dark matter*, Nuclear Physics B **333** (1990), no. 1 173–194.

[263] Y. Kim and A. Kobakhidze, *Topologically induced black hole charge and its astrophysical manifestations*, 2020.

[264] I. Bah and P. Heidmann, *Topological stars and black holes*, Physical Review Letters **126** (Apr., 2021).

[265] I. Bah and P. Heidmann, *Topological stars, black holes and generalized charged weyl solutions*, Journal of High Energy Physics **2021** (Sept., 2021).

[266] J. Maldacena, A. Milekhin and F. Popov, *Traversable wormholes in four dimensions*, 2020.

[267] J. A. Dror, B. V. Lehmann, H. H. Patel and S. Profumo, *Discovering new forces with gravitational waves from supermassive black holes*, Physical Review D **104** (Oct., 2021).

[268] M. O. E. Hadj and S. R. Dolan, *Conversion of electromagnetic and gravitational waves by a charged black hole*, Physical Review D **106** (Aug., 2022).

[269] H. Reissner, *Über die Eigengravitation des elektrischen Feldes nach der Einsteinschen Theorie*, Oct., 2018.

[270] G. Nordström, *On the Energy of the Gravitation field in Einstein's Theory*, Koninklijke Nederlandse Akademie van Wetenschappen Proceedings Series B Physical Sciences **20** (Jan., 1918) 1238–1245.

[271] R. Emparan, M. Mart´inez and M. Zilhão, *Black hole fusion in the extreme mass ratio limit*, Physical Review D **97** (Feb., 2018).

[272] R. Emparan and D. Mar´in, *Precursory collapse in neutron star-black hole mergers*, Physical Review D **102** (July, 2020).

[273] S. Bernuzzi and A. Nagar, *Binary black hole merger in the extreme-mass-ratio limit: A multipolar analysis*, Physical Review D **81** (Apr., 2010).

[274] A. Nagar, T. Damour and A. Tartaglia, *Binary black hole merger in the extreme-mass-ratio limit*, Classical and Quantum Gravity **24** (May, 2007) S109–S123.

[275] A. Buonanno and T. Damour, *Effective one-body approach to general relativistic two-body dynamics*, Physical Review D **59** (Mar., 1999).

[276] T. Damour, A. Nagar, M. Hannam, S. Husa and B. Brügmann, *Accurate effective-one-body waveforms of inspiralling and coalescing black-hole binaries*, Physical Review D **78** (Aug., 2008).

[277] S. Albanesi, A. Nagar and S. Bernuzzi, *Effective one-body model for extreme-mass-ratio spinning binaries on eccentric equatorial orbits: Testing radiation reaction and waveform*, Physical Review D **104** (July, 2021).

[278] A. Nagar, A. Bonino and P. Rettegno, *Effective one-body multipolar waveform model for spin-aligned, quasicircular, eccentric, hyperbolic black hole binaries*, Physical Review D **103** (May, 2021).

[279] S. Bernuzzi, A. Nagar and A. Zenginoğlu, *Binary black hole coalescence in the extreme-mass-ratio limit: Testing and improving the effective-one-body multipolar waveform*, Physical Review D **83** (Mar., 2011).

[280] T. Damour and A. Nagar, *The effective one body description of the two-body problem*, 2009.

[281] A. Strominger and C. Vafa, *Microscopic origin of the bekenstein-hawking entropy*, Physics Letters B **379** (June, 1996) 99–104.

[282] S. M. Carroll, M. C. Johnson and L. Randall, *Extremal limits and black hole entropy*, Journal of High Energy Physics **2009** (Nov., 2009) 109–109.

[283] L. S. Finn, *Gravitational Wave Astronomy*, p. 95–110. Springer Netherlands, 1997.

[284] A. W. Peet, *Tasi lectures on black holes in string theory*, in *Strings, Branes and Gravity*, p. 353–433, WORLD SCIENTIFIC, Oct., 2001.

[285] S. L. Shapiro, S. A. Teukolsky and J. Winicour, *Toroidal black holes and topological censorship*, Phys. Rev. D **52** (Dec, 1995) 6982–6987.

[286] L. Lehner, N. T. Bishop, R. Gómez, B. Szilagyi and J. Winicour, *Exact solutions for the intrinsic geometry of black hole coalescence*, Physical Review D **60** (July, 1999).

[287] S. Husa and J. Winicour, *Asymmetric merger of black holes*, Physical Review D **60** (Sept., 1999).

[288] M. Siino and T. Koike, *Topological classification of black hole: Generic Maxwell set and crease set of horizon*, Int. J. Mod. Phys. D **20** (2011) 1095–1122 [gr-qc/0405056].

[289] M. Abramowitz and I. Stegun, *Handbook of Mathematical Functions: With Formulas, Graphs, and Mathematical Tables*. Applied mathematics series. Dover Publications, 1965.

[290] L. Liu, Christiansen, W.-H. Ruan, Z.-K. Guo, R.-G. Cai and S. P. Kim, *Gravitational and electromagnetic radiation from binary black holes with electric and magnetic charges: elliptical orbits on a cone*, The European Physical Journal C **81** (Nov., 2021).

[291] L. Liu, Z.-K. Guo, R.-G. Cai and S. P. Kim, *Merger rate distribution of primordial black hole binaries with electric charges*, Physical Review D **102** (Aug., 2020).

[292] J. M. Maldacena, *Tasi 2003 lectures on ads/cft*, 2004.

[293] V. Cardoso, E. Franzin, A. Maselli, P. Pani and G. Raposo, *Testing strong-field gravity with tidal love numbers*, Physical Review D **95** (Apr., 2017).

[294] E. Poisson, *Tidally induced multipole moments of a nonrotating black hole vanish to all post-newtonian orders*, Physical Review D **104** (Nov., 2021).

[295] M. Rai and L. Santoni, *Ladder symmetries and love numbers of reissner-nordström black holes*, Journal of High Energy Physics **2024** (July, 2024).

[296] D. Pereñiguez and V. Cardoso, *Love numbers and magnetic susceptibility of charged black holes*, Physical Review D **105** (Feb., 2022).

[297] P. Charalambous, *Love numbers and love symmetries for p-form and gravitational perturbations of higher-dimensional spherically symmetric black holes*, 2024.

[298] F. J. Zerilli, *Perturbation analysis for gravitational and electromagnetic radiation in a reissner-nordström geometry*, Phys. Rev. D **9** (Feb, 1974) 860–868.

[299] D. Pugliese, H. Quevedo and R. Ruffini, *Circular motion of neutral test particles in reissner-nordström spacetime*, Phys. Rev. D **83** (Jan, 2011) 024021.

[300] D. Pugliese, H. Quevedo and R. Ruffini, *Circular motion in reissner-nordström spacetime*, 2010.

[301] D. Pugliese, H. Quevedo and R. Ruffini, *Equatorial circular orbits of neutral test particles in the kerr-newman spacetime*, Physical Review D **88** (July, 2013).

[302] P. Das, R. Sk and S. Ghosh, *Motion of charged particle in reissner–nordström spacetime: a jacobi-metric approach*, The European Physical Journal C **77** (Nov., 2017).

[303] W. Liu, D. Wu and J. Wang, *Light rings and shadows of static black holes in effective quantum gravity*, Physics Letters B **858** (Nov., 2024) 139052.

[304] K. Meng, X.-L. Fan, S. Li, W.-B. Han and H. Zhang, *Dynamics of null particles and shadow for general rotating black hole*, Journal of High Energy Physics **2023** (2023), no. 11 141.

[305] N. Tsukamoto, *Gravitational lensing by a photon sphere in a reissner-nordström naked singularity spacetime in strong deflection limits*, Physical Review D **104** (Dec., 2021).

[306] L. Speri, S. Barsanti, A. Maselli, T. P. Sotiriou, N. Warburton, M. van de Meent, A. J. K. Chua, O. Burke and J. Gair, *Probing fundamental physics with Extreme Mass Ratio Inspirals: a full Bayesian inference for scalar charge*, 2406.07607.

[307] E. Maggio, M. van de Meent and P. Pani, *Extreme mass-ratio inspirals around a spinning horizonless compact object*, Phys. Rev. D **104** (2021), no. 10 104026 [2106.07195].

[308] J. R. Gair, C. Tang and M. Volonteri, *Lisa extreme-mass-ratio inspiral events as probes of the black hole mass function*, Physical Review D **81** (May, 2010).

[309] V. Baibhav, L. Barack, E. Berti, B. Bonga, R. Brito, V. Cardoso, G. Compère, S. Das, D. Doneva, J. Garcia-Bellido, L. Heisenberg, S. A. Hughes, M. Isi, K. Jani, C. Kavanagh, G. Lukes-Gerakopoulos, G. Mueller, P. Pani, A. Petiteau, S. Rajendran, T. P. Sotiriou, N. Stergioulas, A. Taylor, E. Vagenas, M. van de Meent, N. Warburton, B. Wardell, V. Witzany and A. Zimmerman, *Probing the nature of black holes: Deep in the mhz gravitational-wave sky*, Experimental Astronomy **51** (2021), no. 3 1385–1416.

[310] J. Thornburg, B. Wardell and M. van de Meent, *Excitation of Kerr quasinormal modes in extreme–mass-ratio inspirals*, Phys. Rev. Res. **2** (2020), no. 1 013365 [1906.06791].

[311] A. Cárdenas-Avendaño and C. F. Sopuerta, *Testing gravity with Extreme-Mass-Ratio Inspirals*, 2401.08085.

[312] T. Zi and C. Zhang, *Detecting the massive vector field with extreme mass-ratio inspirals*, 2406.11724.

[313] M. Della Rocca, S. Barsanti, L. Gualtieri and A. Maselli, *Extreme mass-ratio inspirals as probes of scalar fields: Inclined circular orbits around Kerr black holes*, Phys. Rev. D **109** (2024), no. 10 104079 [2401.09542].

[314] M. Rahman, S. Kumar and A. Bhattacharyya, *Probing astrophysical environment with eccentric extreme mass-ratio inspirals*, JCAP **01** (2024) 035 [2306.14971].

[315] M. van de Meent, *Modelling EMRIs with gravitational self-force: a status report*, J. Phys. Conf. Ser. **840** (2017), no. 1 012022.

[316] X. Feng and H. Yang, *Universal gravitational self-force for a point mass orbiting around a compact star*, Phys. Rev. D **110** (2024), no. 4 044066 [2406.02101].

[317] M. van de Meent, *Resonantly enhanced kicks from equatorial small mass-ratio inspirals*, Phys. Rev. D **90** (2014), no. 4 044027 [1406.2594].

[318] M. van de Meent, *Conditions for Sustained Orbital Resonances in Extreme Mass Ratio Inspirals*, Phys. Rev. D **89** (2014), no. 8 084033 [1311.4457].

[319] M. van de Meent, *Orbital resonances in small mass-ratio inspirals*, in *14th Marcel Grossmann Meeting on Recent Developments in Theoretical and Experimental General Relativity, Astrophysics, and Relativistic Field Theories*, vol. 2, pp. 1972–1977, 2017.

[320] B. Bonga, H. Yang and S. A. Hughes, *Tidal resonance in extreme mass-ratio inspirals*, Phys. Rev. Lett. **123** (2019), no. 10 101103 [1905.00030].

[321] P. Gupta, B. Bonga, A. J. K. Chua and T. Tanaka, *Importance of tidal resonances in extreme-mass-ratio inspirals*, Phys. Rev. D **104** (Aug, 2021) 044056.

[322] P. Lynch, V. Witzany, M. van de Meent and N. Warburton, *Fast inspirals and the treatment of orbital resonances*, 2405.21072.

[323] S. Avitan, R. Brustein and Y. Sherf, *Discovering Love numbers through resonance excitation during extreme mass ratio inspirals*, Class. Quant. Grav. **41** (2024), no. 14 145009 [2306.00173].

[324] Y. Jiang, W.-B. Han, X.-Y. Zhong, P. Shen, Z.-R. Luo and Y.-L. Wu, *Distinguishability of binary extreme-mass-ratio inspirals in low frequency band*, The European Physical Journal C **84** (2024), no. 5 478.

[325] K. Meng, H. Zhang, X.-L. Fan and Y. Yong, *Distinguish the EMRI and B-EMRI system by gravitational waves*, arXiv e-prints (May, 2024) arXiv:2405.07113 [2405.07113].

[326] J. Moffat, *Modified gravity (mog), cosmology and black holes*, Journal of Cosmology and Astroparticle Physics **2021** (Feb., 2021) 017–017.

[327] J. W. Moffat, *Black Holes in Modified Gravity (MOG)*, Eur. Phys. J. C **75** (2015), no. 4 175 [1412.5424].

[328] J. W. Moffat, *Scalar-tensor-vector gravity theory*, JCAP **03** (2006) 004 [gr-qc/0506021].

[329] L. Andrianopoli, R. D'Auria, S. Ferrara and M. Trigiante, *Extremal black holes in supergravity*, 2007.

[330] F. Camilloni, *Analytic Approaches to Relativistic Astrophysics*. PhD thesis, Aff1= Kobenhavns Universitet, Faculty of Science, Niels Bohr Institute, Theoretical high energy, astroparticle and gravitational physics, Niels Bohr Institute and Perugia University, 1, 2022.

[331] F. Camilloni, O. J. C. Dias, G. Grignani, T. Harmark, R. Oliveri, M. Orselli, A. Placidi and J. E. Santos, *Blandford-Znajek monopole expansion revisited: novel non-analytic contributions to the power emission*, JCAP **07** (2022), no. 07 032 [2201.11068].

[332] R. D. Blandford and R. L. Znajek, *Electromagnetic extraction of energy from Kerr black holes*, Monthly Notices of the Royal Astronomical Society **179** (07, 1977) 433–456 [https://academic.oup.com/mnras/article-pdf/179/3/433/9333653/mnras179-0433.

[333] R. Penrose, *Gravitational Collapse: the Role of General Relativity*, Nuovo Cimento Rivista Serie **1** (Jan., 1969) 252.

[334] E. Poisson, *The motion of point particles in curved spacetime*, Living Reviews in Relativity **7** (May, 2004).

[335] F. K. Manasse and C. W. Misner, *Fermi Normal Coordinates and Some Basic Concepts in Differential Geometry*, Journal of Mathematical Physics **4** (06, 1963) 735–745 [https://pubs.aip.org/aip/jmp/article-pdf/4/6/735/19206144/735_1_online.pdf].

[336] F. K. Manasse, *Distortion in the Metric of a Small Center of Gravitational Attraction due to its Proximity to a Very Large Mass*, Journal of Mathematical Physics **4** (06, 1963) 746–761 [https://pubs.aip.org/aip/jmp/article-pdf/4/6/746/19206186/746_1_online.pdf].

[337] K. Alvi, *Approximate binary-black-hole metric*, Phys. Rev. D **61** (May, 2000) 124013.

[338] K. Alvi, *Note on ingoing coordinates for binary black holes*, Phys. Rev. D **67** (May, 2003) 104006.

[339] E. Poisson, *Retarded coordinates based at a world line and the motion of a small black hole in an external universe*, Phys. Rev. D **69** (Apr, 2004) 084007.

[340] S. Comeau and E. Poisson, *Tidal interaction of a small black hole in the field of a large kerr black hole*, Phys. Rev. D **80** (Oct, 2009) 087501.

[341] V. P. Frolov and A. A. Shoom, *Interior of distorted black holes*, Phys. Rev. D **76** (Sep, 2007) 064037.

[342] S. Abdolrahimi, V. P. Frolov and A. A. Shoom, *Interior of a charged distorted black hole*, Phys. Rev. D **80** (Jul, 2009) 024011.

[343] T. Damour and O. M. Lecian, *Gravitational polarizability of black holes*, Phys. Rev. D **80** (Aug, 2009) 044017.

[344] N. Yunes and J. A. González, *Metric of a tidally perturbed spinning black hole*, Physical Review D **73** (Jan., 2006).

[345] X.-H. Zhang, *Multipole expansions of the general-relativistic gravitational field of the external universe*, Phys. Rev. D **34** (Aug, 1986) 991–1004.

[346] S. Detweiler, *Perspective on gravitational self-force analyses*, Classical and Quantum Gravity **22** (jul, 2005) S681.

[347] S. Detweiler, *Radiation reaction and the self-force for a point mass in general relativity*, Phys. Rev. Lett. **86** (Mar, 2001) 1931–1934.